

Ventilated Supercavitating Hydrofoils for Ride Control of High-Speed Craft

Bryce W. Pearce, B.Eng (Hons.)

National Centre for Maritime Engineering and Hydrodynamics
Australian Maritime College

Submitted in fulfilment of the requirements
for the degree of
Doctor of Philosophy

University of Tasmania

May 2011

Declaration of originality and authority of access

This thesis contains no material which has been accepted for a degree or diploma by the University or any other institution. Except by way of background information and duly acknowledged in the thesis, and to the best of the candidates knowledge and belief no material previously published or written by another person except where due acknowledgement is made in the text of the thesis, nor does the thesis contain any material that infringes copyright.

This thesis may be made available for loan and limited copying in accordance with the *Copyright Act 1968*.

.....
Bryce W. Pearce

Declaration of contribution to co-authored work

Pearce, B. W., P. A. Brandner and J. R. Binns. (2010). A numerical investigation of the viscous 2-D cavitating flow over a wall-mounted fence. In *Proceedings of the 17th Australasian Fluid Mechanics Conference*. Auckland, New Zealand: Paper 305.

This work included in this thesis, comprises contributions by the candidate (Bryce Pearce) including development of a boundary element method (BEM) computer code in collaboration with the primary supervisor (Paul Brandner), analysis of the problem using this BEM code, contributions in collaboration with the primary supervisor and co-author (Jonathon Binns) to development of a CFD model, consequently implemented and run by Jonathon Binns, analysis and presentation of the BEM and CFD data in collaboration with the primary supervisor, full preparation of the written manuscript except for an initial draft (Jonathon Binns) of the section on the implementation of the CFD model, including two figures.

.....
Paul A. Brandner (Primary Supervisor)

Abstract

An investigation into the hydrodynamic performance and flow field characteristics of a novel high-speed supercavitating hydrofoil concept proposed by Elms (1999) is presented. The hydrofoil is wedge-shaped with a supercavity detaching from geometric discontinuities at its trailing edges. Lift is generated by the asymmetry of the cavity/flow field created by trailing edge forward- and backward-facing steps. In this way bi-directional lift can be created from a symmetric hydrofoil. To ensure establishment and maintenance of a stable supercavity air is introduced by external ventilation via the hydrofoil base. The formation of the trailing edge steps would be practically realised by the deflection of a trailing flap. At zero incidence and flap deflection there would be no supercavity formed and no lift produced. The cavity formation from a hydrofoil by this mechanism is analogous to the separated flow over an ‘interceptor’ device fitted to the transom of a high-speed hull for trim and/or stearage control. Due to this similarity the concept has been termed an ‘intercepted hydrofoil’.

This hydrofoil configuration is analysed using a potential based 2-D non-linear boundary element method. For a given cavity length, the resulting cavity surface velocity and shape are determined in an iterative manner under prescribed constant pressure and flow tangency boundary conditions. Both infinite and confined flow domain cases of the boundary element analysis are presented. The latter case is of interest in providing blockage correction information for a future companion physical experimental program.

An optimum base-ventilated supercavitating hydrofoil profile is a compromise between limiting of the pressure minimum at the leading edge and maintaining stable cavity detachment from the trailing edges. These are both necessary so as to maintain the hydrofoil surfaces in a wetted condition, thereby ensuring that the generated forces remain steady and predictable. The greatest efficiency is obtained by using the smallest thickness to chord ratio with a sufficient margin against cavity breakdown allowing for variance in operating conditions.

Hydrodynamic performance of the ‘interceptor’ in isolation from the foil, i.e. cavitating flow over a wall-mounted fence, is also presented. Classical analytical, boundary element and Reynolds-Averaged Navier-Stokes equation based computational fluid dynamics methods were used for this analysis. The ‘ideal’ optimum hydrodynamic performance obtained from potential flow analysis is compared with the viscous flow numerical results.

Acknowledgments

It is with thankfulness that I acknowledge the encouragement and support of my Primary Supervisor, Associate Professor Paul Brandner. His enthusiasm, patience, wealth of knowledge and friendship is deeply appreciated.

I am also grateful to my Associate Supervisor, Professor Gregory Walker, for his advice, support and valuable assistance with the material presented in this thesis.

Financial support for this project was provided through an Australian Post Graduate Award, John Bicknell Research Scholarship and with significant additional support from the AMC CRL. Seed funding was also provided by Mr Tony Elms from Seastate Pty Ltd.

Special thanks to Brigid Freeman for advice and support above and beyond the call of duty. Thanks are also due to Dr. Jonathon Binns for his collaborative involvement and general encouragement and advice.

I would also like to express my gratitude to the technical staff at the CRL for their valuable assistance. Particularly to Mr Robert Wrigley, for his willingness to share his wealth of knowledge both technical and otherwise, and especially just for being a top bloke. Thanks also to the colleagues at Maritime Platforms Division Hydrodynamics Group from the DSTO, I have appreciated the advice, assistance, and the company during your visits to the CRL.

I also thank the Engineering Staff and Postgraduate Students, particularly to those I have shared an office with, here at AMC for providing a friendly and supportive environment throughout my studies and research.

I wish to express my indebtedness to my wife Melanie and our boys, for their continuous support, patience and love. I am also grateful to everyone else who provided encouragement and inspiration along the way.

Contents

| | |
|---|-----------|
| Abstract | iii |
| Nomenclature | viii |
| 1 Introduction | 1 |
| 1.1 Cavitating Lifting Surfaces | 1 |
| 1.2 Project Description | 7 |
| 1.3 Interceptor flows | 10 |
| 1.4 Hydrodynamic Performance Criteria | 12 |
| 1.5 Thesis Outline | 14 |
| 2 Modelling Free-Streamline (FS) Flows | 15 |
| 2.1 Introduction | 15 |
| 2.2 Analytical Methods | 17 |
| 2.2.1 Ideal flow over a normal plate | 18 |
| 2.2.2 FS flow over a normal plate - $\sigma_c = 0$ | 19 |
| 2.2.3 FS flow over a normal plate - $\sigma_c > 0$ | 20 |
| 2.3 Boundary Element Methods (BEM) | 23 |
| 2.3.1 Overview | 23 |
| 2.3.2 A BEM for 2-D Free-Streamline Flows | 24 |
| 2.3.3 Modelling Issues | 29 |
| 2.3.4 Comparison with other data | 34 |
| 2.4 Modelling cavitation with CFD | 34 |
| 2.5 Summary | 37 |
| 3 Wall-Mounted Fence Flow with Cavitation - Analytical and Numerical Methods | 38 |
| 3.1 Introduction | 38 |
| 3.2 Cavity shape | 39 |
| 3.3 Analytical analysis - Flow normal to a flat plate | 40 |
| 3.3.1 Ideal non-cavitating flow | 40 |
| 3.3.2 Free-streamline flow - $\sigma_c = 0$ | 41 |
| 3.3.3 Free-streamline flow - $\sigma_c > 0$ | 43 |
| 3.3.4 Results | 45 |
| 3.4 BEM analysis | 49 |

| | | |
|----------|---|------------|
| 3.4.1 | Fence Geometry | 49 |
| 3.4.2 | Boundary element model | 51 |
| 3.4.3 | Results: Cavity Shape | 53 |
| 3.4.4 | Results: Pressure distributions | 55 |
| 3.4.5 | Results: Hydrodynamic Coefficients | 64 |
| 3.5 | CFD analysis | 67 |
| 3.5.1 | CFD model | 67 |
| 3.5.2 | Results: Flow topology & cavity shape | 68 |
| 3.5.3 | Results: Upstream wall pressure distribution | 71 |
| 3.6 | Conclusions | 73 |
| 4 | Intercepted Base Ventilated Supercavitating Foil Flow - Numerical Analysis | 74 |
| 4.1 | Introduction | 74 |
| 4.2 | Criteria for Geometry Definition | 77 |
| 4.3 | Foil Section Geometry | 77 |
| 4.4 | The Foil/Cavity Body - Constraints and Dependencies | 83 |
| 4.5 | Surface Discretisation | 84 |
| 4.6 | Results | 87 |
| 4.6.1 | Cavity Shape | 87 |
| 4.6.2 | Pressure Distributions and Minima | 91 |
| 4.6.3 | Hydrodynamic Forces | 105 |
| 4.7 | Conclusions | 113 |
| 5 | Blockage Analysis of Supercavitating Foil Flow | 116 |
| 5.1 | Introduction | 116 |
| 5.2 | Results: Flat-Plate Foil | 118 |
| 5.2.1 | Cavity Shape | 118 |
| 5.2.2 | Pressure Distributions | 125 |
| 5.2.3 | Hydrodynamic Forces | 129 |
| 5.2.4 | Choked Flow | 136 |
| 5.3 | Results: Intercepted Foil | 141 |
| 5.4 | Conclusions | 146 |
| 6 | Conclusions and Future Recommendations | 147 |
| 6.1 | Conclusions | 147 |
| 6.2 | Future Recommendations | 150 |
| A | Publications Arising from the Work Undertaken in this Thesis | 151 |
| B | Experimental Design | 152 |
| B.1 | Introduction | 152 |
| B.2 | Aims | 152 |
| B.3 | Experimental Setup | 153 |
| B.3.1 | Foil Models | 153 |
| B.3.2 | AMC CRL Cavitation Tunnel Particulars | 157 |

| | | |
|----------|--|------------|
| B.3.3 | Model Arrangement in Test Section | 158 |
| B.4 | Experimental Procedure | 161 |
| B.4.1 | Basic Test Procedure | 161 |
| B.4.2 | Measurement of cavity pressure/cavitation number . . . | 161 |
| B.4.3 | Ventilation Air Supply and Measurement | 164 |
| C | Additional Foil Numerical Analysis Data | 165 |
| C.1 | Hydrodynamic coefficients versus σ_c with γ a parameter | 165 |
| C.2 | Hydrodynamic coefficients versus σ_c with h/c a parameter . . . | 170 |
| D | Additional Foil Numerical Analysis Blockage Data | 175 |
| D.1 | Flat-Plate Foil Data | 175 |
| D.1.1 | Cavity Shape | 175 |
| D.1.2 | Hydrodynamic Forces | 180 |
| D.2 | Intercepted Foil Data | 191 |
| D.2.1 | Cavity Shape | 191 |
| D.2.2 | Wall Pressure Distribution | 195 |
| D.2.3 | Hydrodynamic Data | 201 |
| E | Numerical analysis of basic base-ventilated supercavitating foil sections | 207 |
| E.1 | Introduction | 207 |
| E.2 | Foil Geometry | 207 |
| E.3 | Numerical Analysis | 210 |
| E.4 | Parameter Space | 210 |
| E.5 | Results | 210 |
| E.5.1 | Cavity Shape | 210 |
| E.5.2 | Pressure Coefficients | 211 |
| E.5.3 | Hydrodynamic Forces | 212 |
| | Bibliography | 228 |

Chapter 1

Introduction

1.1 Cavitating Lifting Surfaces

If the local pressure at some point in a flowing liquid falls below the vapor pressure then a change of phase is likely to occur. This change of phase from liquid to vapour due to a reduction of pressure is termed cavitation. Points of weakness are necessary within the liquid for this to occur. They are present in real liquids in the form of small gas or vapour inclusions¹ which operate as initiation sites for the liquid breakdown. These microbubbles within the bulk liquid are termed cavitation nuclei. In the absence of these sites it is possible for a liquid to withstand tensile stresses, i.e. negative absolute pressures, as do solids. For a description of nuclei and their influence on cavitation behaviour see Brennen (1995) and Franc and Michel (2004)².

A lifting surface or hydrofoil operating in a liquid at high speed and at an angle of incidence to the oncoming flow is susceptible to cavitation occurrence. The vaporisation of the liquid will occur at the point of lowest pressure, particularly in the vicinity of the leading edge suction peak if present. Cavitation on a lifting surface is usually detrimental in that it can result in the loss of performance and flow unsteadiness (Franc, 2001; Laberteaux and Ceccio, 2001). The latter effect results in the generation of noise and vibration and can lead to surface erosion damage (Auslaender, 1962; Conolly, 1975; Breslin and Andersen, 1994). The design and operation of these devices is focussed on the elimination or at least minimisation of cavitation. Hydrofoils are defined as lift producing devices operating immersed in a liquid medium. Within the context of marine vehicles, which are of interest here, the liquid is sea or fresh water. In the following text, the use of the term foil is used interchangeably with hydrofoil. If instead an aerofoil (i.e. a lift producing device operating in a gaseous medium) is to be considered then this will be explicitly stated.

The extent of the cavitating region which develops depends upon the flow conditions and the shape of the foil. A necessary, but insufficient, dimensionless

¹These may be present as either free bubbles or as inclusions on porous impurities (see Johnson and Hsieh, 1966).

²Nucleation phenomena is a specialised area and beyond the scope of the present work.

number or parameter of similitude applicable to characterise these flows is a form of the Euler number generally termed the cavitation number:

$$\sigma_v = \frac{p_\infty - p_v}{\frac{1}{2}\rho U_\infty^2} \quad (1.1)$$

where the static pressure in the numerator is expressed relative to the cavity pressure, assumed for vaporous cavities to be the liquid vapour pressure. p_∞ is the free stream static pressure; U_∞ the free stream velocity; p_v liquid vapour pressure; and ρ the liquid density.

Following Franc and Michel (2004) two distinct steps in cavitation development are identified:

- cavitation inception, describing the transition period between the non-cavitating and cavitating flow regimes; and
- developed cavitation, which is maintained after initiation by liquid vaporisation and diffusion of other non-condensable gases across a well-defined liquid-gaseous interface (i.e. cavity surface).

Cavitation inception, i.e. the initial formation of a cavity or a number of small cavities, is dependent on the presence of suitable nuclei. It will occur at the location of the minimum value of the pressure coefficient, $C_{p_{min}}$, if

$$-C_{p_{min}} = -\frac{p - p_\infty}{\frac{1}{2}\rho U_\infty^2} \geq \sigma_v \quad (1.2)$$

The amount that the minimum local pressure falls below the vapour pressure is termed the static delay to cavitation, and is a function of the nucleation conditions. In many practical circumstances this delay is small; it is usual to take as an estimate for the cavitation number at inception

$$\sigma_{vi} = -C_{p_{min}} \quad (1.3)$$

The negative sign stems from the definition of the pressure coefficient wherever the local pressure is reduced below that of the free stream static pressure.

The types of developed cavitation which occur vary substantially depending on the flow geometry and conditions. There is a large body of published work covering this complex field of research. Some of the more recent textbooks on the subject include Brennen (1995), Lecoffre (1999) and Franc and Michel (2004). Within the present context of 2-D foils at moderate angles of incidence to the oncoming flow³ attached or sheet cavities are formed over part or all of the suction side of the foil.

A further distinction is made between partial cavities which close on the foil surface and supercavities which close downstream from the foil trailing edge

³The type of cavitation varies significantly between small and moderate angles of incidence. The range of moderate incidence angle varies with the type of foil, but generally lies from 2 – 3° to 10° (see Lecoffre, 1999, p.72).

within the bulk liquid. This is an important distinction, particularly with regards to the effect that the unsteady cavity closure region has on the foil with partial cavitation (see Franc and Michel, 2004, Ch.7). This dynamic/unsteady cavity behaviour is the cause of the detrimental effects mentioned earlier in this section, i.e. the fluctuating force production, noise, vibration and surface damage. With supercavitation, once the cavity closure is sufficiently distant downstream of the foil trailing edge the foil is no longer affected by the unsteady closure region; a steady cavity is then formed in the vicinity of the foil trailing edge. In this regime the forces developed on the foil are steady and the noise, vibration and erosion effects are absent. To achieve this steady cavity flow the required minimum downstream distance to the cavity closure has been found to be ≈ 2 chord lengths (see Auslaender, 1962; Watanabe et al., 2001).

Figure 1.1 illustrates the development of cavitation in the flow over a foil as the cavitation number, σ_v , is reduced (from top to bottom). The top condition is that of a cambered sub-cavitating foil with no cavitation present. As σ_v is decreased⁴ cavitation inception is initially observed on the upper surface/suction side of the section as shown. On further decrease in σ_v a developed vapour cavity forms over a portion of the foil surface with the cavity closing onto the foil surface, i.e. a partial cavity. As σ_v is reduced further the partial cavity eventually grows in length until the cavity closure region is within the liquid and a supercavity is instead formed. The flow condition labelled buffeting is where the foil is still affected by the cavity closure region with resulting unsteady forces and vibration. Upon further reduction in σ_v the cavity length grows and once the closure region is sufficiently downstream ($> 2C$) the steady supercavitating condition is reached with the absence of the detrimental effects felt in the buffeting regime.

With developed cavitation, the cavity may contain a mixture of vapour and incondensable gas. The presence of the latter may arise either by diffusion from within the liquid across the cavity interface (Gadd and Grant, 1965; Brennen, 1969) or by addition from some external source. If gas addition is via the latter this is termed ventilation, and a ventilated cavity results. Gas may be externally introduced into the cavity either by direct injection or as a consequence of the flow field having some passage of communication between the cavity and the atmosphere. Forced and natural ventilation are the terms used to differentiate between the direct or consequential addition of gas into a cavity or wake. For a discussion on the natural ventilation of surface piercing foils see Swales et al. (1971, 1974). For strut supported foils the passage of communication for natural ventilation typically occurs along the base of the blunt strut (Tulin, 1961; Johnson and Starley, 1962; Dawson and Bate, 1962). A broader description of ventilation phenomena is given by Wadlin (1958), Acosta (1973) and Franc and Michel (2004).

⁴A variation in σ_v (Eq. 1.1) can be achieved by either a change in U_∞ , or by varying the pressure term through changing the foil submergence (i.e. p_∞), or by the addition of non-condensable gas into the cavity (termed ventilation) to increase the pressure above p_v (which gives instead Eq. 1.4).

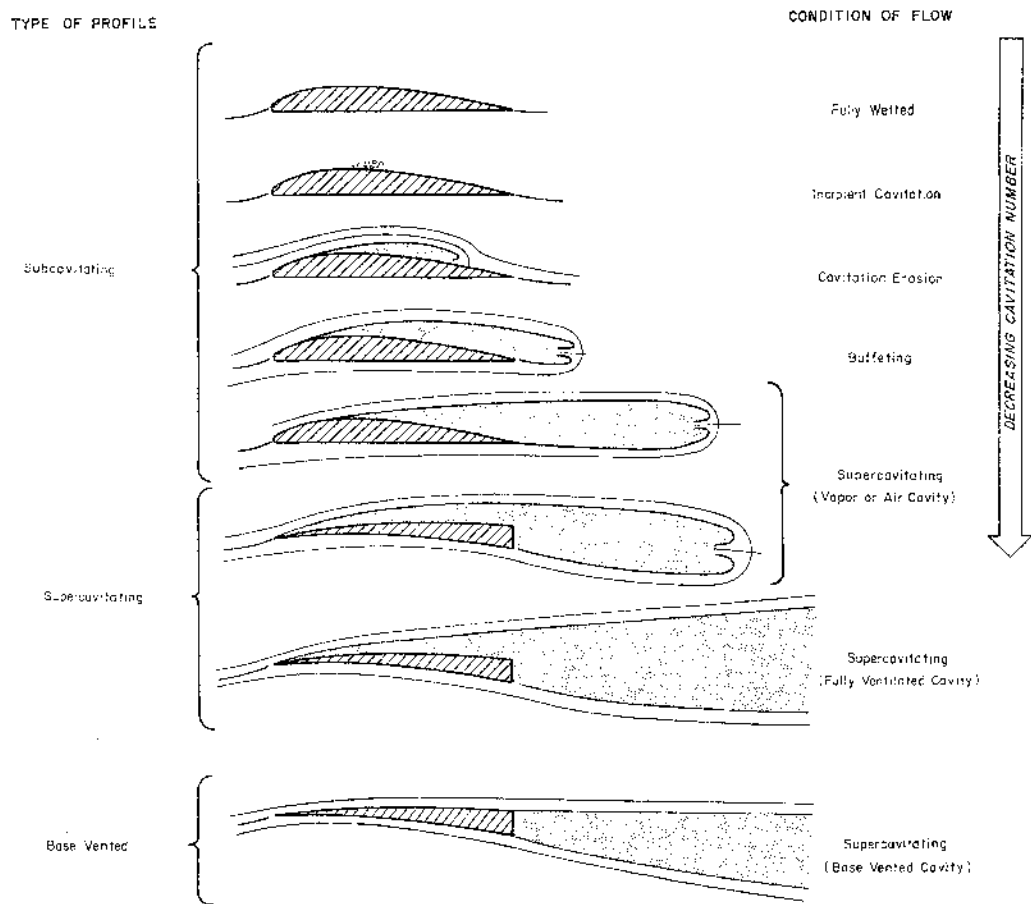


Figure 1.1: Foil flow regimes. From sub- to supercavitating. (from Auslaender (1962))

The foil profile has a significant effect on the performance in either sub-cavitating (i.e. fully-wetted or without cavitation present) or cavitating conditions. The various profile types described in the following are also indicated in Figure 1.1 as appropriate. Optimum sub-cavitating foil sections have an upper speed limit of about 45 knots (Conolly, 1975). For stable operation at higher speeds, where cavitation cannot be avoided, special supercavitating foil sections were developed which operate with the suction side of the foil completely un-wetted (Johnson, 1957, 1958; Wu, 1956). This is achieved with the super-cavity forming off sharp leading and trailing edges, as shown in the lower portion of Figure 1.1. Interest in the use of these supercavitating hydrofoil sections was directed to high-speed hydrofoil borne craft, super-cavitating propellers and seaplane hydro-skis (Conolly, 1975; Johnson, 1958; Tulin, 1964).

Sub- or supercavitating foils designed for high-speed operation, and at shallow submergence, are required to have thin sections to obtain suitable efficiency in performance⁵. Such thin sections, in addition to low camber, are necessary on sub-cavitating foils to eliminate the occurrence of cavitation and a thin leading edge is required on supercavitating sections to ensure cavity detachment is maintained at this point. These thin profiles, together with the high loadings, present significant structural trade offs in the achievement of suitable practical high-speed foil sections of either type (Huang, 1965). To overcome this difficulty an alternative section with both wetted upper and lower surfaces and an open thickness distribution was proposed. The additional form drag (See Section 1.4) due to the added thickness of these sections is compensated for by increasing the pressure in the wake by the introduction of a ventilated cavity detaching from the trailing edges of the blunt base, (Lang, 1959; Fabula, 1961), as illustrated in the bottom of Figure 1.1. A number of experimental investigations have shown that these base vented, structurally desirable thicker sections, could achieve comparable or greater efficiency operating at speeds in the 40-100 knots range (Johnson and Rasnick, 1959; Lang and Daybell, 1961; Christopher, 1961; Huang, 1965).

As a consequence of the cavity pressure possibly being different from the vapour pressure, an alternative cavitation number or cavity underpressure coefficient is useful. This is defined as:

$$\sigma_c = \frac{p_\infty - p_c}{\frac{1}{2}\rho U_\infty^2} \quad (1.4)$$

where p_v is substituted by p_c , which is the actual pressure in the cavity. The value of p_c is the cumulative total of the partial pressures of the liquid vapour and any incondensable gases present. Note that the same σ_c can be achieved at higher free stream static pressures by increasing p_c via ventilation. It is important to also note that σ_c and σ_v can be varied independently, based upon ventilation flow rate and free-stream static pressure respectively. This is significant considering that foil leading-edge vapour cavitation depends on

⁵Efficiency is defined in terms of the lift to drag ratio, $\eta = L/D$, of the foil section (See Sect. 1.4).

the free stream static pressure independent of base-ventilated⁶ cavities created from non-condensable gas injection. In the limit where $p_c \rightarrow p_\infty$, then from Equation 1.4 $\sigma_c \rightarrow 0$. The $\sigma_c = 0$ case is the classical free streamline flow case with the cavity extending to infinity (see Lamb, 1932; Birkhoff, 1950; Batchelor, 1967).

The development of the theoretical analysis of finite-span (3-D) supercavitating foils has been reviewed by Kinnas and Fine (1993). A number of experimental studies have also been reported on, covering both supercavitating (Schiebe and Wetzel, 1961; Kermeen, 1961; Tsen and Guilbaud, 1974; Leehey and Stelling, 1975) and base ventilated foils (Verron and Michel, 1984). Just as in fully wetted flow, the principal three-dimensional effect in supercavitating and base-ventilated flows is on the lift-slope (Acosta and Furuya, 1975; Verron and Michel, 1984). Numerical results from Tsen and Guilbaud (1974) for the spanwise circulation distribution for a supercavitating foil with rectangular planform shows a relatively constant value out till past $0.9s$, where s is the half-span of the foil, after which the circulation then drops rapidly to zero at the tip.

An estimate of the three-dimensional lift slope from lifting-line theory (Glauert, 1947) is:

$$\frac{\partial C_{L3D}}{\partial \alpha} = a_0 \frac{\lambda}{\lambda + 1 + \frac{a_0}{\pi}} \quad (1.5)$$

where

$$a_0 = \frac{\partial C_{L2D}}{\partial \alpha} \quad (1.6)$$

and λ is the aspect ratio of the foil, $\lambda = S/C$. From linear theory the values of a_0 are 2π and $\pi/2$ for the supercavitating and base-ventilated regimes respectively giving

$$\frac{\partial C_{L3D}}{\partial \alpha} = \frac{\pi}{2} \frac{\lambda}{\lambda + 1.5} \quad \text{- Supercavitating} \quad (1.7)$$

and

$$\frac{\partial C_{L3D}}{\partial \alpha} = 2\pi \frac{\lambda}{\lambda + 3} \quad \text{- Base-ventilated} \quad (1.8)$$

The finite-span experimental results obtained by Verron and Michel (1984) are of particular interest to the present study as they are also for base-ventilated foil sections with a rectangular planform. It was found in this study that the cavity shape was generally two-dimensional except at the tip. It was also observed that the force coefficients measured were not significantly affected by the geometric peculiarities of the resulting tip cavities. Verron and Michel concluded that it should be possible to model a base-ventilated foil without explicitly considering the great complexity of the cavity structures occurring

⁶the base-ventilated foil concept is explained in the following section

at the foil tip. In view of these findings for 3-D flow over supercavitating and base-ventilated foils, results from a simplified 2-D analysis will provide a useful description of the flow over the majority of the finite-span foil.

1.2 Project Description

The motivation for this present work has been to investigate the suitability of a novel base-ventilated supercavitating hydrofoil design for use in high-speed vessel motion control devices and other possible marine applications. This concept has been proposed by Australian Naval Architect Tony Elms as embodied in the patent application titled “Improved Hydrofoil Device” (Elms, 1999).

The basis of the “Improved Hydrofoil Device” concept is in the use of a symmetrical foil section from which a trailing supercavity is formed from geometric discontinuities, located between the mid-chord and trailing edge, on both the upper and lower surfaces. This two-part foil/cavity system is illustrated in Figure 1.2. On one surface the discontinuity is a forward-facing step (FFS) whilst on the opposing surface a backward-facing step (BFS) is formed. This is achieved by rotating the tail of the foil up or down as shown in Figure 1.3. With the supercavity detaching from the steps formed on the foil surfaces the tail section of the foil is then, if suitably shaped, situated wholly within the cavity. Due to the flow asymmetry, caused by the steps with detached cavity surfaces, lift is consequently produced. The pressure side of the foil is the one with the FFS formed on it as there is a pressure distribution formed upstream of a FFS with detached cavity as discussed in the next section. With the ability to rotate the tail section and form a FFS on either the upper or lower foil surfaces, lift can then be produced in either direction from a symmetrical foil section at zero incidence.

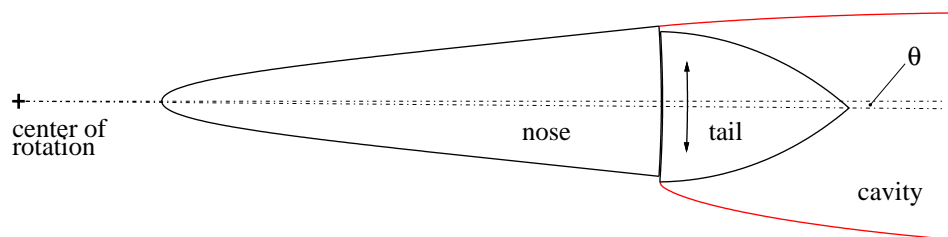


Figure 1.2: Two-part foil with cavity.

A symmetric blunt-based foil section with an asymmetric cavity detaching from the trailing edges is analogous to a symmetric sub-cavitating foil section with flap. In both cases lift can be produced from an uncambered section

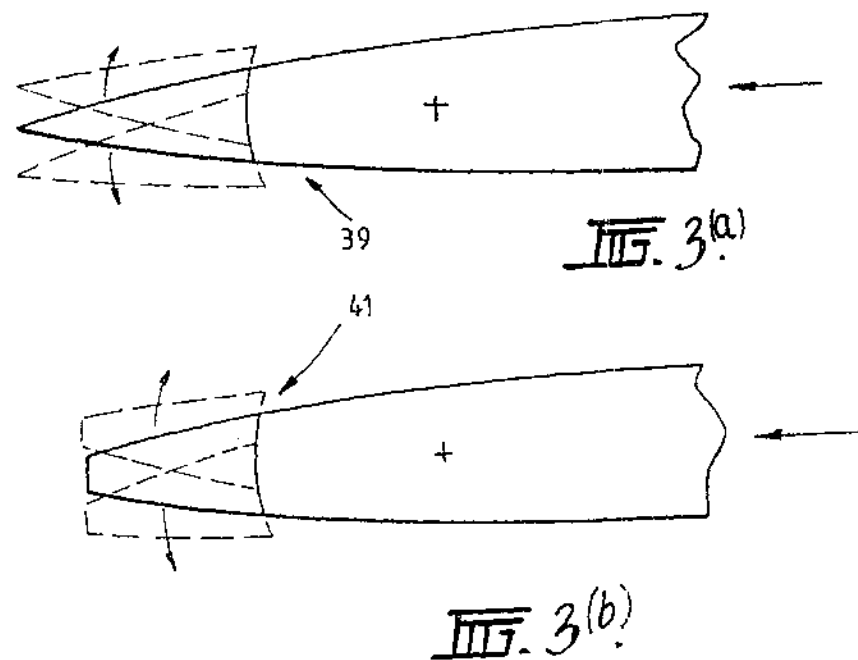


Figure 1.3: Steps on foil surface formed by rotation of a separate tail section (from Elms, 1999).

at zero incidence. A flapped foil carries a significant increased drag penalty (Abbott and von Doenhoff, 1959), whereas a ventilated foil operating with σ_c close to zero has a negligible form drag component due to the increased cavity pressure acting over the base area.

An overview of the historical development of various supercavitating foil sections for marine vehicle application is given in Pearce and Brandner (2007). For base-vented foil sections in particular, in addition to the earlier work discussed in the previous section, further investigations were also undertaken by a number of French researchers in the 1970's & 80's (Rowe and Michel, 1975; Rowe and Kueny, 1980; Verron and Michel, 1984). The most recent of these publications was the only one concerned with symmetric profile shapes. However only simple wedge shaped profiles with rounded leading edges were used, as the main interest was in the three-dimensional effects related to the plan-form shape. An investigation into stepped and rotating tail foils with some similarities to the present work was published by Rowe (1979), but was concerned only with cambered profiles. Of closer relevance to the present study was an experimental investigation into a family of base-vented foils as reported on by Brentjes (1962). A symmetric parabolic profile was used, but with the maximum thickness located forward of the trailing edge. Historically then, the main interest in symmetric base-vented sections has been for the application to surface-piercing struts for the mounting of high-speed foils (Tulin, 1961; Johnson and Starley, 1962) rather than directly for lifting surface applications. So, although a significant body of work reporting the design and operation of base-vented foil sections is openly available, the intercepted base-vented foil concept of interest here appears novel, at least as far as the open literature is concerned.

This thesis will investigate the following issues and possible limitations concerning the hydrodynamic performance of blunt-based ventilated supercavitating hydrofoils of symmetric section:

- foil section profile
- cavity shape characteristics
- interceptor height
- incidence variation⁷
- leading edge natural cavitation occurrence
- cavity moving forward of trailing edge detachment points.

The approach taken in this investigation has been a numerical one, involving the use of a 2-D non-linear potential flow boundary element formulation, with a companion experimental program planned to follow this work, using the

⁷For motion control applications a design incidence of $\alpha = 0^\circ \pm 2.5^\circ$ due to seakeeping response, has been chosen here as the range of practical interest (Elms, 2003).

variable pressure water (cavitation) tunnel at the AMC Cavitation Research Laboratory (CRL). The experimental data is required for comparison with the numerical predictions and to investigate certain aspects that are not captured in the potential flow based BEM used, particularly the:

- ventilation characteristics i.e. air flow rates
- viscous and surface tension effects.

Apart from the face and edge where the cavity separates from the remaining part of the foil, the rotatable tail portion (Figure 1.2) has no hydrodynamic effect whilst a cavity is present. So from the hydrodynamic viewpoint an identical flow field could be produced by removing the tail and placing a normal fence at the upper or lower trailing edge of the remaining front section of the foil. To adequately model the hydrodynamic aspects of this foil-cavity system, the tail portion can then be neglected and only the front foil section with a fence attached to one of the trailing edges considered. This approach has been adopted for the numerical analysis, and also for the experimental work reported here.

1.3 Interceptor flows

A related concept that has been successfully applied to high speed transom stern craft is the fitting of a retractable interceptor to the bottom and side edges of the transom to provide steering and trim control respectively (Widmark, 2001; Faltinsen, 2005, p.225-6). The interceptor is simply a flat plate projected into the flow perpendicular to the hull surface. Figure 1.4 illustrates the flow over an interceptor protruding from the lower edge of a transom with flow separation from the interceptor's bottom edge. The resulting free surface, and therefore also the back face of the interceptor, has atmospheric pressure acting over it. The pressure field which develops upstream of the interceptor applies an upward or lift force onto the hull of the vessel.

The fitting of interceptors to high speed craft has been a fairly recent concept within naval architecture, with conference publications on the topic appearing from the late 1990's onwards (Zaninovic, 1997; Tsai et al., 2001; Widmark, 2001). A comprehensive research program, based on experimental model testing at the Norwegian University of Science and Technology, has resulted in a number of theses (Økland, 2004; Breivik, 2005; Lysdahl, 2005) and conference publications (Hansvik and Steen, 2006; Steen, 2007). There has been little published work regarding numerical analysis of the related hydrodynamic aspects of these flows, except for one paper concerning the CFD analysis of interceptor flows by Brizzolara (2003). An analytical approach based on the method of matched asymptotics applied to two-dimensional planing lifting surfaces with spoilers (Rozhdestvensky and Fridman, 1991; Fridman, 1998) was recently applied by these authors (Fridman et al., 2007) to the theoretical analysis of interceptor flows.

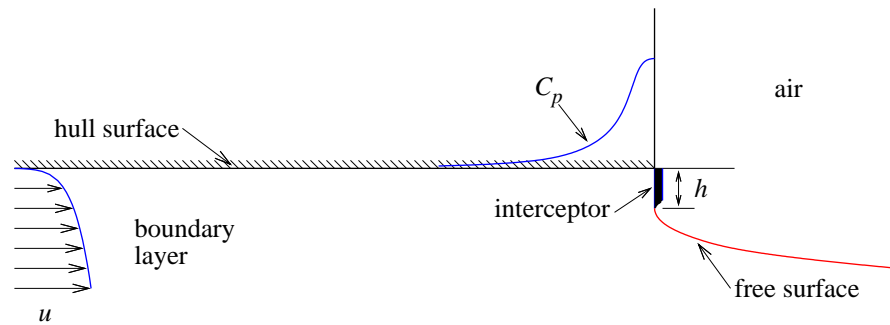


Figure 1.4: Interceptor flow field (From, Faltinsen, 2005, Fig. 7.6).

The interceptor flow is analogous to the separated flow over a wall-mounted fence, which has been extensively studied within the field of single-phase fluid mechanics over a long period of time (see, for example, Arie and Rouse, 1956; Good and Joubert, 1968; Bradshaw and Wong, 1972; Ranga Raju et al., 1976; Durst and Rastogi, 1980; Kim and Lee, 2001b; Sonnenberger, 2002). One practical application has been in the measurement of wall shear stress with a surface fence as reported by Dengel et al. (1982) and with a sublayer fence as termed by Gasser et al. (1993). There has been interest in wall-mounted fence flows within the aerodynamics field for the use of spoilers (i.e. fences) as control devices (Woods, 1953a,b), and later the use of oscillating fences for active control of flow separation (Miau and Chen, 1991; Miau et al., 1991). The term Gurney flap is commonly used in flight and automotive aerodynamics for trailing edge fences fitted to aerofoils and automotive rear wings as lift augmentation devices (see, for example, Neuhart and Pendergraft, 1988; Storms and Jang, 1994; van Dam and Yen, 1999; Sims-Williams et al., 1999; Li et al., 2003; Troolin et al., 2006; Gerontakos and Lee, 2008). There has also been considerable interest in the study of wall-mounted fence flows, particularly porous fences, in the wind engineering/atmospheric fluid mechanics area, with particular emphasis on the downstream wall pressure distribution and other characteristics of the wake (Castro and Fackrell, 1978; Jacobs, 1985; Yaragal et al., 1997; Lee and Kim, 1999; Kim and Lee, 2001a; Lee and Lim, 2001; Park and Lee, 2001; Lee et al., 2002; Park and Lee, 2002). Despite the wealth of published work on wall-mounted fence flows, the particular regime of cavitating flow detaching from a fence is not covered in the open literature. The closest work encompassing cavitating wall flow is that associated with backward facing steps (Young and Song, 1975; Laali and Michel, 1984; Ramamurthy et al., 1991; Maitre and Pellone, 2001; Brice, 2006).

The topology of the interceptor projecting into the flow with a free surface

separating from its edge is analogous to a forward facing step/wall mounted fence with a vapour-gas cavity detaching from the outer edge, with the former equivalent to the $\sigma_c = 0$ infinite cavity case of the latter. Hence the terms fence, wall-mounted fence and interceptor will be used interchangeably throughout the rest of this thesis. These flows are included as a part of the present work as they enable the viscous corner flow to be studied in the absence of the pressure distribution created by the foil. The main features of interest concern:

- the normal force (lift) on the upstream wall resulting from the pressure distribution produced due the presence of the fence
- the effect of the relative boundary layer height on the cavity characteristics and fence face and upstream wall pressure distributions.

1.4 Hydrodynamic Performance Criteria

The resultant forces acting on the cavitating bodies in this study are defined with respect to a flow fixed coordinate system with the origin at the midchord of the body as illustrated in Figure 1.5. The resultant normal force acting on the body, obtained by integrating the pressure over the surface of the body, is resolved into a component normal to the oncoming flow, termed the lift, L , and a component in line with the flow termed the drag, D , on the body. The resultant moment, M , is defined as being positive when acting clockwise about the origin as shown.

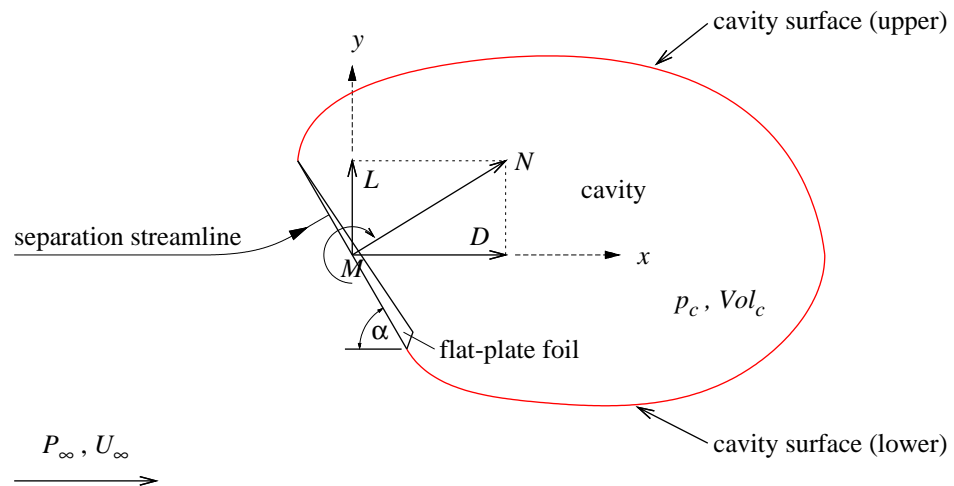
These components are non-dimensionalised by dividing the forces and moment per unit span by the free stream dynamic pressure, $q = 0.5\rho U_\infty^2$ and the chord length, to give

$$C_L = \frac{L}{qc}, \quad C_D = \frac{D}{qc} \quad \& \quad C_M = \frac{M}{qc}$$

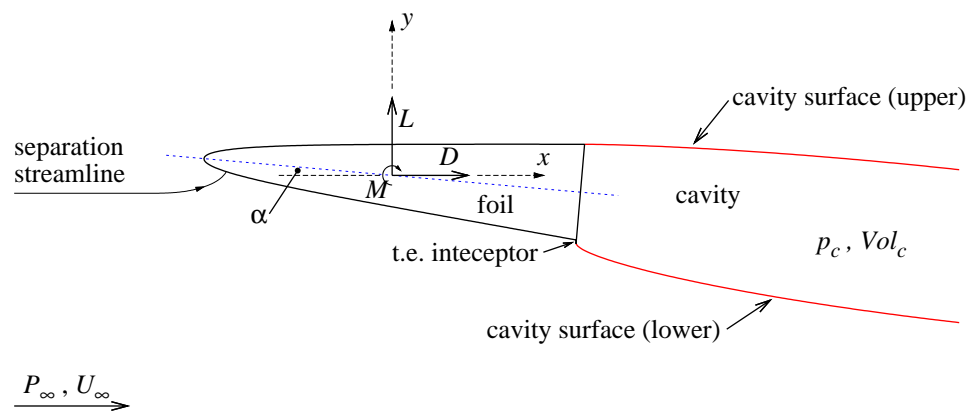
The hydrodynamic efficiency of the body defined by:

$$\eta = \frac{L}{D} = \frac{C_L}{C_D}$$

The hydrodynamic performance of a cavitating body will be assessed using these quantities. The susceptibility to leading edge natural cavitation occurrence and stable cavity detachment conditions, will also be examined.



(a) Flat-plate foil



(b) Base-ventilated foil

Figure 1.5: Sketch of cavitating flow detaching from a flat plate foil and a base ventilated foil at an angle of incidence, α . Flow-fixed coordinate system with origin at foil mid-chord.

1.5 Thesis Outline

The contents of this thesis are presented in six chapters. Chapter 2 outlines the theory behind the analytical and numerical methods used in the analysis of fully developed cavity flows over bluff bodies. A description of the low-order, non-linear, 2-D boundary element method as implemented in the numerical code SUPCAV is presented. The implementations for both infinite and confined flow are described. Examples of the surface discretisation used, with descriptions of the problematic issues involved, and some typical convergence data is presented. Comparison of the method with analytical prediction and experimental data is also presented.

In Chapter 3, the numerical analysis of the cavitating flow over a wall mounted fence is presented. This being of interest as a basic study of the interceptor in isolation from the foil; and also to the study of the performance of transom mounted interceptors. The analysis includes: inviscid analytical; boundary element method; and viscous flow RANSE CFD results.

The boundary element method analysis of intercepted supercavitating base-ventilated foils is dealt with in Chapter 4. The influence of foil geometry and flow parameters on the resulting supercavity shape and foil/cavity hydrodynamic performance is assessed. Also considered is the criteria necessary to maintain detachment of the trailing cavity; and the prevention of formation of leading edge vapour cavitation.

In Chapter 5, the analysis of supercavitating foils in confined flow is presented and is of interest for experimental design and comparison of experimental and numerical results.

Chapter 6 outlines the conclusions of the analysis and the results presented in the previous chapters and lists some recommendations for future work.

Chapter 2

Modelling Free-Streamline (FS) Flows

2.1 Introduction

Except for the creeping flow case ($Re \rightarrow 0$), the flow past a bluff body is accompanied by separation of the boundary layer and the formation of a wake region. This wake region is attached to the body and contains slower moving structures, the characteristics of which typically vary as Reynolds number increases. A description of the wake resulting from the flow over a circular cylinder, i.e. a typical bluff body flow, is given by Schlichting and Gersten (2000, p.22) for the complete range of Re . At a sufficiently high Reynolds number the wake contains a region of slow moving fluid relative to the free-stream flowing past, separated by a high-velocity gradient shear layer. The wake region in this case is termed a “dead air” or “dead water” region or fully-developed wake.

In the flow of a liquid over a bluff body, at sufficiently low cavitation numbers, vapour structures form and develop in extent as the cavitation number reduces, as described by Brennen (1995, §7.8). At a sufficiently low cavitation number, the wake region becomes a single vapour/gas filled void which Brennen terms a “fully-developed” or “attached” cavity. The free-surface interface between the liquid flow and the vapour/gas cavity can be considered to be acted upon by a constant pressure, p_c . This is an accurate assumption, except in the vicinity of the closure, as due to the low density of the vapour/gas compared with the liquid, the nature of the contents of the fully developed cavity have little effect on the liquid flowing past. For a more detailed discussion of fully-developed cavity flow see Brennen (1995, §8.1).

One of the earliest analytical approaches to these bluff body wake flows was the application of free-streamline methods. A free-streamline is analogous to a free surface where it is considered that there is a constant pressure acting all along it. Figure 2.1 shows a bluff body with a fully developed cavity attached. Noted on the figure is the terminology used in free-streamline analysis. The usage of the term “free” in both the free surface and free-streamline cases

stems from the aspect that the location of the streamline or surface is initially unknown, and must be found as a part of the flow solution. The first use of free-streamline analytical methods for bluff body wake flows can be traced back to Helmholtz (1868) and Kirchhoff (1869). These authors presented a solution to the flow over a normal flat plate with a wake extending infinitely far downstream. In this case the constant pressure in the wake is equal to that in the undisturbed stream. An application of free-streamline methods to fully developed cavity flows did not occur until the early part of the next century. For a survey of published work on this topic, see, Brennen (1995, §8.1). An alternate linearised theory approach was first introduced by Tulin (1953), applicable if the body-cavity is sufficiently thin, which is usually valid for $\sigma_c \rightarrow 0$.

The issues of cavity detachment and modelling the unsteady cavity closure are addressed in free-streamline methods by various means. Firstly addressing the issue of cavity detachment. As the pressure in the cavity is assumed to be lower than at any other point in the liquid, the cavity surface (i.e. free-streamline) must be convex when viewed from the fluid. This then precludes streamline detachment with a concave curvature. Generally, cavity detachment from a bluff body falls into two classes. Where the cavity detaches from a discontinuity in the slope of the body, e.g. a forward- or backward-facing step, it is referred to as an “abrupt” detachment. Otherwise the cavity detachment is instead termed “smooth” as indicated in Figure 2.1. The position of the abrupt detachment is known from the geometry, whereas the smooth detachment point is initially unknown. A detachment criteria is needed to select one solution from the family of valid possible solutions. Commonly a Brillouin-Villat (Brennen, 1995, p. 240) or Brillouin-Armstrong (Franc and Michel, 2004, p. 99) condition is applied which ensures that the free-streamline detachment is tangential to the body surface. This thesis is only concerned with flows with abrupt detachment and so the detachment point is initially known, but the streamline convex curvature criteria will be used to assess cavity validity in the analysis of intercepted supercavitating foil flow (see, Chapter 4).

Secondly, the complex processes that occur in the cavity closure region cannot be incorporated into a potential flow model. A number of different artifices have been employed in the vicinity of the rear stagnation point to effect termination of the cavity as described by Wu (1968) and Brennen (1995, §8.2). The analytical methods used in this chapter use an open wake model where the cavity surfaces extend parallel to infinity far downstream. The boundary element method employed here does not use an explicit closure model as such, but it is handled instead by the surface discretisation used in the closure region as described in Section 2.3.3.

Due to the inaccuracy of the constant wake pressure assumption, free-streamline methods only had partial success in predicting the hydrodynamic characteristics of single-phase bluff body fully-developed wake flows. For example, where the pressure over the front surface of a flat plate is predicted well (Brennen, 1995, Fig. 8.12), there is an error in the drag coefficient prediction

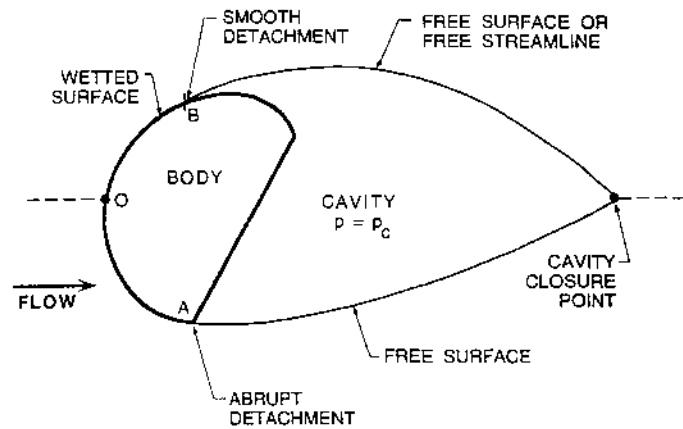


Figure 2.1: Free-streamline analysis terminology (Brennen, 1995, Fig. 8.1).

due to the variance in the wake pressure acting over the rear surface of the plate. In the case of fully-developed cavity flows the constant cavity pressure assumption is more accurate than in the single-phase flow case, and the free-streamline methods give a good prediction for both body pressure distributions and force coefficients (Brennen, 1995, §8.6).

The remainder of this chapter will give an overview of the analytical and numerical (BEM and CFD) methods used in this thesis in the analysis of bluff body fully-developed cavity flows.

2.2 Analytical Methods

The classical free streamline solution methods for steady 2-D plane potential flows used conformal mapping techniques (Vallentine, 1969) where the physical plane is mapped through intermediate planes where the unknowns in the physical plane are more easily determined by the use of appropriate transformations. (See, for example, Lamb, 1932; Birkhoff and Zarantonello, 1957; Batchelor, 1967; Wu, 1968). In summary, the flow field is such that the velocity components in the x and y coordinate directions are given respectively by

$$u = \frac{\partial\phi}{\partial x} = \frac{\partial\psi}{\partial y} \quad \text{and} \quad v = \frac{\partial\phi}{\partial y} = -\frac{\partial\psi}{\partial x} \quad (2.1)$$

with the complex physical plane given by

$$z = x + iy \quad \text{where} \quad i = \sqrt{-1} \quad (2.2)$$

and the complex potential function defined as

$$w = \phi + i\psi \quad (2.3)$$

The z -plane is mapped onto the w -plane by means of the hodograph variable or complex velocity

$$\nu = \frac{dw}{dz} = u - iv = qe^{-i\theta} \quad (2.4)$$

Alternately, a logarithmic hodograph variable,

$$\Omega = \ln \frac{1}{\nu} = \ln \frac{dz}{dw} = \ln(u - iv)^{-1} = \ln q^{-1} + i\theta \quad (2.5)$$

is employed in some methods. The inverse of the complex velocity is also often used:

$$\zeta = \frac{1}{\nu} = \frac{1}{q} e^{i\theta} = \frac{dz}{dw} \quad (2.6)$$

The mapping of the z -plane to the w -plane and the ν -, ζ - or Ω -planes is usually accomplished via one or more additional auxiliary planes with the desired solution in the physical plane obtained by integration of the resulting function, $\zeta(w)$, to give

$$z(w) = \int \zeta dw \quad (2.7)$$

and from Bernoulli's equation for total pressure, which is constant along a streamline, the corresponding static pressure coefficient values can be determined from

$$C_p = 1 - \frac{1}{|\zeta|^2} \quad (2.8)$$

2.2.1 Ideal flow over a normal plate

The ideal flow over a normal plate without separation is not a free streamline flow. However it is of interest as it provides the zero cavity length limit of fully-developed cavity flows. To obtain an analytical solution to the ideal flow over a normal plate a series of three conformal transformations is employed as illustrated in Figure 2.2 (from Robertson, 1965, §9.3).

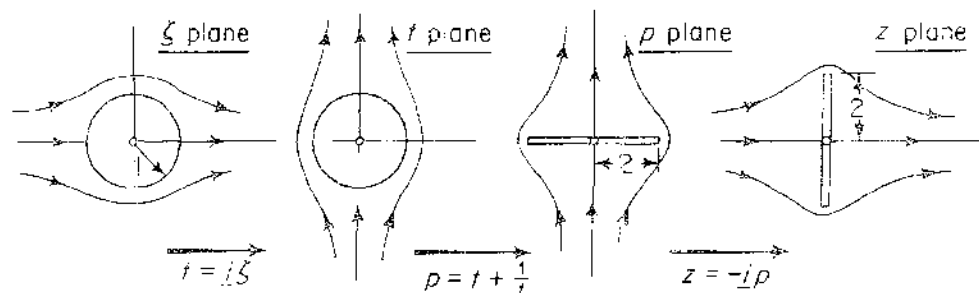


Figure 2.2: Derivation of the ideal flow over a normal flat plate by conformal transformations (Robertson, 1965, Fig. 9.7).

Use is made of the property that multiplication by i gives a rotation of 90° ; and the Joukowski transformation $p = t + a^2/t$ which maps the circle $\zeta = ae^{i\theta}$, into a straight line (of length $4a$), giving the relation

$$z = \zeta - \frac{1}{\zeta}$$

The complex potential for the flow over a normal plate is then given by

$$\begin{aligned} w &= \phi + i\psi \\ &= U_\infty \sqrt{z^2 + 4a^2} \end{aligned} \quad (2.9)$$

Rearranging and collecting like terms gives, for the real part of w ,

$$\phi^2 - \psi^2 = U_\infty^2 (x^2 - y^2 + a^2) \quad (2.10)$$

As the pressure on the back face of the plate is equal in magnitude but in opposite direction to that acting on the front face, the net force or drag on the plate $D = 0$, which is not observed in a real viscous fluid.

2.2.2 FS flow over a normal plate - $\sigma_c = 0$

The solution (from Batchelor, 1967) of the free streamline flow over a normal plate with an infinite cavity, via the logarithmic hodograph plane and two auxiliary planes, \sqrt{w} & λ , is shown in Figure 2.3.

The relation between w , Ω and λ is given by

$$\begin{aligned} \lambda &= -(kU/w)^{\frac{1}{2}} = i \sinh \Omega \\ &= \frac{1}{2}i \left(U \frac{dz}{dw} - \frac{1}{U} \frac{dw}{dz} \right) \end{aligned} \quad (2.11)$$

giving

$$\frac{1}{U} \frac{dw}{dz} = -i \left(\frac{w}{kU} \right)^{\frac{1}{2}} + \left(1 - \frac{w}{kU} \right)^{\frac{1}{2}} \quad (2.12)$$

Integration of Equation 2.12 gives

$$\begin{aligned} \frac{z - z_0}{k} &= 2i \left(\frac{w}{kU} \right)^{\frac{1}{2}} + \left(\frac{w}{kU} \right)^{\frac{1}{2}} \left(\frac{w}{kU} - 1 \right)^{\frac{1}{2}} + \frac{1}{2}\pi i \\ &\quad - \ln \left\{ \left(\frac{w}{kU} \right)^{\frac{1}{2}} + \left(\frac{w}{kU} - 1 \right)^{\frac{1}{2}} \right\} \end{aligned} \quad (2.13)$$

where the constant, z_0 , is zero as $w = 0$ at $z = 0$. The constant k is given by

$$k = \frac{2b}{\pi + 4} \quad (2.14)$$

with plate length = $2b$.

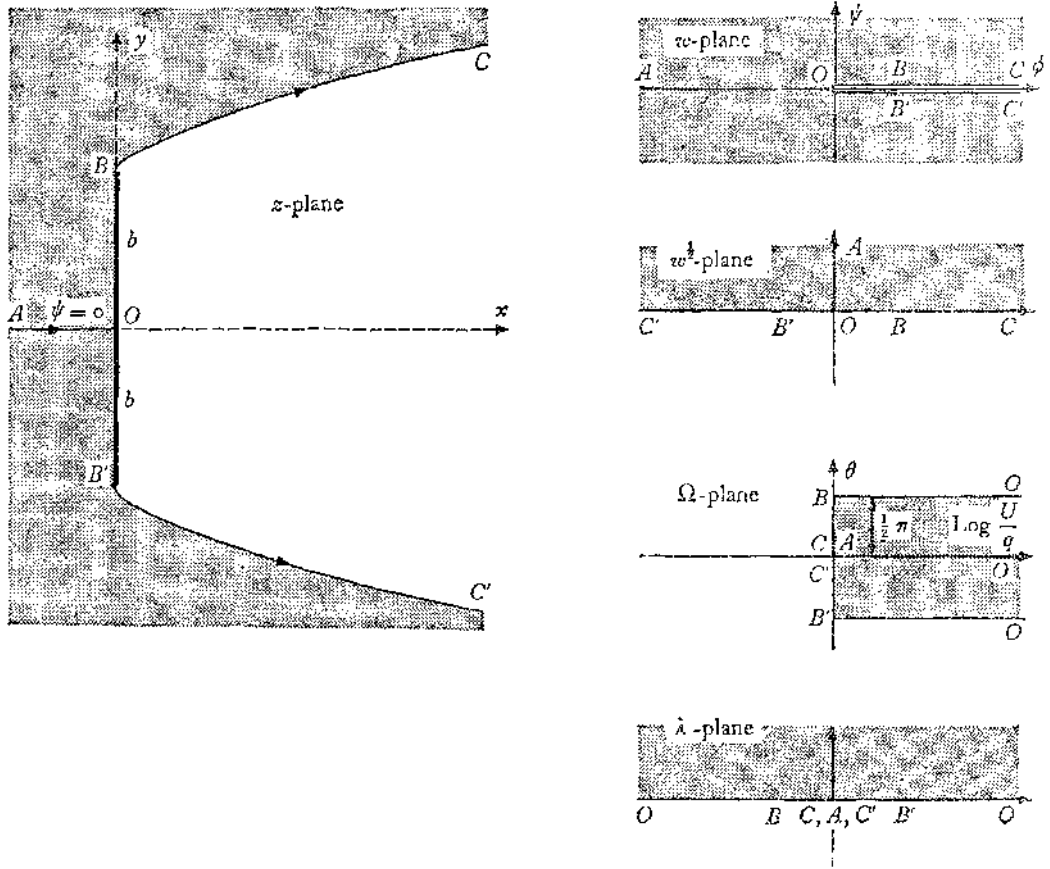


Figure 2.3: Derivation of the infinite cavity flow over a normal flat plate by conformal transformations (Batchelor, 1967, Fig. 6.13.2).

2.2.3 FS flow over a normal plate - $\sigma_c > 0$

For finite cavity length flows, i.e. $\sigma_c > 0$, Roshko (1954) used the conformal transformations shown in Figure 2.4 to map the flow. This was termed the “notched hodograph solution” due to the notch in the circular sector hodograph from B' to I to B in the ν -plane. The notch is due to U_∞ being set to equal $1/k$, keeping $q_c = 1$ as with the infinite cavity case. The parameter k is the value that the cavity surface velocity would be if $U_\infty = 1$, and is given by $k^2 = 1 + \sigma_c$. The method makes use of auxiliary planes χ , t and t^{-1} via the following transformations:

$$\chi = \frac{i}{2} \left(\zeta - \frac{1}{\zeta} \right)$$

$$t = \frac{h^2 + \chi^2}{h^2 + 1}$$

where

$$h = \frac{k^2 - 1}{2k}$$

and

$$w = \frac{1}{t^2}$$

Solving for ζ gives

$$\zeta = \pm i \frac{k^2 + 1}{2k} \left(\sqrt{\frac{1}{\phi} - \frac{1}{a^2}} + \sqrt{\frac{1}{\phi} - 1} \right) \quad (2.15)$$

where

$$a = \frac{k^2 + 1}{k^2 - 1} \quad (2.16)$$

Integration of Equation 2.15 then gives

$$z = \pm i \frac{k^2 + 1}{2k} \left(\sqrt{w(1-w)} + \tan^{-1} \sqrt{\frac{w}{1-w}} + \frac{1}{a} \sqrt{w(a^2-w)} + a \tan^{-1} \sqrt{\frac{w}{a^2-w}} \right) \quad (2.17)$$

The plate length d is also a function of k given by (Roshko, 1954, eqn.14) as

$$d = \frac{k^2 + 1}{k} \left(\frac{\pi}{2} + \frac{k^2 + 1}{k^2 - 1} \tan^{-1} \left(\frac{k^2 - 1}{2k} \right) \right) \quad (2.18)$$

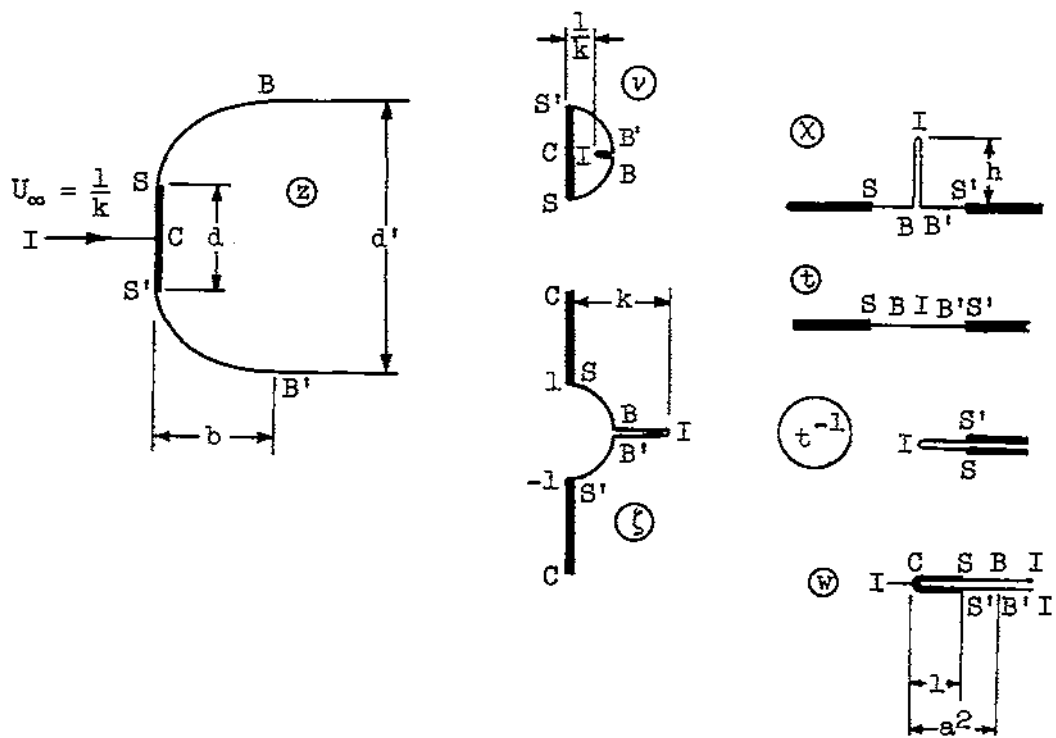


Figure 2.4: Derivation of the finite cavity flow over a normal flat plate by conformal transformations, (notched hodograph solution) (Roshko, 1954, Fig. 3).

2.3 Boundary Element Methods (BEM)

2.3.1 Overview

Boundary element method (BEM) techniques are well established for the solution to a wide range of scientific and engineering problems. They have an advantage over domain type methods, such as finite element and finite difference techniques, in that there is generally a much smaller set of equations to solve and the computational time is correspondingly significantly less. The method is well suited to solving infinite domain problems such as those in aero- and hydrodynamics, i.e. the immersed body problems relevant to the present work, and also to other such diverse applications as soil mechanics, stress analysis, bubble dynamics and free-surface flows. The term ‘boundary elements’ refers to the external surface of the ‘body’ to be analysed being broken up, or discretised, into a series of elements over which some influence function or functions are considered. For a general overview of the boundary element method see Brebbia (1984) and Hall (1994).

A description of the application of BEM techniques to the numerical solution of the flow over lifting surfaces of arbitrary geometry, immersed in an infinite domain, is given by Moran (1984) and Katz and Plotkin (2001). These authors use the term ‘panel methods’ to describe these solution techniques and it is commonly used in both the aero- and hydrodynamics fields. These methods are based on the surface distribution of singularity elements with the solution found by determining the unknown strength of these elements. The method was first published by Hess and Smith (1966) and the subsequent development of the method and its application to various problems in fluid dynamics including propellers and free-surface flows is reviewed by Hess (1990).

A review of the development of BEM techniques as applied to cavitating lifting surfaces is given by Kinnas (1998). Initially, velocity based methods using a surface vorticity formulation were used (Uhlman, 1987, 1989). Later, an alternative formulation was developed, solving for the velocity potential directly rather than for the velocity, which was termed a potential based method (Kinnas and Fine, 1991, 1993; Lee et al., 1992). This latter formulation was found to converge much more quickly with correspondingly fewer iterations making it more computationally efficient than the velocity based methods. The potential based formulation has been used for the BEM analysis undertaken herein.

Figure 2.5 gives a sketch of a number of different types of bluff body shapes that have been analysed in this thesis using the boundary element method. The solution method, as implemented in FORTRAN 90 with the code SUPCAV, is described in the following section.

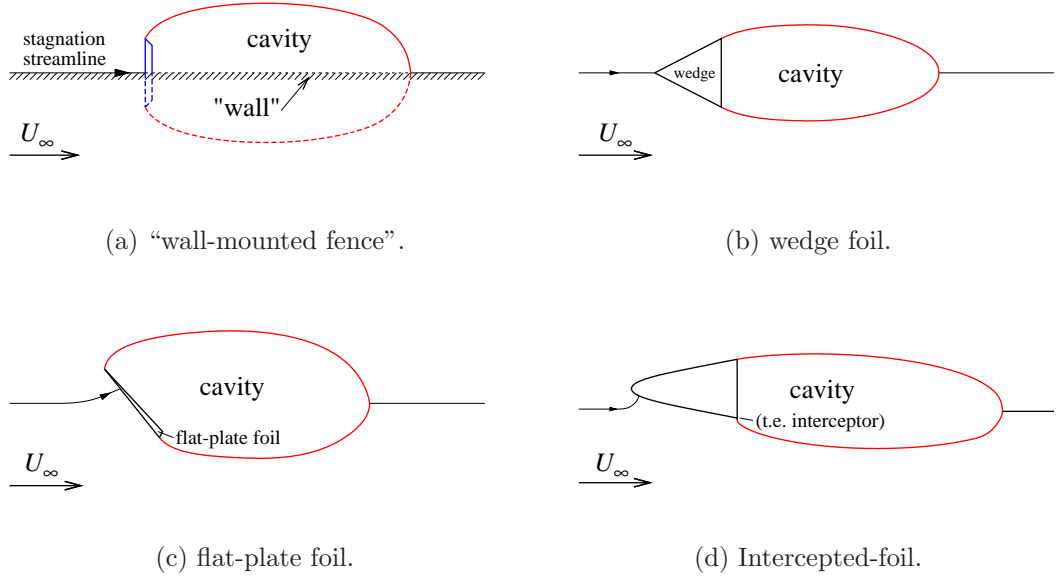


Figure 2.5: Two-dimensional cavitating bluff bodies. (a) "Wall-mounted fence", (b) Wedge foil, (c) Flat-plate foil and (d) Intercepted base-ventilated foil.

2.3.2 A BEM for 2-D Free-Streamline Flows

Consider the planar flow over a bluff body and cavity shown in Figure 2.6. Assuming the flow to be inviscid and irrotational implies the existence of a total velocity potential which satisfies Laplace's equation:

$$\nabla^2 \Phi = 0 \quad (2.19)$$

where the total potential, Φ , is composed of the sum of the free-stream potential and a perturbation potential:

$$\Phi = \phi_\infty + \phi_p \quad (2.20)$$

Equation 2.19 may be solved through the application of Green's theorem to a bounded region within the flow domain:

$$2\pi\phi_p = \int_S \left(\frac{\partial\phi}{\partial\hat{n}} \ln r - \phi \frac{\partial}{\partial\hat{n}} \ln r \right) ds - \int_W \Delta\phi \frac{\partial}{\partial\hat{n}} \ln r ds \quad (2.21)$$

Here p is a general point in the flow domain, r the distance from a surface element ds to p , and \hat{n} a unit normal to the foil or cavity surface. The surface S includes the foil and cavity, and W is the trailing wake sheet. This formulation is that derived by Morino and Kuo (1974) for aerodynamic applications; the method as applied here for 2-D cavitating flows is that by Kinnas and Fine (1991), among others. A review is provided in Kinnas (1998). The Green's function is $\ln r$ and Equation 2.21 may be regarded as representing a distribution, on the foil and cavity surface, of sources of strength proportional

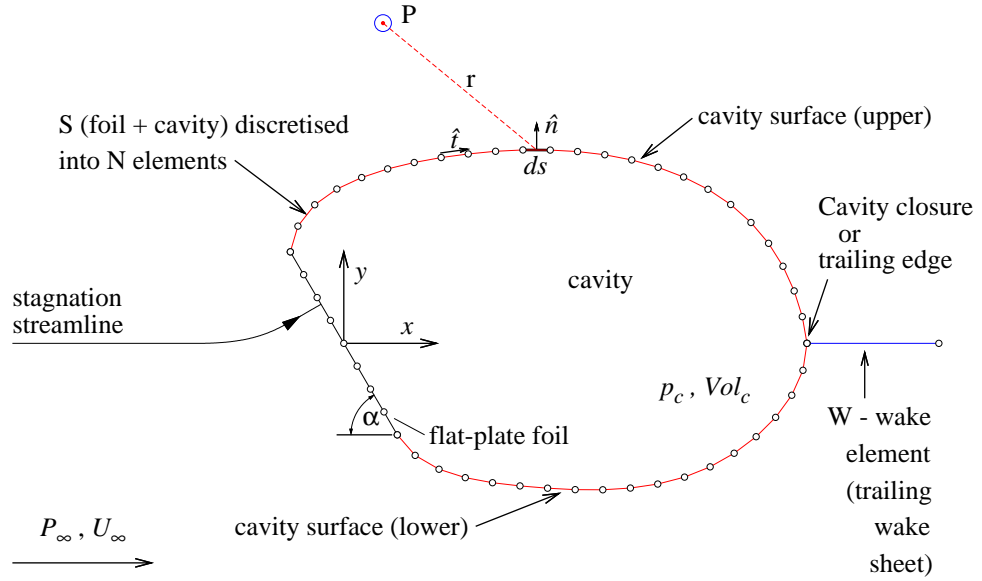


Figure 2.6: Boundary element method - flow solution description.

to $\partial\phi/\partial n$ and doublets of strength proportional to ϕ , and on the wake sheet of doublets of strength proportional to $\Delta\phi$.

The solution to Equation 2.21 is found with the application of the following boundary conditions. On the surface of the foil and cavity the kinematic boundary condition requires that the flow be tangent to the surface:

$$\frac{\partial\phi}{\partial\hat{n}} = -U_\infty \cdot \hat{n} \quad (2.22)$$

and at infinity the perturbation velocities should diminish to zero,

$$\lim_{r \rightarrow \infty} \nabla\phi = 0 \quad (2.23)$$

which is satisfied by the use of source and doublet singularities whose influence diminishes at infinity.

On the cavity surface the dynamic boundary condition requires that the pressure be constant and equal to the cavity pressure:

$$p = p_c \quad (2.24)$$

and therefore from Bernoulli's equation:

$$p_\infty + \frac{1}{2}\rho U_\infty^2 = p_c + \frac{1}{2}\rho U_c^2 \quad (2.25)$$

it follows that cavity velocity is also required to be constant:

$$U_c = U_\infty \sqrt{1 + \sigma} \quad (2.26)$$

with

$$U_c = \nabla\Phi \cdot \hat{t} = U_\infty \cdot \hat{t} + \frac{\partial\phi}{\partial s} \quad (2.27)$$

where s is the arclength along the cavity surface, $s_o \leq s \leq s_L$, and \hat{t} is the unit vector tangent to the cavity surface. These equations for U_c then give:

$$\frac{\partial\phi}{\partial s} = -U_\infty \cdot \hat{t} + U_\infty \sqrt{1 + \sigma} \quad (2.28)$$

which on integration yields:

$$\phi(s) = \int_{s_o}^s \left(-U_\infty \cdot \hat{t} + U_\infty \sqrt{1 + \sigma} \right) ds + \phi_0 \quad (2.29)$$

for the doublet strength distribution over the cavity surface, where ϕ_0 is the potential at the cavity detachment point.

The Kutta condition requires that the velocity at the trailing edge of the foil or cavity be finite, or that the pressures on the upper and lower side be equal. While the velocity or pressure must be equal at the trailing edge, a jump in potential is permitted and is required to set the circulation and thus the lift generated by the foil:

$$\Delta\phi = \phi_U - \phi_L \quad (2.30)$$

where U and L denote the upper and lower surfaces of the trailing edge or cavity closure respectively.

Equation 2.21 may be solved using Equation 2.22 (kinematic b.c.) to set the source strengths on the foil surface, leaving the doublet strengths on the foil and source strengths on the cavity as the unknowns. The doublet strengths on the cavity may be expressed in terms of those on the foil using Equation 2.22 (dynamic b.c.) and hence those on the wake sheet in terms of those at the trailing edge of the foil or cavity using Equation 2.30 (Kutta condition).

The cavity shape and velocity (and hence cavitation number) are unknown, for a fixed cavity length, and introduce non-linearity to the problem necessitating an iterative solution. A suitable initial cavity shape¹ is defined which is then updated upon each iteration. The new cavity surface position is obtained by integrating the following ordinary differential equation involving the velocity from Equation 2.22 and the calculated source strength:

$$U_c \frac{dh}{ds} = \frac{\partial\phi}{\partial \hat{n}} + U_\infty \cdot \hat{n} \quad (2.31)$$

where s is the position along the surface from the cavity leading edge and h , is the updated cavity position taken normal to the surface² giving:

¹What constitutes a “suitable” initial cavity shape is discussed in 2.3.3

²local coordinate system defined with s , the coordinate direction along, and h , the coordinate direction normal to the cavity surface (with \hat{t} and \hat{n} the respective unit vectors)

$$h(s) = \frac{1}{U_c} \int_0^s \left(\frac{\partial \phi}{\partial \hat{n}} + U_\infty \cdot \hat{n} \right) ds \quad (2.32)$$

A cavity closure condition must also be specified from Equation 2.28, i.e. $h(s_L) = 0$ at the specified cavity end which forms a further equation to be solved with Equation 2.21 for the cavity velocity:

$$h(s_L) = 0 = \frac{1}{U_c} \int_0^{s_L} \left(\frac{\partial \phi}{\partial \hat{n}} + U_\infty \cdot \hat{n} \right) ds \quad (2.33)$$

The foil and cavity surfaces may be represented by N boundary elements and Equation 2.21 discretised to a set of N linear equations:

$$\sum_{j=1}^N B_{ij} \frac{\partial \phi}{\partial \hat{n}} + \sum_{j=1}^N C_{ij} \phi_j + C_{wj} \Delta \phi_{wj} = 0, \quad i = 1, \dots, N \quad (2.34)$$

where the influence coefficients B_{ij} and C_{ij} are the potential at i due to a constant unit strength distribution of source and doublet singularities respectively of an element with collocation point at j :

$$B_{ij} = \frac{1}{2\pi} \int_{panel} \ln r_{ij} ds \quad (2.35)$$

$$C_{ij} = \frac{1}{2\pi} \int_{panel} \frac{\partial}{\partial \hat{n}} \ln r_{ij} ds \quad (2.36)$$

Analytical evaluations of these integrals are found extensively in the literature, e.g. Katz and Plotkin (2001).

Equation 2.28 may be discretised as follows and must be applied to both upper and lower cavity surfaces:

$$\phi_j = \phi_0 + \sum_{k=1}^j \left(-U_\infty \cdot \hat{t}_k + U_\infty \sqrt{1 + \sigma} \right) \Delta s_k \quad (2.37)$$

The strength of the wake doublet may be expressed in terms of the difference in doublet strengths at the cavity trailing edge from Equation 2.37. The substitution of Equation 2.37 into 2.34 leads to N equations for the unknown doublet strengths on the foil surface and the source strengths on the cavity. Finally Equation 2.32 may be discretised to form an additional equation for the cavity velocity which must be applied to both upper and lower cavity surfaces:

$$\sum_{k=1}^{j_{cte}} \left(\frac{\partial \phi}{\partial \hat{n}_k} U_\infty \cdot \hat{n}_k \right) \Delta s_k = 0 \quad (2.38)$$

The source strengths on the cavity surface and cavity velocity obtained from solution of the above formulation may then be used to update the cavity surface in the normal direction using the discretised version of Equation 2.32:

$$\Delta h = \frac{1}{U_c} \sum_{k=1}^j \left(\frac{\partial \phi}{\partial \hat{n}_k} + U_\infty \cdot \hat{n}_k \right) \Delta s_k \quad (2.39)$$

Confined flow BEM solution

The above description is for the boundary element method implementation of the potential flow solution for a bluff body with cavity in an infinite flow domain. BEM based solutions for the confined single-phase flow over lifting surfaces have been developed based on: the method of images; a total potential formulation; and a perturbation potential formulation (see Ojha and Shevare, 1985; Choi and Kinnas, 1998). A method of images solution was also presented by Kinnas and Mazel (1993) for the confined flow analysis of supercavitating foils. The perturbation potential formulation of Choi and Kinnas (1998) has been extended here to confined supercavity flows. The addition of confining walls has been implemented in a version of the present boundary element method as described in Figure 2.7. The total body surface S in Equation 2.21 is now composed of the foil, cavity and walls. Flow tangency (kinematic boundary condition, Equation 2.22) is imposed on the wall surfaces, and the solution procedure is in all other aspects the same as for the infinite flow domain problem. An increased computation time does result however, due to the additional wall elements in N , adding to the size of the equation matrix being solved (Equation 2.34).

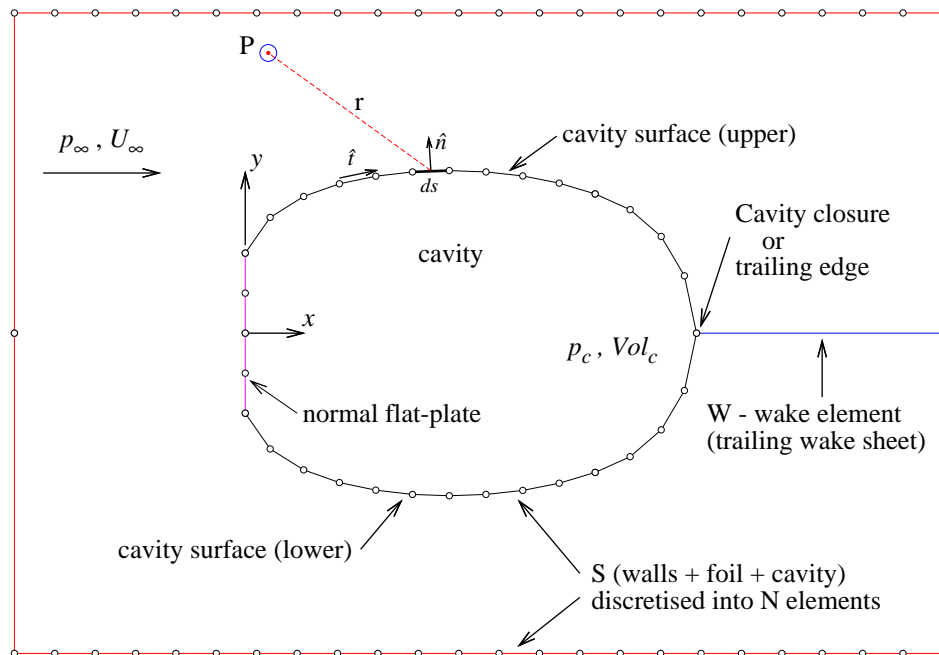


Figure 2.7: Boundary element method - confined flow solution description.

2.3.3 Modelling Issues

Surface discretisation

The discretisation of the body and cavity surfaces involves consideration of several issues. Numerical differentiation of the surface potential is required to calculate surface velocity and so element lengths need to vary smoothly to minimise error. Elements also need to be finely graded in regions of high pressure gradient and surface curvature. For computational efficiency a cosine discretisation has been implemented to obtain the small element lengths required at the ends of the individual surfaces and also at the leading edge of bodies with thickness. Figure 2.8 shows a typical example of the discretised surfaces. To maintain smooth variation of element lengths across the foil/cavity interfaces element numbers on the cavity surface are adjusted with cavity length. In the same way if the number of elements on the body is varied the number of cavity elements is varied to suit.

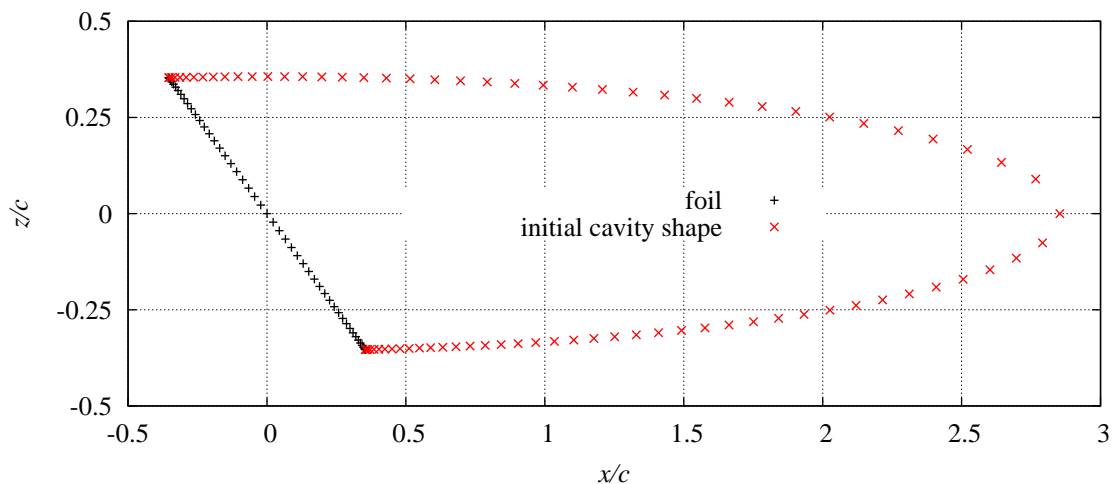


Figure 2.8: Typical surface discretisation for a flat-plate foil with initial (first iteration) cavity shape.

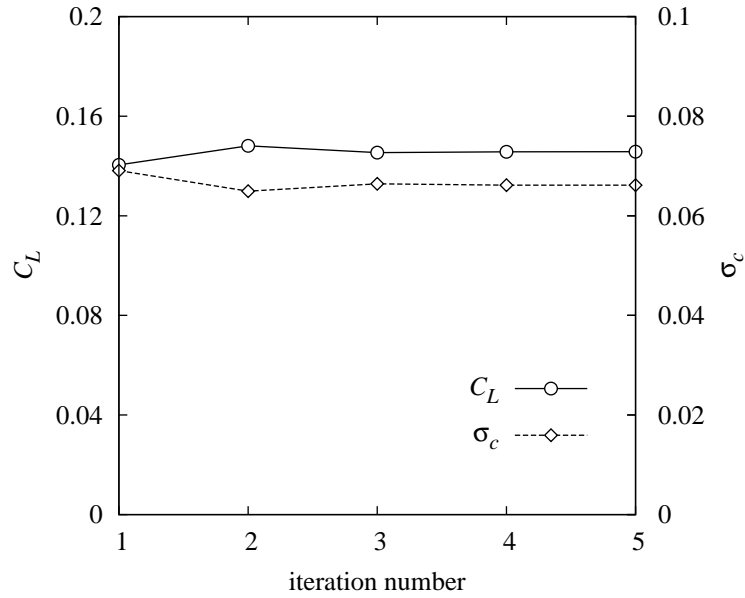
Also of concern is the discretisation in the vicinity of the cavity closure region. The implementation used for this analysis did not include an explicit closure model to account for the deceleration of the cavity surface velocity back to free stream value. If the elements in the closure region are too small a re-entrant jet type structure forms as the cavity surface is adjusted with successive iterations. These solutions are numerically unstable and do not converge. Increasing the element size in the closure region by using a half-cosine discretisation on each cavity surface removes this behaviour and results in a stable solution. By not properly modelling the physics of the closure region some error will likely be inherent in the solution. It is assumed that with the closure far away from the foil it will have a negligible effect on the local flow geometry about the foil and hence the forces produced. This is a reasonable assumption

except possibly for the shorter cavities as the comparison with experiment and theory shows (Figure 2.12). A cavity termination model (Kinnas and Fine (1991)) which uses a transition length over which the velocity is continuously varied between the constant value on the cavity surface down to the free stream value was implemented and assessed. It however made little difference to the results obtained and in any case is an artifice as the re-entrant jet cavity closure is an inherently unsteady structure dominated by viscous forces and so cannot be accounted for within a steady potential flow method. The results obtained show that de-resolving of the re-entrant jet behaviour gives adequate flow modelling for super-cavities of practical length.

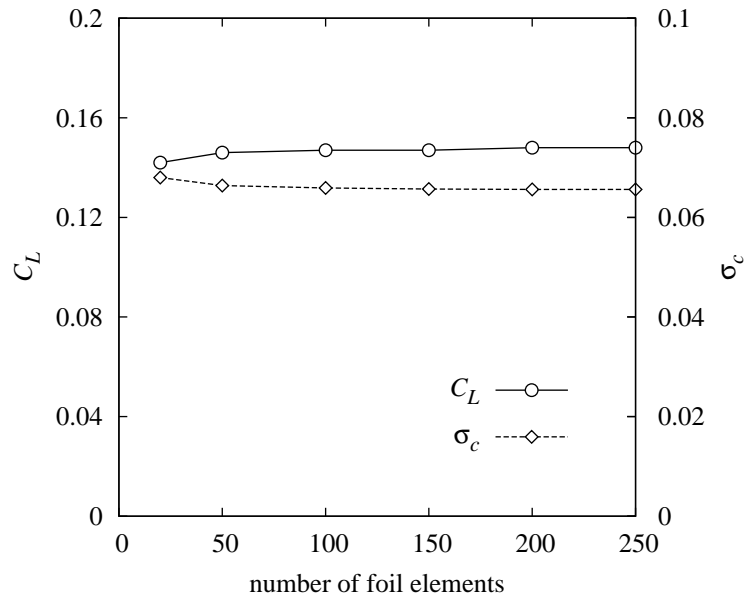
Convergence

The solution converges quickly, within 3 to 4 iterations, as can be seen in Figure 2.9a. This example is of a flat-plate supercavitating foil ($\alpha = 5^\circ$ and $\sigma_c = 0.66$), with the parameters C_L and σ_c plotted against the number of solution iterations. The method was found to be insensitive to the initial (1st iteration) cavity shape chosen. An elliptical shape was used as it provided a sufficient separation between the elements adjacent to the cavity closure point. Otherwise instabilities arose, particularly at large cavity lengths, causing the solution to diverge. An example of the parameter convergence with increasing number of elements, for a constant α and σ_c , is shown in Figure 2.9b. A converged solution in this case is achieved by 100 to 150 foil elements.

An example of the cavity shape progression through 5 iterations is shown in Figure 2.10. Iteration 1 is the initial prescribed shape. Iteration 2 is an under-prediction of the converged shape: then iteration 3 is an over-prediction; with iteration 4 being the converged result, as confirmed by the iteration 5 prediction. Magnified views of the leading and trailing edge zones of a flat-plate foil are given in Figure 2.11. The element end points are shown and the trajectories of the 5th point in each case is plotted to indicate the element movement through the iterations. The cosine spacing; and the matching of the lengths of the foil edge and 1st cavity surface elements (1st iteration), can be seen.



(a) Convergence with number of iterations.



(b) Convergence with number of foil elements.

Figure 2.9: Convergence of C_L and σ_c for a flat-plate supercavitating foil, ($\alpha = 5^\circ$ and $\sigma_c = 0.66$) with: (a) number of iterations; (b) number of foil elements.

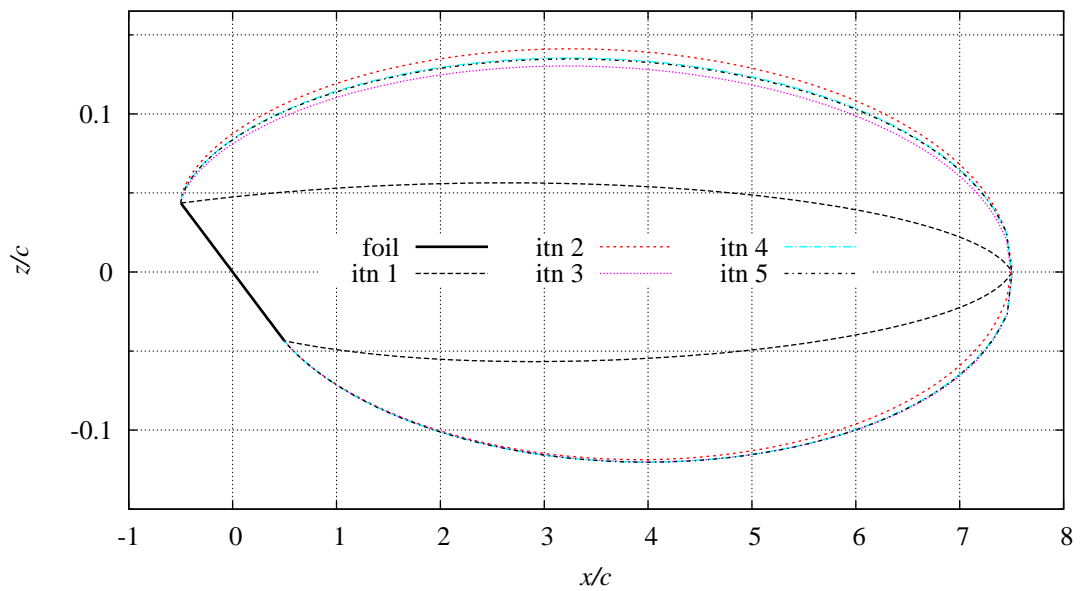
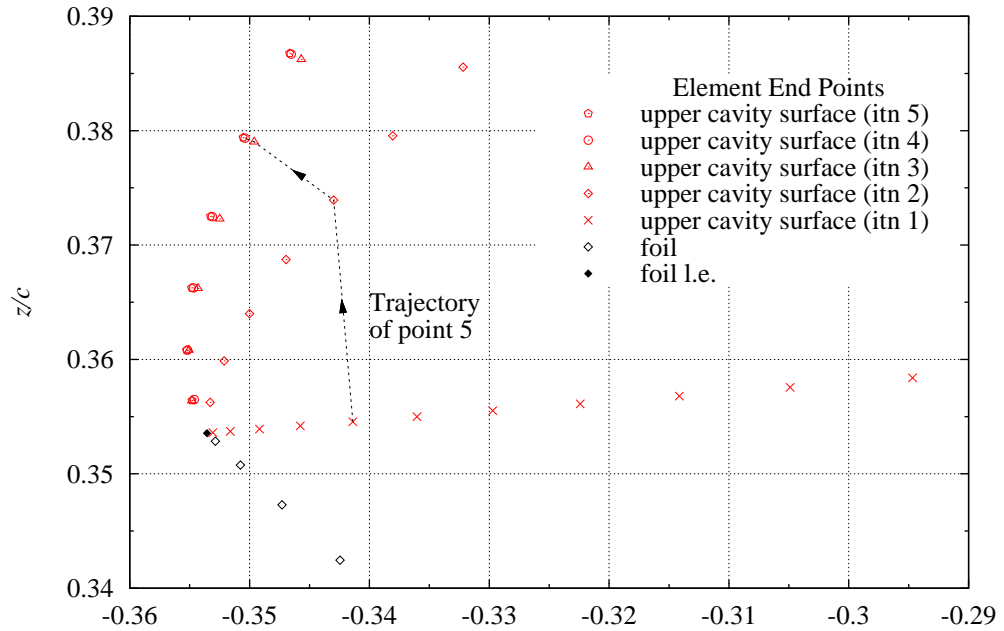
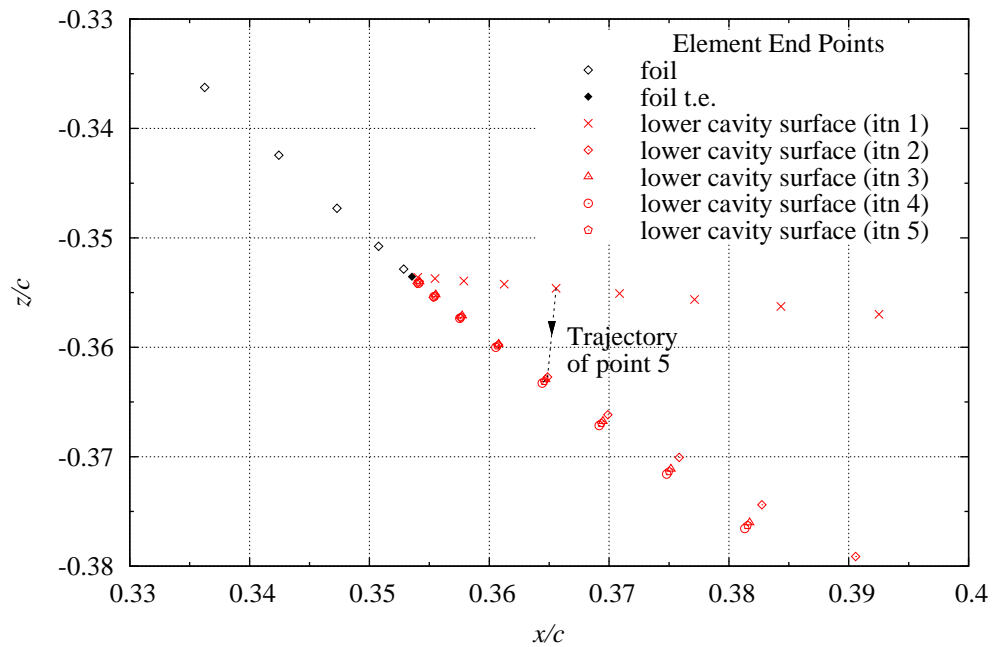


Figure 2.10: Cavity surface progression (first 5 iterations) for a flat-plate foil with $\alpha = 5^\circ$ and $\sigma_c = 0.66$.



(a) Leading edge region.



(b) Trailing edge region.

Figure 2.11: Surface discretisation for a flat-plate hydrofoil (five cavity surface iterations shown) in the region of the (a) leading edge and (b) trailing edge.

2.3.4 Comparison with other data

A comparison of the BEM results with theory (Wu, 1956) and experimental data (Parkin, 1956) is given in Figure 2.12 for a flat-plate supercavitating foil at $\alpha = 15^\circ$. The results are in good agreement except for large σ_c values, corresponding to short cavity lengths (for $\sigma_c = 0.52$, $l_c/C = 2$). The inadequacy of the potential flow models to adequately account for the physics of the cavity closure, may explain the discrepancy with the experimental data for large σ_c values.

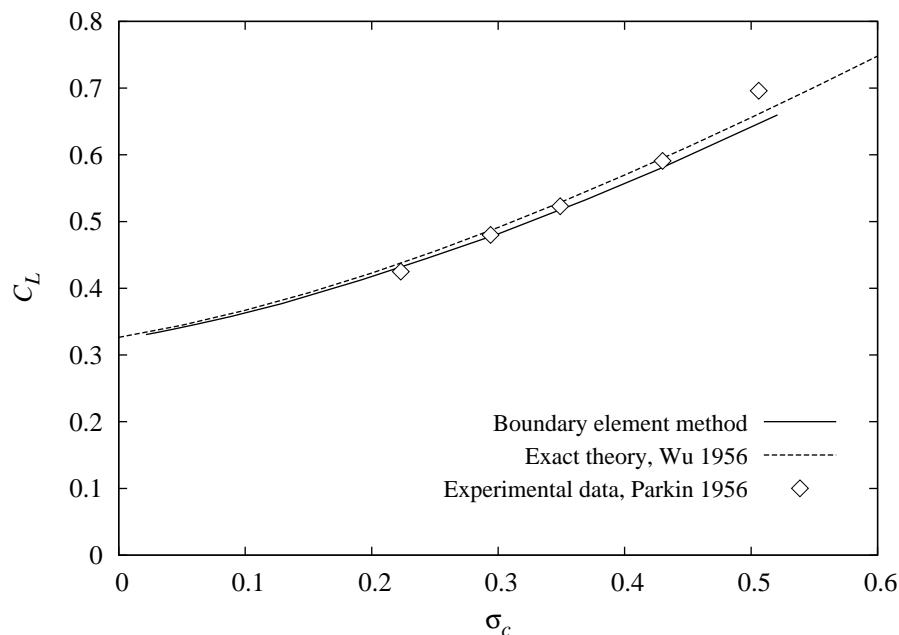


Figure 2.12: Comparison of boundary element method results with experimental data from Parkin (1956) and Wu's exact theory (Wu, 1956) for a flat-plate supercavitating hydrofoil with $\alpha = 15^\circ$.

2.4 Modelling cavitation with CFD

As discussed in the introduction to this chapter, the physics involved in the unsteady cavity closure cannot be modelled accurately with potential based methods. The effect of an upstream boundary layer approaching a wall mounted fence is another aspect that cannot be modelled realistically with inviscid flow models. The ongoing development of computational fluid dynamics codes, solving the viscous Reynolds-Averaged Navier-Stokes (RANS) equations, have seen the inclusion of various cavitation models. With this enhancement to the CFD models, the 2-D and 3-D viscous analysis of cavitating flows involving various submerged bodies, e.g. hydrofoils, projectiles, propellers, pump impellers etc., is in general use (See, for example, Kunz et al., 1999; Singhal et al., 2002; Nohmi et al., 2003; Kimura et al., 2009). To under-

take the viscous 2-D analysis of the cavitating flow over a wall mounted fence in the present study, the commercial CFD package ANSYS-CFX 12.1 was used. An unsteady two dimensional finite volume method with a structured hexahedral mesh has been used. Additional detail of the overall modelling is given in Section 3.5.1

The modelling of cavitating flows within the scope of CFD analysis can be broadly grouped into the following categories (See Bakir et al., 2004):

- Solutions using single-phase conservation equations, with the addition of an empirical Barotropic state law $\rho(p)$, to determine the two-phase mixture conditions. The two-phase flow is assumed to be homogeneous, i.e. a no-slip condition between the components, and local thermal equilibrium is assumed between the phases (Reboud et al., 1998).
- Solutions treating each phase separately, with a variety of approaches to the non-equilibrium exchange of heat, mass and momentum between the phases (See, for example, Athavale et al., 2002).
- Interface tracking methods (Tryggvason et al., 2007), although generally these methods do not solve for the full transport equations in both the single and two-phase regions.

ANSYS-CFX 12.1 provides one cavitation model based on an interphase mass transfer model with the option for custom implemented ‘user defined models’. The ANSYS-CFX 12.1 cavitation model was used for this initial analysis. Other models may be investigated in future work when experimental data is available for comparison with CFD results. The ANSYS-CFX 12.1 cavitation model falls into the second category listed above, with the derivation and validation given by Bakir et al. (2004). Cavitation is assumed to be solely driven from mechanical effects, i.e. liquid-vapour pressure differences. The process is assumed to occur too rapidly for thermal effects to be important. In summary, the model is derived from a simplified and linearised version of the Rayleigh-Plesset equation, neglecting viscosity and surface tension. This is applied to an assumed homogeneous bubbly flow from which two equations for rate of vaporisation and condensation respectively are derived. The vapour volume fraction, determined from the rate equations, is introduced into the source terms of the volume-of-fluid. The change of phase is initiated from nucleation sites, i.e. microbubbles (See, Section 1.1) assumed to contain non-condensable gas (air), homogeneously distributed throughout the volume. The rate equations for vaporisation and condensation as implemented in ANSYS-CFX 12.1 (Eq.4.265 and Eq.4.266 ANSYS, 2009, p.147) are given here as Equations 2.40 and 2.41 respectively.

$$\dot{m}_{fg} = F \frac{3r_g \rho_g}{R_{nuc}} \sqrt{\frac{2}{3} \frac{|p_v - p|}{\rho_l}} \text{sgn}(p_v - p) \quad (2.40)$$

where: F is an empirical factor which differs for condensation and vaporization, due to these processes occurring at different rates; r_g is the vapour volume fraction; R_{nuc} is the nucleation site (bubble) radius; with the subscripts f and g designating the liquid and vapour phases respectively. With vaporisation the vapour volume fraction increases. The nucleation site density must be correspondingly decreased as there is less liquid. This is accounted for by replacing r_g with $r_{nuc}(1-r_g)$ where r_{nuc} is the volume fraction of the nucleation sites. For vaporisation Equation 2.40 then becomes:

$$\dot{m}_{fg} = F \frac{3r_{nuc}(1-r_g)\rho_g}{R_{nuc}} \sqrt{\frac{2}{3} \frac{|p_v - p|}{\rho_l}} \text{sgn}(p_v - p) \quad (2.41)$$

The ANSYS-CFX 12.1 default values for the empirical factor F and the nuclei concentration and size are specified as:

- $R_{nuc} = 1\mu\text{m}$
- $r_{nuc} = 5 \times 10^{-4}$
- $F_{vap} = 50$
- $F_{cond} = 0.01$

These default values were used for the CFD analysis of the cavitating flow over a wall mounted fence presented in Section 3.5. It was found though that by varying any one of them, the resulting flow field varied, and in some cases quite considerably. A variation in nuclei seeding has been found experimentally to have a substantial effect on the occurrence and extent of cavitation for a given flow (Brennen, 1995; Franc and Michel, 2004), so it is not unexpected that the CFD data will be similarly dependent. This will be a point of considerable interest when comparing CFD predictions with experimental data obtained from the upgraded AMC CRL cavitation tunnel. The new facility will have control over both the size and distribution of the nuclei for accurate modelling of cavitation phenomena (Brandner et al., 2006, 2007, 2010).

2.5 Summary

Various approaches to the analysis of cavitating flows have been presented in this chapter. The primary method chosen to undertake the analysis in this thesis has been the boundary element method. Its attractiveness and suitability for the bluff body supercavitating flows of interest in this work is due to the following aspects:

- generally supercavitating flows are suited to modelling with potential methods
- direct, exact nonlinear method
- considerably reduced computational time and hardware resource when compared with CFD
- arbitrary body shapes can be modelled
- both infinite and confined flow solutions.

Use has been made of some classical analytical methods for bodies of simple shape, e.g. flow over a normal plate and a flat-plate foil, for comparison with the BEM predictions. CFD has been used to examine the effect of viscosity, i.e. the presence of a boundary layer, on the cavitating flow over a wall-mounted fence which cannot be accounted for in the boundary element model.

As the aim of this study was to investigate a suitable foil section to meet specific requirements (Section 1.2), an efficient method where a large range of parameters could be assessed, within a sensible time frame, was desirable. The BEM used served this purpose adequately. Particular details of the flow, the effect of viscosity, surface tension, ventilation rates etc., not included in this potential flow method, have and will need to be investigated by CFD and ultimately only fully assessed by experiment.

Chapter 3

Wall-Mounted Fence Flow with Cavitation - Analytical and Numerical Methods

3.1 Introduction

The present study is concerned with the use of a fence or ‘so called’ interceptor at the trailing edge of a blunt based hydrofoil to generate bi-directional lift. This is achieved by the forming of a sharp edge that induces stable cavity detachment, with lift resulting from the upstream surface pressure distribution. As discussed in Section 1.3, this is the principle of operation of the transom mounted interceptor used for ride control of high speed craft.

To gain a basic understanding of the hydrodynamic performance of this arrangement, the analysis of the interceptor flow in isolation from the foil is first considered. A study of the 2-D flow about a fence attached to a flat wall is the simplest case of such a flow, and is the subject of the present chapter. This investigation will then also provide a basic analysis of the ship transom interceptor problem. The fence geometry is systematically varied to find its effect on cavity shape and surface pressure distribution and the resulting L/D . Figure 3.1 gives a sketch of the basic arrangement: a flat-faced fence mounted normal to a flat wall with a vapour/gaseous cavity detaching from the sharp fence tip. Also indicated is the wall boundary layer and the typical shape of the upstream surface pressure distribution. The unsteady nature of the cavity closure region is indicated by a re-entrant jet/vortical type topology.

As discussed in Chapter 2 the classical approach to the analysis of bluff-body cavitating flow of simple geometry was to employ free-streamline analytical methods based on conformal transformations. The flow over a normal flat plate has been modelled with the present boundary element method (BEM) and comparison made with analytical results. From this inviscid analysis, data for wall-mounted fence flow has been obtained via use of symmetry, i.e. by considering the dividing streamline as representing a wall and one half of the body-cavity representing the wall-mounted fence with associated cavity behind

it. Although both of these approaches are inviscid, use is made of them here to provide the ‘ideal’ upper limit to the efficiency that could be expected in these wall-mounted fence flows.

To obtain a more realistic estimate the flow has also been analysed using a RANS based CFD code which includes the effects of viscosity including the presence of a boundary layer and flow separation upstream of the fence. At the time of undertaking this analysis experimental data was not yet available, and so comparison could only be made with the other analytical/numerical results presented in this chapter to assess the appropriateness of the CFD parameter settings and applied boundary conditions used.

As the foil numerical analysis (see Chapter 4) was undertaken with a boundary-element method, which is also an inviscid model, it was considered of interest here to investigate if a curved-face fence could be used in the foil model to account for the viscous effect of the interceptor operating within the foil boundary layer. To this end boundary-element simulations on ramp flows were also performed and reported on here. The term ‘ramp’ is used here to describe a curved rather than a flat fence.

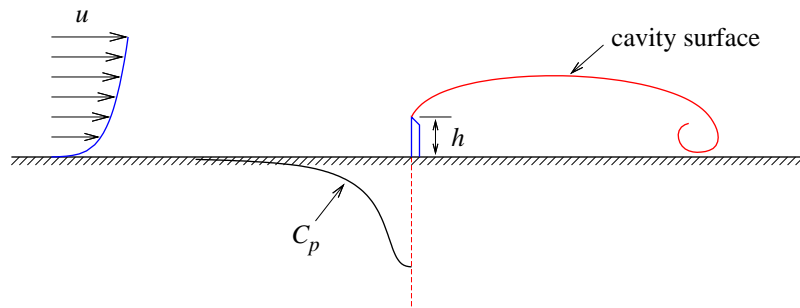


Figure 3.1: Sketch of the cavity flow over a normal wall-mounted fence immersed in the wall boundary layer. A typical wall pressure distribution is indicated.

3.2 Cavity shape

In supercavitating flows there is a general relation between the length of the cavity, measured from the detachment point to the closure, and the cavity under pressure coefficient, σ_c . From linearised theory, for a finite length cavity behind a symmetric body in an infinite flow field, this relation is predicted to be:

$$\frac{l_c}{c} \propto \sigma_c^n \quad \text{or} \quad \frac{l_c}{c} = A\sigma_c^n \quad (3.1)$$

where A is a constant and $n = -2$ (Tulin (1953); Franc and Michel (2004)). Note that the linearised theory makes the assumption that σ_c is small.

In this chapter comparisons between the classical linear theory predictions, other exact analytical methods, and the present non-linear BEM will be presented for various parameters including cavity length where applicable

3.3 Analytical analysis - Flow normal to a flat plate

3.3.1 Ideal non-cavitating flow

Attached flow over a fence is considered as an extreme case (non-cavitating - $\sigma_c = \infty$) for comparison with the cavitating cases. The ideal flow normal to a flat plate (see Section 2.2.1) is given by¹,

$$\phi^2 - \psi^2 = U_\infty^2 (x^2 - y^2 + a^2) \quad (3.2)$$

where a is plate half-length as shown in Figure 3.2.

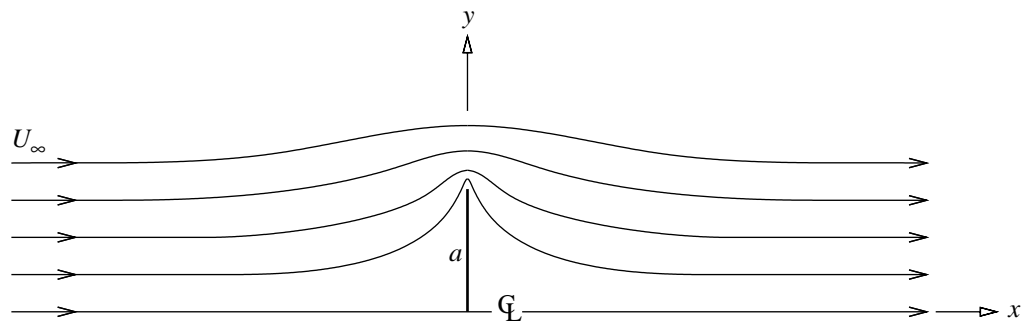


Figure 3.2: Streamlines for the 2-D ideal flow over a flat plate oriented normal to the flow. Only the upper half of the symmetric flow field is shown, with the full plate length = $2a$.

To obtain the ideal flow pressure distribution along the wall upstream of a fence we can consider, due to symmetry, the dividing streamline as the wall and one half plate as the fence. The pressure distribution along the dividing streamline is then the desired wall pressure distribution. On the dividing streamline upstream of the plate, i.e. for $y = 0$ and $x \leq 0$, $\psi = 0$. With $U_\infty = 1$ and $a = 1$ Equation 3.2 then gives

$$\phi = -\sqrt{x^2 + 1} \quad (3.3)$$

and

¹(See also White, 2010, p.557)

$$u = \frac{\partial\phi}{\partial x} = \frac{x}{\sqrt{x^2 + 1}} \quad (3.4)$$

The pressure distribution along the dividing streamline can then be determined from Bernoulli's equation giving

$$\begin{aligned} C_p = \frac{(p - p_\infty)}{\frac{1}{2}\rho U_\infty^2} &= 1 - \left(\frac{u}{U_\infty}\right)^2 \\ &= 1 - u^2 \quad \text{for } U_\infty = 1 \end{aligned} \quad (3.5)$$

Equation 3.5 can now be integrated along the wall upstream from the fence to obtain the lift produced due to its presence.

Next the pressure distribution over the face of the plate is determined. For the front face of the plate, i.e. for $x = 0$ and $0 \leq y \leq 1$, again $\psi = 0$. Note also that $u = 0$ as the plate is normal to the flow. With $U_\infty = 1$ and $a = 1$ Equation 3.2 gives

$$\phi = -\sqrt{1 - y^2} \quad (3.6)$$

and

$$v = \frac{\partial\phi}{\partial y} = \frac{y}{\sqrt{1 - y^2}} \quad (3.7)$$

Again the pressure coefficient is determined from Bernoulli's relation along a streamline giving

$$C_p = 1 - v^2 \quad (3.8)$$

As the flow is symmetrical about the plate the net force is zero, i.e. $C_D = 0$. As discussed in Section 2.2 this is not a realistic flow, and hence the concept of an L/D is irrelevant in this instance.

3.3.2 Free-streamline flow - $\sigma_c = 0$

The flow over a normal plate of width $2b$ with an infinite cavity detaching from its edges, i.e. $\sigma_c = 0$ (Batchelor, 1967, p.499), is shown in Figure 3.3.

From free-streamline theory as described in Section 2.2.2 the flow field is given, in terms of the complex velocity $w = u + iv$, from Equation 2.13 by

$$\begin{aligned} \frac{z}{k} &= 2i \left(\frac{w}{kU}\right)^{\frac{1}{2}} + \left(\frac{w}{kU}\right)^{\frac{1}{2}} \left(\frac{w}{kU} - 1\right)^{\frac{1}{2}} + \frac{1}{2}\pi i \\ &\quad - \ln \left\{ \left(\frac{w}{kU}\right)^{\frac{1}{2}} + \left(\frac{w}{kU} - 1\right)^{\frac{1}{2}} \right\} \end{aligned} \quad (3.9)$$

$$\text{where } k = \frac{2b}{(\pi + 4)}$$

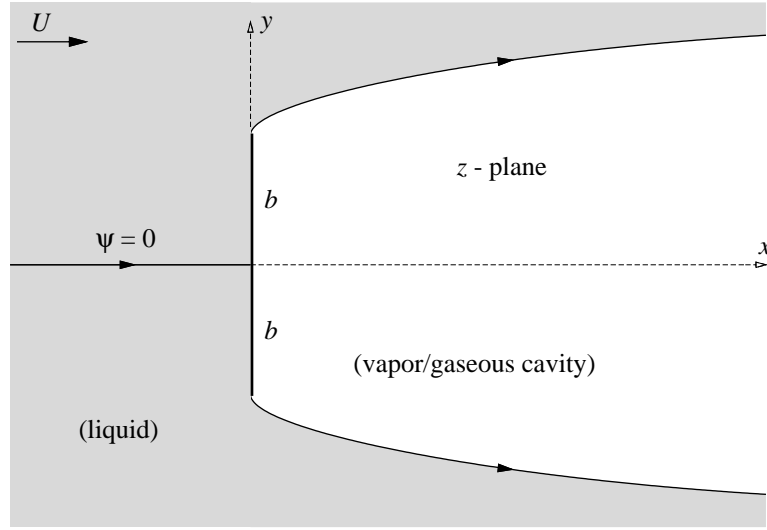


Figure 3.3: 2-D free-streamline flow over a perpendicular flat plate with the pressure in the cavity equal to the free-stream value at infinity, i.e. $\sigma_c = 0$.

Along the dividing streamline upstream of the fence, i.e. along $y = 0$ for $x \leq 0$, $\psi = 0$ and therefore $w = \phi$ with $\phi < 0$. Upon substituting $-(-\phi)$ for ϕ into Equation 3.9 gives

$$x = -k \left[2 \left(\frac{-\phi}{kU} \right)^{\frac{1}{2}} + \left(\frac{-\phi}{kU} \right)^{\frac{1}{2}} \left(\frac{-\phi}{kU} + 1 \right)^{\frac{1}{2}} + \ln \left\{ \left(\frac{-\phi}{kU} \right)^{\frac{1}{2}} + \left(\frac{-\phi}{kU} + 1 \right)^{\frac{1}{2}} \right\} \right] \quad (3.10)$$

As the velocity results from the derivative of the velocity potential, and as $v = 0$ in this case, Equation 2.6 then gives

$$\zeta = \frac{\partial x}{\partial \phi} = \frac{1}{u} \quad (3.11)$$

Differentiating Equation 3.10 with respect to ϕ therefore gives

$$\zeta = -\frac{1}{2U} \left[2 \left(\frac{-\phi}{kU} \right)^{-\frac{1}{2}} + \left(\frac{-\phi}{kU} \right)^{-\frac{1}{2}} \left(\frac{-\phi}{kU} + 1 \right)^{\frac{1}{2}} + \left(\frac{-\phi}{kU} \right)^{\frac{1}{2}} \left(\frac{-\phi}{kU} + 1 \right)^{-\frac{1}{2}} + \left(\frac{\left(\frac{-\phi}{kU} \right)^{-\frac{1}{2}} + \left(\frac{-\phi}{kU} + 1 \right)^{-\frac{1}{2}}}{\left(\frac{-\phi}{kU} \right)^{\frac{1}{2}} + \left(\frac{-\phi}{kU} + 1 \right)^{\frac{1}{2}}} \right) \right] \quad (3.12)$$

and as $q = u = 1/\zeta$, the pressure distribution along the centre streamline upstream of the plate is obtained from

$$C_p = 1 - \frac{1}{\zeta^2} \quad (3.13)$$

The resulting lift is obtained by integrating this pressure distribution.

Along the front face of the plate $x = 0$ and $\phi \geq 0$. All terms in Equation 3.9 must then be complex, i.e. $\phi \leq kU$. (If $\phi = kU$ then $z = i$ with $x = 0$ and $y = 1 = a$). To find the pressure acting on the front face of the plate Equation 3.9 is evaluated for $x = 0$ and $0 \leq \phi \leq kU$. Substituting $-(1 - \phi/kU)$ for $(\phi/kU - 1)$ gives

$$z = ik \left[2 \left(\frac{\phi}{kU} \right)^{\frac{1}{2}} + \left(\frac{\phi}{kU} \right)^{\frac{1}{2}} \left(1 - \frac{\phi}{kU} \right)^{\frac{1}{2}} + \frac{\pi}{2} - \tan^{-1} \left\{ \left(\frac{kU - \phi}{\phi} \right)^{\frac{1}{2}} \right\} \right] \quad (3.14)$$

The velocity is then obtained by differentiating Equation 3.14

$$\zeta = \frac{\partial y}{\partial \phi} = \frac{1}{v} \quad (3.15)$$

giving

$$\zeta = k \left[\frac{1}{kU} \left(\left(\frac{\phi}{kU} \right)^{-\frac{1}{2}} + \frac{1}{2} \left(\frac{\phi}{kU} \right)^{-\frac{1}{2}} \left(1 - \frac{\phi}{kU} \right)^{\frac{1}{2}} - \frac{1}{2} \left(\frac{\phi}{kU} \right)^{\frac{1}{2}} \left(1 - \frac{\phi}{kU} \right)^{-\frac{1}{2}} \right) + \frac{1}{2\phi} \left(\frac{kU}{\phi} - 1 \right)^{-\frac{1}{2}} \right] \quad (3.16)$$

with again the pressure coefficient calculated from

$$C_p = 1 - \frac{1}{\zeta^2} \quad (3.17)$$

The drag on the plate is then obtained by integrating this pressure distribution and the resulting L/D is the ratio the lift acting on the wall to the drag on the plate.

3.3.3 Free-streamline flow - $\sigma_c > 0$

A method for analysing free-streamline flows with cavities of finite extent, termed a notched hodograph, was developed by Roshko (1954) as described in Section 2.2. The basic flow features are shown in Figure 3.4 with the undisturbed flow velocity at infinity in this case being equal to $1/k$ instead of unity where $k^2 = 1 + \sigma_c$.

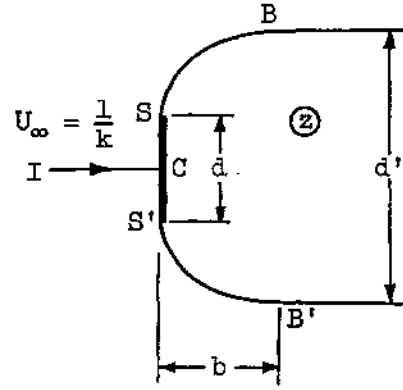


Figure 3.4: Notched hodograph flow over a normal flat plate, i.e. for $\sigma_c > 0$ (Roshko, 1954, Fig. 3).

Equation 3.18 (also 2.17, and see Roshko, 1954, Eq.3) gives the flow field over a normal flat plate in terms of the complex potential function w , as a function of only the parameter k :

$$z = \pm i \frac{k^2 + 1}{2k} \left(\sqrt{w(1-w)} + \tan^{-1} \sqrt{\frac{w}{1-w}} + \frac{1}{a} \sqrt{w(a^2-w)} + a \tan^{-1} \sqrt{\frac{w}{a^2-w}} \right) \quad (3.18)$$

The pressure is obtained from $\zeta(w)$, given by Roshko (1954, Eq.2) as

$$\zeta = \pm i \frac{k^2 + 1}{2k} \left(\sqrt{\frac{1}{\phi} - \frac{1}{a^2}} + \sqrt{\frac{1}{\phi} - 1} \right) \quad (3.19)$$

Using the relation from Equation 3.8, but with instead $U_\infty = 1/k$ gives

$$C_p = 1 - \frac{k^2}{\zeta^2} \quad (3.20)$$

Along the dividing streamline upstream of the fence, i.e. along $y = 0$ for $x \leq 0$, $\psi = 0$ and therefore $w = \phi$ with $\phi < 0$. With these values, and substituting $-(-\phi)$ for ϕ in Equation 3.18, gives

$$x = \frac{k^2 + 1}{2k} \left(-\sqrt{-\phi(1-\phi)} - \ln \left\{ \sqrt{1-\phi} + \sqrt{-\phi} \right\} - \frac{1}{a} \sqrt{-\phi(a^2-\phi)} - a \ln \left\{ \frac{\sqrt{a^2-\phi} + \sqrt{-\phi}}{a} \right\} \right) \quad (3.21)$$

and

$$\zeta = \frac{k^2 + 1}{2k} \left(\sqrt{\frac{1}{a^2} - \frac{1}{\phi}} + \sqrt{1 - \frac{1}{\phi}} \right) \quad (3.22)$$

The pressure coefficient is again calculated by substituting this expression for ζ in Equation 3.20, and the lift is then obtained by integration.

3.3.4 Results

The predicted pressure distribution over the face of the plate for the three analytical methods considered (from Equations 3.8, 3.17 and 3.20) is shown in Figure 3.5. When a cavity is present the pressure at the plate edge will be equal to the cavity pressure; so for a normal plate the pressure will vary from stagnation ($C_p = 1$) at the centre to the cavity pressure, $-\sigma_c$, at the plate edge.

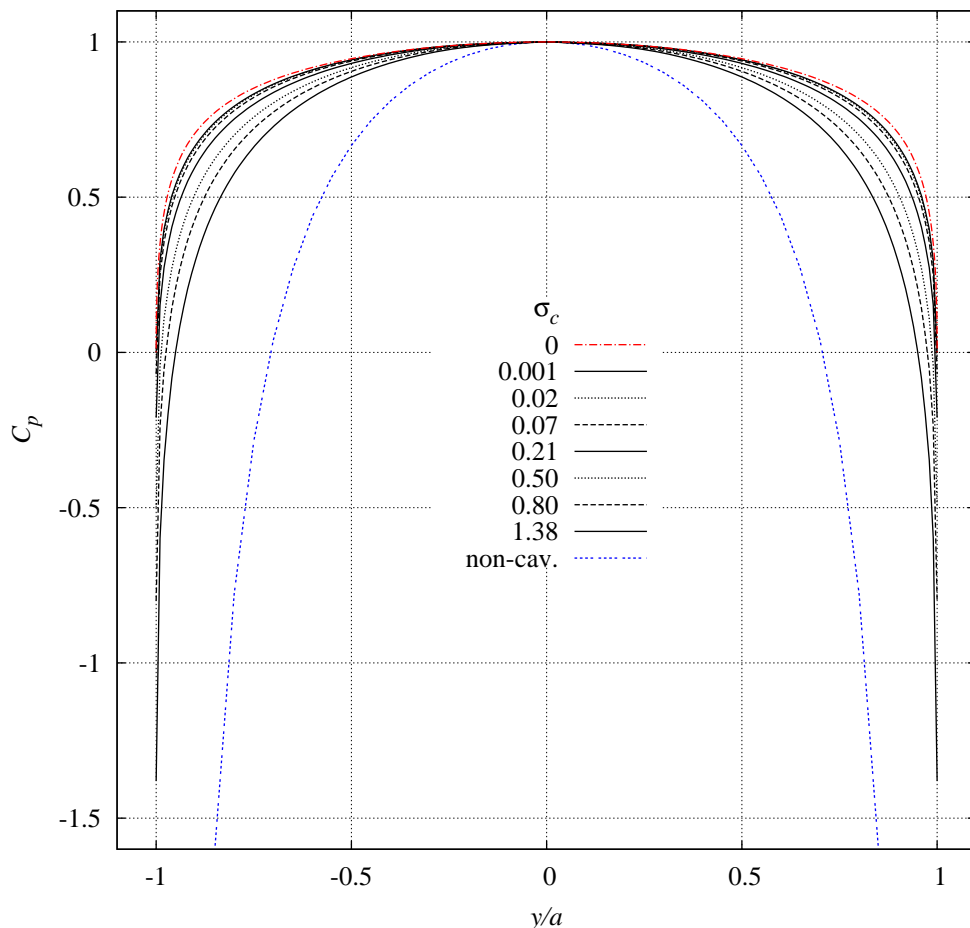


Figure 3.5: C_p distribution over the front of a normal plate. Comparison between the ideal flow (non-cavitating), a family of notched hodograph ($\sigma_c > 0$) results, and the infinite cavity ($\sigma_c = 0$) case.

For the infinite cavity case where $p_c = p_\infty$, C_p at the plate edge will be 0. As

the cavity length decreases (i.e. σ_c increasing), the pressure distribution over the plate reduces, with the plate edges becoming increasingly exposed instead to negative pressure. Note also that the back face of the plate is subject to the constant cavity pressure, p_c . Hence as σ_c increases (i.e. p_c decreases), the integral of the pressure differential between the front and rear sides of the plate, i.e. the drag, correspondingly decreases. The $\sigma_c = 0.001$ case in Figure 3.5 shows that the notched hodograph method result approaches, but does not match exactly, the infinite cavity solution. As σ_c increase the curves are trending towards the shape of the non-cavitating flow pressure distribution, but as expected will never reach it. The ideal-flow (non-cavitating) pressure distribution is unrealistic, with the $C_p = -\infty$ at the plate edge as can be seen from Equations 3.7 and 3.8 with $y = 1$.

A comparison of the Rhosko result with another analytical method (Wu, 1962) and some experimental data is shown in Figure 3.6. The analytical predictions are in good general agreement with each other and with the available experimental data for the $\sigma_c = -C_p = 1.38$ case. The experimental data is taken from the work of Fage and Johansen (1927), which was of air flow over a normal flat plate rather than a cavitating liquid flow. It is not strictly correct to use the term ‘cavitation number’ with respect to a single phase flow. As the wake or cavity pressure is assumed constant in free-streamline theory use of a cavitation number, based on p_c , is reasonable in this context irrespective of whether the flow is single- or two-phase. In the case of a real single-phase flow over a normal plate, $p \neq \text{const.}$ over the rear of the plate as assumed, consequently free-streamline theory gives a poor drag estimate. However, the estimate of pressure distribution on the front of the plate is more accurate, as shown by the comparison with single-phase flow experimental data in Figure 3.6.

The predicted pressure distributions along the dividing streamline upstream of the plate for the three analytical methods considered (from Equations 3.5, 3.13 and 3.20) are shown in Figure 3.7. Far upstream of the plate, the pressure in all cases exhibits a power law relationship with the exponent varying from -2 for the ideal (non-cavitating) flow, through -1 for the notched hodograph results ($\sigma_c > 0$), to -0.5 for the infinite cavity ($\sigma_c = 0$) case. As with the pressure distributions over the front of the plate (Figure 3.5), the notched hodograph results along the dividing streamline approach the $\sigma_c = 0$ result as σ_c approaches zero. With $\sigma_c \gg 1$ the notched hodograph results converge to an asymptotic limit, but not to the non-cavitating flow result. Note that both the $\sigma_c = 10$ and 100 cases would not correspond to practical cavities (i.e. a cavity would not be present at such high cavitation numbers in a real flow). These cases are only included to illustrate the limit of the solution.

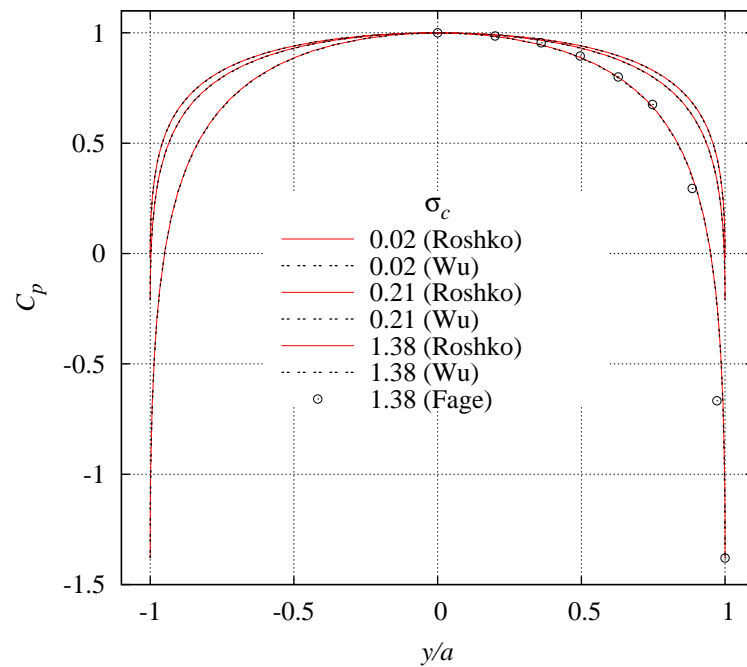


Figure 3.6: Comparison of the pressure distribution over the front of a normal plate predicted by the analytical methods of Roshko (1954) and Wu (1962) for $\sigma_c = 0.02, 0.21$ and 1.38 . Also included is experimental data for $C_p = -1.38$ from Fage and Johansen (1927).

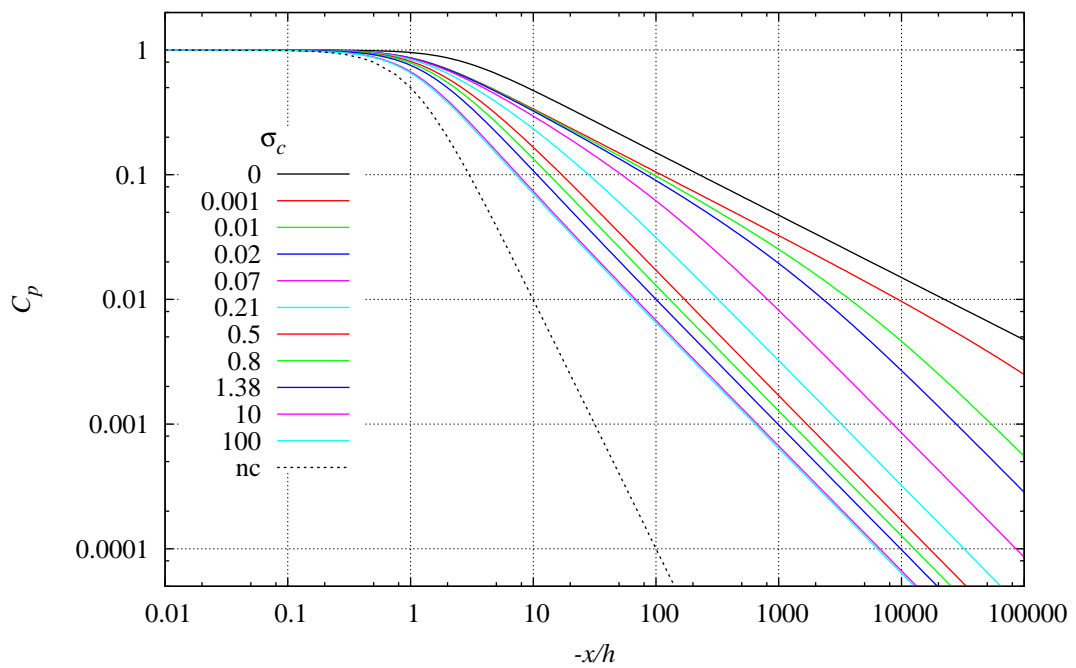


Figure 3.7: C_p distribution along the dividing streamline. Comparison of the infinite cavity ($\sigma_c = 0$), notched hodograph - finite cavity ($\sigma_c > 0$), and the non-cavitating flow (nc) results. The distributions in all cases show a power law relationship far upstream of the plate with the exponent varying from -2 for the ideal flow, through -1 for the ($\sigma_c > 0$) cases, to -0.5 for the $\sigma_c = 0$ case.

3.4 BEM analysis

3.4.1 Fence Geometry

This section describes the geometry of the wall-mounted fence arrangement of interest here. A “wall” in the present context is a flat horizontal surface unless otherwise indicated, and a “fence” is any sharp edged protrusion from the wall orientated transverse to the flow direction. The wall is considered to be of infinite extent and the fence has a length (i.e the normal projection of the fence onto the wall) of $O(h)$ where h is the perpendicular height of the fence as shown in Figure 3.8a. As the cavity detaches from the fence tip any portion of the fence downstream of the tip will be located wholly within the cavity, and thus will not affect the flow. Consequently only the fence shape up to the tip has been modelled in the following analysis.

The attachment of a fence to a wall can be geometrically discontinuous, have a smoothly varying form (i.e. with continuous curvature), or involve some combination of these extremes. The simplest discontinuous shape is a flat faced fence at some angle, β , to the wall (see Figure 3.8a). The orientation of principal interest here is the perpendicularly mounted fence (i.e. with $\beta = 90^\circ$). A smoothly varying fence must initially match the slope and curvature of the wall (i.e. $dy/dx = 0$; $\kappa = 0$ respectively) with slope then varying smoothly to the outer edge at some angle, β , relative to the wall (see Figure 3.8b).

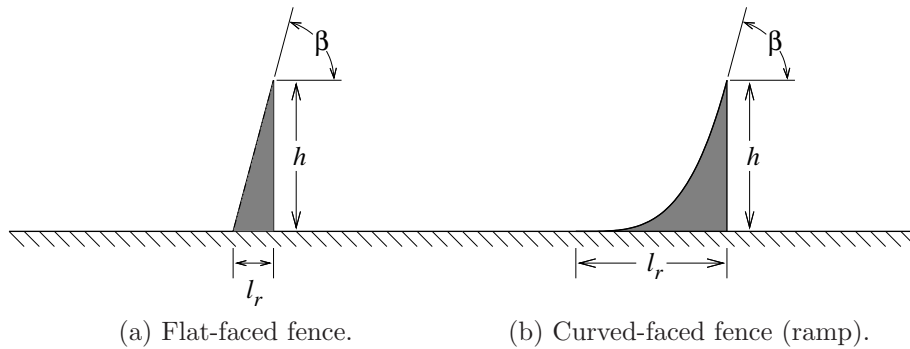


Figure 3.8: Examples of simple wall mounted fence shapes: (a) discontinuous; (b) smoothly varying.

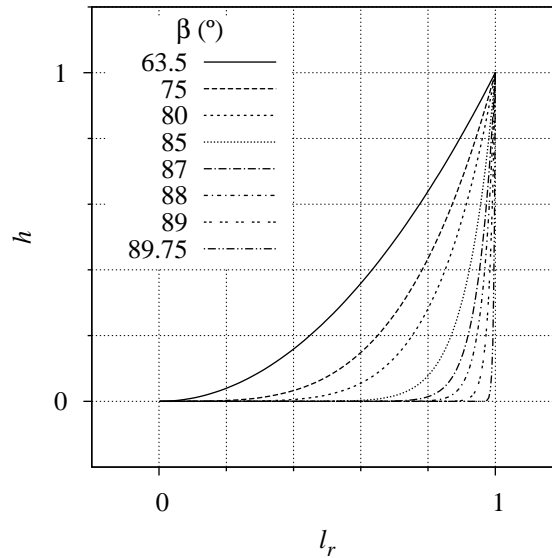
A simple function, for a ramp of unit length, which satisfies the requirement for $dy/dx = 0$ and $\kappa = 0$ at $x = 0$ and which varies monotonically along to $x = 1$ giving a smooth curved shape is:

$$y = Ax^n, 0 \leq x \leq 1 \quad (3.23)$$

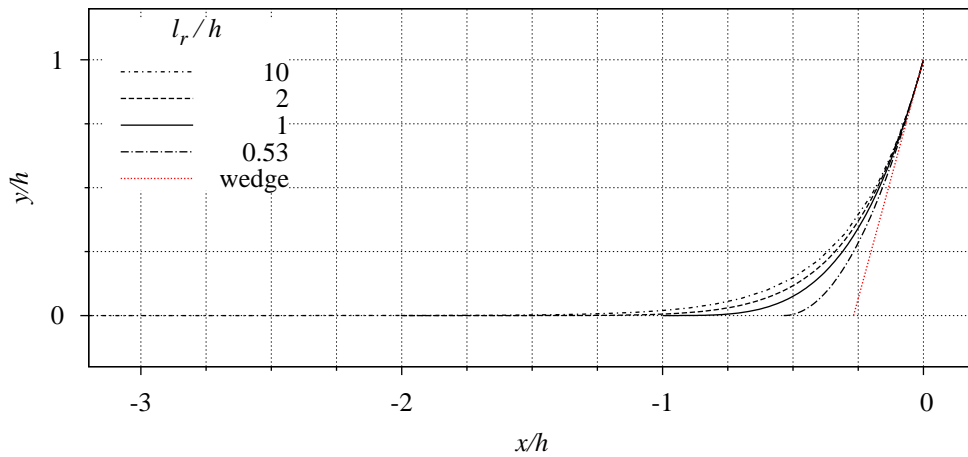
with $A = h/l_r$ and $n = y'/A$ at $x = 1$.

This function has been used to model a range of ramp shapes (curved-faced fences) by varying the aspect ratio (h/l_r) and the outer edge slope. Figure 3.9 shows two example families of ramp shapes generated by holding one parameter

fixed and varying the other as indicated. Also included in Figure 3.9b is the flat faced fence (wedge) with the same β for comparison. The $\beta = 63.5^\circ$ profile in Figure 3.9a is the minimum value for a valid curve, i.e. smoothly varying, for that particular value of l_r/h . In the same way the $l_r/h = 0.53$ profile in Figure 3.9b is also the minimum l_r/h allowable for the $\beta = 75^\circ$ example given.



(a) Smooth curved fence profiles - $l_r/h = 1$.



(b) Smooth curved fence profiles - $\beta = 75^\circ$.

Figure 3.9: Smooth curved fence shapes defined by $y = Ax^n$: (a) $l_r/h = 1$ with β a parameter; (b) $\beta = 75^\circ$ with l_r/h a parameter. The flat faced fence (wedge) with $\beta = 75^\circ$ is also shown for comparison.

3.4.2 Boundary element model

As explained in Chapter 2, modelling cavitating flows with SUPCAV is based on a closed body-cavity system in an infinite flow domain. Wall type flows can be modelled, with the use of symmetry, by considering the dividing streamline as representing a wall and one half of the body-cavity representing the wall-mounted fence with associated cavity behind it. The pressure distribution along the wall (dividing streamline) can be calculated from the contribution from each of the singularities in the usual manner. This procedure is suitable for any discontinuously shaped fence but not for curved fences (ramps) which blend smoothly into the wall, such as those defined by Equation 3.23, which result in a cusped leading edge of the full symmetric body.

There are two issues in attempting to model ramps using SUPCAV. Firstly, the cusp formed at the leading edge of the combined symmetric body leads to the inherent difficulty of obtaining the minimum element separation required for a stable solution. This problem can be overcome using a small but finite leading edge surface slope with element lengths of length similar to the local leading edge thickness. Secondly, there is the stagnation point at the leading edge which would not be present at the smoothly continuous junction between the ramp and wall.

To overcome these issues an alternative body shape was analysed to model the wall-mounted ramp configuration. In this alternate model, a section of flat wall is added to the ramp extending far upstream ($x/h > 1000$). The wall and ramp body is then offset by a small increment in the y direction, i.e. normal to the wall. After discretisation of the wall/ramp surface the last wall element is modified so that the free end is moved down onto axis of symmetry, and the resulting body is then mirrored to form the full closed geometry. In this way the continuous curvature of the fence/wall junction is obtained and the leading edge singularity is moved sufficiently to the far field to nullify its effect on the flow in near field of the fence.

To check the validity of this alternate geometry, comparison was made between the results for a normal flat plate with and without the additional wall modelled. Figure 3.10 shows good agreement between the upstream wall pressure distributions predicted by the two models for a typical case. At a upstream distance of h there is a difference of 0.01% between the two results, and by $500h$ this increases to 0.6%.

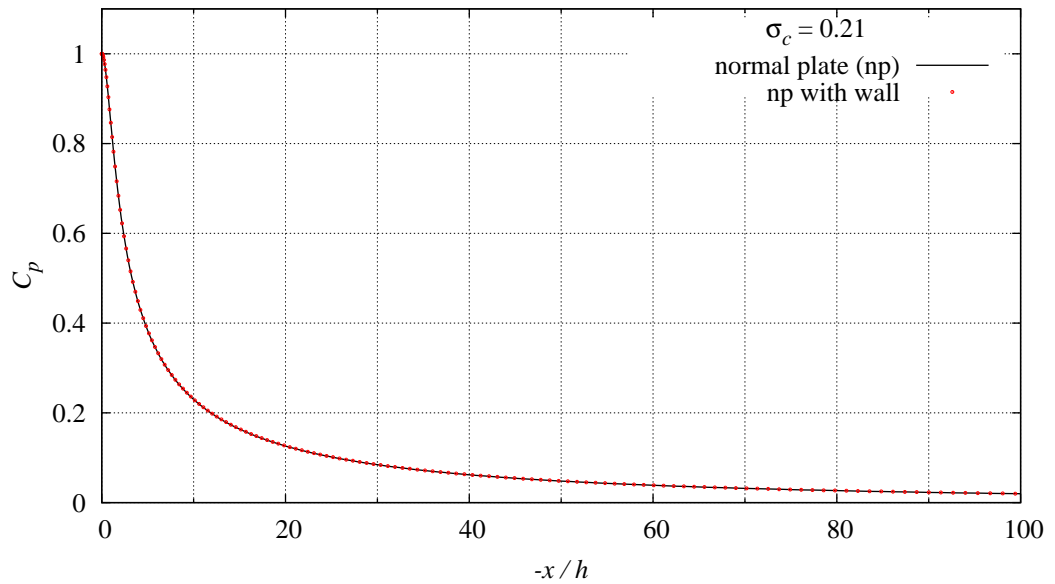


Figure 3.10: Upstream wall C_p distribution for a normal flat plate. Comparison between the result with and without an attached horizontal plate of large but finite extent. Result shown for $\sigma_c = 0.21$ as a typical example. The small difference between the two result increases with upstream distance. At a distance of h the difference is 0.01%, becoming 0.6% by $500h$.

3.4.3 Results: Cavity Shape

The relationship between cavity shape and cavitation number for these wall-mounted fence flows is shown as a log-log plot in Figure 3.11. The curves are essentially linear for all but large values of σ_c . A straight line fit to the linear portion of these curves gives an exponent $n = -1.92$ (see Equation 3.1) which is close to the value of -2 predicted by the classical linearised theory for $\sigma_c \rightarrow 0$.

The effect on the cavity parameters of a change in β for a fixed ramp length is shown in Figure 3.11a and Figure 3.12. A change in β does not change the slope of the curves but gives an offset, reducing each of the cavity parameters, as β is reduced. In the cavity length case (Figure 3.11b) this effect equates to a 0.25% increment in l_c/h per degree change in β . As for the cavity length case (Figure 3.11a) the variation of cavity volume and thickness also have a general power law trend with σ_c , but with the curves lifting off the straight line as σ_c becomes large. This is most pronounced with the cavity thickness case (Figure 3.12b).

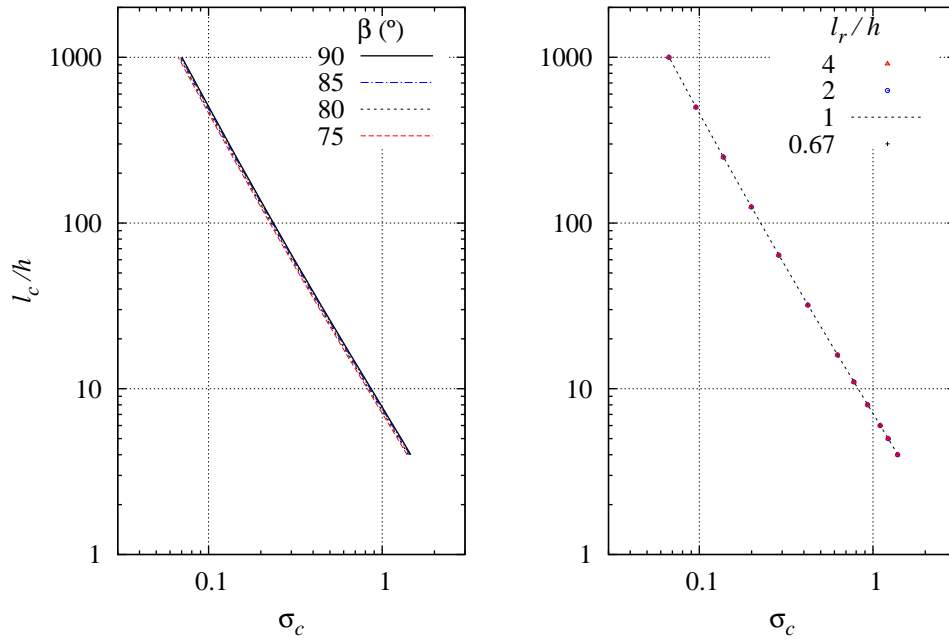
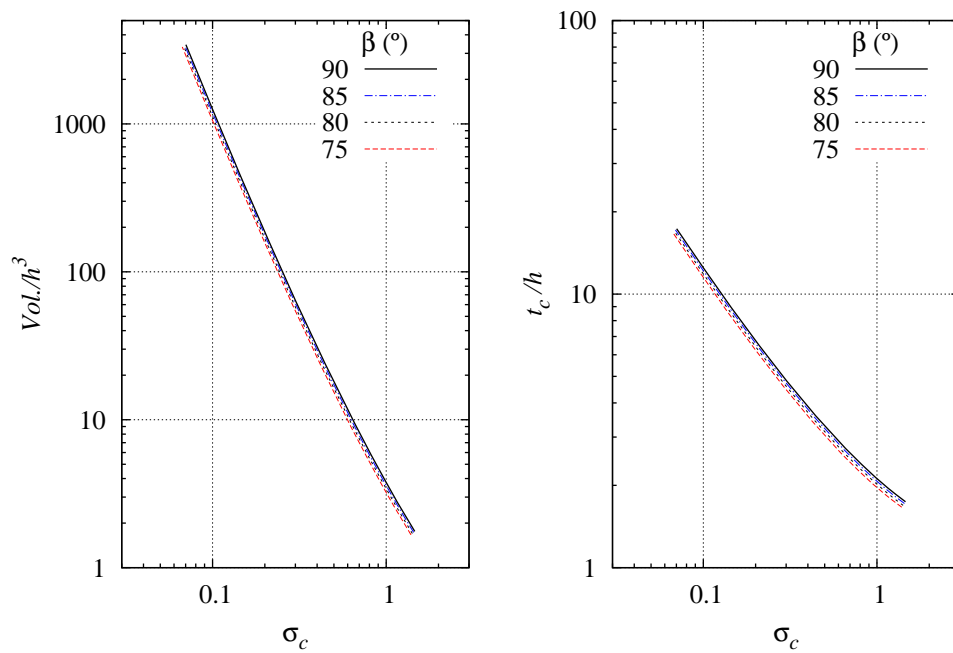
(a) $l_r/h = 1$.(b) $\beta = 75^\circ$.

Figure 3.11: Effect of ramp parameters on the variation of cavity length with σ_c . The relationship is well represented by a power law function of σ_c (see Equation 3.1) with β not affecting the slope but giving a constant offset to the curves. In (a) for the $l_r/h = 1$ case, it equates to a 0.25% increment in l_c/h per degree change in β . Where (b) shows that a variation in ramp shape with constant β has no effect on cavity shape.



(a) Cavity volume as a function of σ_c . (b) Cavity thickness as a function of σ_c .

Figure 3.12: Effect of ramp parameters on the variation of cavity volume and thickness with σ_c . As with cavity length (Figure 3.11a) these relationships also have a general power law trend with σ_c (see Equation 3.1) but with the curves deviating from a straight line as σ_c becomes large. Decreasing β does not affect the slope but gives a constant negative offset to the curves.

3.4.4 Results: Pressure distributions

To compare the present boundary element method results with analytical predictions, a typical example of the pressure distribution on the face of a normal plate is given in Figure 3.13. The BEM results are seen to be in close agreement with the analytical solutions. (See also Figure 3.6 for the comparison of the analytical solution with experimental data for $\sigma_c = 1.38$).

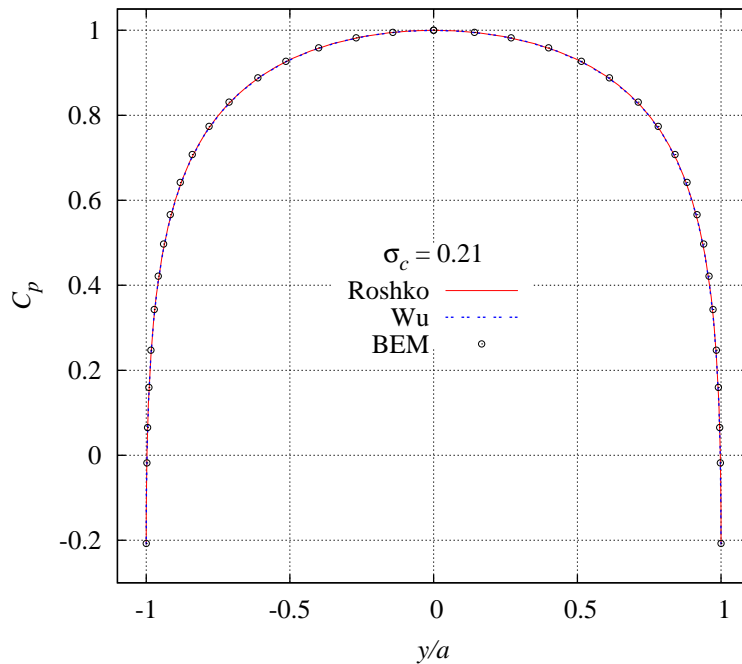


Figure 3.13: Comparison of the predicted pressure distribution over a normal plate by the analytical methods of Roshko (1954) and Wu (1962) with that from the present BEM. The analytical and numerical solutions are in close agreement. The $\sigma_c = 0.21$ case is shown as a typical example.

The pressure distribution along the dividing streamline predicted by the notched hodograph method and BEM are shown in Figure 3.14. As with the pressure on the face of the plate there is close agreement between the two methods, but only in the near field. The extent of this close agreement is dependent on σ_c , with the upstream length decreasing as the cavity length shortens. From Figure 3.14a the pressure distributions are seen to agree out to past $100h$ for the small cavitation number case ($\sigma_c = 0.07$), progressively reducing to $10h$ and $3h$ as is σ_c is increased to 0.21 and 0.8 respectively. The comparative over-prediction of the analytical method is most likely attributable to the infinite open wake model employed leading to the upstream flow field also not being modelled realistically. In the BEM solution the finite extent of the cavity is modelled explicitly; so this method may be predicting the complete flow field, in addition to just the body and its near field, more realistically. As very long cavities occur at small cavitation numbers, these flow conditions match more

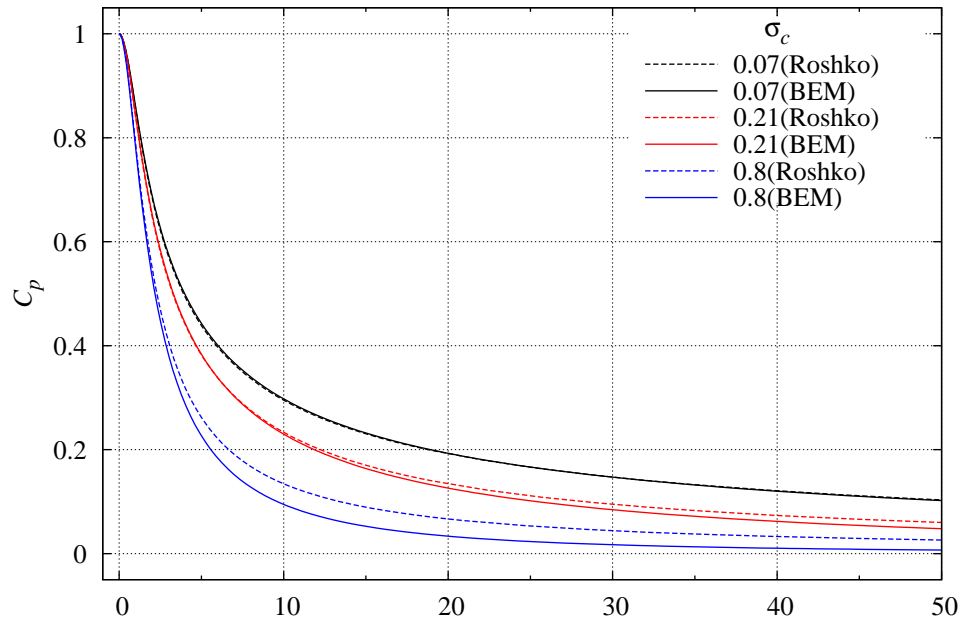
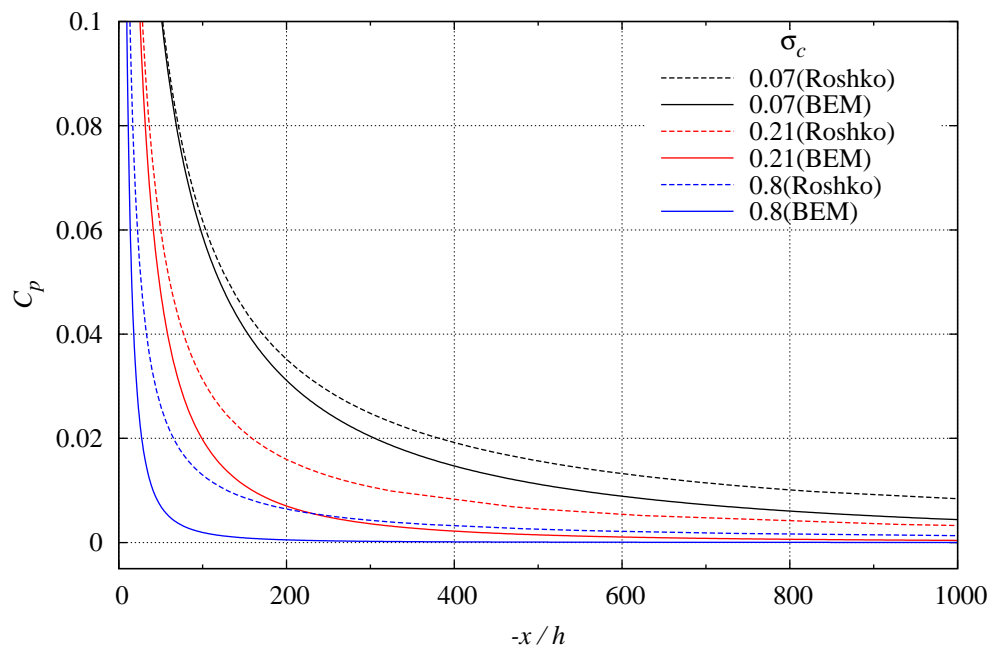
(a) C_p along dividing streamline to $-50h$.(b) C_p along dividing streamline to $-1000h$.

Figure 3.14: Comparison of the upstream dividing streamline pressure distribution between the notched hodograph (Roshko method) and the present BEM for a normal plate. There is good agreement only in the near field of the plate, with the range of agreement reducing as σ_c increases.

closely the geometry of the analytical model. It follows then that there would be a better agreement between the methods at low σ_c values, as is shown in Figure 3.14.

Due to the relative over-prediction of the analytical method (Figure 3.14) the lift calculated from the pressure distribution is also greater. Lift data is presented in the next section, but only for the BEM solution as this appears the more realistic of the two methods examined.

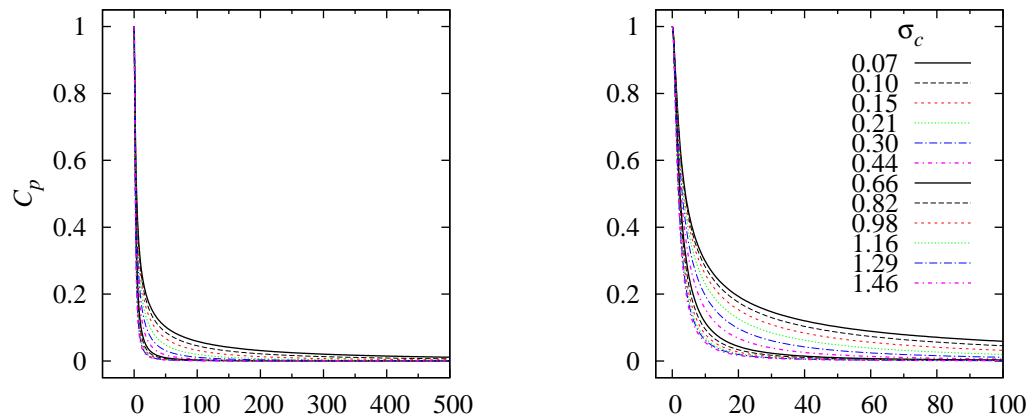
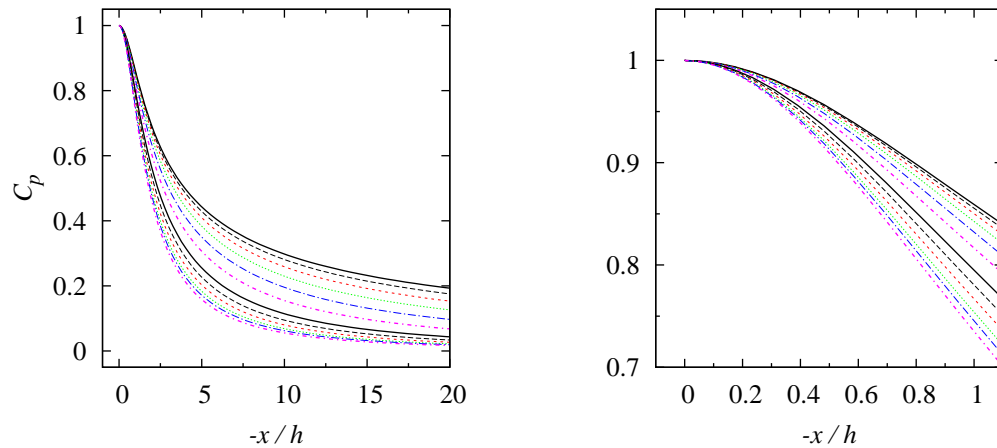
(a) C_p along dividing streamline to $-500h$.(b) C_p along dividing streamline to $-100h$.(c) C_p along dividing streamline to $-20h$.(d) Region of C_p max.

Figure 3.15: Pressure distributions along the dividing streamline upstream of a normal fence, with σ_c a parameter.

A family of curves, with σ_c a parameter, for the pressure distribution along the upstream dividing streamline of the cavitating flow over a normal plate or 'fence' is shown in Figure 3.15. As the flow is inviscid, the C_p increases from $-\sigma_c$ at the fence edge to stagnation at the fence base with $C_p = 1$. Only the wall pressure is shown in Figure 3.15 so the curves all begin at $C_p = 1$. From this maximum the pressure distributions decrease asymptotically to 0

as $-x/h \rightarrow \infty$. The rate at which this occurs depends on σ_c . To compare this result with a curved-fence or ramp, a typical upstream wall pressure distribution, with the ramp trailing edge/cavity detachment point at $x = 0$, is shown in Figure 3.16. This is for a ramp with $h/l_r = 1\%$ and $\beta = 75^\circ$ with σ_c a parameter. The pressure distributions are very similar to those for the fence. They differ in that the C_p at $x = 0$ is $-\sigma_c$. It then rises within a short distance ($\approx 0.5h$) to a value a little less than stagnation ($0.91 \rightarrow 0.96$), and then subsequently falls asymptotically to 0 as $-x/h \rightarrow \infty$ as in the fence result. A log-log plot of this same data is given in Figure 3.17, from which the power law relation between pressure and distance when far upstream from the cavity detachment point is again evident. The slope of the curves in the far upstream region, i.e. the exponent in the power law relation, is ≈ -2 .

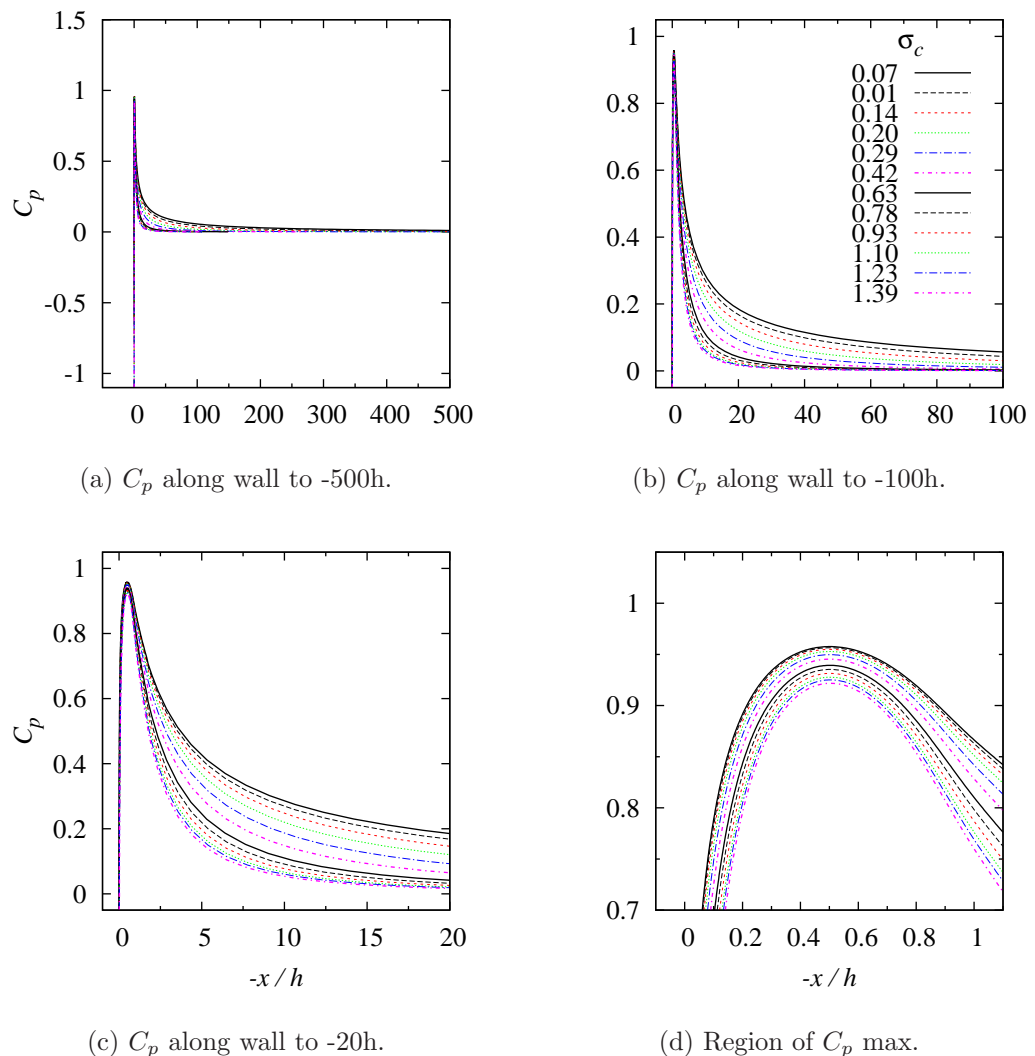
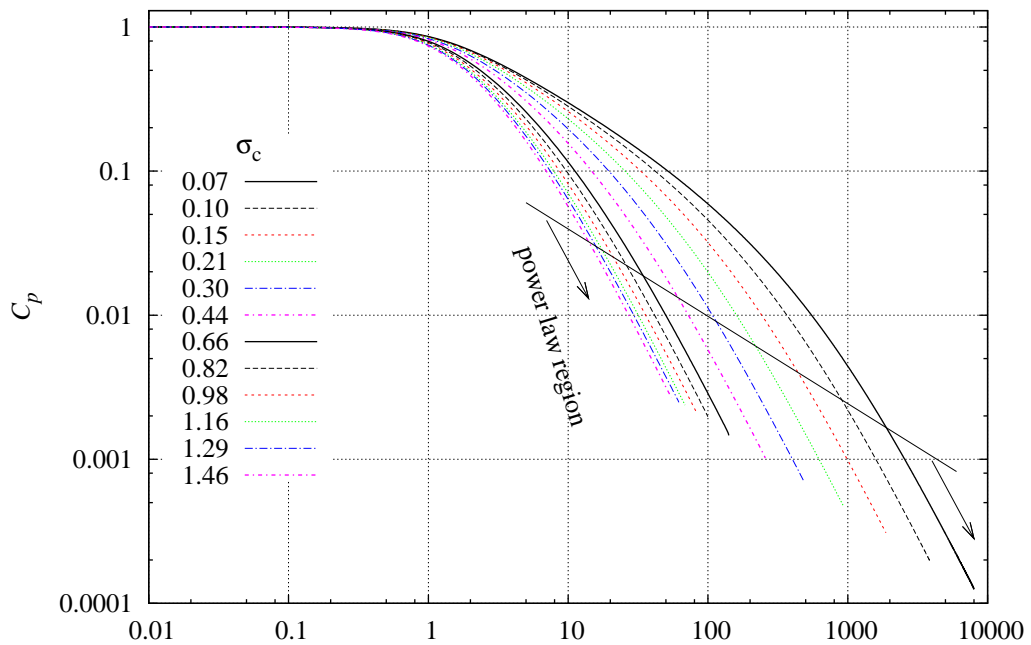


Figure 3.16: Typical wall pressure distribution upstream of a ramp, with σ_c a parameter. (Data shown for $h/l_r = 1\%$ and $\beta = 75^\circ$).



(a) Wall pressure distribution upstream of a normal fence.

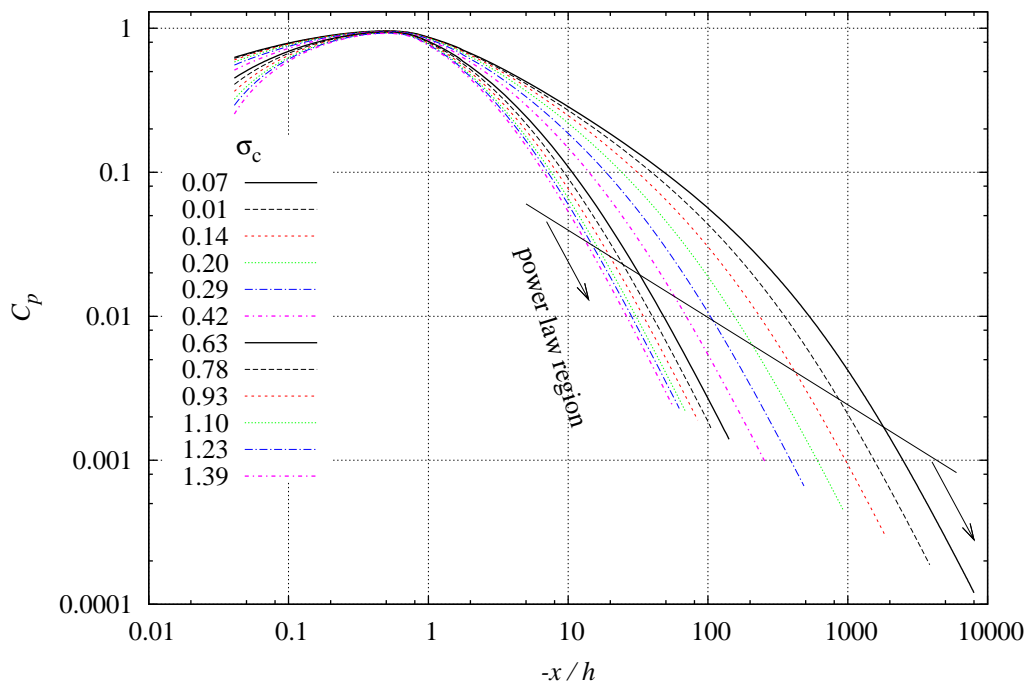
(b) Wall pressure distribution upstream of a ramp ($\beta = 75^\circ$ and $l_r/h = 1$).

Figure 3.17: The wall pressure distribution as in Figure 3.15 and Figure 3.16 but as a log-log plot. The power law relation far upstream of the cavity detachment is clearly evident. The slope of the curves in this region, i.e. the exponent in the power law relation, is ≈ -2 .

Larger scale plots of the plate and ramp upstream wall pressure distributions out to $-100h$ (Figure 3.15b and Figure 3.16b) are shown for comparison in Figure 3.18. The largest difference between the two flows occurs at the smallest cavitation number, and this comparison is shown in Figure 3.18c. The two pressure distributions are in close agreement after an upstream distance of $\approx 60h$, with the pressure being generally less in the nearer field for the ramp flow.

Wall pressure distributions for a family of ramps with constant β are given in Figure 3.19. The pressure distributions only vary significantly within $\approx h$ upstream of the ramp trailing edge. The maximum C_p is seen to increase with decreasing ramp length as is most clearly indicated by the magnified x -axis scale in Figure 3.19c. In addition to having a larger maximum C_p , the shorter ramp pressure distributions initially decrease more rapidly before merging by $\approx 3h$.

If instead the ramp length is held constant and β is varied, the wall pressure distributions vary both in the maximum C_p developed; and also that the curves remain separated to well into the far field as shown for a typical family of ramps in Figure 3.20. The collapsing of the pressure curves onto a common curve occurs by about $500h$ for the low σ_c data presented in Figure 3.20. The fence data ($\beta = 90^\circ$) has been included for comparison.

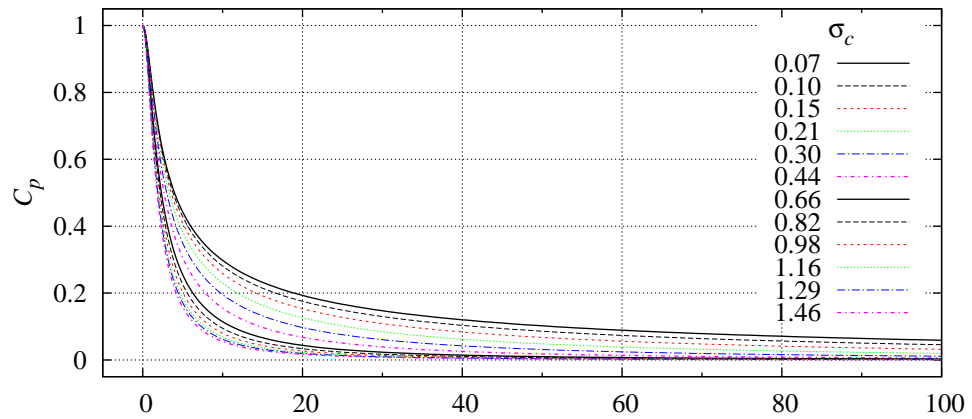
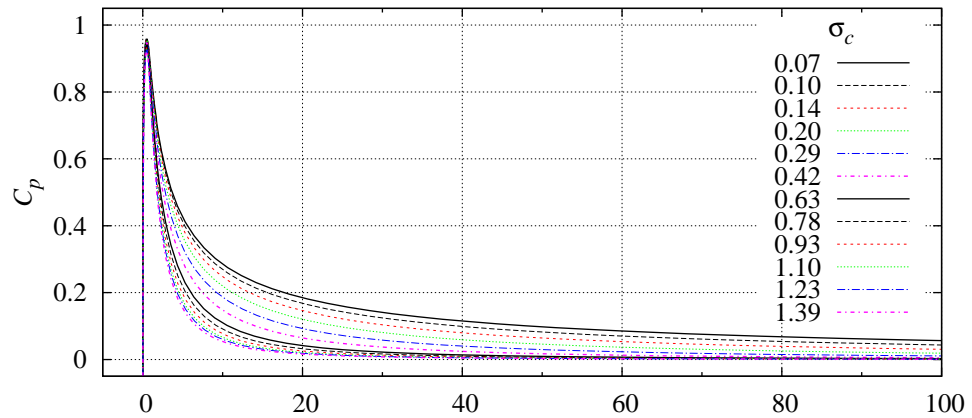
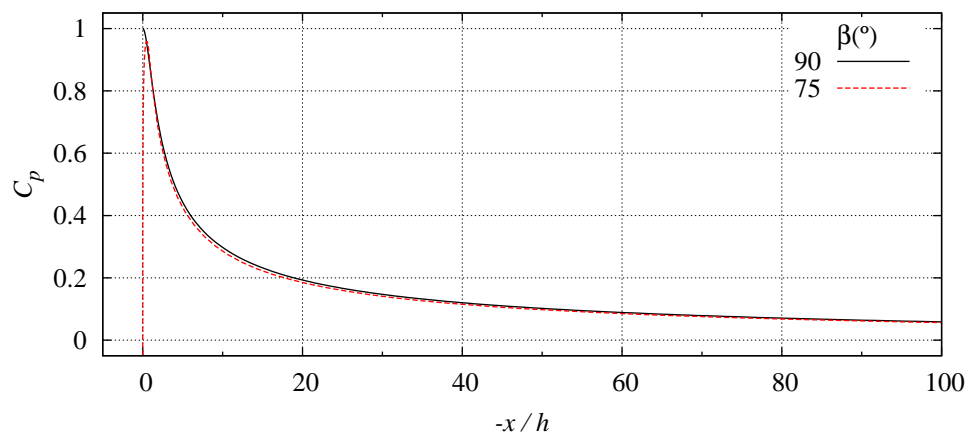
(a) Fence: $\beta = 90^\circ$.(b) Ramp: $\beta = 75^\circ$.(c) Comparison between fence and ramp results ($\sigma_c = 0.07$).

Figure 3.18: Comparison of the upstream wall pressure distribution between a fence $\beta = 90^\circ$ and ramp $\beta = 75^\circ$, with σ_c a parameter. In (c) the maximum difference between the two results occurs at the smallest σ_c .

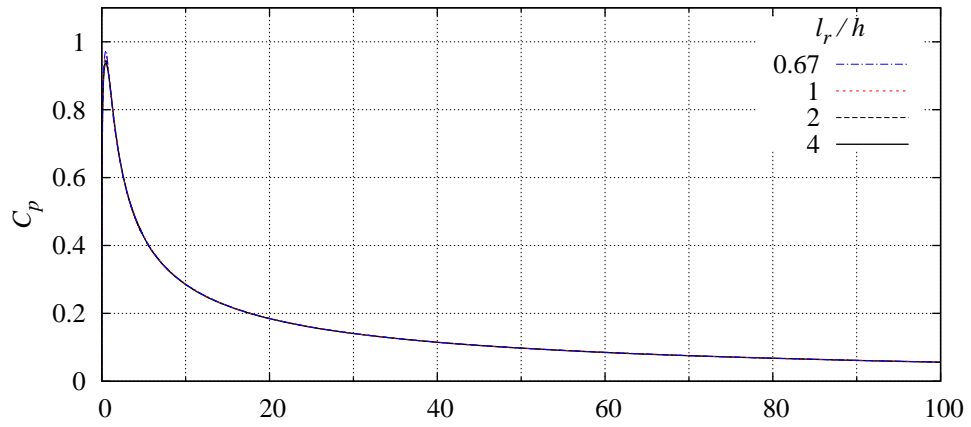
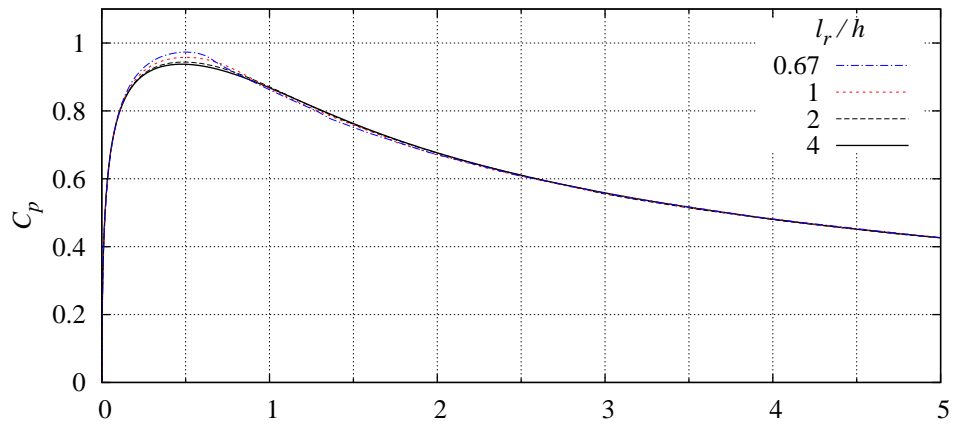
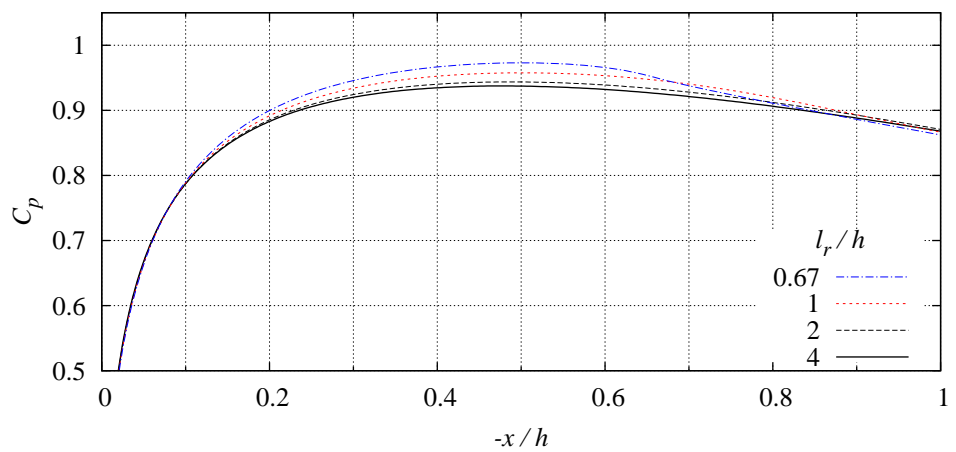
(a) C_p along wall to $-x/h = 100$.(b) C_p along wall to $-x/h = 5$.(c) C_p along wall to $-x/h = 1$.

Figure 3.19: Typical wall pressure distributions for a family of ramps with constant β and l_r/h a parameter. (Data shown for $\beta = 75^\circ$ and $\sigma_c = 0.07$).

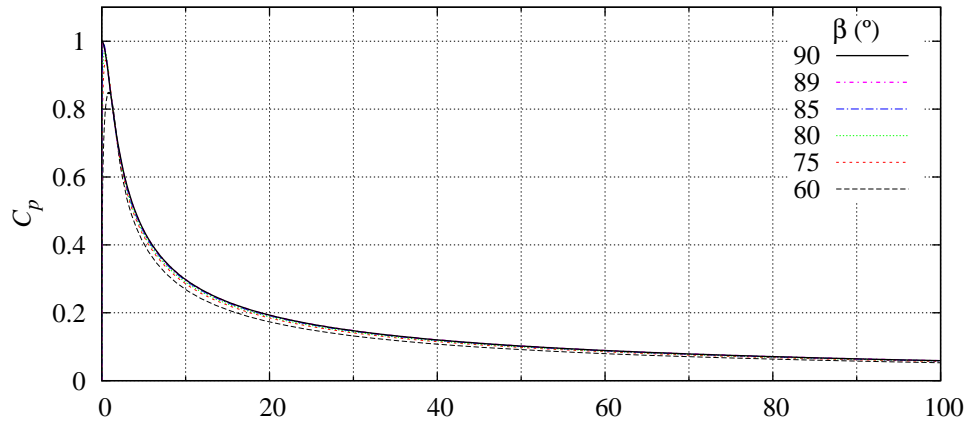
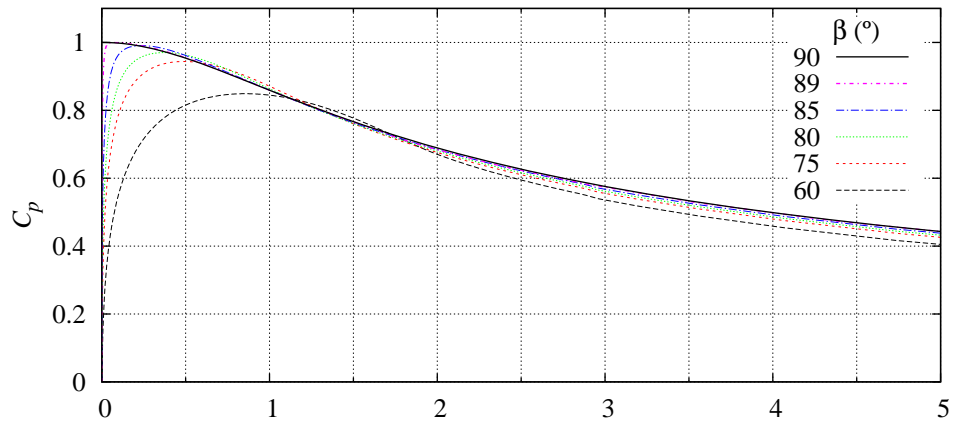
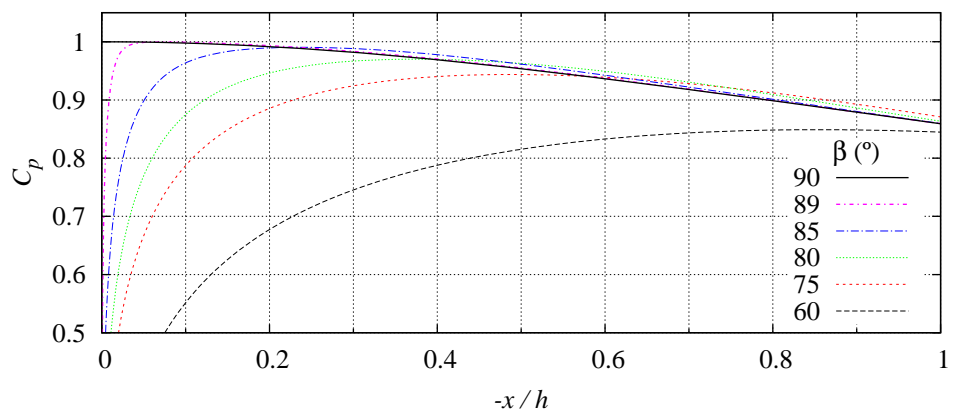
(a) C_p along wall to $-x/h = 100$.(b) C_p along wall to $-x/h = 5$.(c) C_p along wall to $-x/h = 1$.

Figure 3.20: Typical wall pressure distributions for a family of ramps with constant h/l_r and β a parameter. (Data shown for $l_r/h = 2$ and $\sigma_c = 0.07$). The fence data ($\beta = 90^\circ$) has been included for comparison.

3.4.5 Results: Hydrodynamic Coefficients

The normal force on the wall, i.e. the lift generated by the flow, is calculated by taking the integral of the pressure distribution over some appropriate length. As can be seen from Figure 3.17, the wall pressure falls away as a power law (but never attaining $C_p = 0$) in the far field. To obtain the theoretical maximum lift the integral needs to be calculated out to infinity, giving $C_{L\infty}$. To restrict the boundary element model to a practical size the following method is used. The lift is first calculated from the BEM solution out along the wall to a suitable distance, X , so as to extend into the asymptotic region. Then the remaining portion out to infinity is extrapolated using the property that in the far field the pressure curve is of a power law form with an exponent $n = -2$. This additional portion, termed C_L^+ , is then the integral from X to ∞ of the power law relation as shown in Equation 3.24 giving Equation 3.25. The value of the coefficient A is calculated from the known pressure at X .

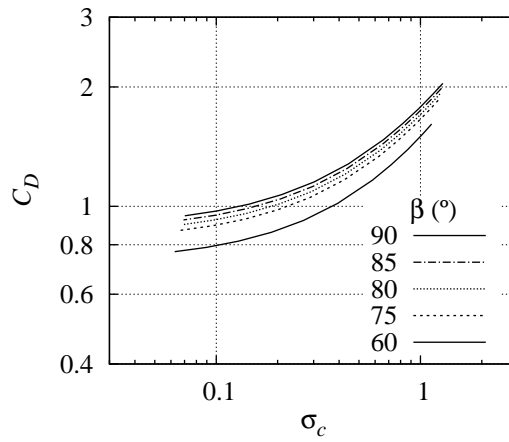
$$C_L^+ = \int_X^\infty Ax^n dx = \left[\frac{1}{n+1} Ax^{n+1} \right]_X^\infty \quad (3.24)$$

For $n = -2$, Equation 3.24 gives

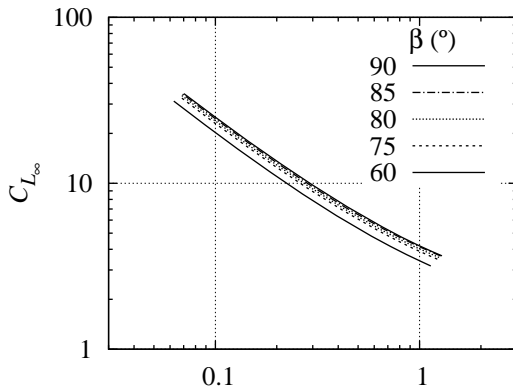
$$C_L^+ = \frac{A}{X} \quad (3.25)$$

The lift up to some finite distance upstream is also of interest, with a typical marine application of an interceptor height being in the order of $h/c = 1\%$. Hence lift data is also presented here calculated out to $100h$ upstream, termed $C_{L_{100h}}$. A typical result for these lift values is given in Figure 3.21c, together with the drag results in Figure 3.21a. Both lift and drag increase with β , but have slopes of opposite sign as a function of σ_c . This results in the L/D_∞ curves virtually falling on the one line except for large σ_c as shown in Figure 3.21e. The difference at small σ_c for the L/D_{100h} data is due to the small σ_c pressure distributions dropping away to zero more slowly (see Figure 3.18), and so a greater proportion of the contribution to lift production comes from the far field. This highlights the aspect that the large L/D_∞ values obtained, especially at small σ_c , cannot be practically realised due to the finite length of upstream wall that would be available.

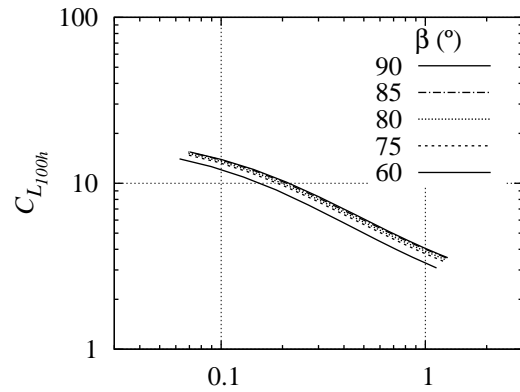
Figure 3.22 shows the results for a family ramps with constant β and the ramp length varied. The lift, drag and efficiency as a function of σ_c are seen to be independent of ramp length, l_r .



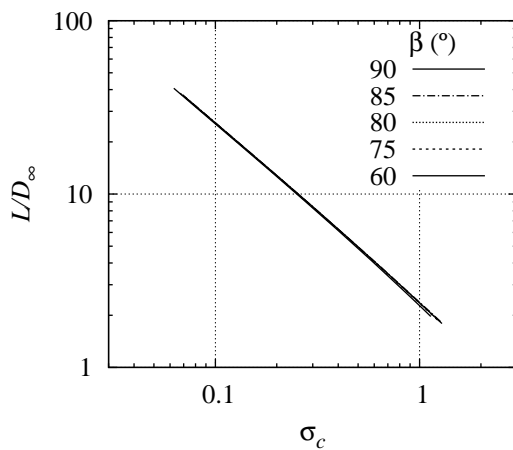
(a) Drag.



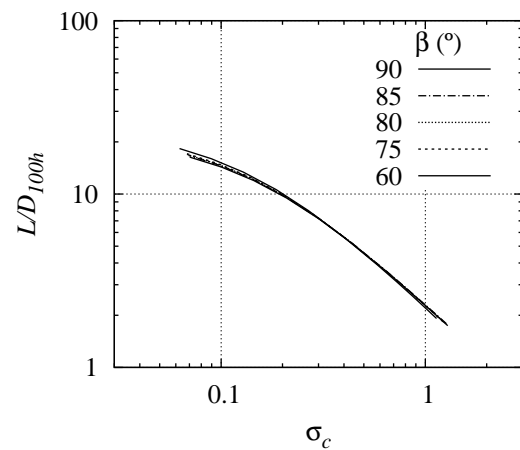
(b) Lift (out to infinity).



(c) Lift (out to 100h).

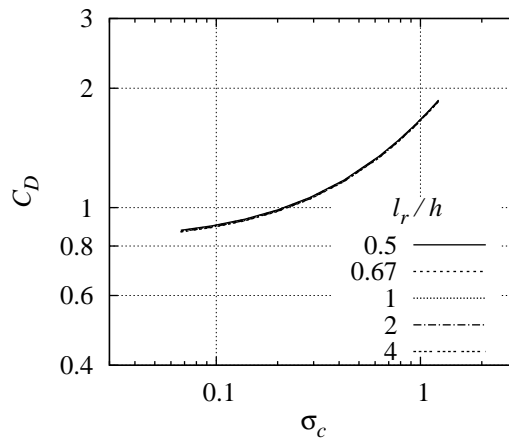


(d) Efficiency (infinite).

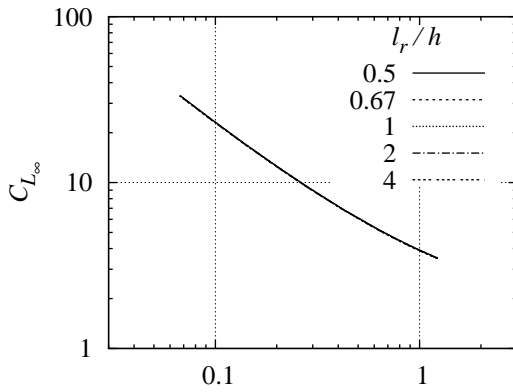


(e) Efficiency (100h).

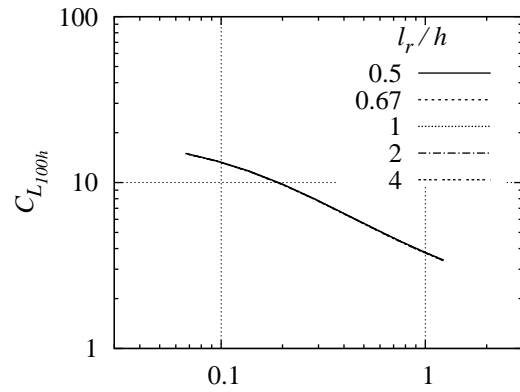
Figure 3.21: Typical plots of the C_L , C_D and L/D for a family of ramps for $l_r/h = 2$ and β a parameter. Data for the infinite and 100h intervals is shown. The fence data ($\beta = 90^\circ$) has been included for comparison.



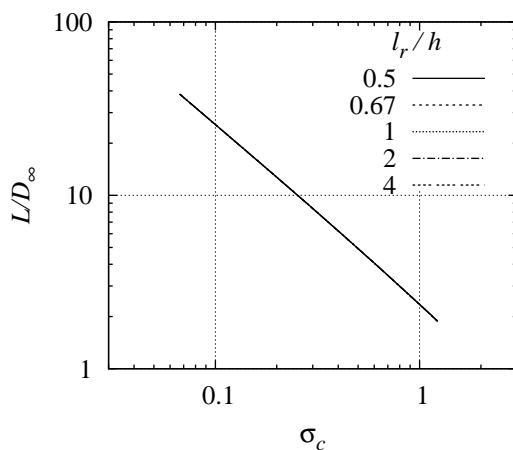
(a) Drag.



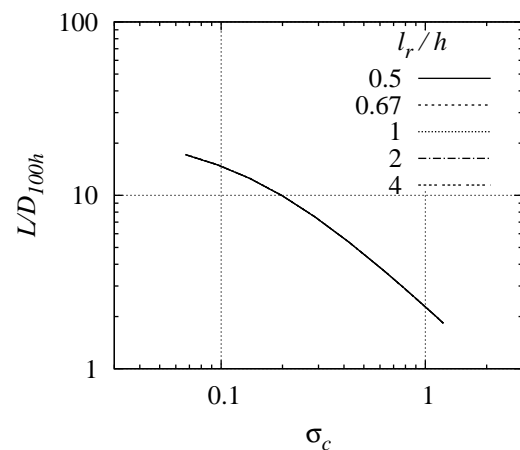
(b) Lift (out to infinity).



(c) Lift (out to 100h).



(d) Efficiency (infinite).



(e) Efficiency (100h).

Figure 3.22: Typical plots of C_L , C_D and L/D for a family of ramps with $\beta = 75^\circ$ and l_r/h a parameter.

3.5 CFD analysis

3.5.1 CFD model

The commercial computational fluid dynamics (CFD) code, ANSYS-CFX, was used for the viscous numerical analysis presented here². An unsteady two dimensional finite volume method has been used with a structured hexahedral mesh and a high resolution discretisation scheme (third order accurate (ANSYS, 2009, pp.248-252)). A standard RANSE k - ϵ turbulence model was chosen to capture viscous flow features. The interface between vapour and water has been modelled using a volume-of-fluid volume fraction method. The occurrence of vaporisation or condensation is determined by the difference between the absolute pressure and the vapour pressure (here set to be 3574 Pa) and the rate at which it occurs is controlled by a Rayleigh-Plesset equation derived model as implemented in ANSYS-CFX (ANSYS, 2009, p.146). A more detailed explanation of the cavitation model is given in Section 2.4. To enable future comparison with experimental data, where the fence will be located on the test section ceiling, a buoyancy force was applied away from the bottom wall in the numerical model.

The computational domain used is shown in figure 3.23a. The fence was modelled within this domain as an infinitely thin wall protruding 10 mm into the flow as shown in the inset. Local refinement normal to the bottom wall and around the fence was used, which is shown for the coarsest grid used in figure 3.23b.

For the computational domain used, both temporal and spatial grid sensitivity studies were performed. For the spatial variation, grid sizes were varied from 5,750 elements to 1,068,000 elements. From this it was concluded that the length of the cavity formed behind the fence for a grid size of 237,452 elements was within 0.8% of the grid independent solution. Temporal convergence was checked by analysing the spatially converged grid with time steps ranging from 43 ms to 1.5 ms. From this analysis it was concluded that a time step of 2 ms predicted a cavity length within 0.7% of the grid independent solution. As a constant inlet velocity of 8 m/s ($Re = 8 \times 10^5$, chosen to enable comparison with future experimental data) has been used throughout, the relationship between spatial convergence and temporal convergence has been assumed to be constant for all runs completed. Using this setup, spread across four partitions on a multi-node cluster (purchased in 2008), runs typically took 30-40 hours to complete.

Cavitation number variation was realised by varying the reference pressure from 8.75 kPa to 25 kPa. Boundary layer thickness variation was achieved by adjusting the wall velocity boundary condition between the upstream domain limit and the fence. boundary layer ($\delta = 0$) was achieved by applying a wall velocity equal to U_∞ (i.e. a wall free slip condition) all along the wall up to

²This study was presented at the 17th Australian Fluid Mechanics Conference by Pearce et al. (2010), (See the statement of authorship in the thesis preamble).

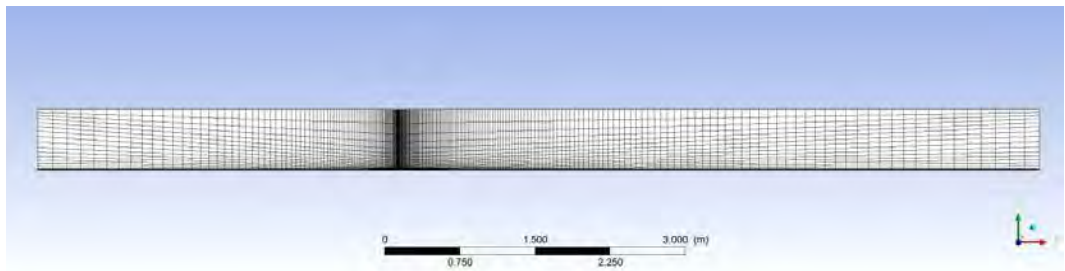
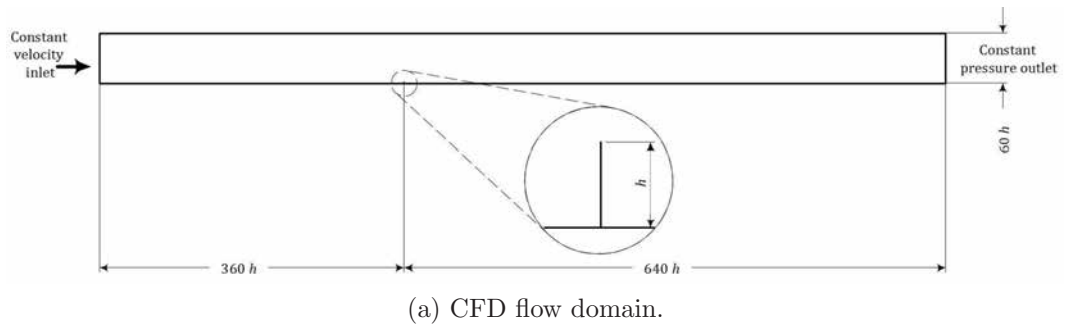


Figure 3.23: CFD flow domain with the fence attached to the bottom wall and the flow from left to right. A coarse grid is shown (b) to illustrate the grading, in both the x- and y- axes, with local refinement adjacent to the fence (attached to the bottom surface).

the fence. Conversely the thickest boundary layer was achieved by setting a zero wall velocity (i.e. a wall zero-slip condition) along the complete upstream length. Intermediate values of boundary layer thickness were then realised by reducing the length of wall subject to the zero-slip condition upstream of the fence, maintaining the fence in the same position in the domain for all cases. In this way numerically stable boundary layers were obtained in the vicinity of the fence, whilst maintaining an easily varied boundary layer thickness. Although a singularity is introduced along the wall due to this mixed boundary condition convergence rates for the various combinations did not vary. The measured boundary layer thickness (at $x = 0$) for each condition was obtained with the fence removed with all other parameters unchanged.

3.5.2 Results: Flow topology & cavity shape

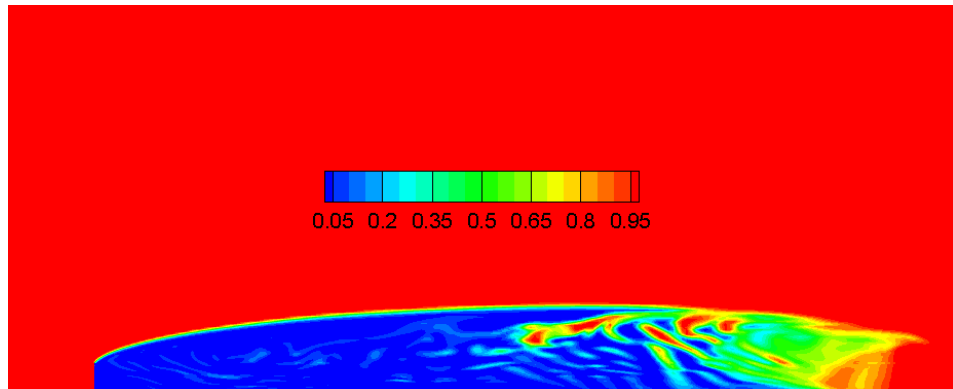
Cavity flows generally have an unsteady closure. The cavity length oscillates about a mean position with coherent cycles of vapour structures being shed into the wake and cavity regrowth with re-entrant jet reformation. An unsteady analysis was undertaken to model the physics involved with this process and in figure 3.24 there is a typical result shown for a cavity shape at an instant in time. The cavity shape is visualized by plotting contours of void fraction. With the potential flow model the cavity has a surface of discontinuity across which the density jumps from that of the water on one side, to the vapour on

the other. In a CFD simulation this surface is instead a layer of some finite thickness across which the density gradually reduces till the change of phase is complete. This behaviour can be seen in the solution shown in figure 3.24. The closure region is apparent as a mixture of vapour and liquid as fluid is drawn into the cavity by the re-entrant jet. From the streamlines plotted in vicinity of the cavity closure region (figure 3.24c) the rear stagnation point is found to be further downstream into the mostly liquid region. It was decided to use this point as the extent of the cavity rather than the furthest extent of some arbitrary value of void fraction as this was the point of division of the re-entrant jet flow back into the cavity from that continuing on into the wake.

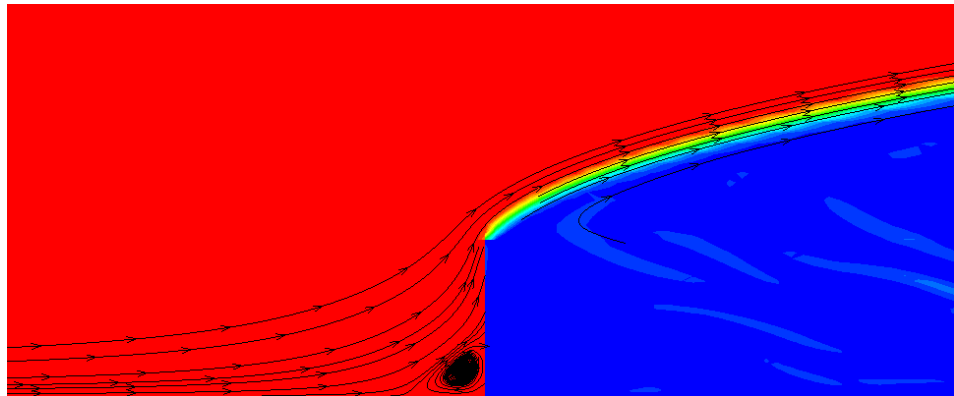
Of interest also is the flow topology just upstream of the fence when a boundary layer is present. From the streamlines, as plotted in figure 3.24b, the separated region with reverse flow is present as expected from the results of non-cavitating flows over wall-mounted fences or forward-facing steps (Largeau and Moriniere, 2007). The separation point on the wall is $\approx 0.5h$ upstream of the fence and also at $\approx 0.5h$ up the fence face. This did not vary substantially with the range of δ examined ($0 < \delta/h \leq 3.7$). This may require additional analysis with finer discretisation in this region to establish more definitely the behaviour of the separation region.

Figure 3.25 shows the relationship between cavity length, l_c , and σ_c for both the inviscid and viscous analyses. The relationship between cavity length and σ_v for potential flow in an infinite domain is a power law ($l_c = 4.54\sigma_v^{-1.71}$) and is shown for reference. Additionally the potential flow relationship for a blocked flow with $D/h = 60$ is shown for direct comparison with the CFD results (where D is the separation of the walls confining the flow). The CFD results for the cases of $\delta/h = 0$ and 1.2 follow the trend of the potential flow blocked relationship. The effect of the boundary layer is to offset the curve $\delta/h = 0$ downwards, i.e. a shorter cavity is obtained at the same σ_v .

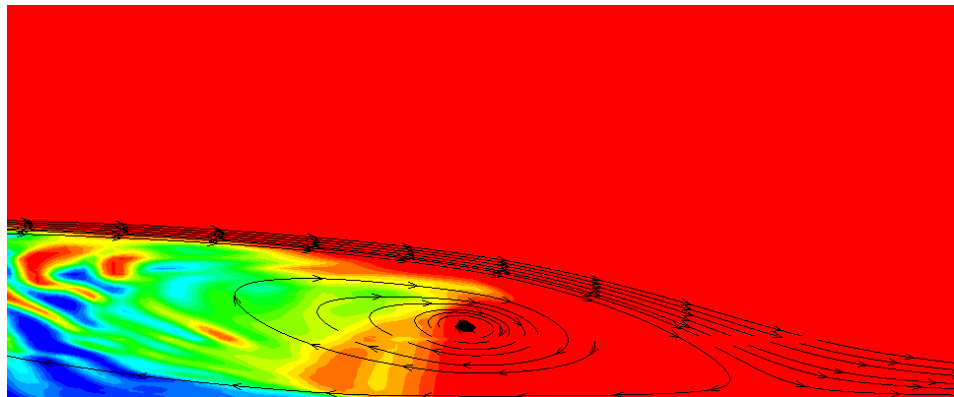
In the simulations performed, solutions for cavity lengths of $l_c/h > 100$ were not converging satisfactorily. This issue will need further investigation as part of ongoing work in this area.



(a) Fence with attached cavity shown with contours of void fraction.



(b) Streamlines illustrating the upstream flow topology.



(c) Streamlines illustrating the cavity closure topology.

Figure 3.24: Typical CFD result for cavity flow over a wall-mounted fence ($\sigma_c = 0.44$ & $\delta/h = 1.2$) with (a) extent of cavity shown as contours of void fraction (0 {100% vapour} to 1.0 {100% liquid}), (b) view of fence with streamlines added showing the separation region in the fence/wall corner, and (c) a view of the cavity closure region showing dividing streamlines either side of stagnation with flow continuing into the wake or reversing forming a re-entrant jet.

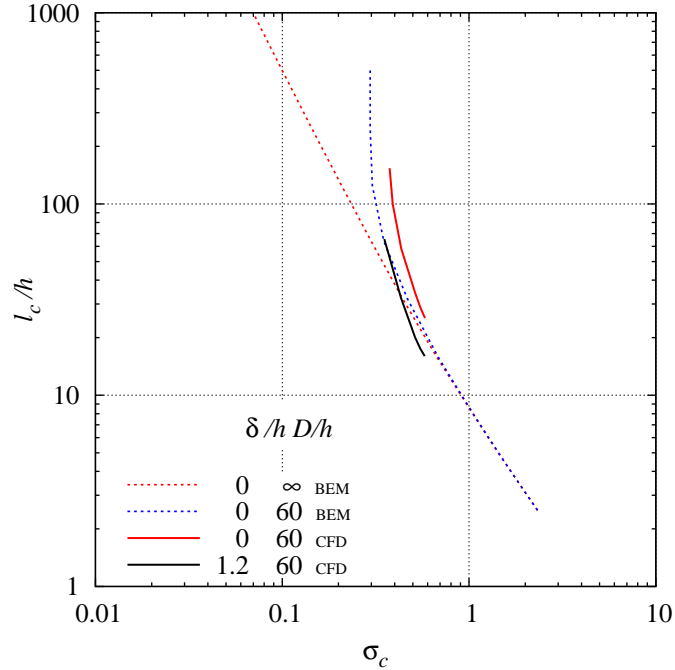
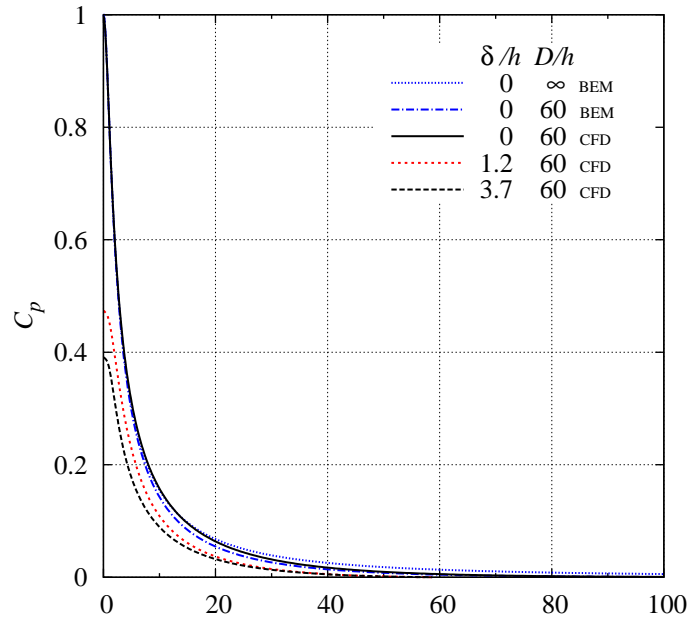
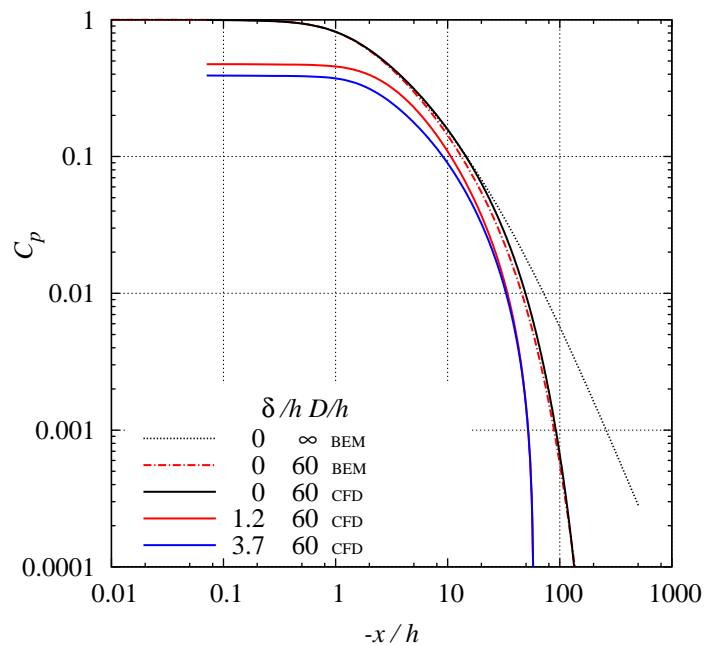


Figure 3.25: Dependence of cavity length on σ_c for both the viscous and inviscid results. Also plotted is the infinite flow inviscid result for reference.

3.5.3 Results: Upstream wall pressure distribution

The resultant upstream wall C_p distribution is shown in figure 3.26. Both the viscous $\delta/h = 0$ and the inviscid results agree well in the near field out to about $20h$. The discrepancy farther upstream is attributable to the presence of solid blockage in the confined CFD flow whereas the BEM result is for an infinite flow. The effect of the presence of a boundary layer is significant. For a δ/h of about 1 the maximum C_p obtained is reduced to about 0.5, i.e. half of the stagnation value obtained at the fence wall junction ($x = 0$) in the absence of a boundary layer. Upon further increase in δ/h there is a further reduction of the C_p extending out to about $x = 30h$. Past this point the two pressure distributions converge and $C_p \rightarrow 0$ by about $x = 55h$. This reduction in magnitude of the wall pressure signature with increase in δ/h is expected. The reduced wall pressure reflects the reduced momentum flux due to the presence of a boundary layer, as the flow is deflected from the wall by the presence of the fence. The integration of the pressure distribution over the wall results in a C_L value for the thin boundary layer ($\delta/h = 1.2$) of 3.6, and 2.9 for the thicker boundary layer ($\delta/h = 3.7$). This equates to a reduction of approximately 50% on the inviscid BEM values ($C_{L\infty} \approx 7$ and $C_{L100} = 6.5$), which is of the same order as the reduction in the maximum wall C_p between the two results.

(a) Upstream wall C_p distribution.

(b) log-log plot of (a).

Figure 3.26: Variation in the upstream wall pressure distribution due to a boundary layer for $\sigma_c = 0.44$. The inviscid results (infinite and confined) and viscous result without a boundary layer are shown for comparison.

3.6 Conclusions

The cavitating flow over a wall-mounted fence has been analysed both analytically, and numerically using a BEM. Some additional CFD results have been presented to investigate the effect of a boundary layer. The analytical and BEM predictions were found to be in good agreement in the near field, i.e. the pressure distributions on the face of the fence, and on the wall just upstream on the fence. Far upstream of the fence the wall pressure distribution was over-predicted by the analytical method compared to the BEM result, with the discrepancy increasing with decreasing σ_c . This can be attributed to the open wake model used in the analytical solution only adequately modelling the flow geometry for large cavities, i.e. $\sigma_c \rightarrow 0$.

The wall pressure distributions were found to fall away in the far field with a power law relation in both the analytical and BEM results. The value of the exponent, i.e. the slope of the curve on the log-log plot, varied from -0.5 for $\sigma_c = 0$ (analytical), -1 for $\sigma_c > 0$ (analytical) to -2 for the finite cavity length BEM result. The steeper slope for the BEM data equates to a greater reduction of the C_p within the same distance, in comparison with the analytical method, as indicated above. The results from the CFD analysis show a reduction of the wall pressure distribution to zero in a shorter distance than the BEM result. This feature is in addition to the maximum C_p at the wall/fence juncture being reduced by approximately 50%.

The reduction in the wall pressure distribution for curved shaped fences ($\beta < 90^\circ$ in comparison to the normal fence ($\beta = 90^\circ$), though significant, does not capture the much greater reduction in the magnitude and extent of the wall pressure distribution in the viscous flow result. The simple modification to the BEM model then, of replacing the normal fence with a curved fence, does not sufficiently account for the effect of the boundary layer, although some reduction in the lift obtained does result.

The results show that the ‘ideal’ maximum efficiency of an interceptor flow, i.e. the free-streamline flow over a wall mounted fence, is obtained at small σ_c and is $L/D > 40$. Even with the consideration of a only ‘practical’ upstream wall length, this value is reduced to $L/D \approx 20$. The results from the example ($\sigma_c = 0.44$) analysed with CFD showed a reduction of about 50% in the C_L value obtained in the viscous flow regime. The CFD results though informative, can only be considered as preliminary at this stage. Experimental data for comparison with the CFD analysis is required. This will enable the choice of appropriate values of the nuclei size and concentration parameters in the CFD cavitation model, which have a significant influence on the result obtained.

Comparison of BEM data for the curved and flat fence geometries revealed that the cavity characteristics, e.g. length, were found to be a function of the angle of detachment of the cavity. The determining parameter was then the fence trailing edge slope with the shape of the fence upstream of the trailing edge having no effect on the resulting cavity.

Chapter 4

Intercepted Base Ventilated Supercavitating Foil Flow - Numerical Analysis

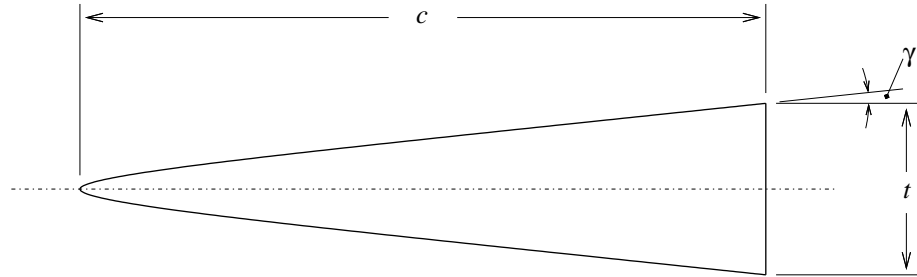
4.1 Introduction

The performance of supercavitating hydrofoils has been extensively investigated and reported on in the classical literature, as reviewed in Chapter 1. These foil sections can be divided into those operating with one or two wetted sides, termed fully ventilated and base ventilated conditions respectively. The former has the upper cavity surface detaching from a sharp leading edge, while the latter has both upper and lower surfaces wetted and cavity detachment from the edges of the unwetted blunt base, as depicted in Figure 1.1.

A variant of the blunt-based foil shape is one without camber as depicted in Figure 4.1a. As discussed in Section 1.2, the main interest in these uncambered base ventilated sections has been in the application to surface piercing struts, rudders, etc. on high-speed craft (Tulin, 1961). The optimum shape of these sections as regards drag minimisation was found to be parabolic, based on linearised potential flow theory (Tulin, 1955).

For the reasons discussed in Section 1.2 the two-part foil with cavity concept of interest herein is modelled using the forward section only, with a forward-facing step added to one of the trailing edges. The foil chord length used in the presentation of results is that relating to the forward section only, designated as c rather than that referring to the chord length, C , of the complete two-part foil. The addition of the step to the foil surface is akin to an interceptor attached to the edge of a transom (see Sections 1.3 and 1.2), so the term intercepted foil is used for this arrangement. The simplest step shape is a fence attached to the trailing edge, i.e. at $x/c = 0.5$, as shown in Figure 4.1d. This arrangement models closely the step shape formed by the rotated foil tail section as depicted in Figure 1.2.

The flow approaching the step contains a boundary layer with a thickness in the order of the step height. This viscous flow regime is not modelled here



(a) Symmetric blunt-based foil section.

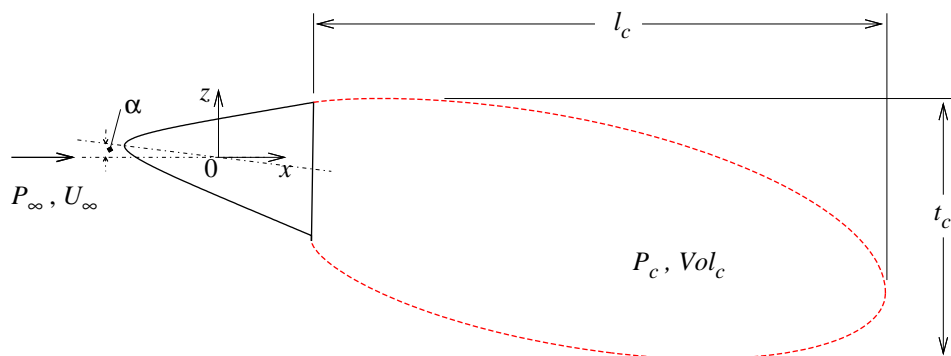
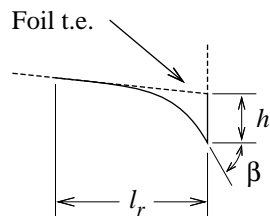
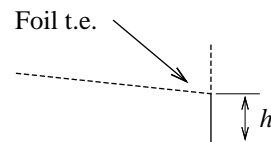
(b) Intercepted base ventilated foil at incidence α with cavity detachment from the upper surface trailing edge and the step edge (shown with an exaggerated vertical scale).(c) Step shape - ramp ($\beta < 90^\circ$).(d) Step shape - fence ($\beta = 90^\circ$).

Figure 4.1: Sketches of: (a) bare foil section; (b) intercepted foil/cavity body, indicating the definition of the geometric and some of the hydrodynamic parameters used. Magnified views of the foil lower surface trailing edge showing the two step shapes used in this analysis: (c) ramp; (d) fence.

however, as a potential flow method is used. In the potential flow model the detachment streamline is common with the surface streamline over the foil and step, with the solid surfaces having a free-slip boundary condition. The cavity surface then detaches tangentially from the step edge. In the case of the potential flow over the fence the cavity is then detaching at an angle of 90° to the foil chord line. The fence immersed in a boundary layer will have a region of separated flow in the corner upstream of the fence face as discussed in Chapter 3. This will modify the pressure distribution significantly from the potential flow result and possibly affect the angle at which the cavity surface detaches from the step edge. It was found in the wall mounted fence analysis (Section 3.4.3), that cavity shape is determined by the angle of cavity detachment and is essentially independent of the fore body shape.

In the aerodynamics field a common method used to correct for the effect of the boundary layer in a potential flow analysis is to inflate the foil surface outwards by a distance equal to the displacement thickness δ^* (see Katz and Plotkin, 2001, p.227). In the case of an intercepted foil the step height is small with respect to the foil chord and is of the same order as the total boundary layer thickness δ . So to inflate the foil surface outwards and either reduce h by δ^* or to attach the full height step to the inflated foil surface would not be appropriate. Alternatively, to adjust the potential flow model to account for the viscous effect on the flow over the step, a second step shape in the form of a ramp was also analysed (see Figure 4.1c and Appendix E for the curve definition). The viscous flow separation streamline was approximated by the ramp curve with the ramp trailing edge slope $\beta < 90^\circ$ giving the adjusted cavity detachment angle. This is a somewhat crude approximation and future experimental results will be compared with predictions to check the usefulness of this adaption to the potential flow model.

In Figures 4.1 a-d sketches of the symmetrical blunt-based foil, intercepted foil/cavity body and trailing edge step shapes are given showing the definition of the geometric and the main hydrodynamic parameters. The angle of incidence of the foil to the incoming flow is defined as positive if the foil, with the step attached to the lower surface of the foil, is rotated clockwise about its midchord point as illustrated in Figure 4.1b. Hydrodynamic forces are defined in flow fixed coordinates with lift in the z direction and drag in the x direction of the axis as shown in Figure 4.1b. The moment is calculated about the midchord point, i.e the origin of the coordinate system, and defined as positive when acting in a clockwise sense.

4.2 Criteria for Geometry Definition

Due to the novelty of this concept and the lack of relevant previously published work to draw upon (as surveyed in Section 1.2), a numerical analysis of two simple foil profiles was undertaken, the details of which are included as Appendix E for reference. The understanding gained from this initial analysis provided a basis for the selection of the bare blunt-based foil shape (i.e. the profile without the addition of a step). The following parameters were found to be significant;

- Thickness to chord ratio, t/c
- Leading edge radius (degree of profile bluntness), r
- Foil trailing edge slope, γ
- Shape and height of the trailing edge step, β and h/c respectively.

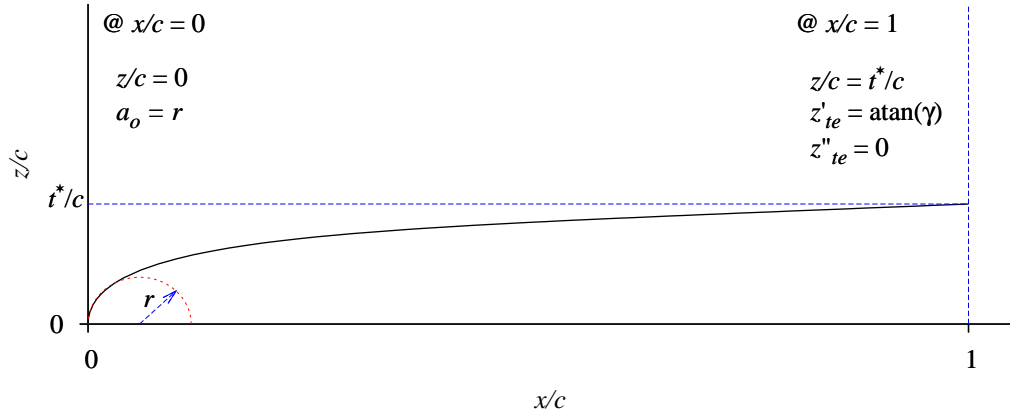
In this chapter the effect of each of these parameters on cavity shape and hydrodynamic performance is systematically investigated.

4.3 Foil Section Geometry

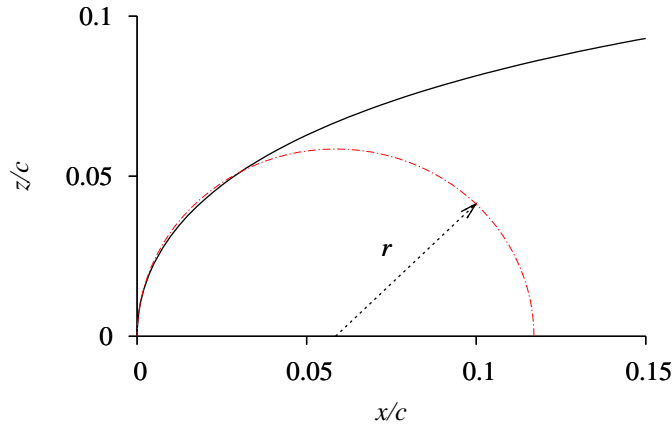
To maintain cavity detachment from the edge of the blunt base the flow should remain attached along the foil suction surface. Apart from aspects particular to the leading edge region (see, for example, Davis, 1980), flow separation over the remainder of the foil surface is prevented if a favourable pressure gradient is maintained. This is achieved if the profile monotonically increases in thickness with chordwise distance from the leading edge. Maximum thickness consequently occurs at the foil trailing edge, $x/c = 1$, and the half-thickness of the foil¹ trailing edge is t^* , as indicated in Figure 4.2. By varying the leading edge radius of the foil section the degree of “bluntness” can be prescribed. The first derivative at the trailing edge must be able to be prescribed to obtain a desired γ . By matching the first two derivatives with the corresponding values of the tail section leading edge, enables the curvature of the two-parts of the complete foil to be made continuous across the join.

A number of functions were investigated for suitability. One that satisfies all these requirements is the design equation for the thickness distribution of the NACA 4-digit-modified-series airfoils (Stack and Von Doenhoff, 1934). The modification over the basic series was introduced to allow variations in the leading-edge radius, providing differing degrees of “bluntness”, and also to allow the chordwise location of maximum thickness to be prescribed (Ladson et al., 1996). The modified series also differs in that the profile definition is separated into two parts, one forward and one after the point of maximum thickness.

¹Unless otherwise specified, a reference to the foil or foil section shape pertains to the forward part only of the complete two-part foil (Figure 1.2).



(a) boundary conditions.



(b) foil leading edge.

Figure 4.2: NACA 4-digit Modified foil profile definition showing: (a) the boundary conditions used; (b) a magnified view of the leading edge illustrating that the radius of curvature of the profile has the value of r only at $x/c = 0$.

Equation 4.1 defines the portion of the NACA 4-digit-modified-series foil profile up to the point of maximum thickness. It is this function that has been used to generate the foil geometry for the present work. The coefficient of the first term, a_0 , is a function only of the radius of curvature at $x/c = 0$, as given in Equation 4.2. This is due to the curvature being finite in the limit as $x \rightarrow 0$, as shown by Ladson et al. (1996). The finite radius of curvature at $x/c = 0$ is considered as the leading edge radius of the foil profile, r , even though it is only that value at $x/c = 0$, as can be seen in Figure 4.2b. The curvature then varies continuously from this point along the chord as shown for a typical foil profile in Figure 4.2a.

$$\frac{z}{c} = a_0 \left(\frac{x}{c}\right)^{1/2} + a_1 \left(\frac{x}{c}\right) + a_2 \left(\frac{x}{c}\right)^2 + a_3 \left(\frac{x}{c}\right)^3 \quad (4.1)$$

$$a_0 = \sqrt{2r} \quad (4.2)$$

The coefficients in Equation 4.1 are determined by the application of specified boundary conditions, as indicated in Figure 4.2a. The value of z'' starts at $-\infty$ at the leading edge and then must reduce in magnitude smoothly and without changing sign for the profile to remain monotonic (i.e. to be a valid profile). For a valid foil shape then it is required that $z''_{te} \leq 0$, but there is also a limited range of values below which the profile is also invalid. Reducing z''_{te} below zero reduces the thickness of the leading edge and so a value of zero has been used to maximise the range of possible foil shapes to be analysed. With a_0 a function of r only (equation 4.2), three equations are needed to solve for the remaining three unknown coefficients. Differentiating Equation 4.1 twice gives two equations and along with Equation 4.1 gives the three required. Using the right hand side boundary conditions, i.e. at $x/c = 1$, the solution for the unknown coefficients in terms of r , t^*/c and γ is then given by:

$$\begin{bmatrix} 1 & 1 & 1 \\ 1 & 2 & 3 \\ 0 & 2 & 6 \end{bmatrix} \begin{bmatrix} a_1 \\ a_2 \\ a_3 \end{bmatrix} = \begin{bmatrix} t^*/c - a_0 \\ \gamma - \frac{1}{2}a_0 \\ \frac{1}{4}a_0 \end{bmatrix} \quad (4.3)$$

which was solved numerically.

For the foil shape to be valid there is an upper limit to the magnitude of the leading edge radius for each particular combination of t^*/c and γ and is termed r_{max} . This relationship can be seen in Figure 4.3 where the curves are the limiting upper boundary where $r = r_{max}$ for three values of γ . Valid profiles are those occurring on and in the region below the curves for each respective value of γ shown. The minimum thickness limit for each of the three γ examples shown is marked as the wedge limit as the profile approaches a triangular or wedge shape as $r \rightarrow 0$. The value is given by $(t^*/c)_{min} = \tan(\gamma)$. In summary the parameter space within which a valid foil shape is found lies within the following ranges:

$$\begin{aligned} 0 &\leq r \leq r_{max} \\ t^*/c &\geq \tan(\gamma) \end{aligned} \quad (4.4)$$

The effect of only varying r on the profile shape is shown in Figure 4.4. This represents a family of profiles within a vertical line segment between the x-axis and the r_{max} bounding curve for the particular γ on Figure 4.3. For the 'wedge limit' case, this family reduces to the one valid profile only with $r_{max} = 0$. Note that the curves with the two largest values of r shown in Figure 4.4 have $r > r_{max}$ and are included as examples of invalid profile shapes.

The parameter space of valid profile shapes based on geometric considerations only is shown in Figure 4.5 for the range $15\% \leq t/c \leq 30\%$ considered of practical interest here. γ is varied from 0° in an initial increment of 2.5° and then in steps of 0.5° until the 'wedge limit' is reached. For clarity, only

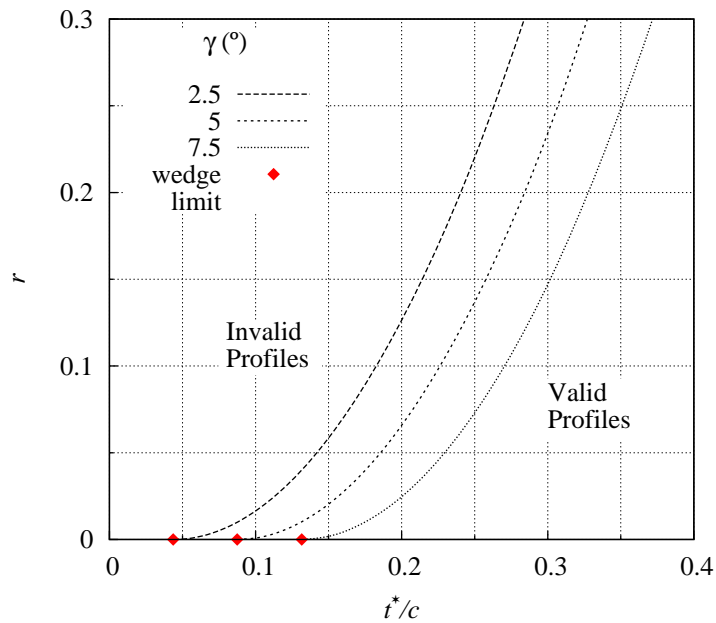


Figure 4.3: Relation between the foil leading edge radius and base thickness showing parameter ranges for a valid foil shape. The curves are the upper bounds, $r = r_{max}$, for constant γ .

the r_{max} profiles are shown with each one being representative of a family of valid profiles of $0 \leq r \leq r_{max}$ as illustrated in Figure 4.4. Again, on the 'wedge limit', the valid foil shape families are reduced to only one profile with $r_{max} = 0$.

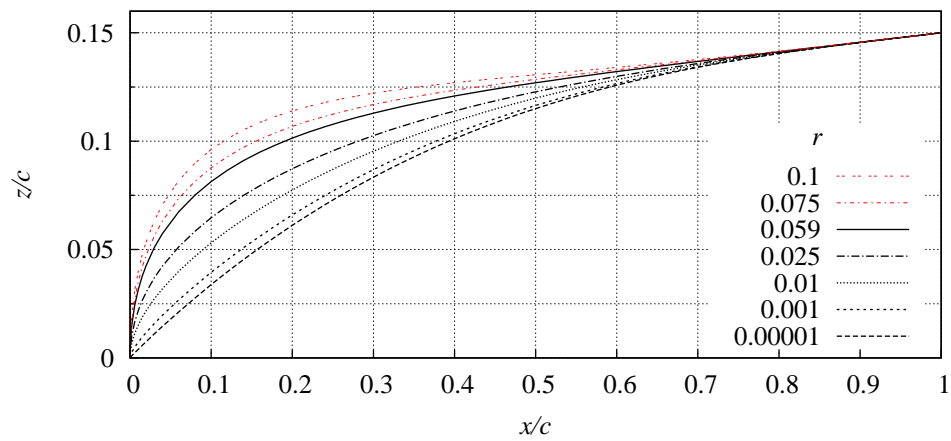


Figure 4.4: A family of foil profiles with only the leading edge radius varied ($t/c = 30\%$ and $\gamma = 2.5^\circ$). The solid line is the profile with $r = r_{max}$. The two profiles with the largest values of r are invalid shapes and shown for comparison only.

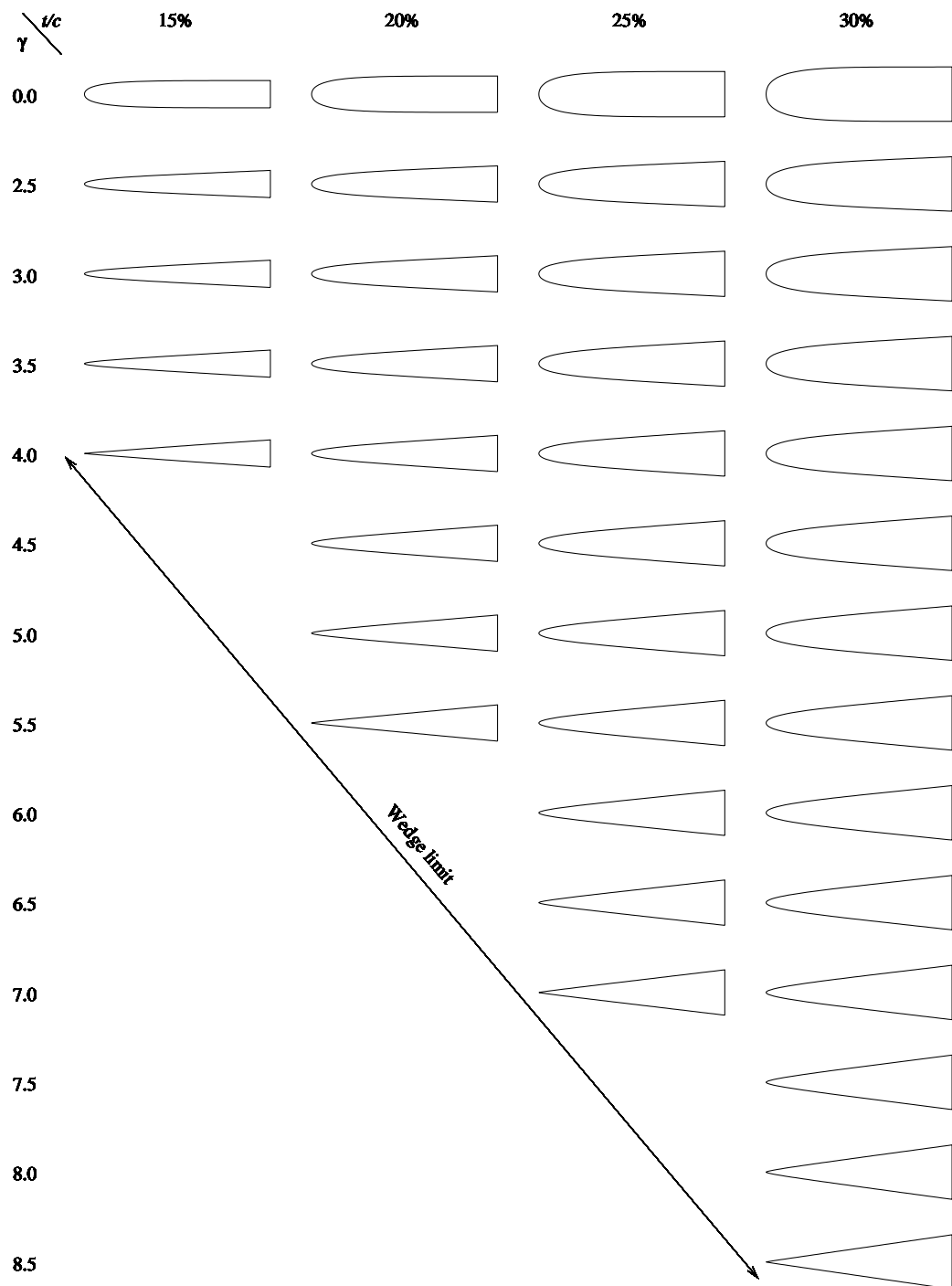


Figure 4.5: Parameter space of geometrically valid foil profiles of practical interest. Each profile shown has $r = r_{max}$ and is representative of a family of profiles covering the range $0 \leq r \leq r_{max}$. For the profiles at the 'wedge limit' the family is reduced to one with $r_{max} = 0$.

4.4 The Foil/Cavity Body - Constraints and Dependencies

To summarise from the previous section, the range of geometric parameters to be investigated are:

- $15\% \leq t/c \leq 30\%$ in increments of 5% giving four foil thicknesses
- $\gamma \geq 0^\circ$ in an initial increment of 2.5° and then in steps of 0.5° until the ‘wedge limit’ is reached
- $0 \leq r \leq r_{max}$.

In addition to these geometric factors there are also the following constraints due to hydrodynamic aspects:

- An upper limit of σ_c corresponding to a minimum cavity length of $l_c/c = 2$ required for a stable supercavity (as discussed in Section 1.1). The opposite extreme is the $\sigma_c = 0$ infinite length cavity case. To maintain a reasonable computational time with the method used, the largest cavity length modelled was $l_c/c = 250$ corresponding to $\sigma_c \approx 0.02$.
- A sufficiently large γ to ensure a valid cavity detachment from the foil suction side trailing edge (as was indicated in Appendix E.5).
- A limit to the minimum value of r due to the the leading edge suction peak magnitude.
- An incidence range of $0^\circ \leq \alpha \leq 2.5^\circ$, (see Section 1.2).

The following list contains the parameters relevant to the present analysis. They are either an input to the problem or one of the various dependent variables upon which to assess a foil’s performance. Note that all parameters have been non-dimensionalised where appropriate.

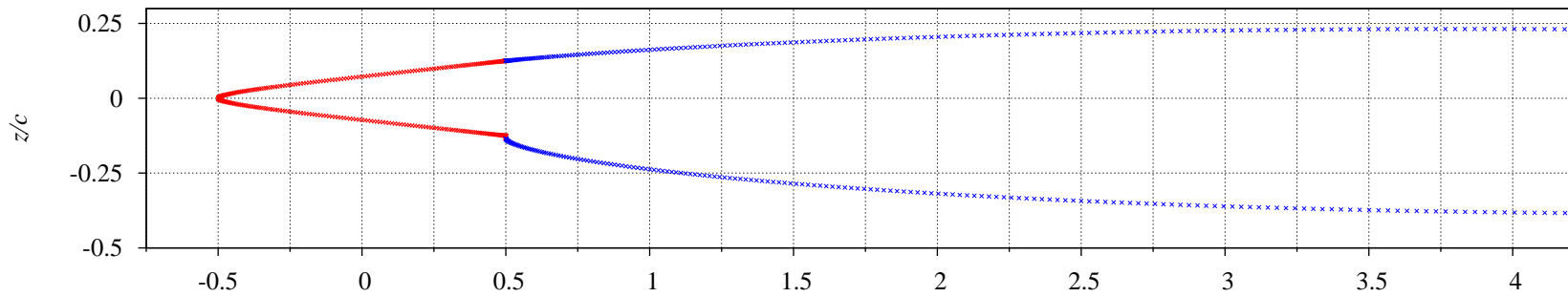
- Foil shape - t/c , r and γ
- Step shape - h/c , h/l_r and β
- Cavity shape - l_c/c , t_c/c , \mathcal{V}/c^3 and σ_c
- Hydrodynamic parameters - α , C_P , C_L , C_D , C_M , and L/D .

4.5 Surface Discretisation

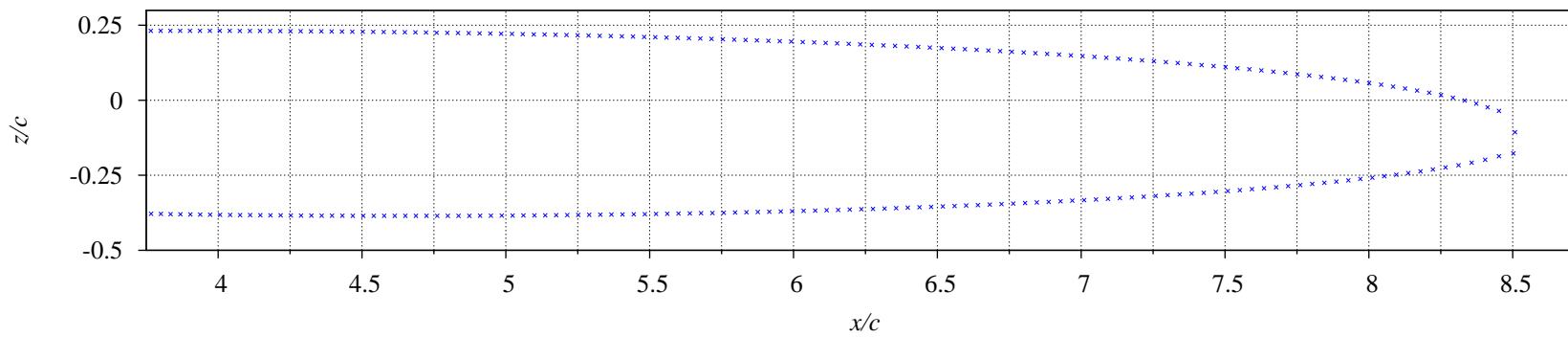
This analysis was performed using the boundary element code SUPCAV which was described in Chapter 2. This section will summarise the issues pertinent to the discretisation of the foil-cavity body. For a full description of the surface discretisation used and the convergence behaviour of the numerical solution, refer to Section 2.3.3.

A typical example of the surface discretisation is shown in Figure 4.6. A relatively short cavity has been chosen here so as to illustrate the main features with the figure drawn at the same scale on both axes. For efficient computation a full-cosine spacing has been used on both the upper and lower foil surfaces (see also Figure 4.7a). The small element sizing is required at the leading edge due to the high pressure gradients there, and also at the trailing edge to adequately resolve the cavity detachment, i.e. the cavity detaching tangentially from the foil surface (see Figure 4.7d). A half-cosine spacing has been used on the cavity surfaces with the resulting large elements at cavity closure serving to overcome the inherent instability of the solution in this region as discussed in Section 2.3.3.

Figure 4.7 gives a larger scale view of the foil from Figure 4.6, and also some magnified sections illustrating the leading edge and trailing edge/cavity detachment details. The fine discretisation of the foil leading edge is shown in Figure 4.7b, and of the trailing edge with attached fence in Figure 4.7c. The transition from foil to cavity surfaces is illustrated in Figure 4.7 d-e.

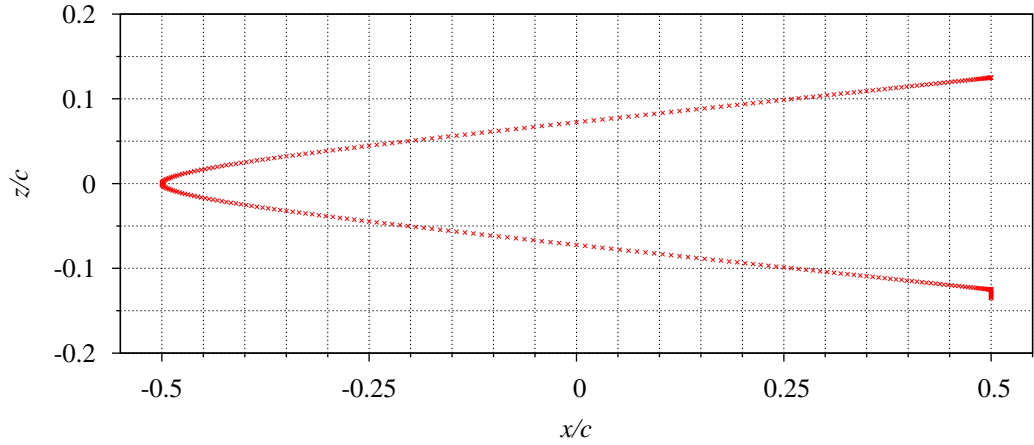


(a) Foil and forward part of the cavity.

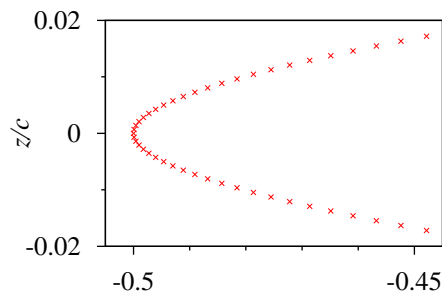


(b) remainder of cavity.

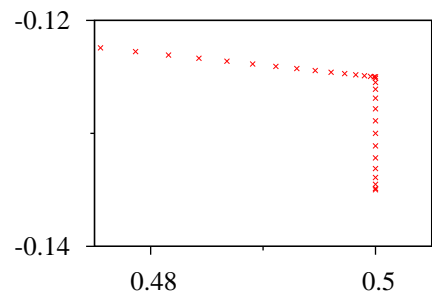
Figure 4.6: Surface discretisation example. Foil with fence: full-cosine spacing - 314 elements (with $\alpha = 0^\circ$, $t/c = 25\%$, $r = 0.00212$ and $\beta = 6^\circ$). Cavity: half-cosine spacing - 600 elements ($\sigma_c = 0.15$). The element end points for the foil are shown in red and those for the cavity in blue.



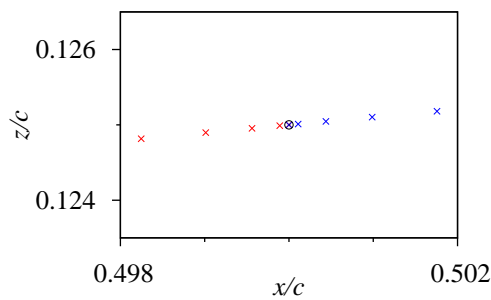
(a) Foil discretisation, half-cosine on both upper and lower surfaces.



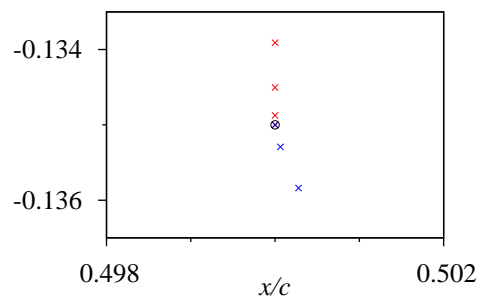
(b) Foil l.e.



(c) Fence attached to foil t.e.



(d) Cavity detachment from foil suction side t.e.



(e) Cavity detachment from fence t.e.

Figure 4.7: Larger scale view of the foil from Figure 4.6 showing magnified sections of the foil edges and cavity detachment. The element end points for the foil are shown in red and those for the cavity in blue. The foil t.e./cavity l.e. point is shown circled in (d) and (e) for clarity.

4.6 Results

4.6.1 Cavity Shape

The cavity shape that develops behind the foil fore-body is characterised as for the fence/ramp cavity flows described in Chapter 3: that is, in terms of length and thickness parallel and perpendicular to the free stream direction respectively and volume, as shown in Figure 4.1b. The general shape of the cavity surface is convex when viewed from the liquid. This is a necessary condition for a cavity shape to be valid here, as the pressure in the cavity is assumed to be the minimum in potential flow theory (Brennen, 1995; Milne-Thomson, 1968). The cavity surface detaching from the edge of the step was found to be convex under all flow conditions examined. On the opposite trailing edge, under certain conditions, the cavity surface detached with an initial concave curvature and then after a distance of $0.5c$ or less behind the trailing edge it inflected to give a convex shape that was then maintained for the remaining length of the cavity surface. Any such cavity shape was considered invalid and not included in the data set.

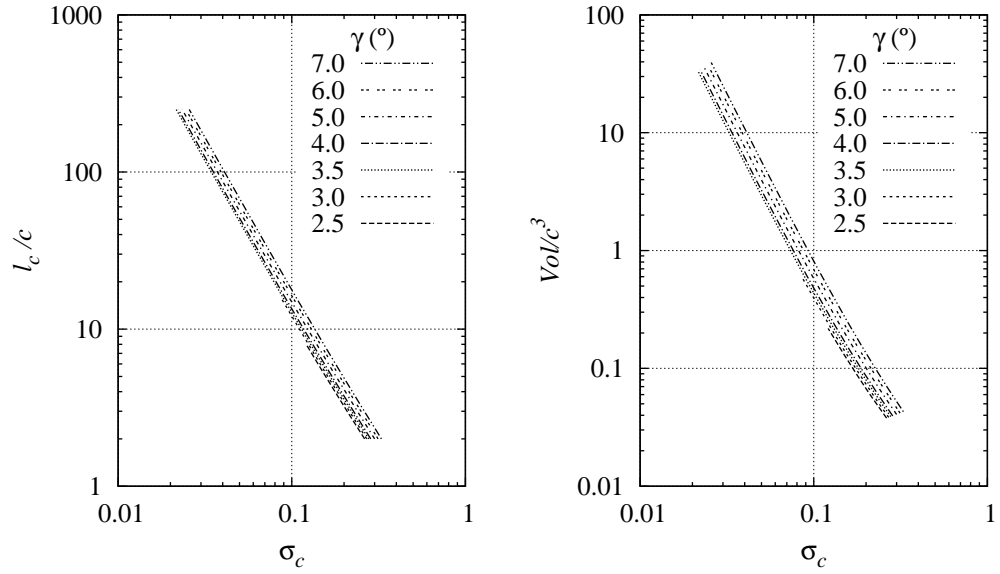
A sample of results for the relationship between the non-dimensional cavity length, thickness and volume and σ_c for the $t/c = 0.25\%$, $h/c = 0.01\%$ foil profile are given in Figure 4.8. These results are typical for the range of foil thicknesses examined. The full set of results obtained is included in Appendix C for reference.

As discussed in Section 3.4.3 there is a power law relationship between cavity length and σ_c for finite length supercavities, expressed by:

$$\frac{l_c}{c} = A\sigma_c^n \quad (4.5)$$

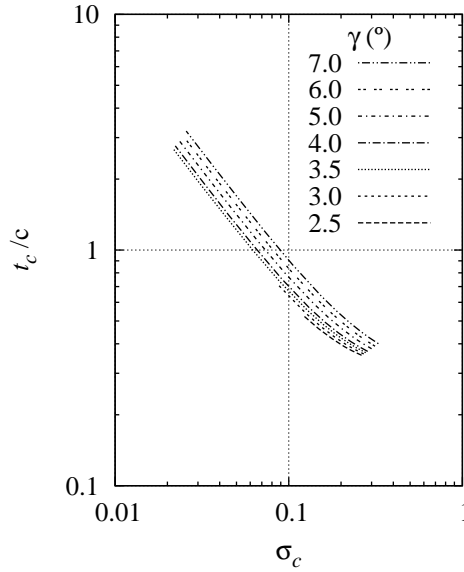
For a symmetric body in an infinite flow field with $\sigma_c \ll 1$ the linearised theory predicts that the exponent $n = -2$. For the intercepted foils in this present study, that are not symmetric due to the addition of the step on one side, this power law relationship still holds as can be seen in Figure 4.8a. The value of the exponent n is increased slightly above that from linearised theory and is found to be invariant with γ but to increase slightly with body thickness, as shown in Figure 4.9a. There is also a similar trend of an increase in n with fence height. The effect of varying γ is shown in Figure 4.8a, with the offset of the curves corresponding to the change in coefficient A of Equation 4.5. This latter relation is a linear function of γ , as shown in Figure 4.9b. For a foil with a 25% t/c and 1% h/c at zero incidence, this relationship is $A = 0.0174\gamma^\circ + 0.0877$. This results in a 10% increment in the dimensionless cavity length l_c/c per degree change in γ for a constant σ_c .

The relationship between cavity volume and σ_c also follows a power law, but deviates over the shorter cavity lengths with the curves bending slightly off the straight line for $\sigma_c > 0.1$ as shown in Figure 4.8b. For cavity thickness (Figure 4.8c) there is again a general power law trend with a similar deviation to that of the volume data over the upper end of the σ_c range.



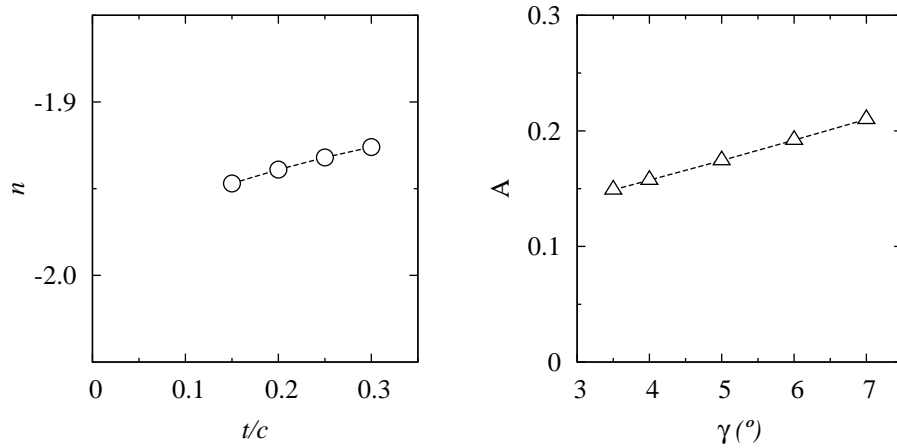
(a) Dimensionless cavity length as a function of σ_c .

(b) Dimensionless cavity volume as a function of σ_c .



(c) Dimensionless cavity thickness as a function of σ_c .

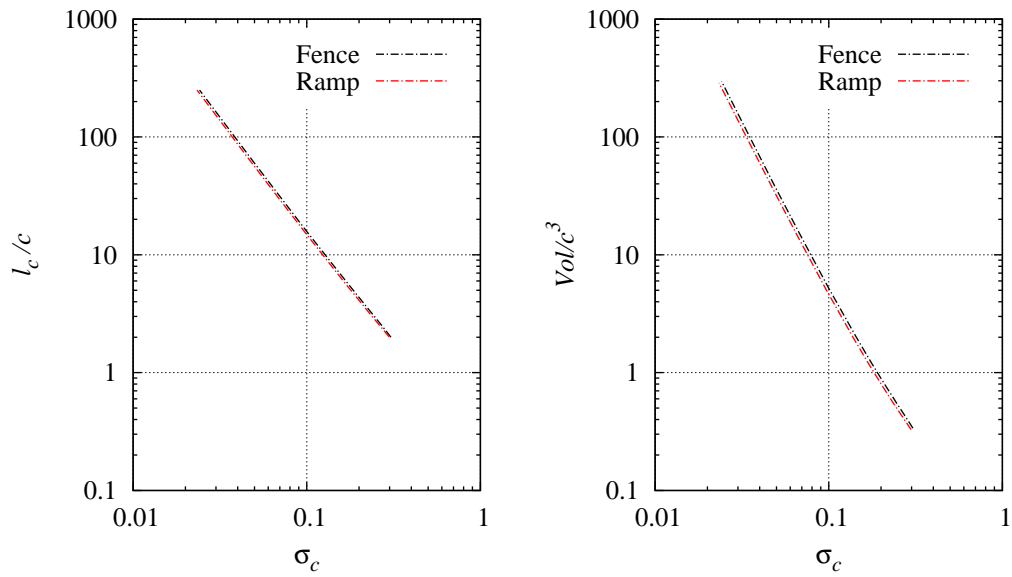
Figure 4.8: Variation of dimensionless cavity geometric properties with σ_c . (with $\alpha = 0^\circ$, $t/c = 25\%$, $h/c = 1\%$ and r_{max} with γ a parameter). These relationships are well represented by a power law function of σ_c (see Equation 4.5) with γ not affecting the slope but giving a constant offset to the curves. In the cavity length case (a), it equates to a 10% increment in l_c/c per degree change in γ .



(a) Exponent n as a function of t/c . (b) Coefficient A as a function of γ .

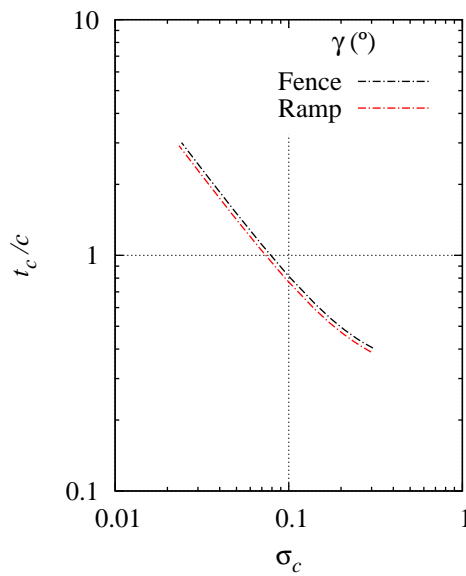
Figure 4.9: From Equation 4.5 ($l_c/c = A\sigma_c^n$) typical results showing: (a) the relation between n and t/c (for $\alpha = 0^\circ$, $h/c = 1\%$), which is invariant to γ ; (b) the linear relation between A and γ (with $\alpha = 0^\circ$, $t/c = 25\%$ and $h/c = 1\%$ gives $A = 0.0174\gamma^\circ + 0.0877$).

The sensitivity of cavity shape to the shape of the step attached to the foil trailing edge is illustrated in Figure 4.10 for two different step profiles with the same flow. Note that the two step shapes examined represent the two extremes of a gentle ramp and a perpendicular forward-facing step, and as such should be indicative of the upper and lower bounds of the effect of the step shape. From the results given in Chapter 3 it was found that for the wedge flows studied, the cavity shape was insensitive to the shape of the wedge fore-body and depended solely on the slope of the trailing edge, i.e. the detachment angle of the cavity. The ramp used has $\beta = 60^\circ$ and the fence $\beta = 90^\circ$ giving a change in β of 30° between the two shapes. Figure 4.10 shows that the cavity shape is relatively insensitive to such a large change in the shape of the step, with a small increase in cavity size over the full range of σ_c . The offset of the cavity length versus σ_c curve (Figure 4.10a) equates to a 6% reduction from the fence to the ramp results, which is a small but not insignificant difference due only to the change in step shape.



(a) Dimensionless cavity length as a function of σ_c .

(b) Dimensionless cavity volume as a function of σ_c .



(c) Dimensionless cavity thickness as a function of σ_c .

Figure 4.10: Effect of the step shape (fence or ramp) on cavity geometry as a function of σ_c . (with $\alpha = 2.5^\circ$, $t/c = 25\%$, $h/c = 1\%$, $\gamma = 6^\circ$, $\beta = 90^\circ$ - fence and $\beta = 60^\circ$ - ramp). There is an equivalent reduction in cavity size with the change from the fence to the ramp for all σ_c . In (a) this offset equates to a 6% decrease in cavity length for a constant σ_c .

4.6.2 Pressure Distributions and Minima

The pressure distribution over the base-ventilated intercepted foil typically shows a leading edge stagnation on the pressure side and a pressure minimum on the suction side. The cavity boundary condition requires that $C_p = -\sigma_c$ at the trailing edges. If the leading edge $C_{pmin} \leq -\sigma_v$ a partial vapour cavity may form there, and this, together with an unfavourable pressure gradient ($dp/dx > 0$) along the foil surface approaching the trailing edge, may lead to a ventilated or un-wetted suction side. These effects will also depend on viscous and surface tension effects which will need to be investigated experimentally. On the pressure side C_p reaches another stagnation value at the connection of the fence to the foil surface before falling suddenly to $-\sigma_c$ at the fence upper edge. As the fence is perpendicular to the x -axis the pressure distribution over it appears as a vertical line on the plot of pressure distribution over the foil. This is shown as the dashed section of the pressure curve in Figure 4.11a. The plot of C_p versus z , i.e. along the forward face of the fence, is given in Figure 4.11b with the pressure decreasing smoothly from stagnation at the fence/foil juncture down to the cavity pressure at the fence edge.

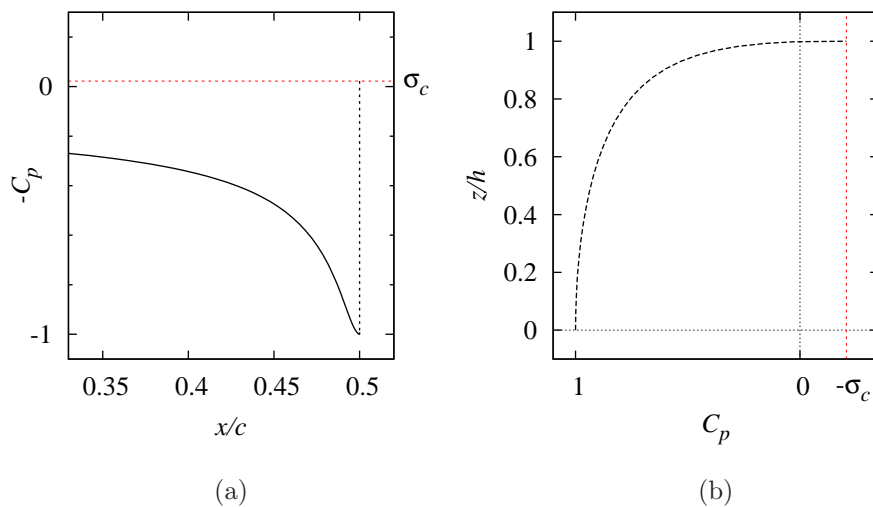


Figure 4.11: Distribution of pressure over: (a) pressure side trailing edge; (b) forward face of the fence with the pressure dropping from stagnation at the foil/fence juncture to the cavity pressure at the fence edge. The distribution over the fence is the vertical (dashed) line on (a) due to the fence being orientated perpendicular to chord line (and hence the x-axis) in this plot.

A typical example of the pressure distribution over a foil with fence fitted to the trailing edge of the lower surface is shown in Figure 4.12. The foil profile is shown above the plot for comparison and the negative of C_p is plotted so that the lower and upper curves relate to the lower and upper surfaces of the foil respectively. The pressure distribution on the foil pressure side, i.e. the side with the attached step, is the lower curve in Figure 4.12. After its initial sudden reduction from the stagnation value the pressure side C_p distribution increases

at a mild gradient (till approximately $0.75c$ (or $x/c > +0.25$)), before suddenly increasing to the stagnation value again at the fence. On the suction side of the foil the pressure reduces to a minimum (the leading edge suction peak or leading edge $C_{p_{min}}$) and then rises to a value above σ_c before reducing again to equal σ_c at the trailing edge (i.e. cavity detachment point). The reduction in pressure approaching the suction side trailing edge gives the favourable pressure gradient ($dp/dx < 0$) required to ensure the cavity detachment is maintained at the trailing edge.

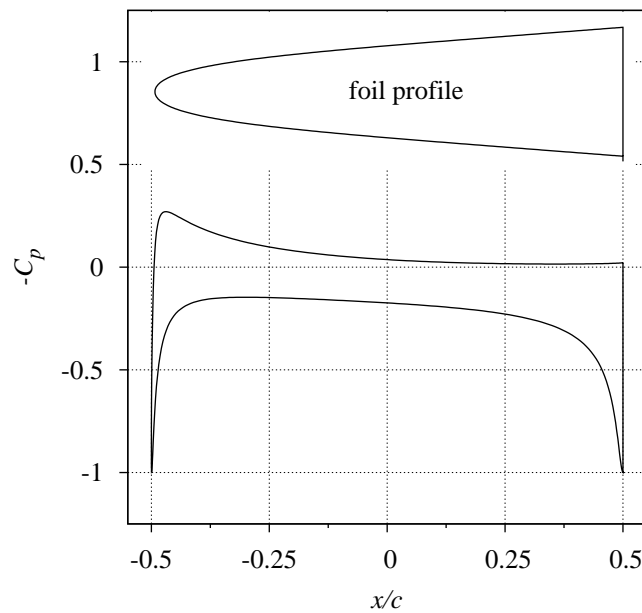


Figure 4.12: Typical pressure distribution over a base-ventilated intercepted foil. ($\gamma = 4^\circ$, $t/c = 25\%$, $h/c = 1\%$, $\alpha = 0^\circ$, r_{max} and at $\sigma_c = 0.022$). The foil geometry is shown above for comparison. Main features: stagnation ($C_p = 1$) at leading edge and the fence/foil juncture on the pressure side; leading edge suction peak and favorable pressure gradient just upstream of the trailing edge on the suction side; pressure equals cavity pressure at both the trailing edges.

Depending on the foil profile the leading edge $C_{p_{min}}$ may not be the global pressure minimum on the foil surface. When σ_c is large (i.e. for the shorter cavities) it is possible, given an appropriate foil geometry that the global $C_{p_{min}} = -\sigma_c$ and for the leading edge $C_{p_{min}}$ to be of some higher value. Figure 4.13 gives an example of this situation. In this case a favourable pressure gradient is guaranteed and therefore the suction side of these foils will never be at risk of becoming ventilated or un-wetted. As a result only the leading edge $C_{p_{min}}$ is investigated in the present analysis as a risk for leading edge vapour cavitation occurrence affecting foil performance. To summarise, at least from a potential flow view point, the requirements on the pressure distribution to ensure the foil suction surface remains wetted are that:

- the leading edge $-C_{p_{min}} < \sigma_v$, to avoid a leading edge vapour cavity;

- $dC_p/dx < 0$, i.e. a favourable pressure gradient, approaching the trailing edge.

The second condition would be assured if the leading edge $C_{pmin} > -\sigma_c$. In the more likely case that this is not so, as will be shown further on in this section, a favourable pressure gradient approaching the trailing edge may still be present dependent on the foil geometry and flow parameters. These factors will also influence the margin against unwetting due to incidence variations resulting from vessel motions in the practical application of a hydrofoil.

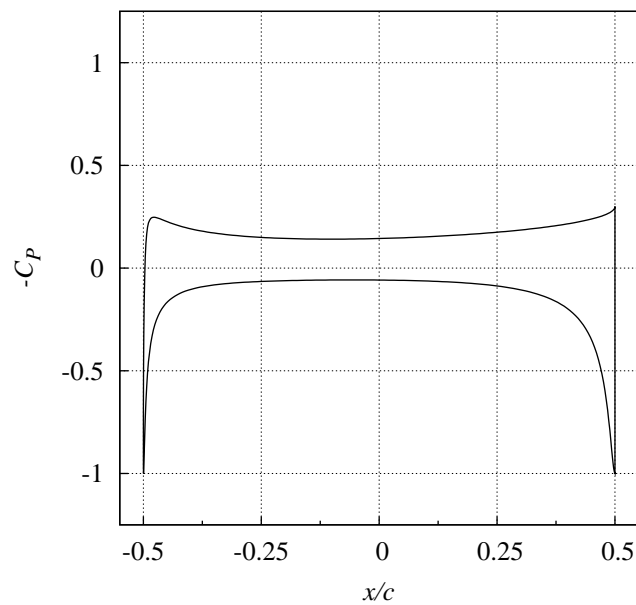


Figure 4.13: Particular case of pressure distribution for a foil where $\sigma_c =$ global $-C_{pmin}$: leading edge $C_{pmin} = -0.248$ and global $-C_{pmin} = \sigma_c = 0.3$. ($t/c = 25\%$, $h/c = 1\%$, $\alpha = 0^\circ$, r_{max} and $\gamma = 5^\circ$).

Note that the stagnation point with $C_{pmin} = 1$ at the base of the fence would not occur in a real flow due to viscous effects. Instead the flow would separate from the foil surface upstream of the fence and a region of separated flow would form in the corner at the junction of the fence and foil surfaces. Stagnation would then occur instead at the separation point on the foil surface and also at the point on the fence where the flow divides as shown in the CFD results of Chapter 3. Note that the stagnation pressure in viscous flow is less than the free stream stagnation pressure.

As γ is increased, for constant foil thickness, the profile becomes sharper. This is also a product of the corresponding reduction of the r_{max} to maintain a valid profile shape as defined in Section 4.3. Figure 4.14 shows the change in pressure distribution as γ is varied. The magnitude of the leading edge suction peak initially decreases and moves forward as γ increases. This continues to a point past which there is a dramatic increase in C_{pmin} making cavitation of

the leading edge likely (if $C_{p_{min}} \leq -\sigma_v$). At the same time the mean pressure over the suction surface rises and thus decreases the lift generated. In contrast to these negative aspects the length of favourable pressure gradient ($dp/dx < 0$) upstream of the trailing edge increases with γ . This is advantageous in ensuring cavity detachment occurs at the trailing edge and not somewhere further forward along the foil surface. On the pressure side the distribution becomes flatter as γ is increased; this adds to the lift being produced, which is opposite to the effect on the suction side. The lift data presented in the next section will show whether there is a net gain or loss in the production of lift from these two effects. The presence of the step is again locally dominant with the change in γ having no noticeable impact near the pressure side trailing edge.

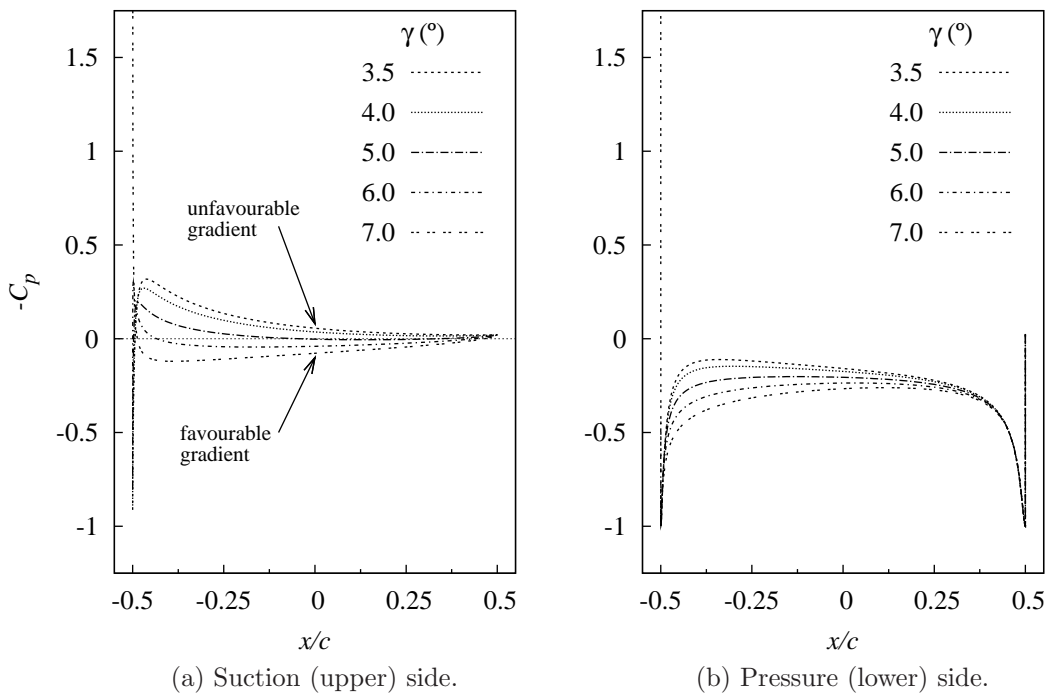


Figure 4.14: Variation of pressure distribution over the foil with γ . ($t/c = 25\%$, $h/c = 1\%$, $\alpha = 0^\circ$, r_{max} and $\sigma_c \approx 0.02$). On the suction side the leading edge $C_{p_{min}}$ initially moves forward and reduces before increasing again by $\gamma = 6^\circ$, and dramatically so by $\gamma = 7^\circ$. Note also that the pressure gradient upstream of the suction side trailing edge becomes more favourable as γ increases. The pressure side distribution is rather flat except at the foil edges, with C_p generally increasing in magnitude as γ increases.

An increase in foil thickness results in the magnitude of the leading edge suction peak reducing to a minimum value and then rising again. For the particular geometry of the foil in Figure 4.15, the minimum of the leading edge $C_{p_{min}}$ occurs at about $t/c = 25\%$. This figure also illustrates the decreasing length of favourable pressure gradient approaching the suction side trailing edge with increase in t/c . This suggests a trade-off between the reduction of leading edge $C_{p_{min}}$ and the extent or degree of favourable pressure gradient achievable. The presence of the fence is again locally dominant with no noticeable change in the pressure distribution just upstream of the pressure side trailing edge.

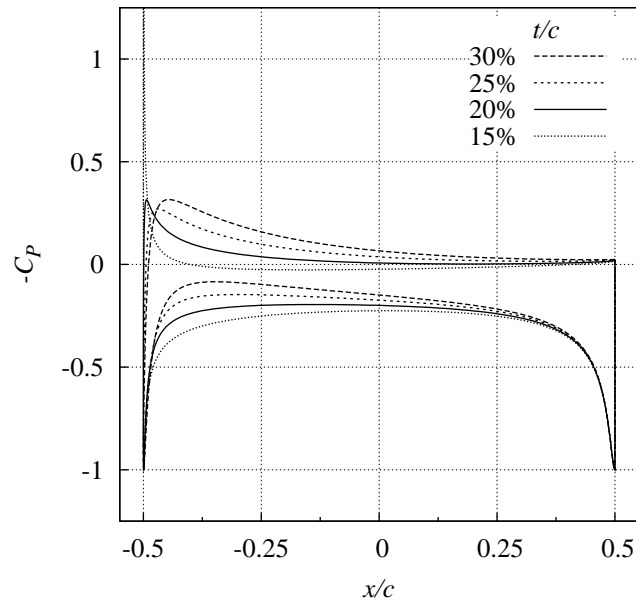


Figure 4.15: Variation of pressure distribution over the foil with t/c . ($h/c = 1\%$, $\alpha = 0^\circ$, $\gamma = 4^\circ$, r_{max} and with $\sigma_c \approx 0.02$). Suction peak minimum C_p at about $t/c = 25\%$; suction side pressure gradient becomes less favourable with increasing t/c .

The effect of σ_c on the pressure distribution is shown in Figure 4.16. A change in σ_c tends to lift both the suction and pressure side curves up and down relative to the boundary conditions, i.e. σ_c and the two stagnation points. There is a minor dependence of the leading edge $C_{p_{min}}$ on σ_c in comparison with the other parameters already discussed. A similar trend to that with t/c is present, with the leading edge $C_{p_{min}}$ decreasing to a minimum and then increasing again as σ_c increases. As σ_c is reduced, the length of favourable pressure gradient approaching the trailing edge decreases as occurred with increasing t/c . This indicates that it is possible for an established stable cavity to become unstable, i.e. for the detachment point to jump forward along the foil surface and make it ventilated, as the cavitation number is reduced. Also,

in contrast to the other parameters already discussed, the change in σ_c has an effect on the pressure distribution much closer to the pressure side trailing edge. (Compare Figure 4.16 with Figures 4.14b and 4.15).

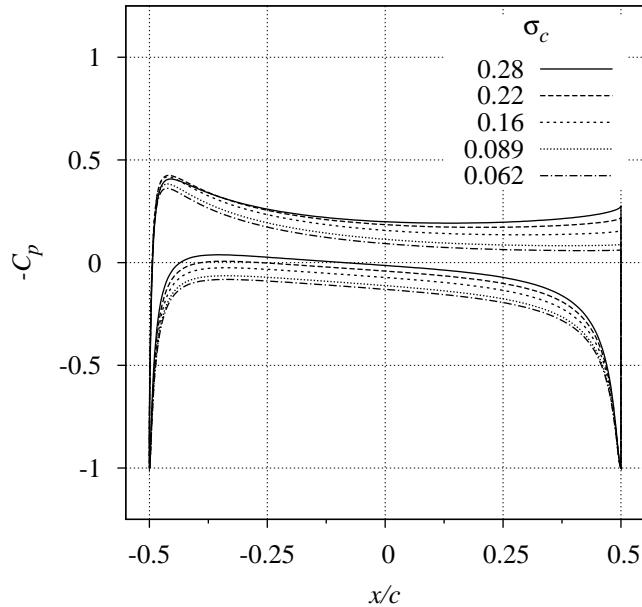
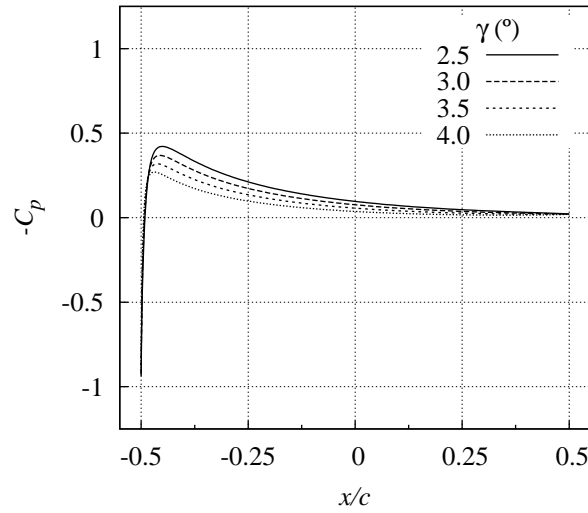


Figure 4.16: Pressure distribution over the foil surface, variation with σ_c . ($t/c = 25\%$, $h/c = 1\%$, $\alpha = 0^\circ$, r_{max} and $\gamma = 3.5^\circ$). The pressure and suction side curves move up and down relative to the boundary conditions of σ_c and the two stagnation points. As σ_c reduces, the length of favourable pressure gradient upstream of the suction side trailing edge reduces.

To distinguish between a valid and an invalid cavity shape, instead of analysing the cavity shape itself an equivalent check can be made to determine if the pressure gradient is favourable leading up to the trailing edge. The present data shows a correspondence between an adverse pressure gradient immediately upstream of the trailing edge and a concave (invalid) cavity surface detaching from it. This also explains why the cavity detachment from the edge of the step, being attached to the foil pressure side, is always convex, as by the nature of the flow over the step there is an acceleration of the fluid to obtain the cavity surface velocity at detachment. In Figure 4.17 the pressure side C_p distribution is shown for 4 foils with varying γ but all other parameters unchanged. The pressure distribution in the trailing edge region is shown magnified for each foil shape with $-C_p = \sigma_c$ on the cavity surface (i.e. for $x/c > 0.5$). The singular behaviour (i.e. a vertical tangent) of the pressure curve for an abrupt detachment (see Franc and Michel (2004, p.130) and Brennen (1995, p.239)) is evident from the figures. The two foils with the lower values of γ have invalid cavity shapes, with the changeover from adverse to favourable pressure gradient clearly seen between Figures 4.17c and 4.17d.

The effect of a variation in the trailing edge step shape (as illustrated in



(a) Suction side C_p distribution for 4 foils with different γ .

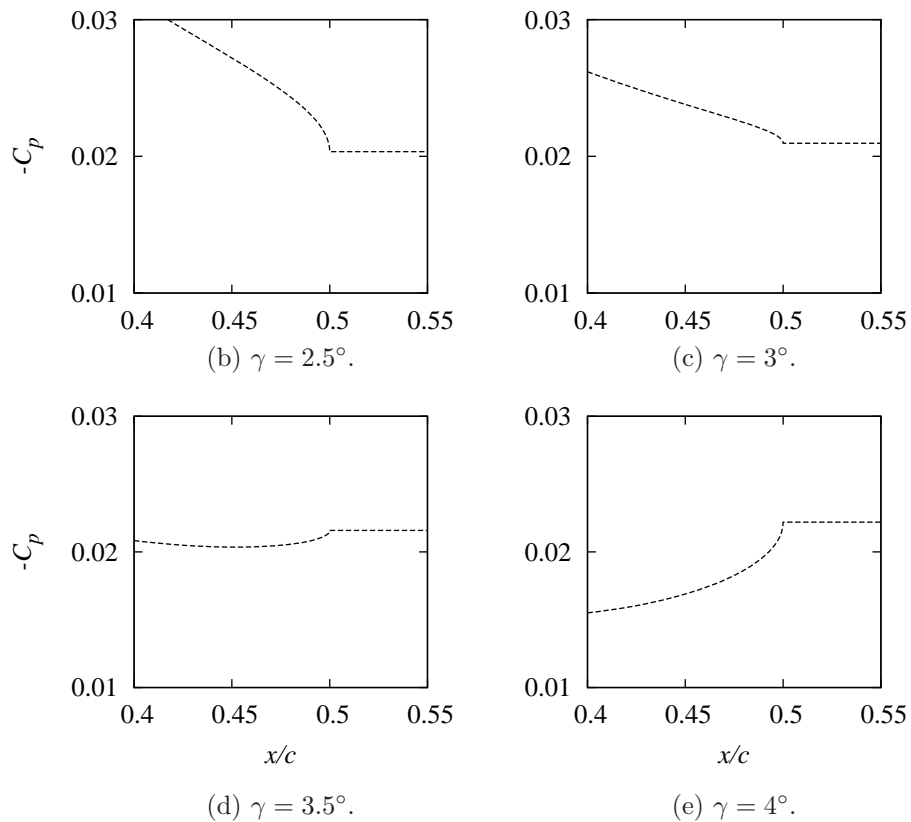


Figure 4.17: Suction side pressure distribution over the foil. ($t/c = 25\%$, $h/c = 1\%$, $\alpha = 0^\circ$, r_{max} , $\sigma_c \approx 0.02$ and four values of γ .) A magnified view of the suction side trailing edge region for each profile illustrating the unfavourable pressure gradient upstream of the trailing edge in (b) and (c), and the favourable pressure gradient present in cases (d) and (e). The former results in invalid cavity shapes, while the latter correspond to valid shapes.

Figure 4.1) on the pressure distribution over the foil is mainly confined to a small adjustment over the pressure side as shown in Figure 4.18. The ramp-shaped step removes the sharp internal corner, present with the fence and foil trailing edge junction, and there is now no longer stagnation at the trailing edge. With the inviscid flow no longer reaching stagnation at the trailing edge this effect is felt along the whole pressure side, reducing the pressure slightly all the way back to the leading edge stagnation point.

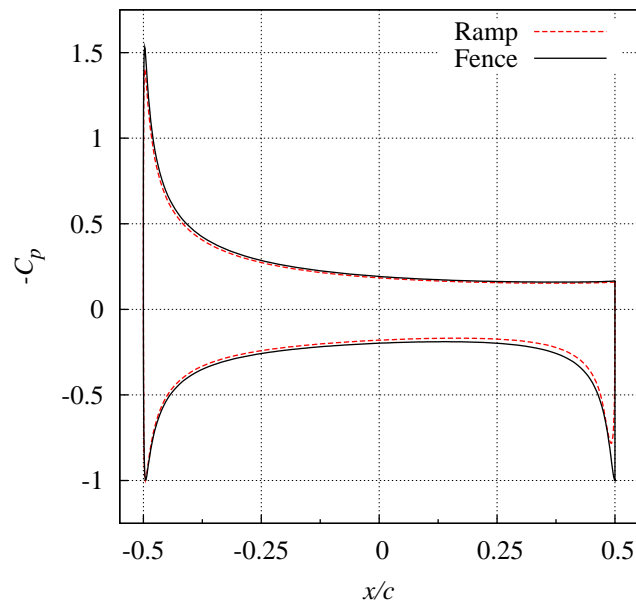


Figure 4.18: Effect of step shape on foil surface pressure distribution. ($\sigma_c = 0.165$, $t/c = 25\%$, $h/c = 1\%$, $h/l_r = 25\%$, $\alpha = 0^\circ$, r_{max} and $\beta = 90^\circ$ - fence, $\beta = 60^\circ$ - ramp). The magnitude is reduced slightly over both surfaces and so the area between the pressure curves is reduced, i.e. the lift is reduced due to the change in step shape.

The magnitude of the suction peak at the foil leading edge, $C_{p_{min}}$, can be used to assess the susceptibility of the section shapes to vapour cavitation occurrence. Figure 4.19 shows the relation between $C_{p_{min}}$ and σ_c with varying γ and t/c . There is only a mild dependence of $C_{p_{min}}$ on σ_c for constant γ or t/c but there are maxima within the ranges of both these parameters. This is more clearly depicted in Figure 4.20 where the data is instead presented as $-C_{p_{min}}$ versus γ for constant σ_c and t/c . For a particular foil thickness there is a distinct maximum of the pressure curve with the lowest value of σ_c the optimum operating condition for that foil profile. Alternatively for a particular value of γ there is an optimum t/c to achieve the maximum leading edge $C_{p_{min}}$, again with the smallest σ_c achieving the optimum operating condition for that shape. The incomplete range of data corresponds to the valid cavity limits for the particular parameters, e.g. for the $\gamma = 2.5^\circ$ and 3° curves in Figure 4.19a.

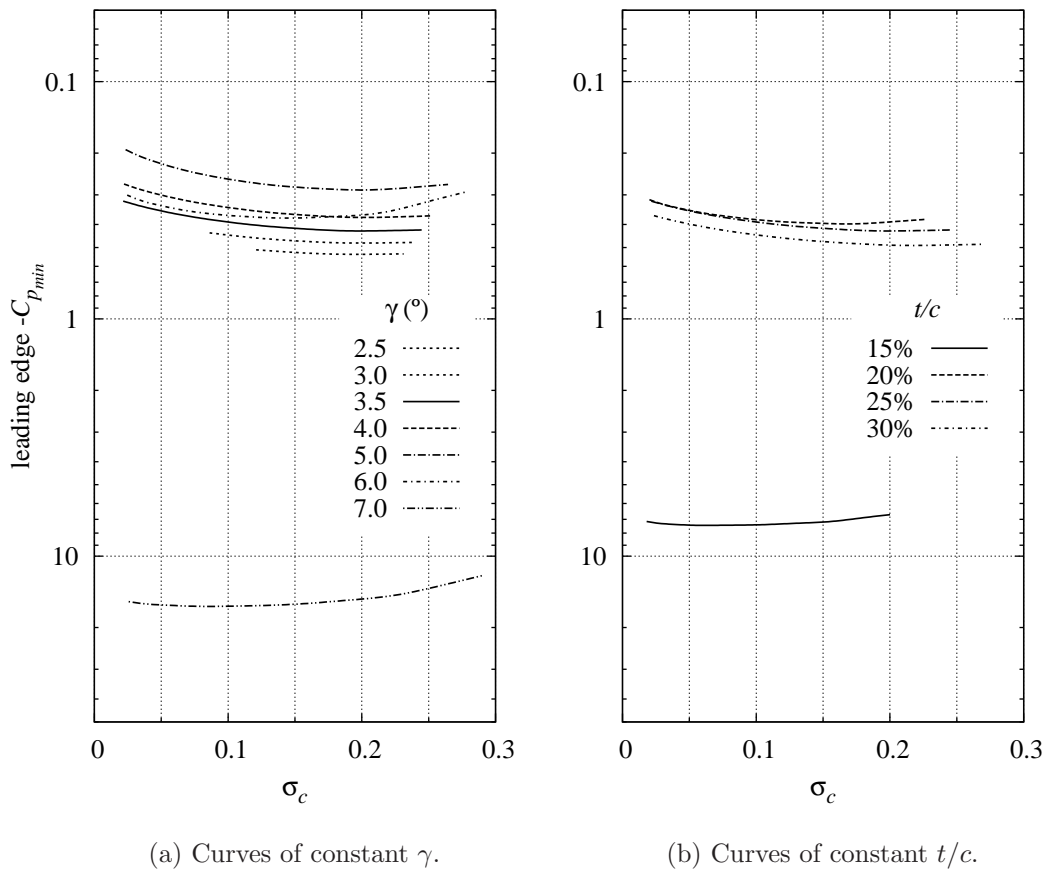


Figure 4.19: Foil leading edge $-C_{p_{min}}$ versus σ_c ($h/c = 1\%$, $\alpha = 0^\circ$ and r_{max}): (a) curves of constant γ and $t/c = 25\%$. Optimum profile (where i.e. $C_{p_{min}}$ is maximum) is with $\gamma = 5^\circ$; (b) curves of constant t/c , $\gamma = 4.0^\circ$. Optimum profile shape when $t/c = 20\%$.

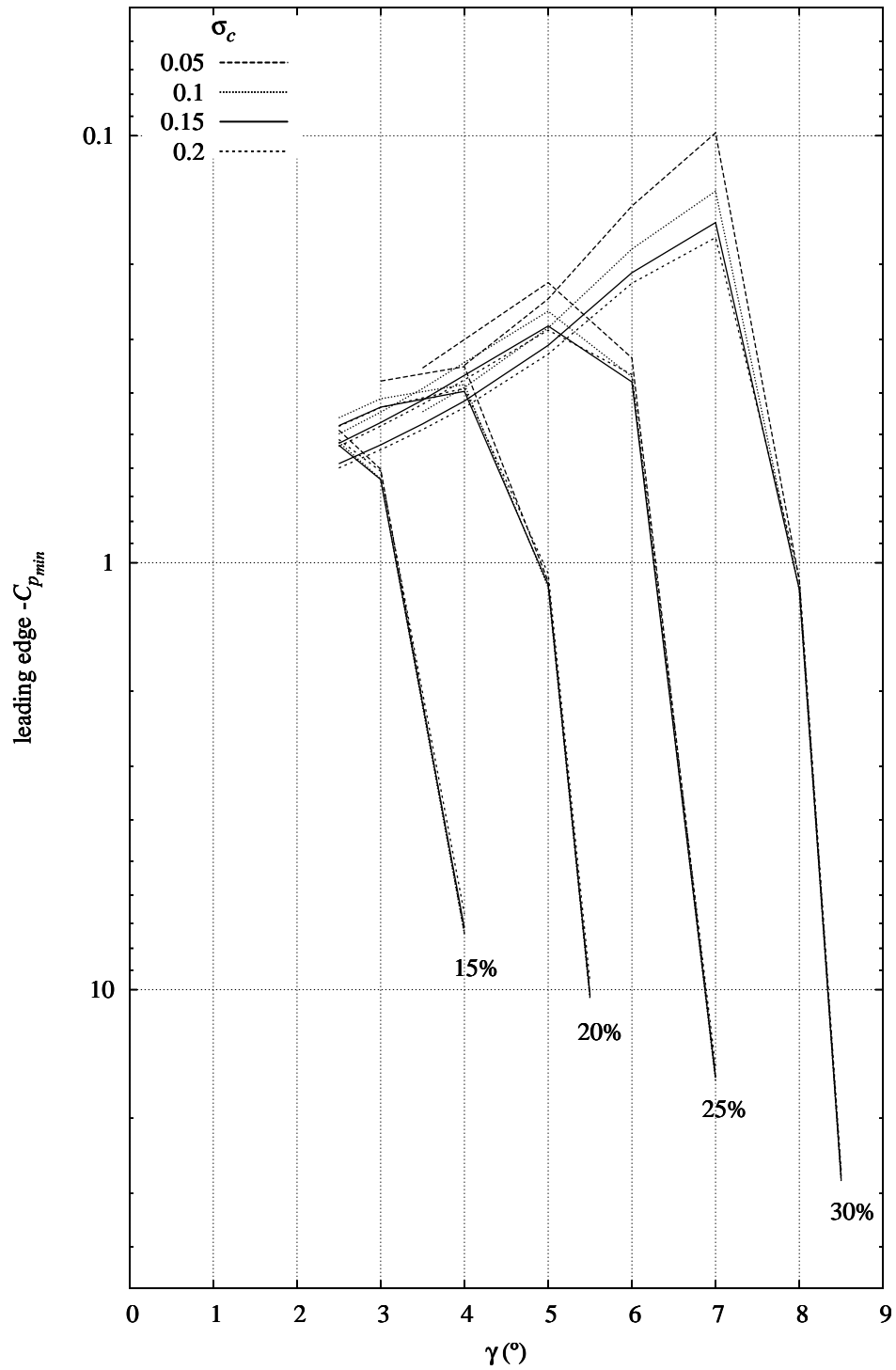


Figure 4.20: Cross-plots of the foil leading edge $C_{p,min}$ versus γ for four values of t/c , with σ_c a parameter ($h/c = 1\%$, $\alpha = 0^\circ$ and r_{max}).

The sensitivity of C_{pmin} to a change in incidence is shown in Figure 4.21 for both a large and small value of σ_c . Data for $\alpha > 0^\circ$ are presented only for three values of γ as this range corresponds to the region of optimum leading edge C_{pmin} in Figure 4.20. There is a general trend for the leading edge C_{pmin} magnitude to increase with incidence, and the optimum γ to decrease as α is increased (i.e the maxima of the curves move to the left with increasing α).

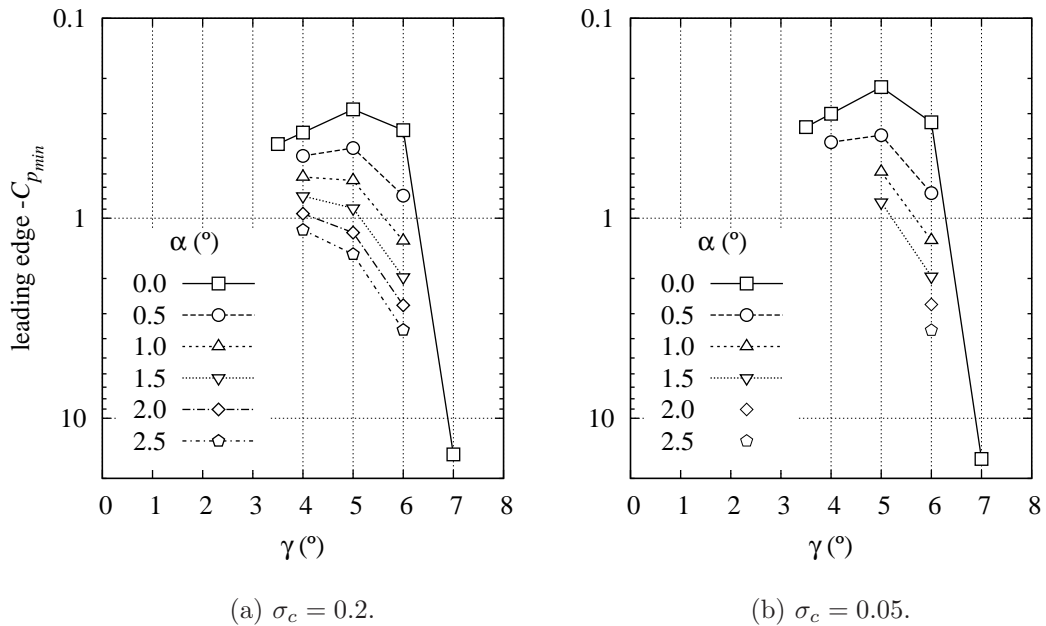


Figure 4.21: Cross-plots of the foil leading edge C_{pmin} versus γ : curves of constant α ($t/c = 25\%$, $h/c = 1\%$ and r_{max}). The leading edge C_{pmin} maximum increases with α , and the γ at which it occurs reduces. The missing data points in (b) reflect the limit of valid cavity shape for those conditions.

The dependence of C_{pmin} on the bluntness of the profile (i.e. the magnitude of the leading edge radius, r) is presented in Figure 4.22. For a particular incidence the data tends to fall on one line with the optimum shape obtained when $r = r_{max}$. It follows that the bluntest profile, for a particular thickness and trailing edge slope, has the least susceptibility to cavitation occurrence on the leading edge.

An increase in fence height results in an increase in the magnitude of C_{pmin} , as can be seen in Figure 4.23 with results presented for the range $0.01 \leq h/c \leq 0.1$. A similar trend of increasing magnitude of C_{pmin} is present over the full range of σ_c for each value of γ .

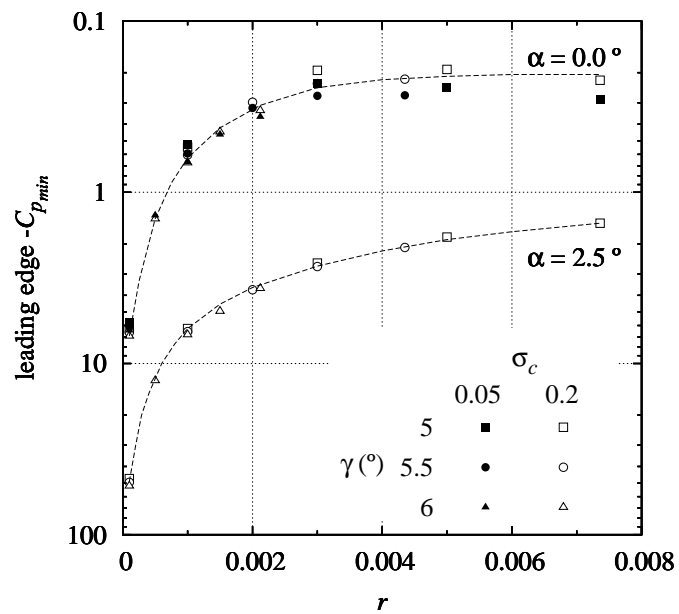


Figure 4.22: Foil leading edge $C_{p_{min}}$ versus r for $\alpha = 0^\circ$ and 2.5° and for large and small values of σ_c ($t/c = 25\%$ and $h/c = 1\%$). Note that data for $\sigma_c = 0.05$ is presented only for $\alpha = 0^\circ$. The dashed lines represent the indicative trend only.

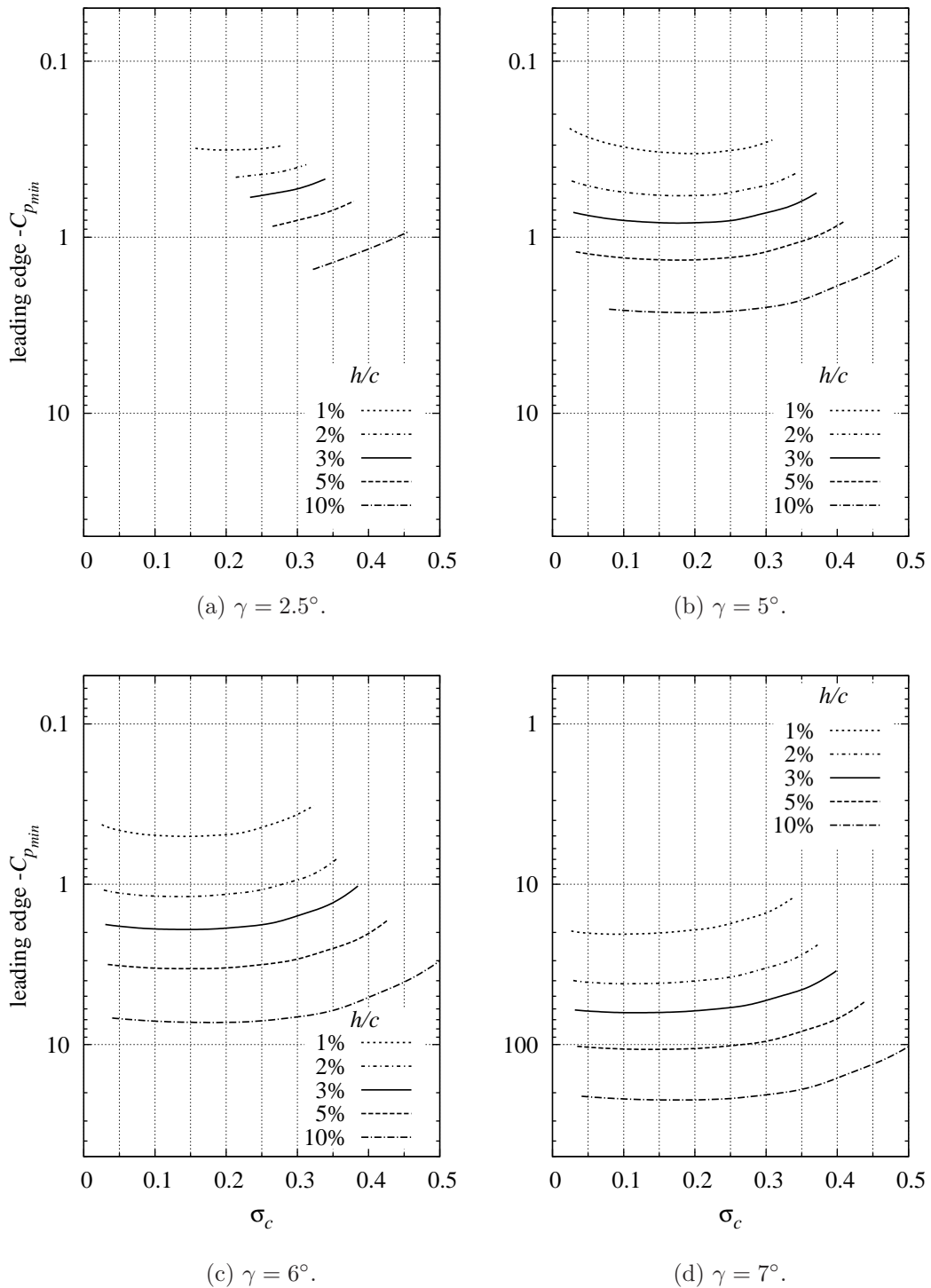


Figure 4.23: Effect of fence height on foil leading edge $C_{p_{min}}$ versus σ_c for four values of γ ($t/c = 25\%$, $\alpha = 0^\circ$ and r_{max}). The general trend is for an increase in the magnitude of the $C_{p_{min}}$ with fence height. There is a similar dependence of the $C_{p_{min}}$ on σ_c across the ranges of γ and h/c .

The sensitivity of the leading edge $C_{p_{min}}$ to the shape of the trailing edge step is shown in Figure 4.24. Again the shape of the fence and ramp are as defined in Figure 4.1. The change in step shape from fence to reamp results in a reduction in the magnitude of $C_{p_{min}}$ for all the values of γ plotted over the full range of σ_c .

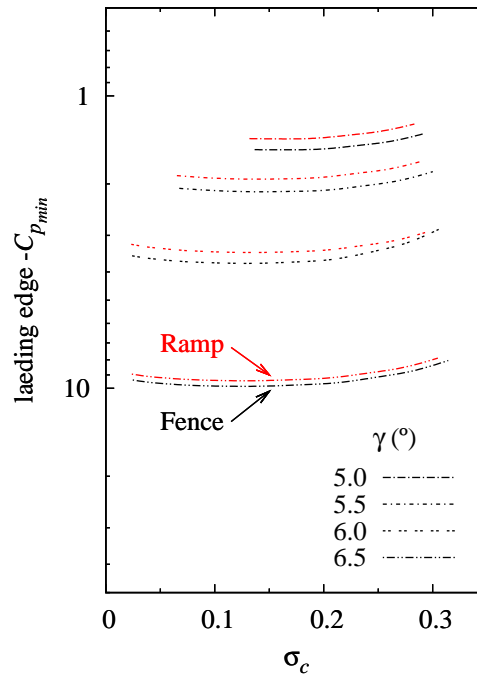


Figure 4.24: Comparison of foil leading edge $C_{p_{min}}$ versus σ_c with γ a parameter for the fence and ramp step shapes ($\alpha = 0^\circ$, $t/c = 25\%$, $h/c = 1\%$, r_{max} , $h/l_r = 25\%$ and $\beta = 90^\circ$ - fence, $\beta = 60^\circ$ - ramp). The ramp shape gives a reduction in magnitude of the leading edge $C_{p_{min}}$ for all γ and σ_c .

4.6.3 Hydrodynamic Forces

The hydrodynamic efficiency or lift to drag ratio for each profile shape is used as the primary measure of foil performance. No viscous drag component has been included as the purpose of the numerical analysis is to gain an appreciation of the effect of parameter variation. It is assumed that the viscous drag will not vary appreciatively over the range of profile shapes examined. The preliminary analysis detailed in Appendix C indicated that the leading edge radius of the profile had an influence on its hydrodynamic performance. For the shape investigated here there was found to be only a mild dependence of L/D on r . The maximum efficiency occurs at $r = r_{max}$ for each profile shape over the full range of both σ_c and α , as can be seen from Figure 4.25. Combining this result with the more significant observation that the optimum C_{pmin} is also obtained with $r = r_{max}$ (see Figure 4.22), all of the following data is presented with $r = r_{max}$ for each profile shape.

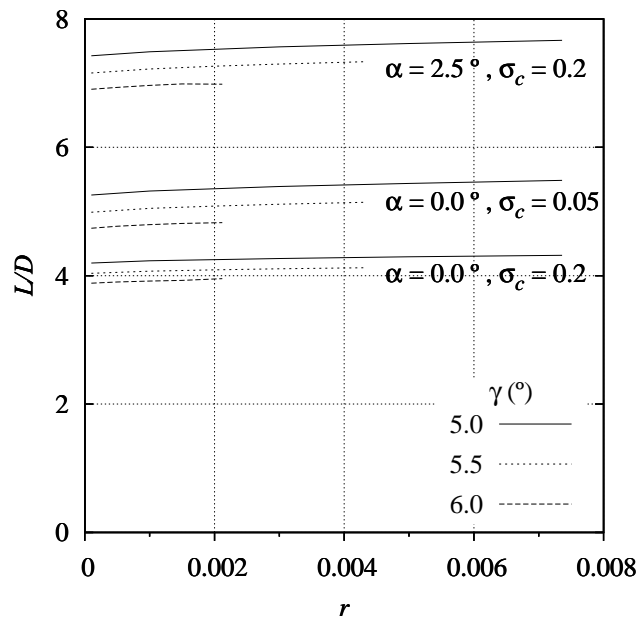


Figure 4.25: Hydrodynamic efficiency (L/D) versus r with γ a parameter ($t/c = 25\%$, $h/c = 1\%$ and two values of α).

The effect of σ_c , γ and t/c on L/D can be seen in Figures 4.26 and 4.27. The reduced length of some of the curves again reflects the range of valid cavities at those parameter values. Efficiency increases with a reduction in magnitude of any of these three parameters. An optimum foil efficiency would be achieved then with the minimum thickness and trailing edge slope operated at the lowest value of σ_c . There are however practical considerations, both structural and hydrodynamic, which will inhibit the realisation of this maximum efficiency. These limitations include the minimum foil thickness that can be practicably achieved due to minimum strength requirements and fabrication

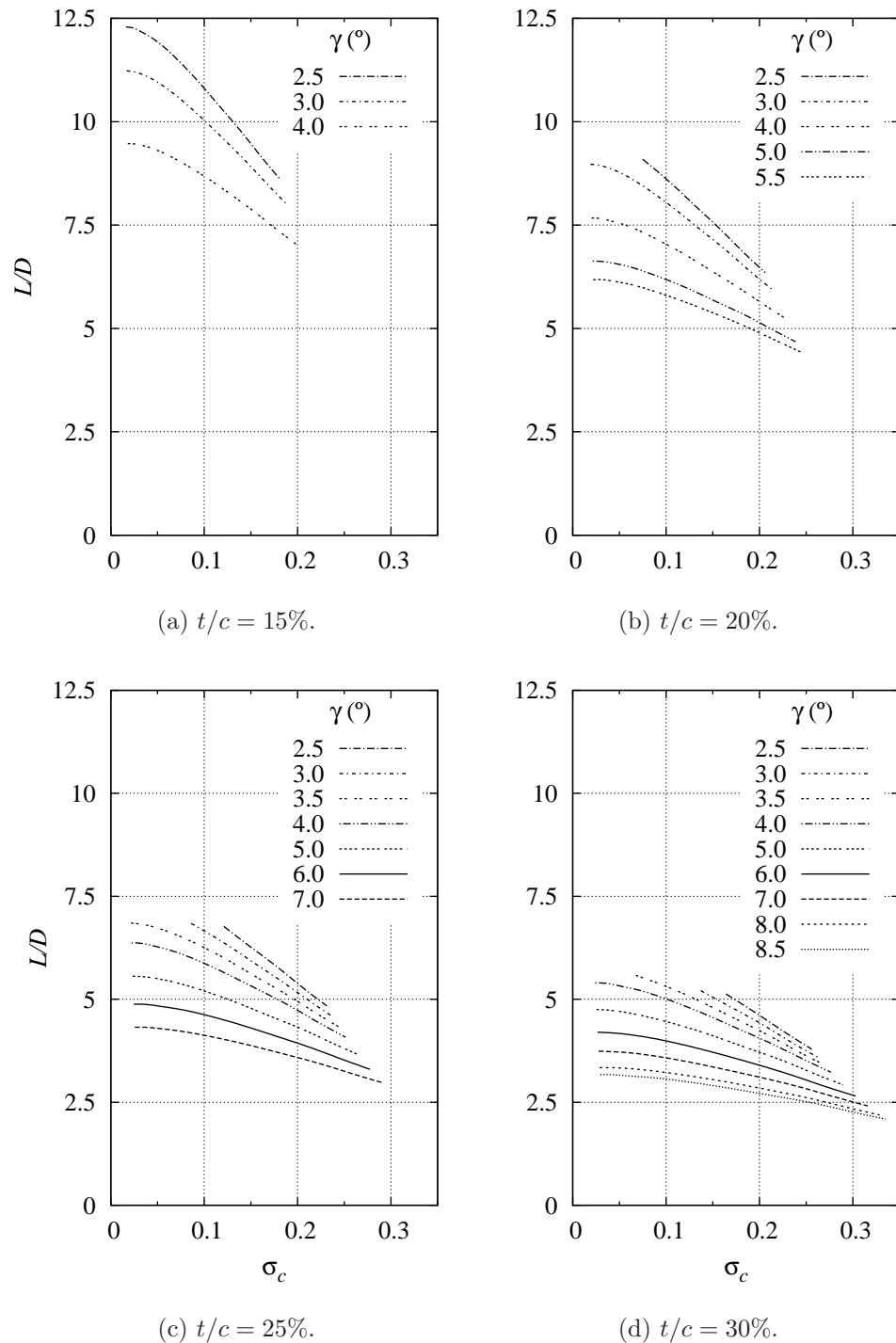


Figure 4.26: Hydrodynamic efficiency versus σ_c with γ a parameter ($h/c = 1\%$, $\alpha = 0^\circ$ and four values of t/c). The optimum L/D for each foil thickness and γ is obtained at the lowest σ_c . Note that the valid cavity shape limit reduces the L/D attainable for some of the smaller γ profiles at low σ_c . In general L/D increases with decreasing γ and σ_c , and also with decreasing t/c .

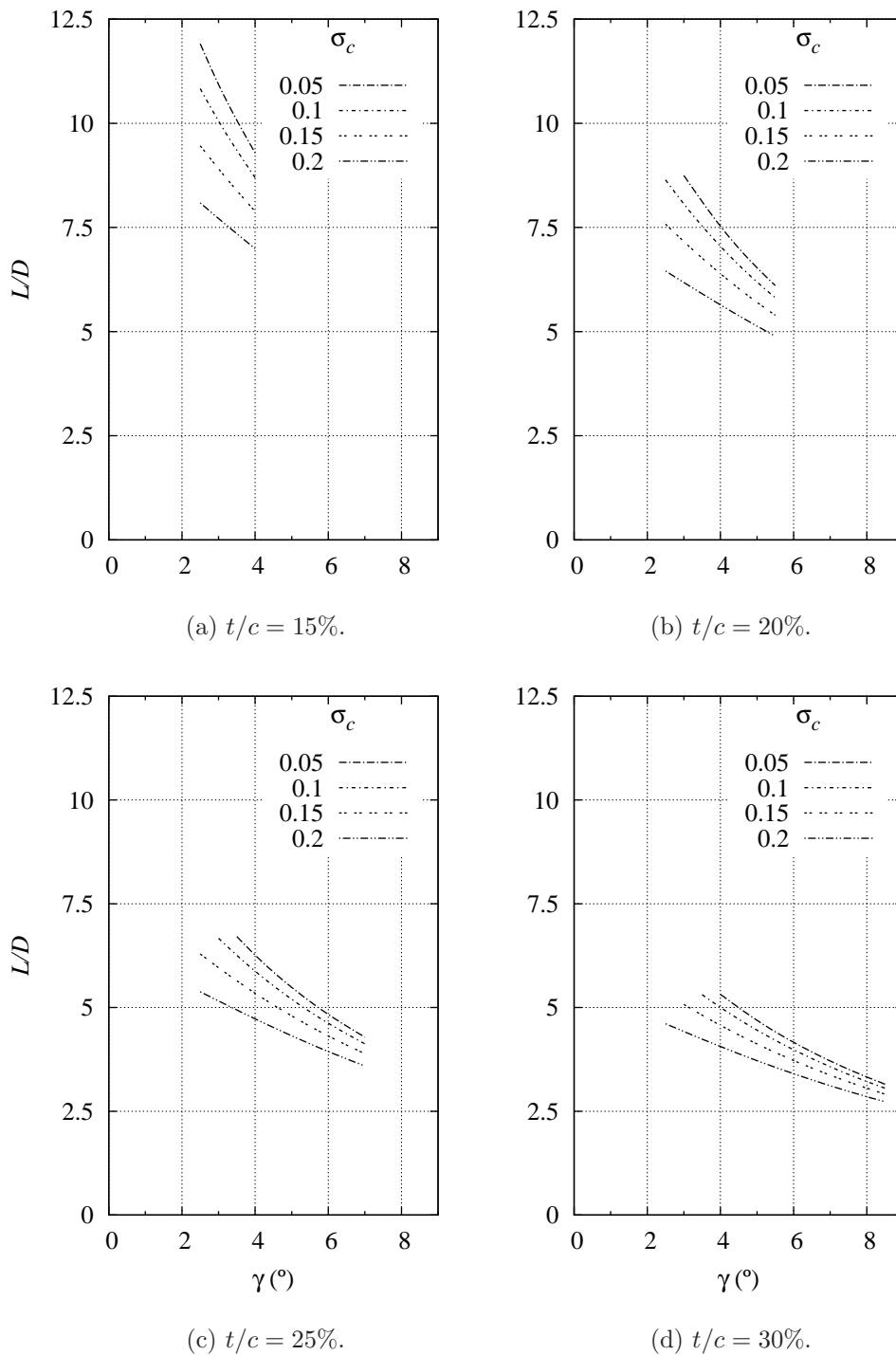


Figure 4.27: Cross-plots of hydrodynamic efficiency versus γ with σ_c a parameter ($h/c = 1\%$, $\alpha = 0^\circ$ and four values of t/c). The optimum L/D for each foil thickness and σ_c is obtained at low values of γ . Note that the valid cavity shape limit reduces the L/D attainable for small σ_c at the lower values of γ . L/D generally increases with decreasing γ and σ_c , and also with decreasing t/c .

issues. Hydrodynamically, the necessity of maintaining a stable cavity detachment from the suction side trailing edge and also the loss of performance due to partial cavitation forming on the foil itself will both need to be considered. For cambered foil sections with only one wetted surface, Pearce and Brandner (2007) obtained L/D values of 15 for small α and low σ_c . The maximum L/D for the wedge-shaped fully wetted foils in the present study is slightly less being ≈ 12.5 for the thinnest section. An experimental study on ventilated finite-span wedge-shaped supercavitating foils by Verron and Michel (1984), gives L/D values of $3 \rightarrow 6$, at small α , $t/c = 25 - 30\%$ and $\sigma_c \ll 1$. For these parameter values the present study gives comparable L/D values as shown in Figure 4.26(c) and (d).

Typically L/D of a lifting surface operating in single phase flow is found to increase with α up to a maximum and thereafter falls off with further increase in incidence (Abbott and von Doenhoff, 1959). An increase in L/D for all α is shown in Figure 4.28, but this may be due to the limited range of α covered with the maximum value not being reached. This data is for the same foil ($t/c = 25\%$) as in Figure 4.27c with additional data for $\gamma = 4, 5$ and 6° profiles (up to $\alpha = 2.5^\circ$ in 0.5° increments). This range of γ was analysed as it corresponds to the region of maximum leading edge $-C_{p_{min}}$, as depicted in Figure 4.20. A typical plot of L/D versus α , for four values of σ_c , is given in Figure 4.29. The relationship is linear for all σ_c over the range of α examined, with the slope $d(L/D)/d\alpha$ increasing slightly with decrease in σ_c .

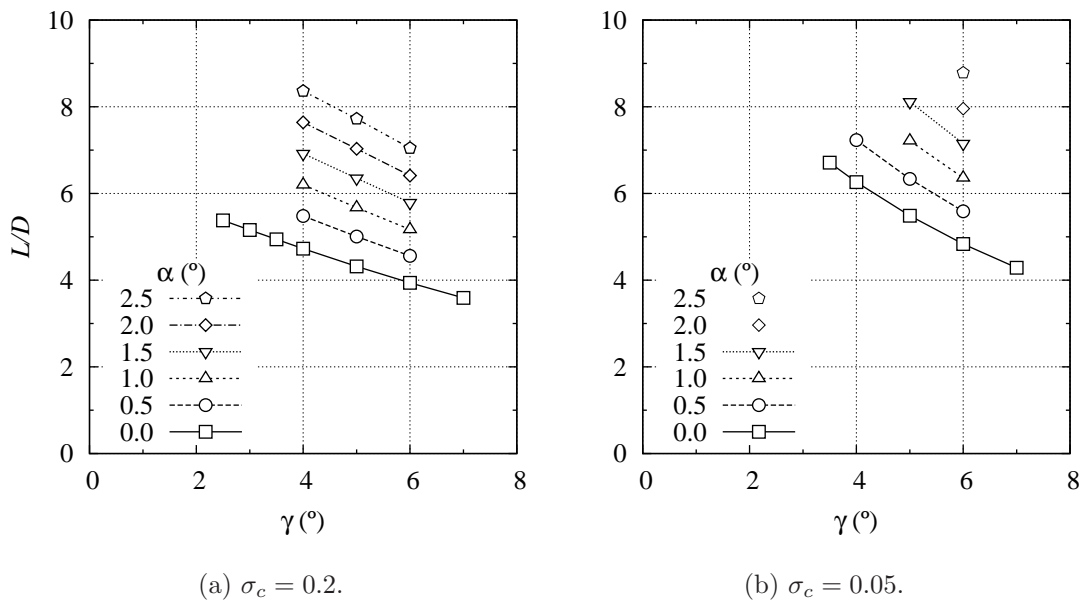


Figure 4.28: Cross-plots of hydrodynamic efficiency, L/D , versus γ with curves of constant α for large and small σ_c ($t/c = 25\%$ and $h/c = 1\%$).

The separate lift and drag curves can be examined to assess the respective influences of these quantities on efficiency. Figure 4.30 gives a typical data set with the three hydrodynamic coefficients and L/D plotted against σ_c for a foil

with $t/c = 25\%$. The complete data set is included in Appendix C for reference. From Figure 4.30a the lift is seen to be only mildly dependent to change in cavity pressure, with a slight drop off in the lift generated with decreasing σ_c . There is also an overall increase in C_L with a decrease in γ across the full range of σ_c . In contrast the drag (Figure 4.30b) falls significantly with an increase in the relative cavity pressure (σ_c reducing) and also decreases with reducing γ . A reduction in drag as σ_c is lowered is to be expected from the foil geometry due to the blunt base. This results from the cavity pressure acting over the end face or base of the foil section producing a drag force component opposite in sign to that due to the wetted surface area. Consequently as the cavity pressure increases, a net reduction in the drag on the foil follows. The principal method of obtaining increased hydrodynamic efficiency of a particular foil profile is therefore by drag reduction from lowering σ_c .

The changes in pressure distribution over the foil as σ_c reduces (see Figure 4.16) combine slightly to reduce the lift generated, but this is more than offset by the net drag reduction giving an overall increase in L/D as σ_c reduces. The effect on C_M (Figure 4.30c) due to the change in the foil pressure distribution is significant, with the centre of pressure moving towards the foil trailing edge as σ_c increases. The minimum C_M also corresponds to the optimum L/D , occurring at the minimum value of σ_c for each profile shape.

For increasing fence height the hydrodynamic coefficient curves remain similar but are offset as h/c is increased. Figure 4.31 gives a typical example for a foil with $\gamma = 5^\circ$ and $t/c = 25\%$. Additional results for other foil profiles are included in Appendix C. The decrease in C_L for high and low values of σ_c becomes more pronounced (see Figure 4.31a) and the slope of the C_D curves increase (Figure 4.31b) as h/c increases. The relative increase in C_D is greater than that in the C_L , as L/D initially rises until $h/c = 5\%$ and then decreases over the majority of the range of σ_c (approximately < 0.35) for the example given in Figure 4.30d. C_M decreases with increase in h/c , with the centre of pressure moving forward of the mid-chord and the sign reversing for low values of σ_c at $h/c = 10\%$ (Figure 4.31c).

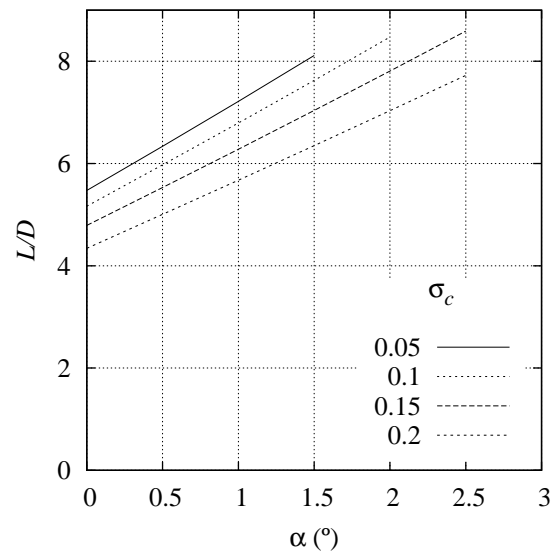


Figure 4.29: Hydrodynamic efficiency versus α with σ_c a parameter. (for $t/c = 25\%$, $h/c = 1\%$ and $\gamma = 5^\circ$). The data show a linear relationship between L/D and α with a slight increase in the slope as σ_c is reduced. Data for the two smallest σ_c values are clipped at high α because of invalid cavity shapes at those incidences.

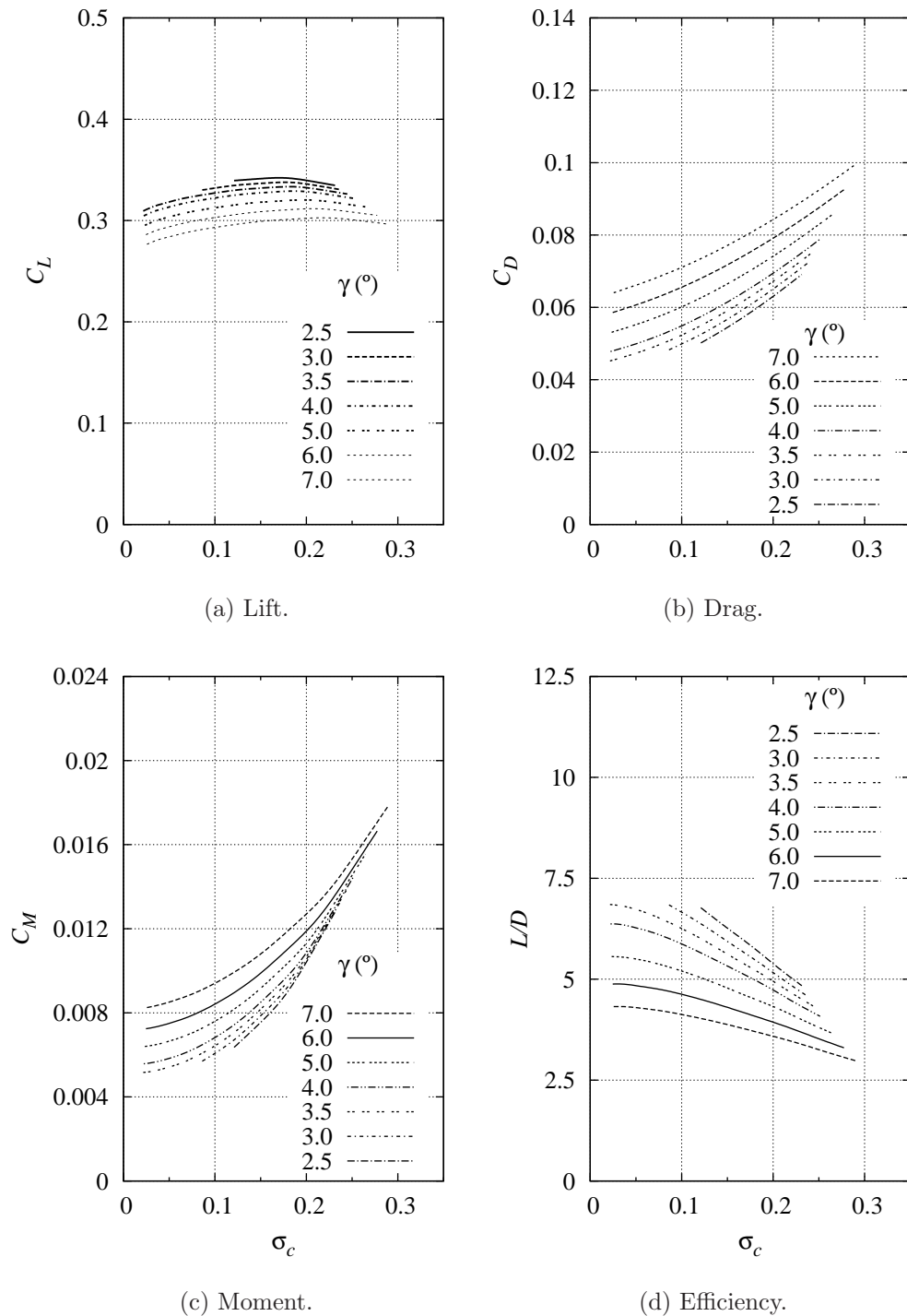


Figure 4.30: Hydrodynamic coefficients versus σ_c with γ a parameter ($t/c = 25\%$, $h/c = 1\%$ and $\alpha = 0^\circ$). Lift is only mildly dependent on σ_c with the main influence on the variation in L/D being the drop in C_D with the increase in cavity pressure (i.e. with reducing σ_c). The moment changes significantly with σ_c tending to an asymptotic limit for large σ_c .

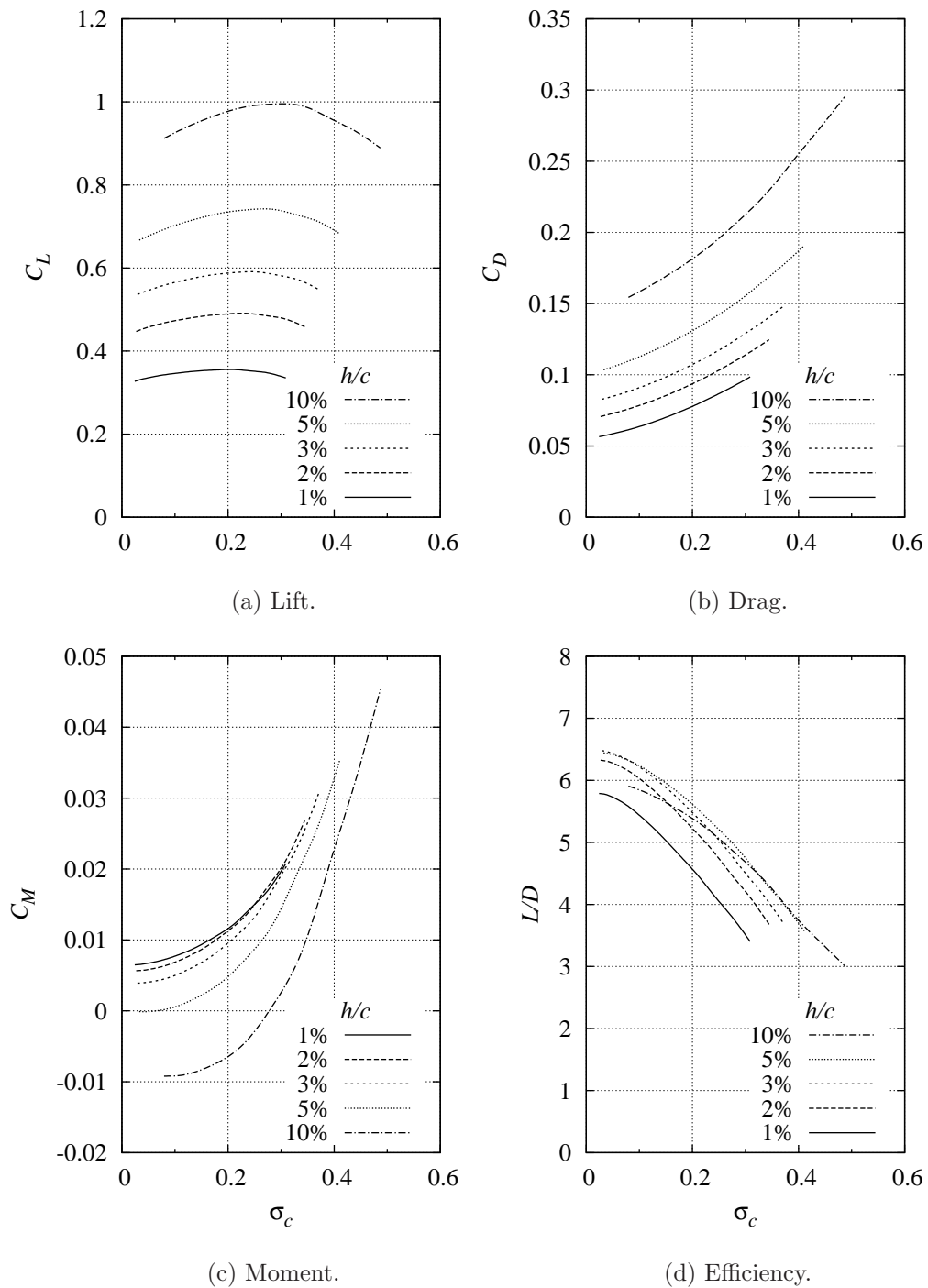


Figure 4.31: Hydrodynamic coefficients versus σ_c with h/c a parameter ($\gamma = 5^\circ$, $t/c = 25\%$ and $\alpha = 0^\circ$). The dependence of lift on σ_c becomes more pronounced as h/c increases. The relative increase of drag compared to lift is greater for small σ_c , as can be seen from the L/D data with the 10% foil values falling below those for the 2, 3, and 5% foils. The moment curves falls, and eventually changes sign for low σ_c as the centre of pressure moves towards the trailing edge with increase in h/c .

The sensitivity of L/D to the trailing edge step shape is shown in Figure 4.32. The step shapes analysed again relate to the fence and ramp as illustrated in Figure 4.1. The ramp results show a small constant reduction in L/D over the full range of σ_c . This fall in L/D is due mainly to the reduced lift, as a consequence of the reduced pressure difference between the foil surfaces, as shown in Figure 4.18.

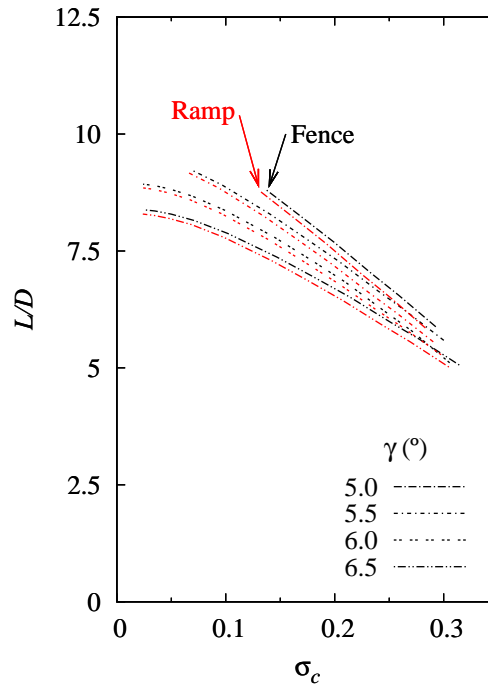


Figure 4.32: Comparison of hydrodynamic efficiency versus σ_c for fence and ramp step shapes, with γ a parameter ($t/c = 25\%$, $h/c = 1\%$, $h/l_r = 25\%$, $\alpha = 0^\circ$ and $\beta = 90^\circ$ - fence, $\beta = 60^\circ$ - ramp). A slight decrease in L/D between the two step shapes corresponding to the reduction in pressure over the foil wetted surfaces as shown in Figure 4.18.

4.7 Conclusions

The preceding analysis has considered how the variation in geometric parameters (see, Section 4.2) affect the hydrodynamic performance of the chosen foil profile. Given that the foil must produce positive or negative lift at a nominal incidence of $\alpha = 0^\circ$ (with a tolerance of $\approx 2.5^\circ$ allowing for vessel motion in waves), the optimum ideal performance is obtained by:

- a thin section, i.e. a low t/c , with the maximum allowable leading edge radius, r_{max} , to maintain a monotonic profile; and
- a small slope at the foil trailing edge, i.e. small γ .

The minimum achievable section thickness will be limited, based on structural requirements and the trade-off against an acceptable leading edge $C_{p_{min}}$ (relative to the free stream cavitation number, σ_v), to provide a reasonable margin against leading edge vapour cavities occurring.

The minimum achievable γ will be determined by the value required to maintain cavity detachment at the trailing edge (i.e. to ensure the foil suction surface remains wetted), with again some reasonable margin considering incidence excursions in a seaway.

Figure 4.33² gives a graphical overview of the interrelationship between the various hydrodynamic characteristics; flow features; and foil geometry, as discussed above. The main features being:

- L/D increases with decreasing γ , and with decreasing t/c
- the lowest leading edge suction peak values occur at intermediate values of γ as indicated
- the most favourable suction side pressure gradient leading up to the trailing edge is gained at maximum γ for a particular t/c , from which it follows that;
- there is a lower limit to γ , dependent on t/c , above which cavity detachment at the foil suction side trailing edge for all σ_c is ensured (valid cavity limit).

A comparison of these ideal flow predictions with future experimental data, may likely reveal that corrections need to be applied to account for real fluid effects. As an example, in a real flow the cavity detachment position might remain at the suction side trailing edge at a lower value of γ than predicted, due to the effect of surface tension and/or the presence of the boundary layer over the foil surface.

To directly compare the intercepted foil performance with conventional foils used for ride control would require estimates of total drag and/or experimental data. However, it should be noted that the present intercepted foil is intended to provide steady control forces at high-speed operation, avoiding the partial cavitating conditions as can occur with conventional ride control foils.

²A repeat of Figure 4.5 with additional annotation.

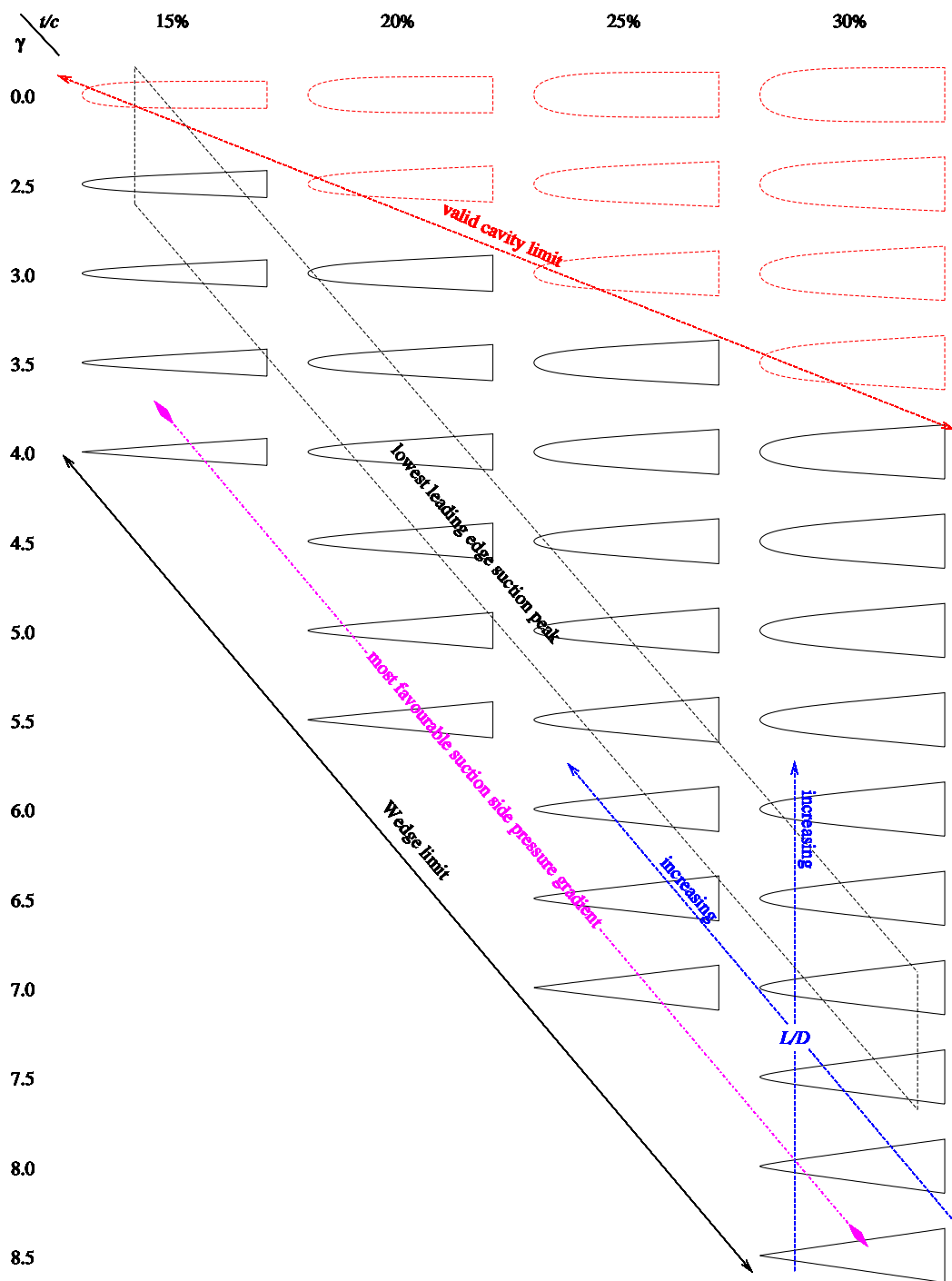


Figure 4.33: Parameter space of geometrically valid foil profiles of practical interest with annotated regions indicating particular hydrodynamic and flow features.

Chapter 5

Blockage Analysis of Supercavitating Foil Flow

5.1 Introduction

The flow conditions in a wind or water tunnel are not the same as those in an infinite domain. The presence of lateral flow boundaries a finite distance from a body produce a number of effects commonly categorized as wall effects. The terms interference, boundary and blockage are also used. Various analytical and numerical methods have been developed to correct the tunnel results to account for these wall effects. For a general overview of wall effects in single phase flow, and the correction methods employed, see Pankhurst and Holder (1952, Ch. 8) and Barlow et al. (1999, Ch. 9).

One of the first significant findings from confined fully-developed cavity flow theory was that there is a limit to the minimum cavitation number achievable (Birkhoff et al., 1950, 1952), termed a blocked or choked cavitation number. This choked cavitation number is denoted here by σ_{ch} . Figure 5.1 shows a sketch of a flat-plate foil at some incidence to the free stream, where the flow has reached the choked condition. At some position, indicated by ‘s’, each of the cavity surfaces become parallel with the confining walls and in an infinite channel they would also extend downstream to infinity. As the flow is parallel in this region, the flow velocity is uniform between the cavity surface and confining wall and from Bernoulli is equal to $U_c = U_\infty \sqrt{1 + \sigma}$ (Equation 2.26).

For an experiment in a cavitation tunnel with a fixed working section height, i.e. a fixed wall separation distance D , the cavity then becomes ‘infinitely’ long, extending parallel into the downstream diffuser, when σ_c reduces to σ_{ch} . For a fixed tunnel pressure p_∞ , and cavity pressure p_c , this implies an upper limit to the tunnel velocity at the choked state. Upon trying to increase the tunnel velocity further, the tunnel pressure will rise to compensate for the increase in velocity, maintaining σ_c constant and equal to σ_{ch} . This phenomenon is analogous to the choked flow that can occur in compressible flow through nozzles (White, 2010, Ch.9).

The ongoing development of theoretical approaches to analysing wall effects

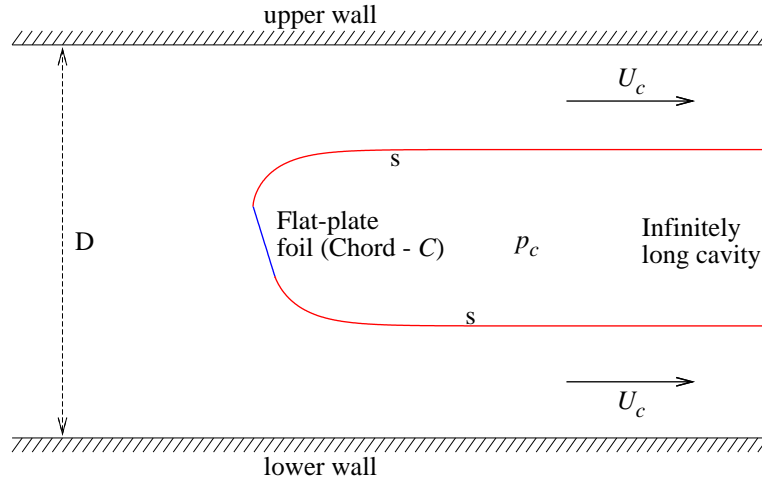


Figure 5.1: Sketch of a supercavitating flat-plate foil between confining walls, shown in the choked flow condition.

on lifting fully-developed cavity flows has been predominantly focussed on the analysis of 2-D choked flows involving simple body shapes, i.e. flat-plate foil sections. A review of progress made by the mid-1960s was authored by Morgan (1966) and again a decade on by Baker (1977). Since the review by Baker only one article, by Hsu (1984), has been published in the open literature concerning further theoretical analysis on the subject. This work covered bodies with finite cavity lengths, and was based on linearised cavity theory (Tulin, 1953) with additional simple second-order non-linear corrections. Again, only results for wedges and flat-plate foils were included. Simple correction rules were developed by Wu et al. (1971) for the correction of 2-D wedge drag data. The correction involved two steps: first the calculation of a corrected or effective cavitation number, σ'_c , for the unconfined flow; then the calculation of the unconfined drag coefficient using σ'_c , the confined C_D , and the blockage ratio b/D (where b is the wedge maximum thickness and D is the wall separation). Equations for the σ'_c , obtained using the minimum coefficient of pressure on the tunnel wall, C'_{pw} , and the subsequent corrected C_D are given by Brennen (1995, Eq. 8.17 and Eq. 8.18):

$$\sigma'_c = \sigma_c + \frac{2C'_{pw}(2 - \sigma_c)}{3(1 - C'_{pw})} \quad (5.1)$$

$$C_D(\sigma'_c, 0) = \frac{1 + \sigma'_c}{1 + \sigma_c} C_D \left(\sigma_c, \frac{b}{D} \right) + O \left(\frac{b^2}{D^2} \right) \quad (5.2)$$

No similar correction rules have been published for confined lift and drag data for the cavitating lifting foil case.

Within the field of aerodynamics, the development of boundary element (panel) methods for the analysis of inviscid flow over arbitrary body geometries

in an infinite domain, were extended to include the flow over a body positioned between confining walls. These methods could then be used to supplement, or provide an alternative to the analytically based methods for assessing wind tunnel interference effects (Ojha and Shevare, 1985; Barlow et al., 1999; Katz and Plotkin, 2001). Following this trend, with the application of boundary element methods to the analysis of hydrodynamic flows, confined flow methods were also developed (Kinnas and Mazel, 1993; Choi and Kinnas, 1998) to numerically model these flows in a water tunnel.

An alternate version of the present boundary element method (BEM) has been implemented, as described in Section 2.3.2, with the addition of confining walls. Using this method, a study of the effect of flow confinement on the supercavitating flow over a flat-plate foil is presented in the following section. These results are compared with the non-linear analytical methods of Wu (1962) and Ai and Harrison (1965) (see also Ai, 1966) for the choked flow condition. Additional results are presented for an intercepted foil, modelled to represent a physical model positioned in the AMC CRL cavitation tunnel¹.

All data presented in this chapter are for foils, with their mid-chord point located mid-way between confining walls separated by a distance D . The results are presented in terms of D/C , where the wall separation distance is non-dimensionalised by the foil chord C or c . C is the chord length of a flat-plate foil and c for an intercepted foil.

5.2 Results: Flat-Plate Foil

To gain a general overview of the effect of confining walls on a cavitating lifting body, the flow over the simplest foil shape, i.e. a flat-plate, was analysed over the complete range of incidence and a large range of wall separation to chord ratios. Data are presented for the following values of these parameters:

- Incidence: $\alpha = 5^\circ, 15^\circ$ and then in steps of 15° to 90°
- Wall separation to chord ratio: $D/C = 5, 10, 20, 40, 100$ and ∞ .

A similar analytical study of flat-plate supercavitating foils by Ai and Harrison (1965) covers the same range of incidence, but a narrower range of wall separation values ($3 \leq D/C \leq 20$). Comparison of the present method with these analytical results is made in the following sections.

5.2.1 Cavity Shape

The presence of confining walls results in an increased cavity length for a particular value of σ_c . A typical example, for $\alpha = 30^\circ$, is shown in Figure 5.2a, with the complete data set for all of the incidence values examined included in Appendix D. The ‘choked flow line’ indicated on Figure 5.2a is the locus of the points on each D/C curve where the minimum cavitation number limit,

¹See Appendix B for a description of the future companion experimental program.

σ_{ch} , is reached. After this point, each curve extends vertically upwards. A family of curves for the range of incidence at the most blocked case (e.g. the right-hand side curve in Figure 5.2a, are shown in Figure 5.2b. Generally, σ_{ch} increases with decreasing D/C (i.e. increasing blockage), and increasing α for a constant D/C , as can be seen from Figure 5.2b. As with the infinite flow data presented in Chapter 4, the maximum σ_c value for each curve corresponds to $l_c/C = 2$, and the minimum σ_c value to $l_c/c = 500$.

From the results for the foil at $\alpha = 90^\circ$ shown in Figure 5.3, i.e. the most extreme case with the plate normal to the flow, it can be seen that there is a minimum wall separation below which the associated σ_{ch} value is higher than the maximum σ_c for the unbounded flow case. In such cases, the cavities formed at those values of σ_c in the confined flow would not be present in the same range of σ_c in the infinite flow. It then follows, as with the correction rules for the pure drag case, that the confined data would need to be corrected in two stages: first a corrected cavitation number is calculated; and then using this value and the blocked coefficients, the corrected C_L and C_D values are obtained. In the absence of simple correction rules for the lifting case, the confined flow numerical data from the present method can be used to directly compare with data obtained from (closed jet) cavitation tunnel experiments.

From the full data set (Appendix D) the following is apparent. For $\alpha = 90^\circ, 75^\circ, 60^\circ$ and $D/C = 5$, σ_{ch} is greater than the unbounded flow maximum σ_c . The data for $\alpha < 60^\circ$ then shows only a partial overlap between the $D/C = 5$ and ∞ curves. The partial overlap is also present with the $\alpha = 90^\circ$, $D/C = 10$ data, the overlapping portion increasing with decreasing α . In the overlap region a cavity would be present at the same σ_c in an infinite flow, but at a reduced length. Where the blocked curve does not overlap with the infinite case, a cavity would not be present in the equivalent infinite flow, as in the non-overlapping case discussed above. The general effect of flow confinement on the cavity length~cavitation number relation then, is to offset the curve both vertically upwards and horizontally to the right from the unconfined data.

Figure 5.4 shows the effect of reducing the blockage ratio for a constant length cavity. This is the plot of cavity shapes where a horizontal line at $l_c/C = 32$ intersects each of the curves in Figure 5.2a. As D/C decreases from ∞ the cavity shape progressively flattens, eventually becoming horizontal over the middle portion when the choked flow condition is reached. For the $\alpha = 30^\circ$ and $l_c/C = 32$ example shown the blockage ratios of 5 and 10 both show the choked flow condition.

If instead the constant D/C case is considered, i.e cases along one curve in Figure 5.2a, then the cavity shape behaviour with increase in cavity length is shown in Figure 5.5. In this case the choked flow limit, σ_{ch} , is shown to correspond to the upper and lower cavity surfaces each obtaining some limiting maximum thickness. Increasing the length of cavity further then has no effect on either the cavity thickness or the cavity pressure.

A further case to consider is that of a vertical line on Figure 5.2a, i.e. the constant cavitation number case. Of particular interest is a value of σ_c

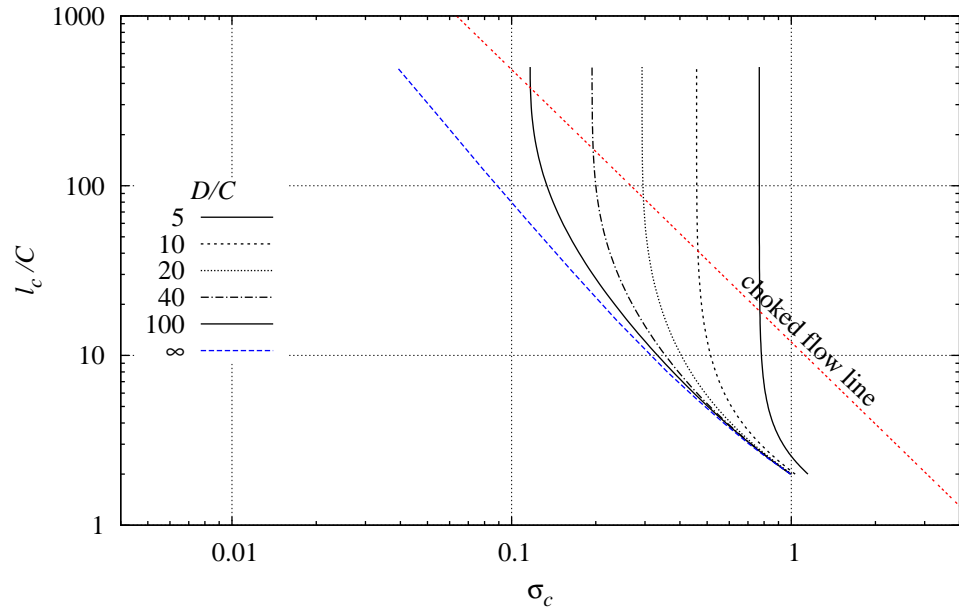
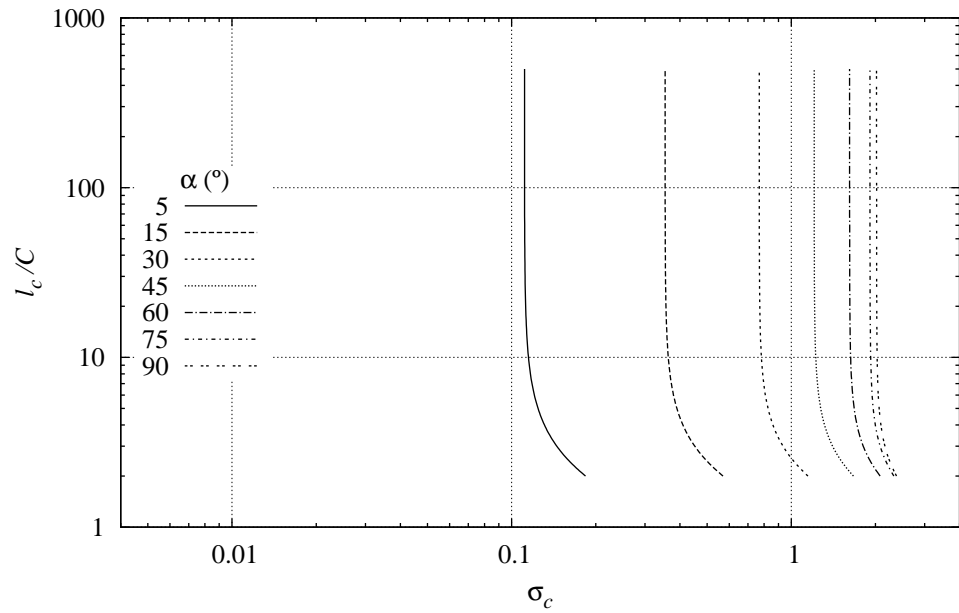
(a) $\alpha = 30^\circ$ (b) $D/C = 5$

Figure 5.2: Dimensionless cavity length versus σ_c : (a) $\alpha = 30^\circ$ with D/C a parameter; (b) $D/C = 5$ with α a parameter.

corresponding to a choked case, and Figure 5.6 gives the cavity shapes corresponding to $\sigma_c = 0.293$ which is σ_{ch} for the $\alpha = 30^\circ$, $D/C = 20$ case. This example compares the extremes of an infinite flow and one subject to the maximum influence of its confining walls, with some intermediate cases showing the transition between the two. As the wall separation is reduced, the changes in cavity shape are shown to be relatively modest until the minimum wall separation is reached where a choked condition results. This behaviour is a general trend, as can be seen from Figure 5.2a and for the other incidence cases included in Appendix D. Also of interest in Figure 5.6 is that the position of the cavity surfaces just after detachment from the foil edges remains invariant with change in wall separation, for σ_c constant.

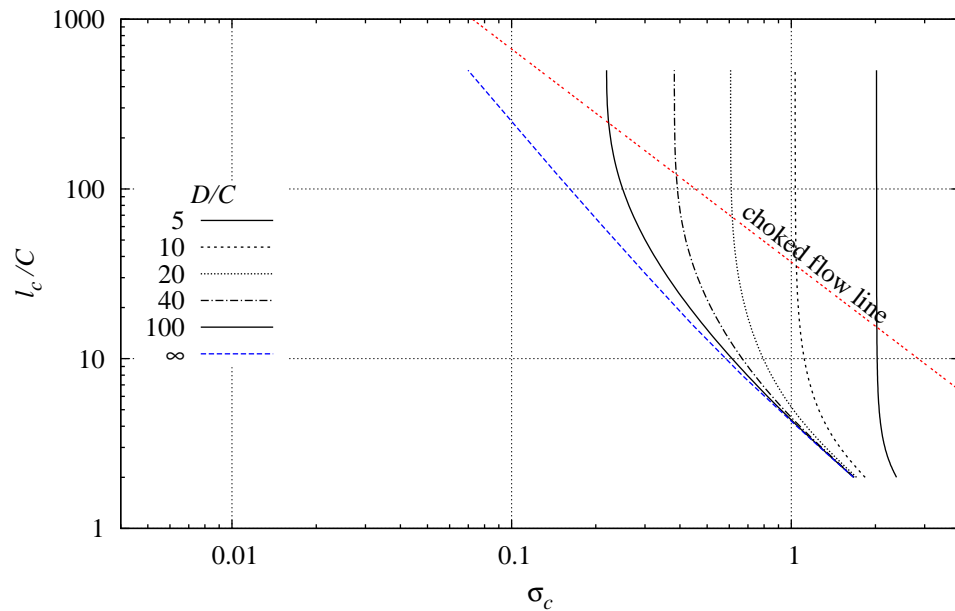


Figure 5.3: Dimensionless cavity length versus σ_c , $\alpha = 90^\circ$ with D/C a parameter.

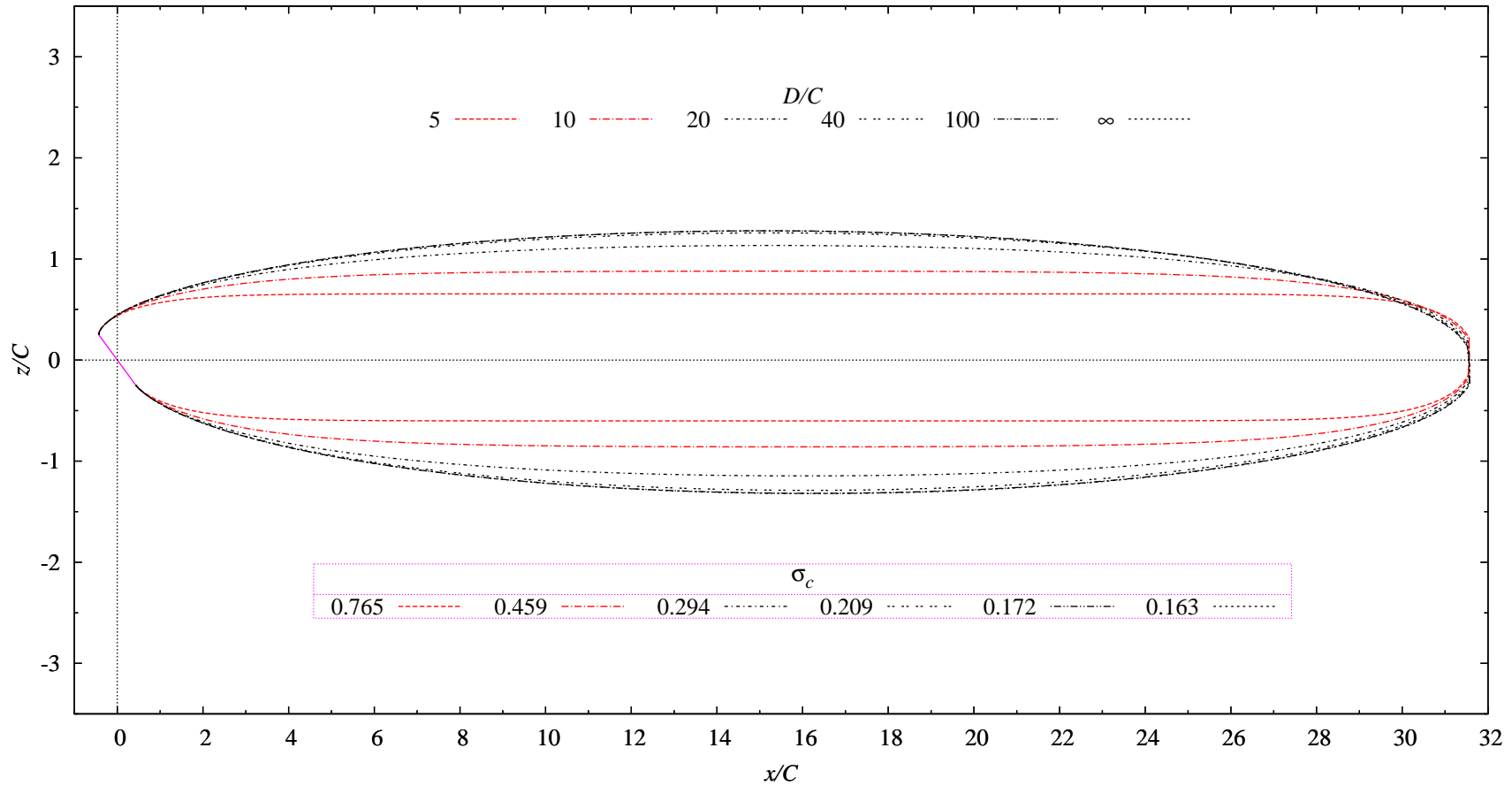


Figure 5.4: Predicted supercavity shapes for a flat-plate foil, $\alpha = 30^\circ$ and $l_c/C = 32$, with D/C a parameter. The σ_c value corresponding to each D/C value is indicated. The curves shown in red indicate choked flow conditions.

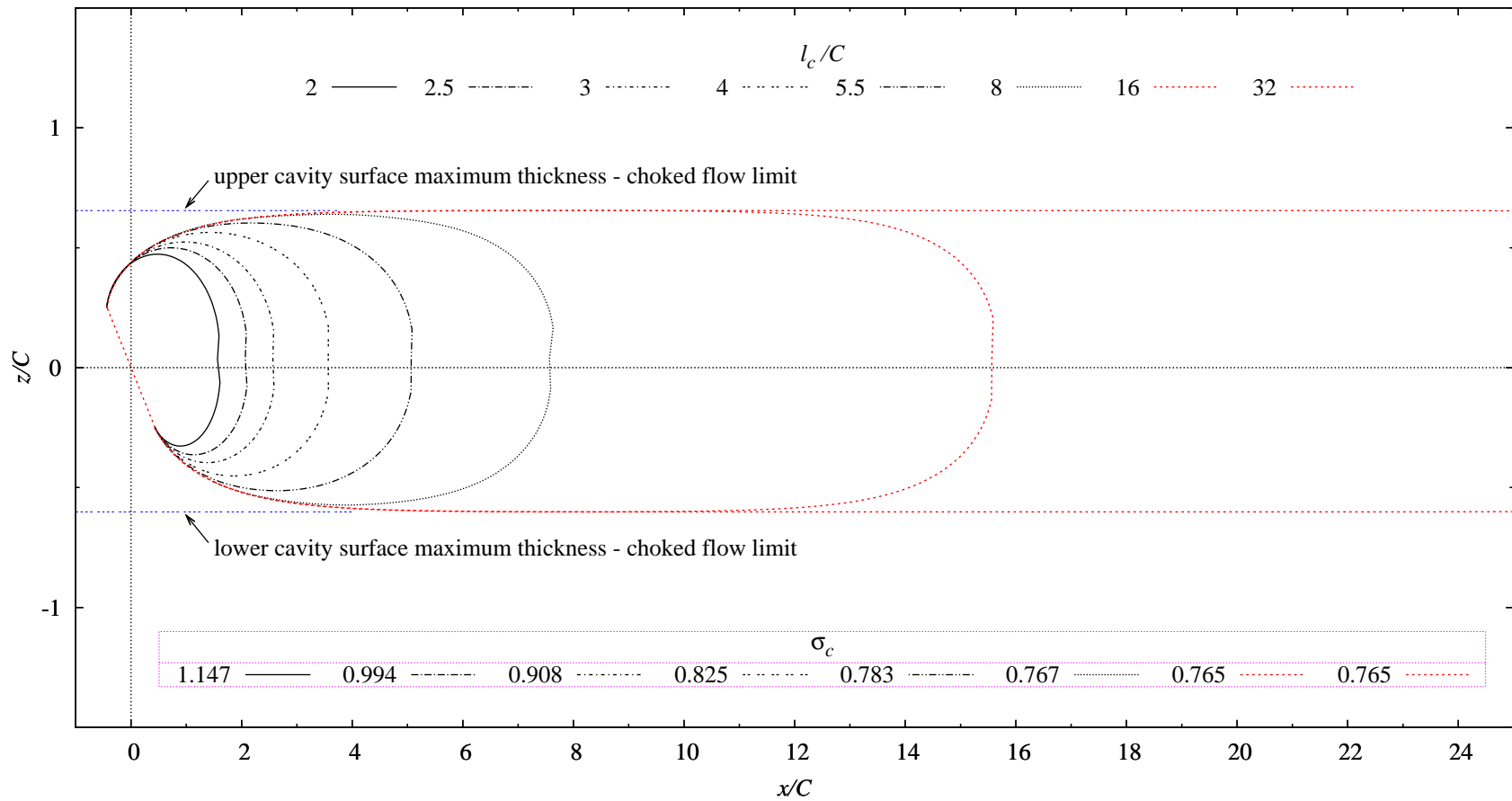


Figure 5.5: Predicted supercavity shapes for a flat-plate foil, $\alpha = 30^\circ$ and $D/C = 5$, with l_c/C a parameter. The σ_c value corresponding to each l_c/C value is indicated. The curves shown in red indicate choked flow conditions. The maximum cavity thickness, i.e. that obtained in choked flow limit, is also indicated.

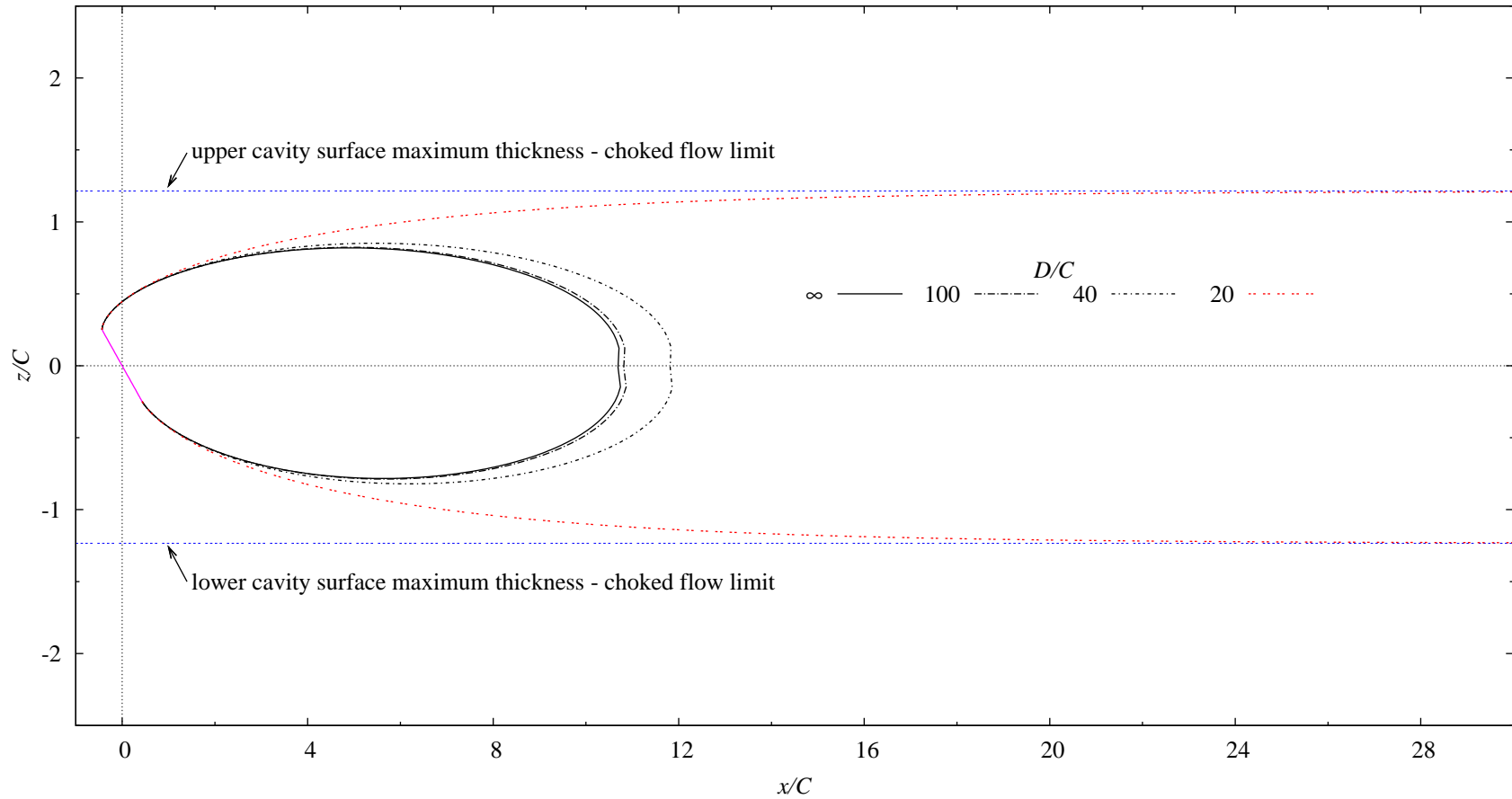


Figure 5.6: Predicted supercavity shapes for a flat-plate foil, $\alpha = 30^\circ$ and $\sigma_c = 0.293$, with D/C a parameter. The curve shown in red indicates a choked flow condition. The maximum cavity thickness, i.e. that obtained in choked flow limit, is also indicated. In this case, i.e. for $\alpha = 30^\circ$ and $\sigma_c = 0.293$, the flow reaches the choked limit at $D/C = 20$ with $\sigma_{ch} = 0.293$.

5.2.2 Pressure Distributions

Figure 5.7 shows a typical example ($\alpha = 30^\circ$ and $D/C = 5$) of the wall pressure distributions for the confined flow over a flat-plate supercavitating foil. These are the matching wall pressure distributions for the cavity shapes shown in Figure 5.5. The choked flow limit is reached when the minimum wall C_p decreases to $-\sigma_{ch}$. Upon further increase in cavity length after the choked limit has been reached, the pressure distribution in the region of the foil remains unchanged, whereas the length of wall subject to $C_p = -\sigma_{ch}$ increases. This shows that, upon choking, the flow downstream of the foil becomes one-dimensional with constant pressure and velocity equal to p_c and U_c respectively which are related from Bernoulli by Equation 2.26, $U_c = U_\infty \sqrt{1 + \sigma}$.

The wall pressure signature extends less than 10 chord lengths upstream of the foil leading edge and downstream of the cavity closure for all blockage ratios. The magnitude and extent of the zone of positive pressure on the lower wall, just upstream of the foil position, reduces with reduction in σ_c , converging to the value corresponding to the choked condition.

The case of constant σ_c with varying wall separation, i.e. the matching wall pressure distribution plots to the cavity shapes given in Figure 5.6 for $\alpha = 30^\circ$, is shown in Figure 5.8. At this incidence choking occurs at a wall separation of $20C$ with a corresponding $\sigma_{ch} = 0.293$. As wall separation is decreased: the wall pressure signature increases till the choked condition is reached; and the cavity length increases as shown in Figure 5.6. Comparison of the larger wall separation data of Figure 5.8 with the $D/C = 5$ data in Figure 5.7 shows that at larger D/C values the wall pressure distributions, though smaller in magnitude, decrease to zero over a much greater wall length.

The associated foil pressure distributions for the constant σ_c wall pressure data presented in Figure 5.8 are shown in Figure 5.9. A magnified view of the mid-chord region is given in Figure 5.9b to enable the detail to be seen more clearly. As wall spacing is decreased there is a small reduction in C_p over the greater part of the foil surface, whilst the pressure distribution near to the edges of the plate are unchanged. The latter effect is due to the pressure at cavity detachment being constant.

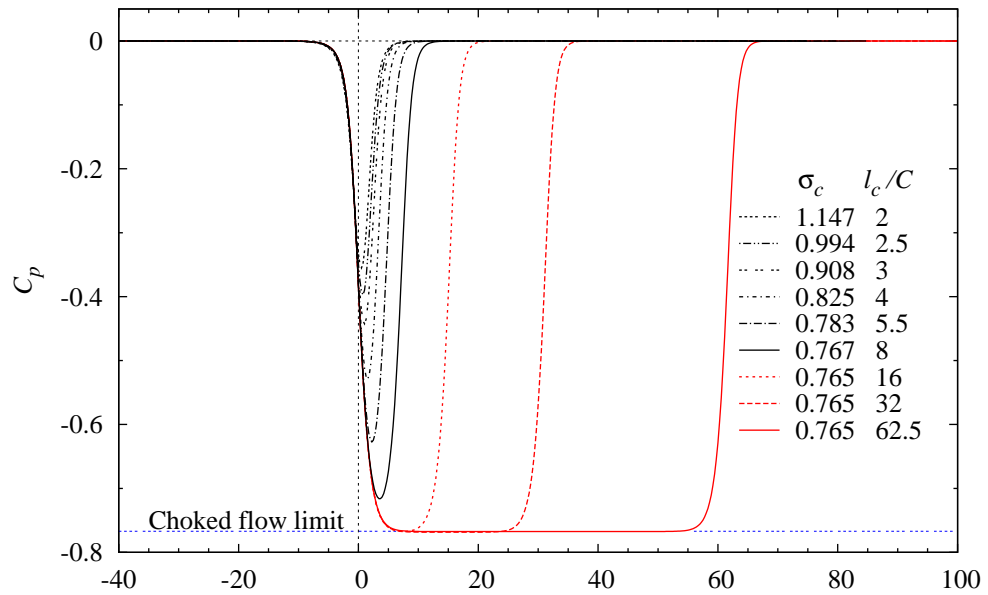
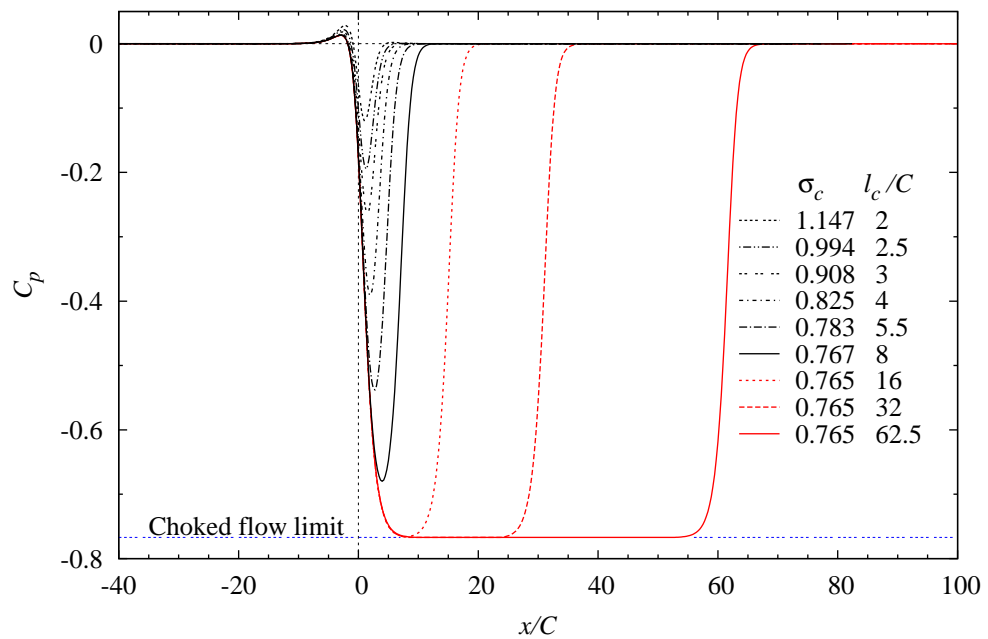
(a) C_p distribution on upper wall.(b) C_p distribution on lower wall.

Figure 5.7: Plots of C_p distribution on the upper and lower confining walls for a flat-plate supercavitating foil ($\alpha = 30^\circ$ and $D/C = 5$) with l_c/C a parameter. The choked flow limit is reached when $C_p = -\sigma_c = -\sigma_{ch}$. These are the matching pressure distributions for the cavity shapes shown in Figure 5.5.

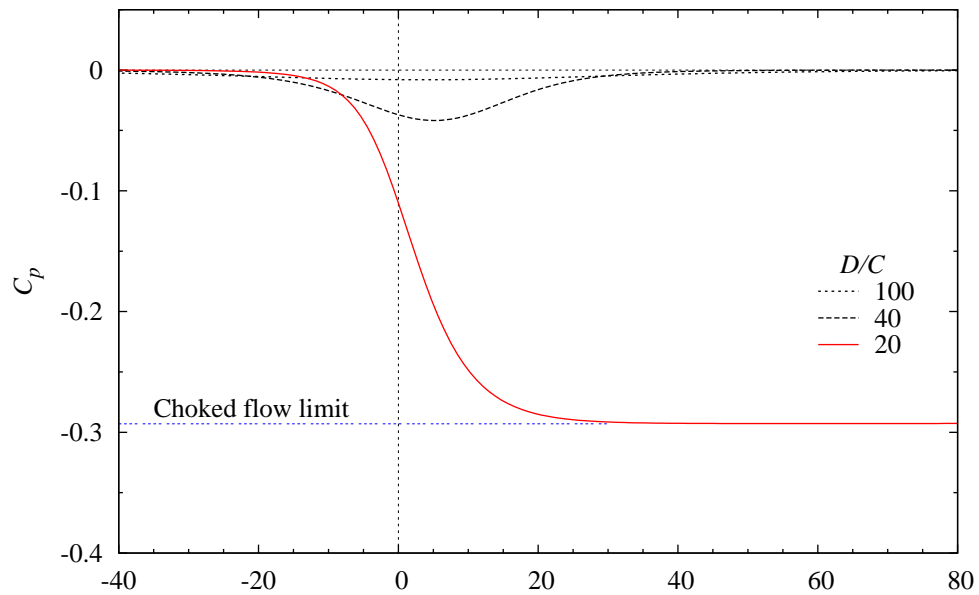
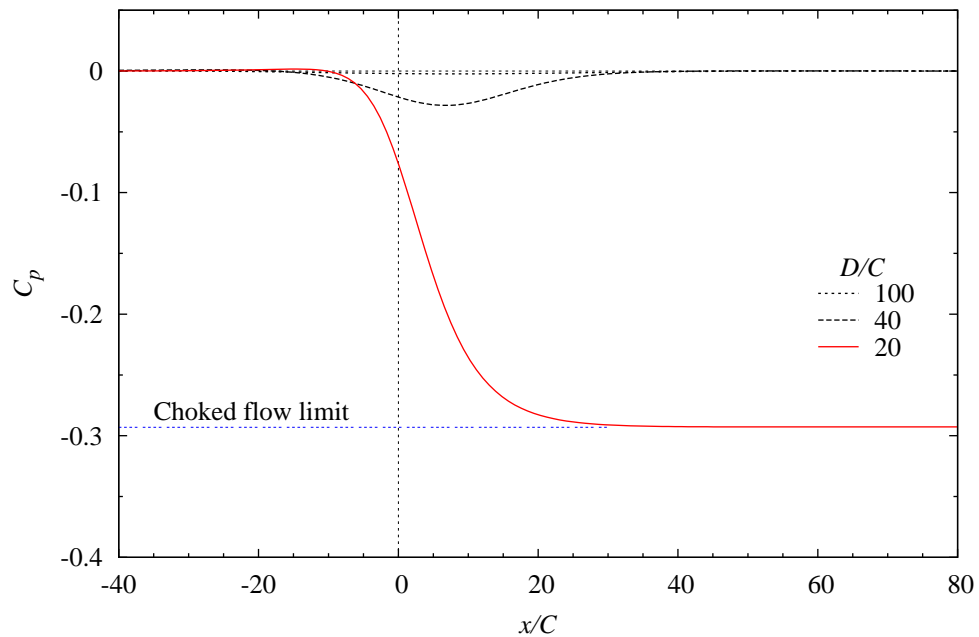
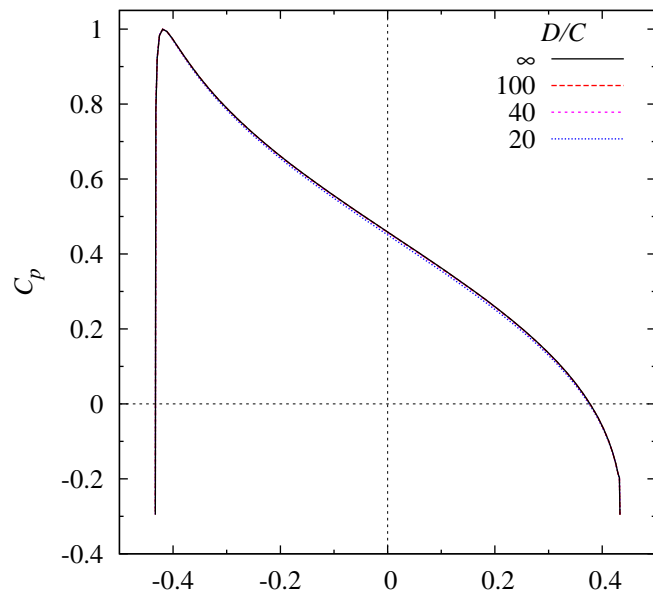
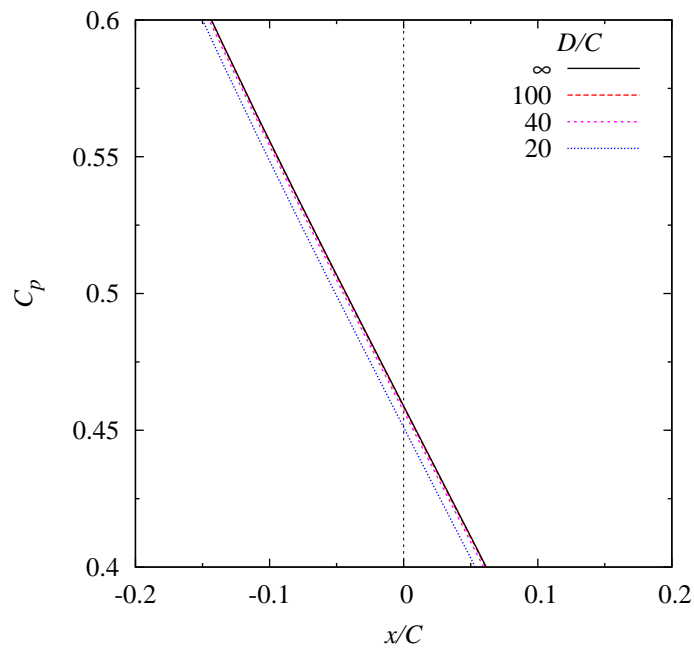
(a) C_p distribution on upper wall.(b) C_p distribution on lower wall.

Figure 5.8: Plots of C_p distribution on the upper and lower confining walls for a flat-plate supercavitating foil ($\alpha = 30^\circ$ and $\sigma_c = 0.293$) with D/C a parameter. The choked flow limit is reached at $D/C = 20$ with $C_p = -\sigma_c = -\sigma_{ch}$. These are the matching pressure distributions for the cavity shapes shown in Figure 5.6.

(a) C_p distribution on foil front face (wetted surface).

(b) Magnified view of (a).

Figure 5.9: Wetted surface C_p distribution of a flat-plate supercavitating foil ($\alpha = 30^\circ$ and $\sigma_c = 0.293$) with D/C a parameter. The choked flow limit is reached at $D/C = 20$ with $C_p = -\sigma_c = -\sigma_{ch}$. These are the matching pressure distributions for the cavity shapes shown in Figure 5.6. In (b) a magnified view of the foil mid-chord region is shown. Decreasing wall spacing results in a small reduction in C_p over the greater part of the foil surface.

5.2.3 Hydrodynamic Forces

Plots of confined flow C_L , C_D and C_M versus σ_c for $\alpha = 5^\circ$ and 75° are shown in Figures 5.10, 5.11 and 5.12 respectively. The two extremes of incidence², $\alpha = 5^\circ$ and 75° , are shown together for comparison. A summary plot of the full data set for each of the hydrodynamic coefficients is shown in Figures 5.13, 5.14 and 5.15. The complete data set of individual plots for all incidence values is included in Appendix D.

The reduction in C_L with decrease in wall separation is shown in the $\alpha = 5^\circ$ data (Figure 5.10a). The same trend is also present in the $\alpha = 75^\circ$ data (Figure 5.10b), though not as apparent due to the larger range of C_L covered at the higher incidence. The trend can be seen if the difference between $D/C = 10$ and ∞ curves is compared for the two incidence cases³. The difference between the data grows slightly with decrease in σ_c so a comparison made at minimum σ_c , i.e. σ_{ch} (the left most point on each D/C curve), will be the maximum difference at each incidence. So then, the maximum difference in C_L between the $D/C = 10$ value corresponding to σ_{ch} and the infinite flow value at the same cavitation number, i.e. the vertical offset between the two curves, is 4% for the 5° data and 6.5% for the 75° . The summary plot (Figure 5.13) shows the offset to the right of the confined flow curves from the infinite curves increasing with incidence, imposed on top of the global behaviour with lift increasing to a maximum ($\alpha \approx 45^\circ$) and then reducing again. The mean slope of the family of curves at each incidence, also decreases as α increases.

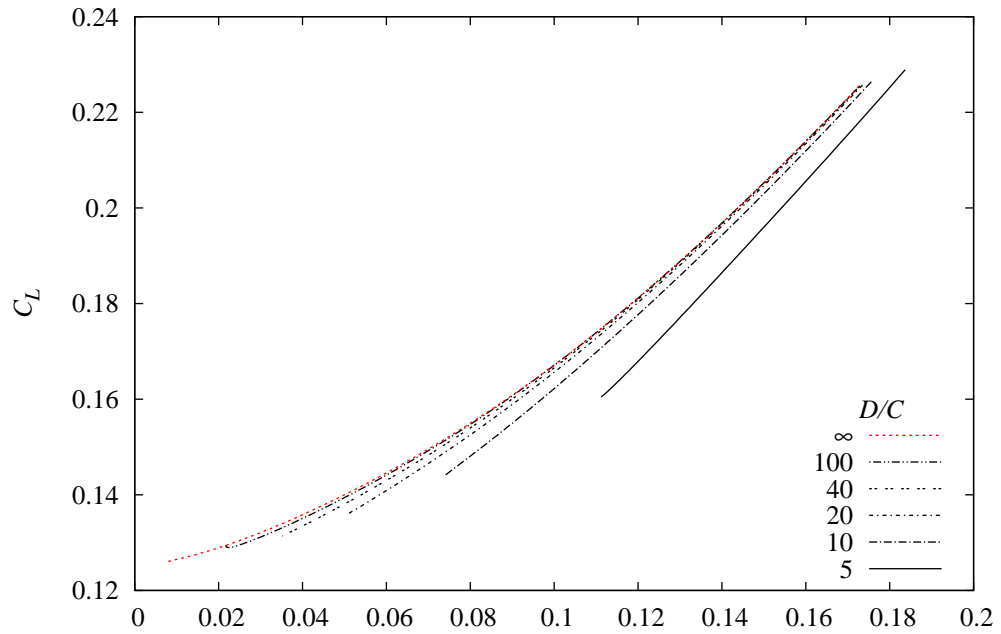
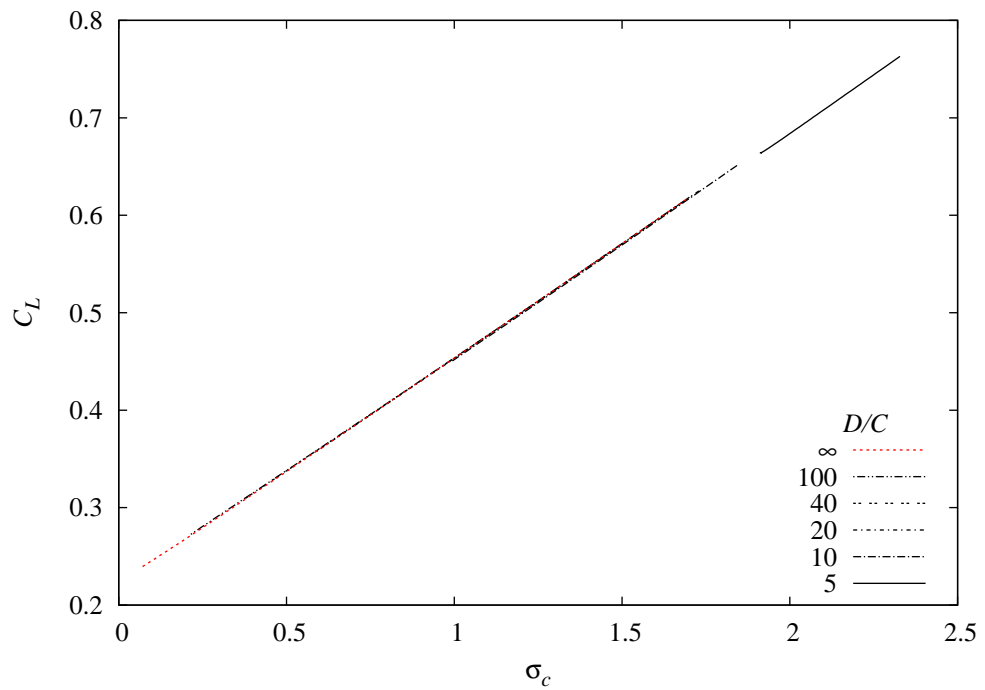
The drag data (Figure 5.11a) shows a similar trend as with the lift in that C_D reduces with decreased wall separation⁴. Globally (Figure 5.14) drag increases with incidence however, as the frontal area becomes increasingly greater. The mean slope of the family of drag curves at each incidence, increases with incidence. This is the opposite trend to the lift data. Efficiency data is of no interest for the flat plate case as it is a function of the incidence only ($L/D = \cot \alpha$).

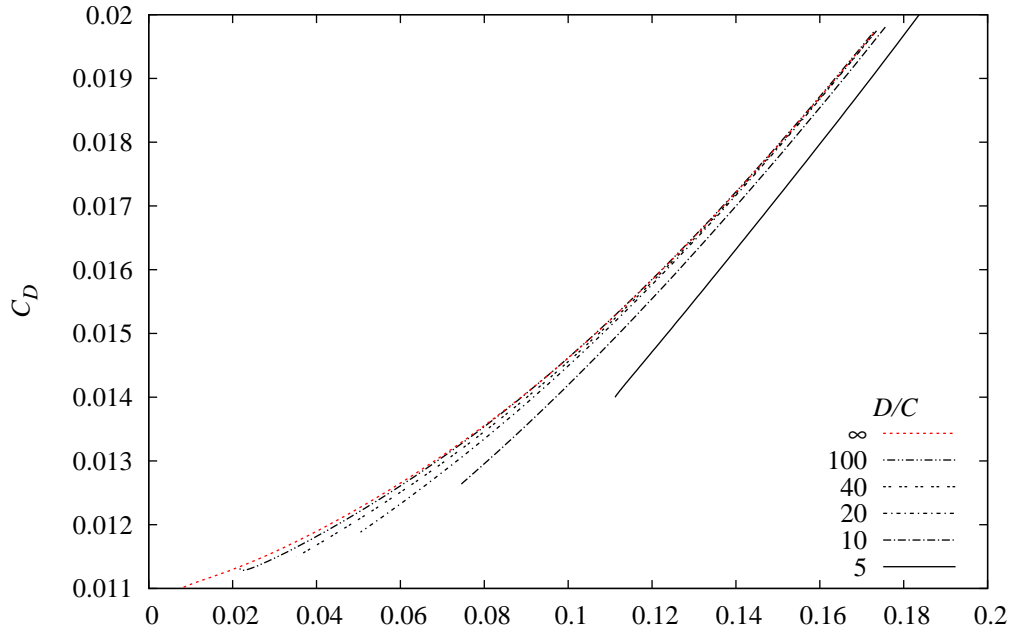
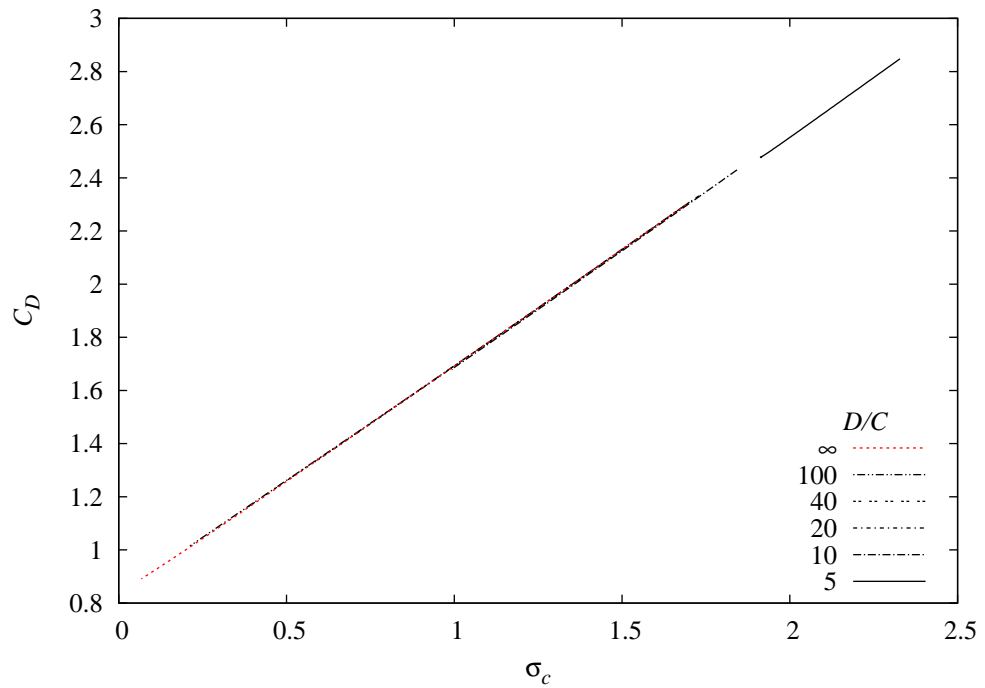
The moment data (Figure 5.12a) shows an increase in C_M with increasing confinement for $\alpha = 5^\circ$. For the $\alpha = 75^\circ$ data this trend reverses with a decrease in C_M with increasing confinement. From the summary plot of the moment data (Figure 5.15), the change in direction of the offset of the confined flow curves relative to the infinite flow curve occurs at approximately $\alpha = 15^\circ$.

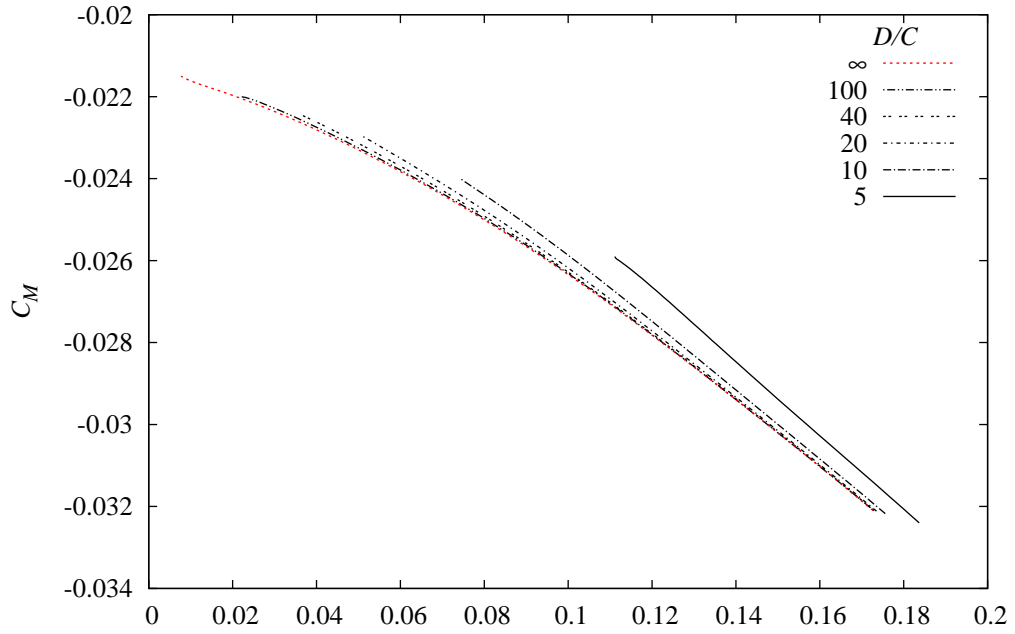
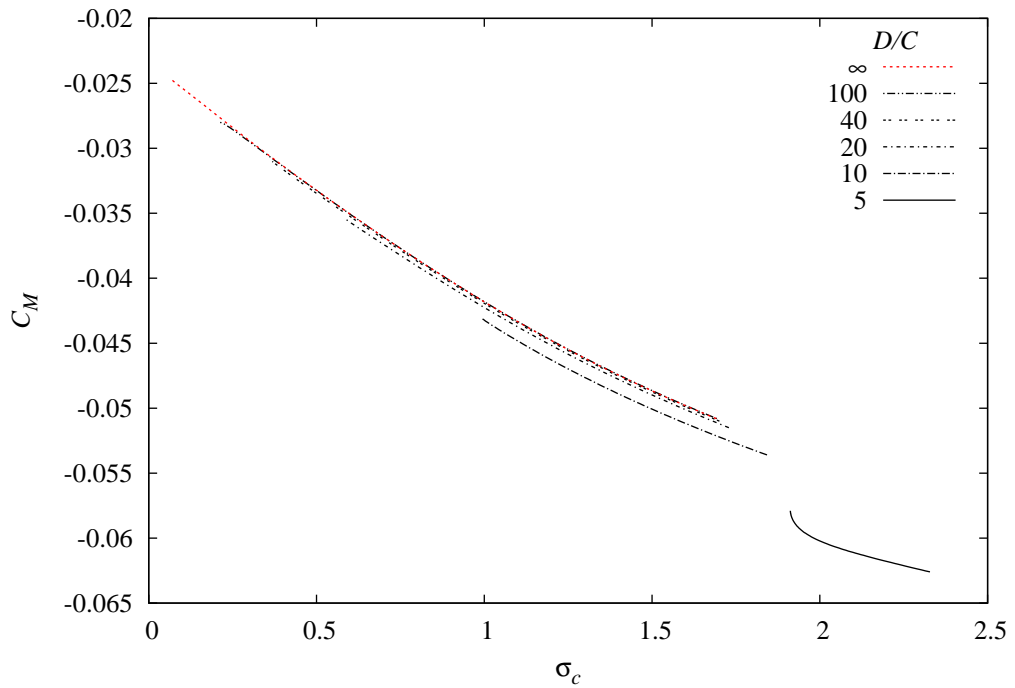
² $\alpha = 75^\circ$ is the highest incidence value which is relevant to all three coefficients. Only drag is applicable to the $\alpha = 90^\circ$ case as due to flow symmetry, both C_L and C_M are zero for this incidence.

³The $D/C = 10$ being the smallest wall separation where the data overlaps for the two incidence cases.

⁴Lift and drag are related via the incidence in the case of a flat plate ($C_D = C_L \tan \alpha$).

(a) $\alpha = 5^\circ$ (b) $\alpha = 75^\circ$ Figure 5.10: Confined C_L versus σ_c for $\alpha = 5^\circ$ and 75° with D/C a parameter.

(a) $\alpha = 5^\circ$ (b) $\alpha = 75^\circ$ Figure 5.11: Confined C_D versus σ_c for $\alpha = 5^\circ$ and 75° with D/C a parameter.

(a) $\alpha = 5^\circ$ (b) $\alpha = 75^\circ$ Figure 5.12: Confined C_M versus σ_c for $\alpha = 5^\circ$ and 75° with D/C a parameter.

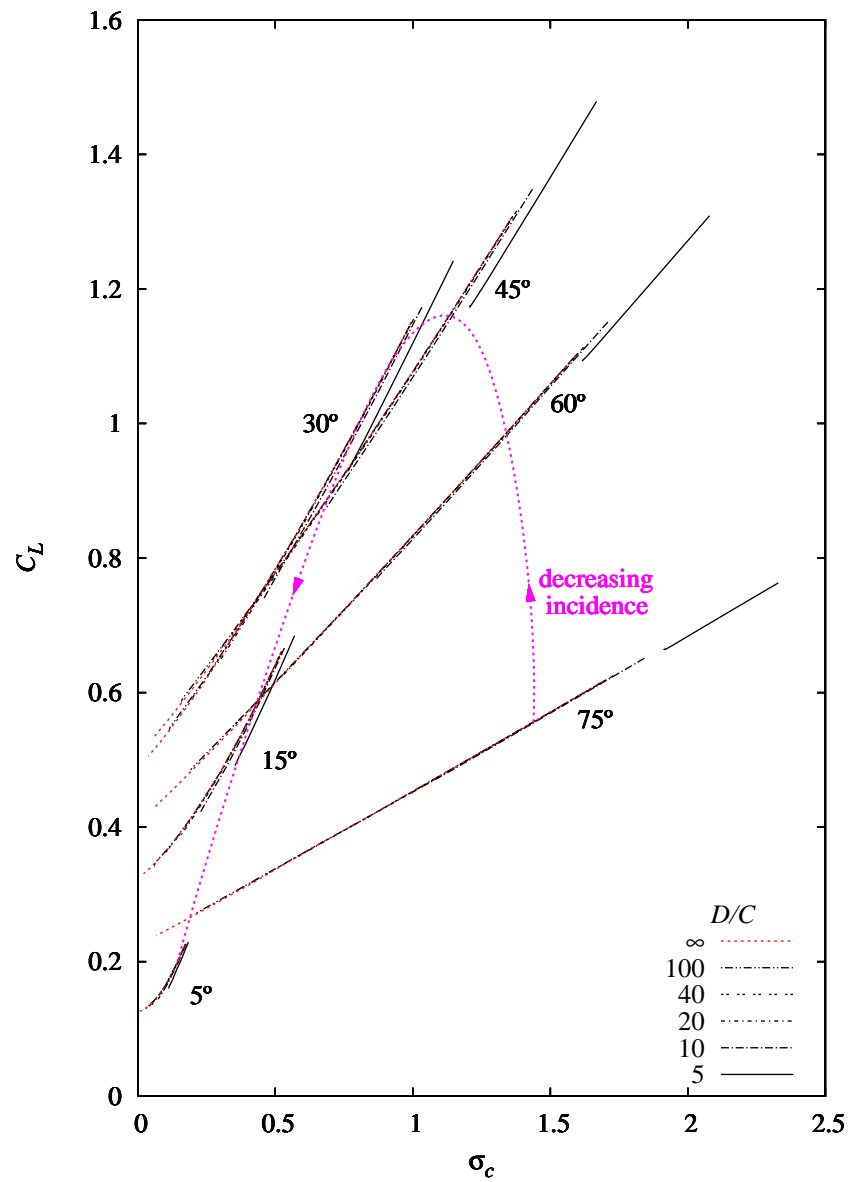


Figure 5.13: Confined C_L versus σ_c for $\alpha = 5, 15, 30, 45, 60$ and 75° with D/C a parameter.

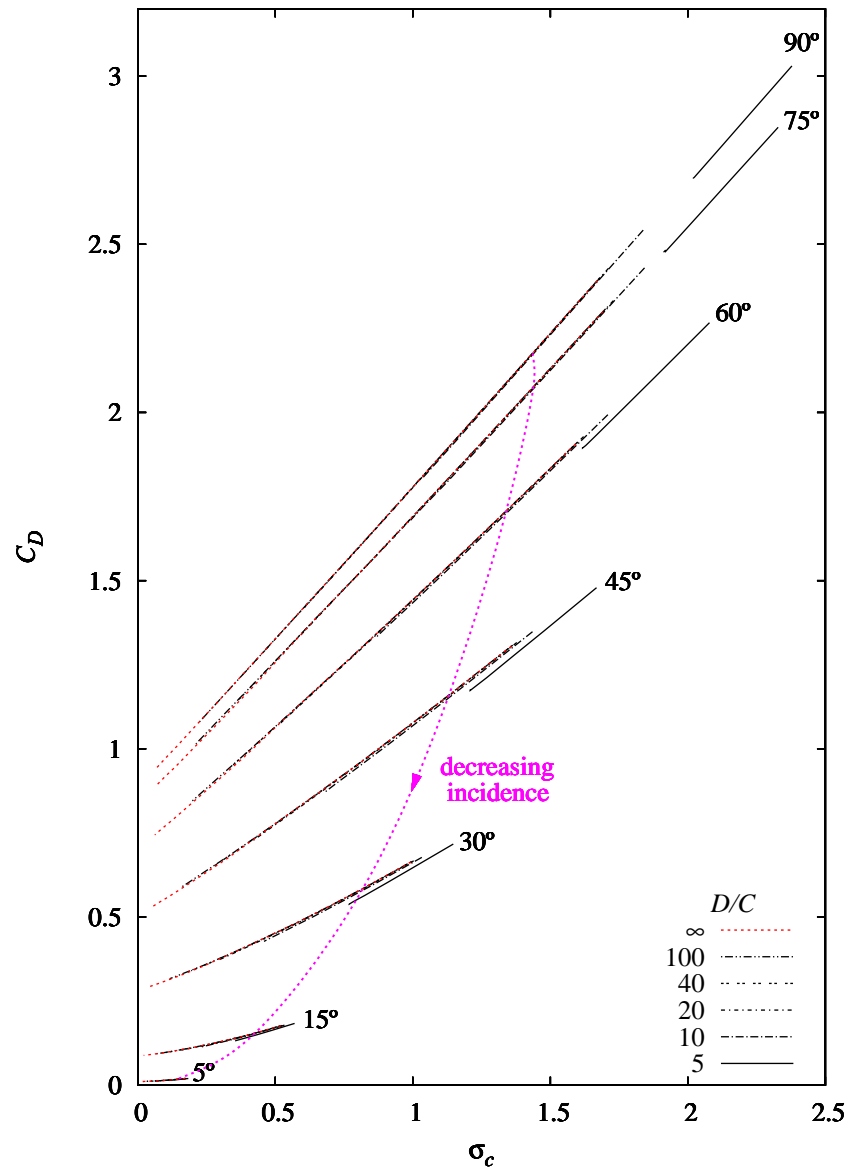


Figure 5.14: Confined C_D versus σ_c for $\alpha = 5, 15, 30, 45, 60$ and 75° with D/C a parameter.

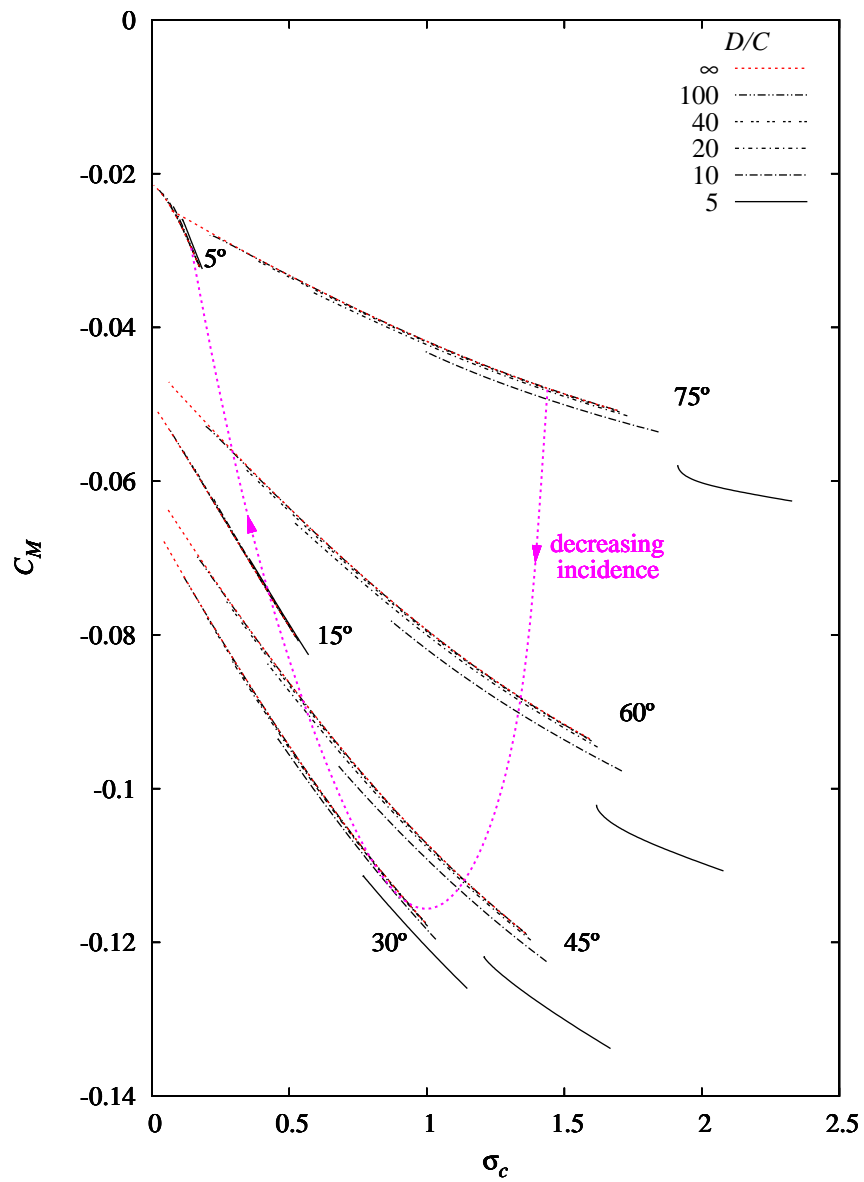


Figure 5.15: Confined C_M versus σ_c for $\alpha = 5, 15, 30, 45, 60$ and 75° with D/C a parameter.

5.2.4 Choked Flow

As can be seen from the results of the previous sections, the choked flow cavitation number, σ_{ch} , is a function of both the foil incidence and the wall separation. Figure 5.16 is a plot of σ_{ch} versus α for the five D/C values analysed. The red curves for $D/C = 5, 10$ and 20 , are derived from graphically presented results by Ai and Harrison (1965) based on non-linear analytical theory. There is good agreement between the BEM data and the non-linear theory at small to moderate values of incidence (up till approximately 45°). At higher incidence values the theoretical prediction underestimates σ_{ch} in comparison with the BEM results, the discrepancy increasing with decreasing wall separation.

In Figure 5.17 the same BEM data is presented but as σ_{ch} versus D/C with curves of constant alpha. The curves are power law curves of best fit, $\sigma_{ch} = A(D/C)^n$, through the data. The power law relation fits the data well except at high incidence. A maximum error of 10% is present at the extremities of the $\alpha = 90^\circ$ curve with the shape of the data points becoming slightly cupped upwards as incidence increases.

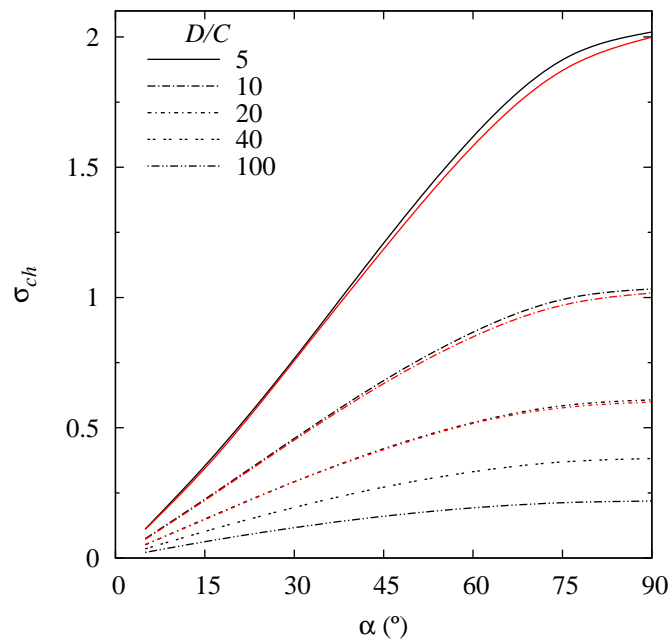
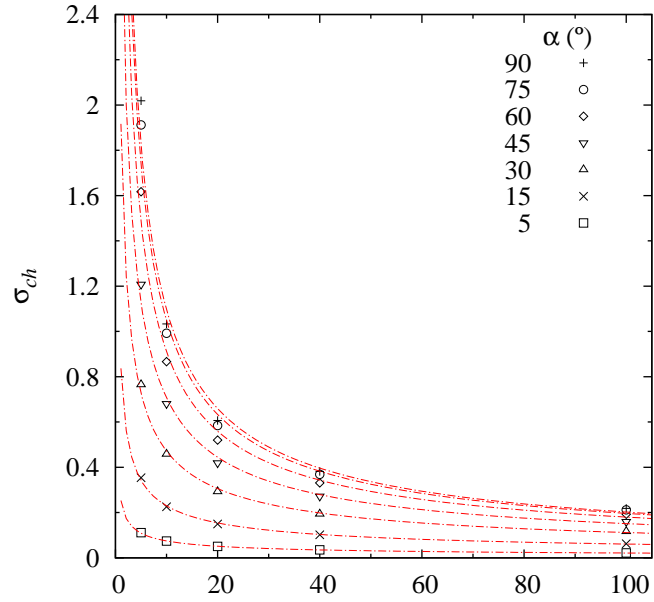
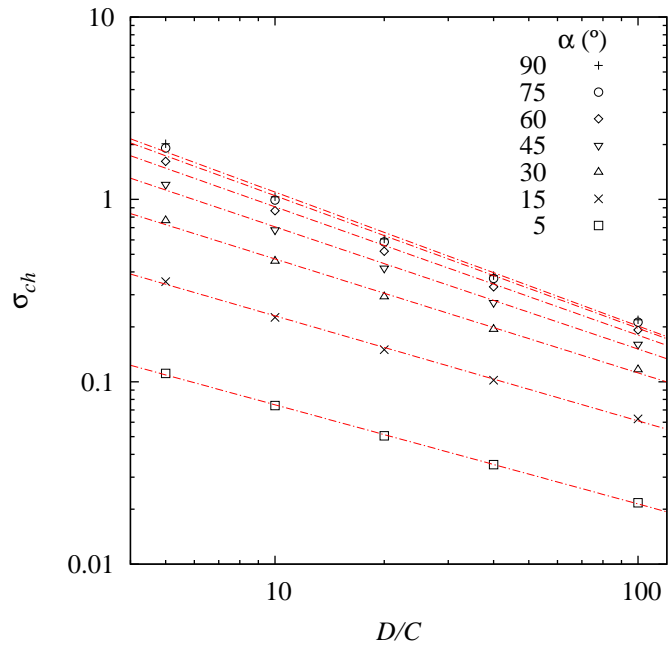


Figure 5.16: σ_{ch} versus α with D/C a parameter. Red curves are the non-linear theory predictions by Ai and Harrison (1965). (Theory data only presented in the reference for $D/C \leq 20$).

(a) σ_{ch} versus D/C .

(b) Log-log plot of (a).

Figure 5.17: Choked cavitation number versus wall separation with α a parameter. (b) is a log-log plot of the same data as presented in (a).

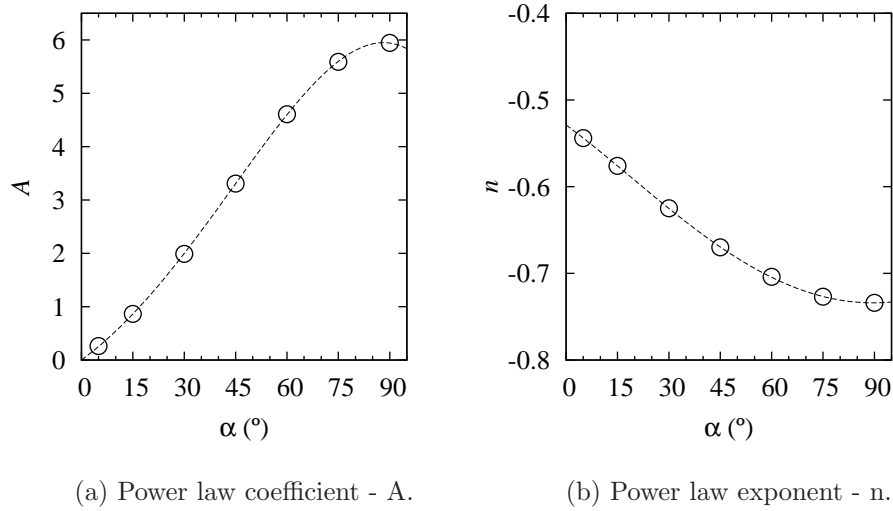


Figure 5.18: Polynomial curve fits through the coefficient, A , and exponent, n , values from the power law fit ($\sigma_{ch} = A(D/C)^n$) of the data in Figure 5.17b.

A plot of the coefficient, A , and exponent, n , from the fitted curves in Figure 5.17b, versus α is presented in Figure 5.18. A polynomial fit through both sets of points gives

$$A = -7.2182 \times 10^{-8} \alpha^4 + 1.5271 \times 10^{-6} \alpha^3 + 6.5135 \times 10^{-4} \alpha^2 + 4.7653 \times 10^{-2} \alpha \quad (5.3)$$

$$n = -1.2312 \times 10^{-9} \alpha^4 + 4.2643 \times 10^{-7} \alpha^3 - 2.1309 \times 10^{-5} \alpha^2 - 2.9185 \times 10^{-3} \alpha - 5.2888 \times 10^{-1} \quad (5.4)$$

and therefore

$$\sigma_{ch} = f\left(\alpha, \frac{D}{C}\right) = A \left(\frac{D}{C}\right)^n \quad (5.5)$$

This is a new relation derived from the BEM results giving the (approximate) choked cavitation number limit for flat-plate foils. Its simple form, may lend to its use in numerical models and preliminary engineering calculations.

The relationship between the blocked C_L and α is shown in Figure 5.19 with D/C a parameter. The data is derived from the BEM analysis unless otherwise indicated. Data from the non-linear analytical methods of: Wu (1962) for $D/C = 5$ and ∞ ; Ai and Harrison (1965) for $D/C = 5$, is included for comparison. A brief summary of these two methods follows.

Wu's open wake theory does not explicitly include confining walls in the problem, but solves the infinite cavity length as a function of the cavitation number. With the free-stream or cavity surface velocity, $U = \sqrt{1 + \sigma_c}$, the normal force coefficient is then given by (Wu, 1962, Eq. 21 and Eq. 16b.)

$$C_N = \frac{\pi(U^{-1} + U)}{KU^2 \sin \alpha} \quad (5.6)$$

where

$$K = 2 \frac{(U^{-1} + U)^2 + (2 \cos \alpha)^2}{(U^{-1} + U)^2 - (2 \cos \alpha)^2} + \frac{\pi(U^{-1} + U)}{2 \sin \alpha} + \frac{(U^{-1} + U)^2 - (2 \cos \alpha)^2}{(U^{-1} - U) \sin \alpha} \tan^{-1} \left(\frac{U^{-1} - U}{2 \sin \alpha} \right) \quad (5.7)$$

and the lift and drag coefficients are given by

$$C_L = C_N \cos \alpha, \quad C_D = C_N \sin \alpha \quad (5.8)$$

In the limit as $U \rightarrow 1$, (or $\sigma_c \rightarrow 0$), Equation 5.6 simplifies to (Wu, 1962, p.170):

$$C_N = \frac{2\pi \sin \alpha}{4 + \pi \sin \alpha} \quad (5.9)$$

which is the Wu infinite flow result plotted on Figure 5.19.

A much simpler relation, derived from momentum considerations, is given by Ai and Harrison (1965, Eq. 4 and Eq. 5) for the choked force coefficients in terms of the wall separation and choked cavitation number:

$$C_D = 2 \frac{D}{C} \left[\left(1 + \frac{\sigma_{ch}}{2} \right) - \sqrt{1 + \sigma_{ch}} \right] \quad (5.10)$$

with the lift coefficient then given by

$$C_L = C_D \tan^{-1} \alpha \quad (5.11)$$

The choked cavitation number in Equation 5.10 is a function of incidence and the wall separation. Obtaining σ_{ch} for a particular flow geometry with Ai and Harrison's method is a complex and lengthy procedure. Their method is based on solving the inverse problem: first choosing the value of appropriate transformation parameters; then iteratively, numerically solving a set of integral equations by trial and error; obtaining the wall separation, choked cavitation number and the location of the foil as the solution (Ai and Harrison, 1965). The present BEM solution solves instead the direct problem, where the wall separation and foil position for a given incidence are specified, and the cavitation number and force coefficients are calculated after iteration to solve for the cavity shape.

There is good agreement between the predictions of choked C_L by the present method (BEM) and the Ai and Harrison non-linear theory for the closest wall separation, $D/C = 5$, as shown in Figure 5.19. Wu's theory comparatively over predicts for $0^\circ < \alpha < 19^\circ$ and $\alpha > 45^\circ$, and under predicts for $19^\circ < \alpha < 45^\circ$. Experimental data for small to moderate incidence values

($\alpha < 20^\circ$) were found by Ai (1966, Fig. 7) to lie in between the predictions of the two theories. The infinite flow result from the BEM and Wu methods are in good agreement.

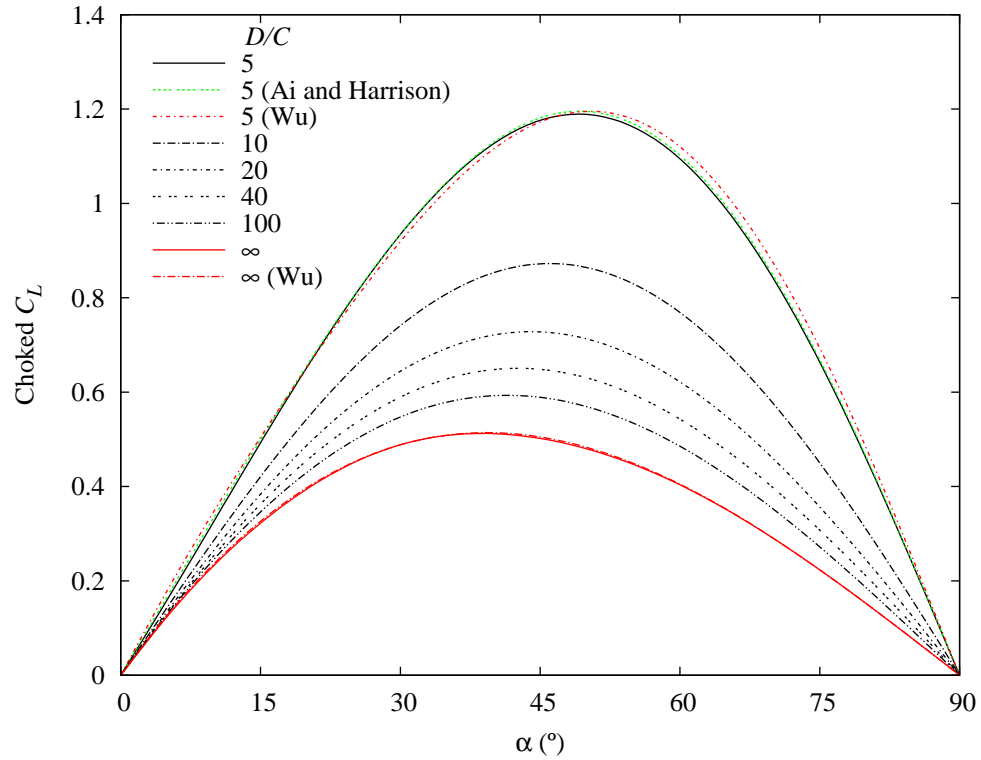


Figure 5.19: Choked C_L versus α with D/C a parameter. Included are theoretical predictions from Wu (1962) for $D/C = 5$ and ∞ , and Ai and Harrison (1965) for $D/C = 5$.

5.3 Results: Intercepted Foil

Of practical interest is the confined flow analysis of a foil shape that is to be tested in a physical cavitation tunnel. A series of 5 intercepted foil profiles have been designed⁵ and manufactured in preparation for a future companion experimental program to the present numerical study. The following data is an example of the confined flow analysis modelling one of the physical models situated in the working section of the AMC CRL cavitation tunnel. The model foils have a chord of 140mm and with the tunnel working section height of 600mm this gives a $D/c = 4.29$. The foil used in this example is designated ‘Foil4’ and has a $t/c = 25\%$, $\gamma = 5^\circ$ and a $h/c = 1\%$ and $\alpha = 0^\circ$ has been used. The details of the full model series is described in Appendix B.

Figure 5.20 gives the non-dimensional cavity length versus cavitation number relation for Foil4 in the confined and infinite flow cases. The data is typical of that for all of the 5 foil profiles, which is included in Appendix D. The behaviour is similar to the high incidence flat-plate supercavitating flow cases where the small wall separation ($D/C = 5$) curves only partially overlap with the infinite flow data.

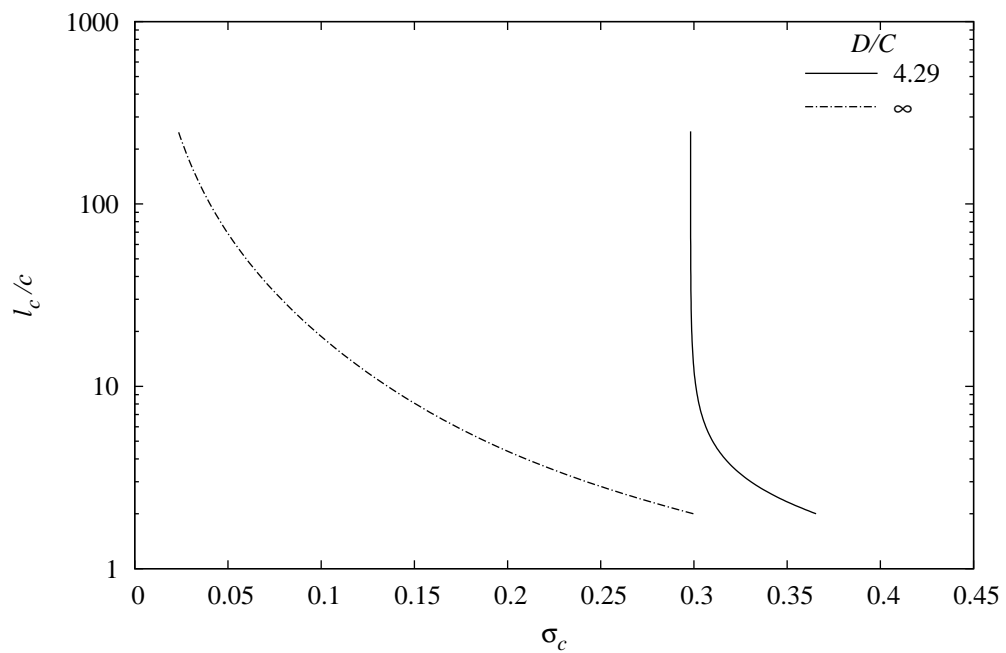


Figure 5.20: l_c/c versus σ_c for model ‘Foil4’ at zero incidence. Comparison of the model in CRL cavitation tunnel ($D/c = 4.29$) with the infinite flow case. (Foil4 geometry: $t/c = 25\%$, $h/c = 1\%$ and $\gamma = 5^\circ$).

The foil pressure distribution is significantly different from that of a flat-plate foil, however, as the intercepted foil has both pressure and suction surfaces wetted, with the constant cavity pressure only acting over the blunt base

⁵The chosen profiles have been selected based on the analysis presented in 4.

surface. The resulting pressure distributions for Foil4 ($D/C = \infty$ and 4.29) are shown in Figure 5.21. The pressure side distributions for the the confined and infinite flow cases differ only slightly. This is similar to the result found for the flat-plate foil in Figure 5.9a. On the suction side there is a sizeable decrease in pressure over the complete foil surface. Going from the infinite to the blocked case results in a greater pressure difference between the two sides and an increase in lift in the confined flow case, as shown in Figure 5.22a. This is opposite to the trend in the flat-plate case where there is a decrease in lift with increasing confinement (See Figure 5.10). The drag trend is for a decrease in C_D with increased confinement. This follows the same trend as for the flat-plate result (See Figure 5.11), but for a different reason. Whereas the decrease in drag for the flat plate was due to the reduction of the C_p distribution over the pressure surface, in the intercepted foil case it is due mainly to the suction side distribution. C_p is increased in magnitude over the surface in the confined case. As C_p is negative, in combination with the negative slope over the complete suction surface, the component of the resultant force in the flow direction acts in the opposing sense, i.e. there is an increase in the magnitude of the drag component acting opposite to the flow direction, and therefore the net drag is reduced in the confined flow case. The combination of the changes to both the lift and drag results in an increased L/D in the confined flow in comparison with the infinite flow case (Figure 5.22b). The lift, drag and efficiency data for all 5 foils show a similar trend, and are all included in Appendix D.

The plots of wall pressure distribution for Foil4 are shown in Figure 5.23. These results are for $D/c = 4.29$ which is the equivalent value for the physical model test in the CRL cavitation tunnel. The data for Foil4 is a typical result and the complete data for the 5 models is included in Appendix D. The general behaviour is similar to that for the flat-plate foil data presented in Figure 5.7.

This blocked wall C_p data is of value in the design of experimental set-up. With it the positioning of the foil, relative to test section wall tapings, can be optimised. In the CRL tunnel there are static pressure tapings on the lower wall at the upstream end. From the Foil4 wall pressure data (Figure 5.23), the model needs to be placed at a distance of greater than $7.5c = 1050$ mm from the static taping position if the pressure reading there is not to be influenced by the presence of the foil and cavity. The Foil4 model therefore needs to be positioned in the mid-way along the test section (overall length = 2.6 m). See Appendix B for a description of the experimental set-up.

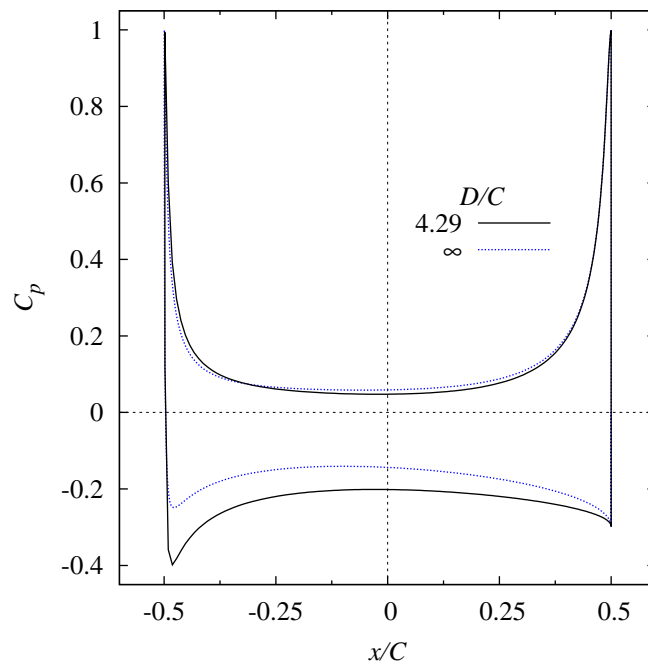


Figure 5.21: C_p distribution over the foil wetted surface for model ‘Foil4’ at zero incidence. Comparison of the model for an equivalent blockage to that for testing in the CRL cavitation tunnel ($D/c = 4.29$), with the infinite flow case. (Foil4 geometry: $t/c = 25\%$, $h/c = 1\%$ and $\gamma = 5^\circ$).

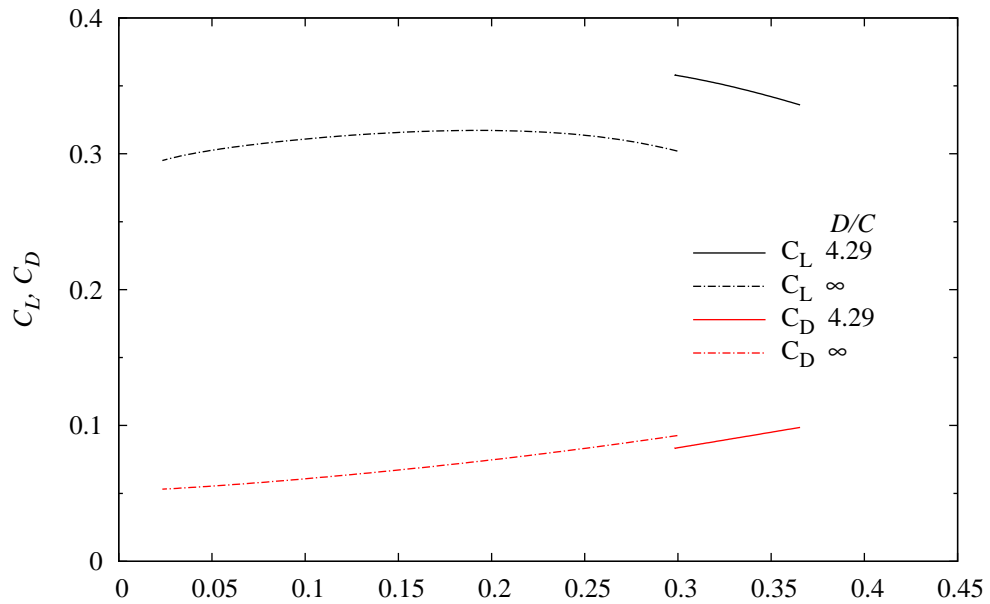
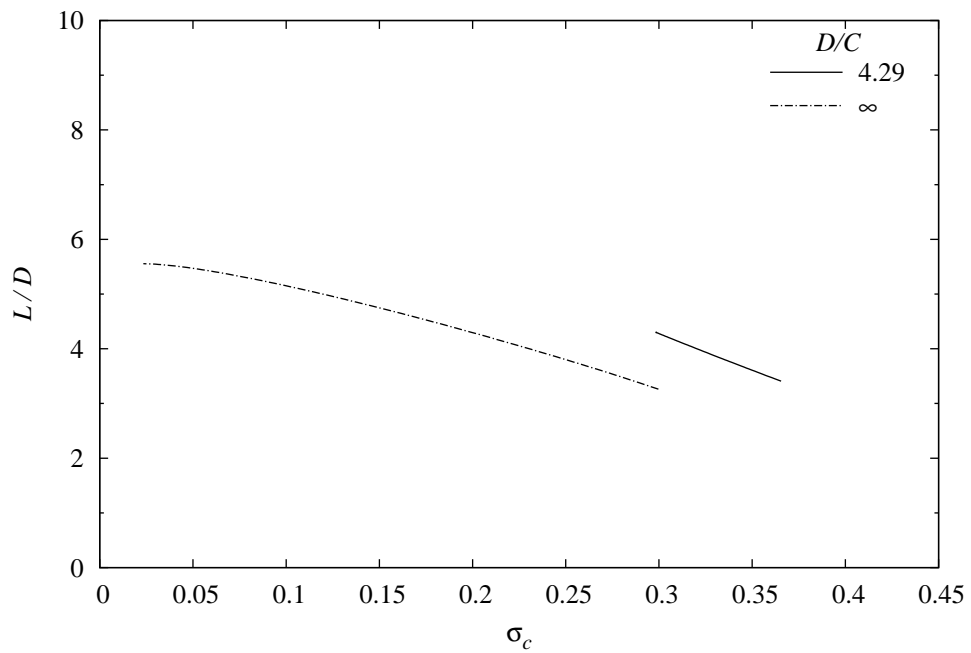
(a) C_L and C_D versus σ_c .(b) L/D versus σ_c .

Figure 5.22: C_L , C_D and L/D versus σ_c for model ‘Foil4’ at zero incidence. Comparison of the model for an equivalent blockage to that for testing in the CRL cavitation tunnel ($D/c = 4.29$), with the infinite flow case. (Foil4 geometry: $t/c = 25\%$, $\gamma = 5^\circ$ and $h/c = 1\%$).

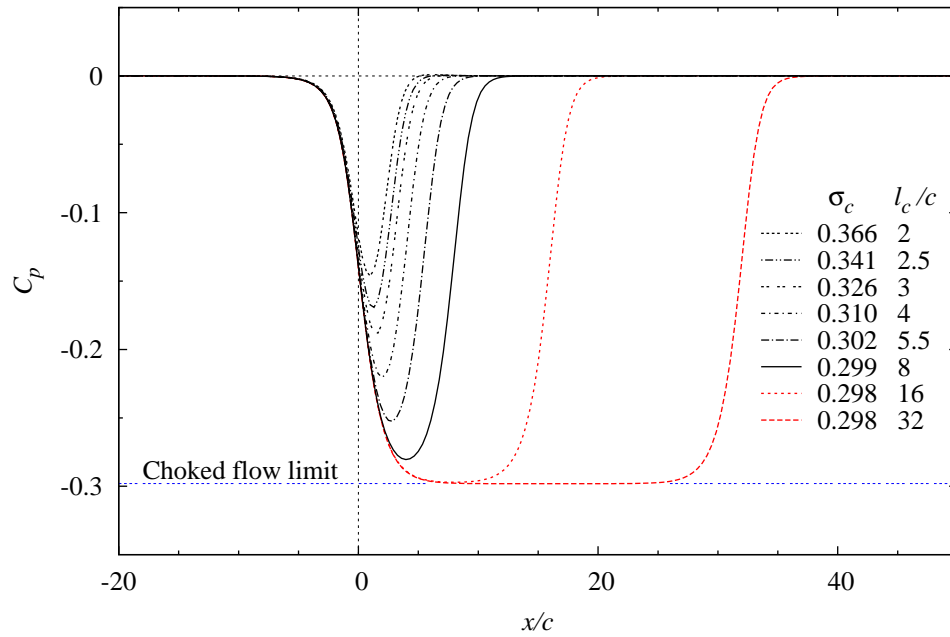
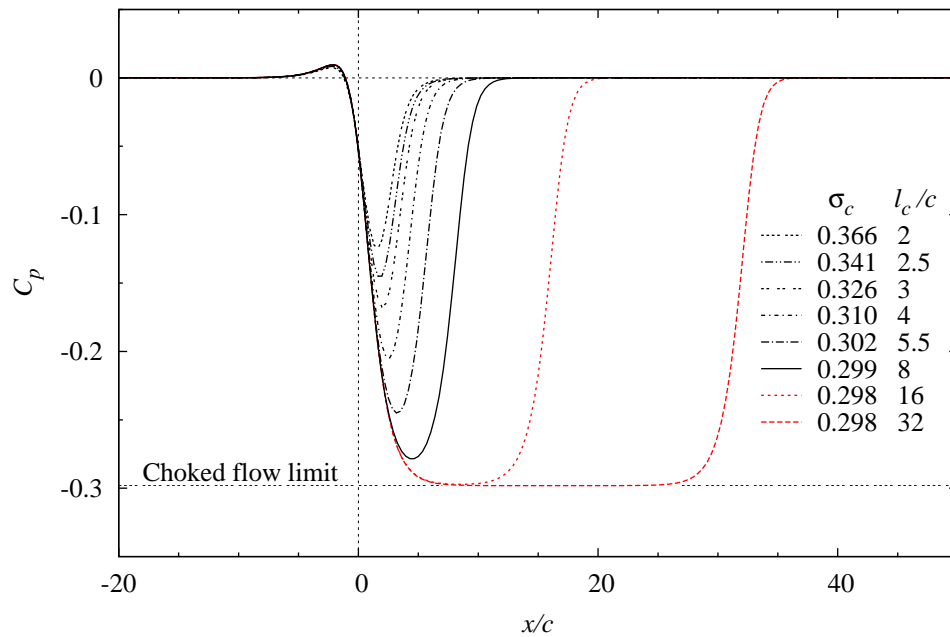
(a) C_p distribution on upper wall.(b) C_p distribution on lower wall.

Figure 5.23: Plots of C_p distribution on the upper and lower confining walls for Foil4 at $D/c = 4.29$ and l_c/c a parameter. Equivalent analysis of the model foil in CRL water tunnel. (Foil4 geometry: $\alpha = 0^\circ$, $t/c = 25\%$, $h/c = 1\%$ and $\gamma = 5^\circ$). The choked flow limit is reached when $C_p = -\sigma_{ch} = -0.298$.

5.4 Conclusions

The effect of flow confinement, or blockage, associated with fully-developed cavity flows can be substantial, in the extreme case leading to the occurrence of choking where a limit to the minimum cavitation number achievable is reached. The effect on the force coefficients is only significant at small values of wall separation, whereas the cavity length can be significantly increased compared with the infinite flow result at any wall separation, depending on the cavitation number, σ_c .

The comparison of the flat-plate and intercepted (base-ventilated) foil data shows that the effect of confinement may either increase or decrease the lift produced. The direction of the offset from the infinite flow result depends on whether only the pressure side (flat-plate foil), or both foil surfaces (base-ventilated foil), remain wetted. Drag in both cases was reduced in the confined flow.

The present boundary element method is in good agreement with non-linear analytical results for the choked flow case, and gives quantitative information about the accuracy and limits of application of analytical theories. It has the added usefulness in its capacity to:

- analyse arbitrary shaped lifting bodies in confined flow, and;
- provide results at cavitation numbers greater than σ_{ch} .

Specific outcomes of this work are:

- derivation from the BEM results of an approximate formula for σ_{ch} for a flat-plate foil as a function of α and D/C
- use of BEM method to design and analyse experimental test for intercepted foil.

Chapter 6

Conclusions and Future Recommendations

6.1 Conclusions

The objective of this thesis was to investigate the significant issues involved in, and possible limitations concerning, the hydrodynamic performance of blunt-based ventilated supercavitating hydrofoils of symmetric section. Flow asymmetry, i.e. the source of the foil lift, being produced due to the presence of a fence, or interceptor, on one foil trailing edge, not primarily from incidence. This objective has been investigated, primarily numerically by means of a non-linear boundary element method, and it has been found that:

- Given that the foil must produce positive or negative lift at a nominal incidence of $\alpha = 0^\circ$, the optimum ideal performance is obtained by: a thin section, i.e. a low t/c ; with the maximum leading edge radius, r_{max} , for that thickness; and a small slope at the foil trailing edge, i.e. small γ . The maximum hydrodynamic efficiency achieved in the present foil analysis (for $h/c = 1\%$) was $L/D \approx 12.5$ for $t/c = 15\%$, $\gamma = 2.5^\circ$ and $\sigma_c = 0.05$.

However,

- The minimum achievable section thickness will be limited, based on structural requirements and the trade-off against an acceptable leading edge $C_{p_{min}}$ (relative to the free stream cavitation number, σ_v), to provide a reasonable margin against leading edge vapour cavities occurring.
- The minimum achievable γ will be determined by the value required to maintain cavity detachment at the trailing edge (i.e. to ensure the foil suction surface remains wetted), with again some reasonable margin considering incidence excursions in a seaway.

The method used (BEM) was found to be computationally efficient, allowing for the analysis of a large parameter space (computation time from a few

seconds to less than an hour depending on the cavity length with the BEM, compared to 30-40 hours for a CFD simulation), in a practical time frame.

For the future comparison of the numerical predictions with experimental data, a numerical analysis of the effect of flow confinement, or blockage, associated with fully-developed cavity flows was conducted. From this blockage analysis it has been found that:

- The effect of flow confinement, or blockage, associated with fully-developed cavity flows can be substantial, in the extreme case leading to the occurrence of choking where a limit to the minimum cavitation number achievable is reached. The effect on the force coefficients is only significant at small values of wall separation, whereas the cavity length can be significantly increased from the infinite flow result at any wall separation, depending on the cavitation number, σ_c .
- The comparison of the flat-plate and intercepted (base-ventilated) foil data shows that the effect of confinement may either increase or decrease the lift produced. The direction of the offset from the infinite flow result depends on whether only the pressure side (flat-plate foil), or both foil surfaces (base-ventilated foil), remain wetted. Drag in both cases was reduced in the confined flow.
- The present non-linear boundary element method is in good agreement with non-linear analytical results for the prediction of the choked flow limit. It has the added usefulness in its capacity to: analyse arbitrary shaped lifting bodies in confined flow, and; at cavitation numbers greater than the choked condition.
- This work quantifies the accuracy and limits of application of the analytical methods considered.
- Derivation from the BEM results of an approximate formula for the choked cavitation number for a flat-plate foil as a function of incidence and the wall separation.

To gain an understanding of the flow physics involved in the flow over the trailing edge fence, including viscous effects, a basic study of the fence flow in isolation from the foil was undertaken. The results from this wall-mounted fence flow study also having application in the performance prediction of transom mounted interceptors on high-speed marine craft. From the analysis of the cavitating flow over a wall-mounted fence it was found that:

- The analytical and BEM predictions were found to be in good agreement in the near field, i.e. the pressure distributions on the face of the fence, and on the wall just upstream on the fence. Far upstream of the fence the wall pressure distribution was over-predicted by the analytical method compared to the BEM result, with the discrepancy increasing

with decreasing cavitation number, σ_c . This can be attributed to the open wake model used in the analytical solution only adequately modelling the flow geometry for large cavities, i.e. $\sigma_c \rightarrow 0$.

- The wall pressure distributions were found to fall away in the far field with a power law relation in both the analytical and BEM results. The results from the CFD analysis show a reduction of the wall pressure distribution to zero with a relatively short upstream distance, e.g. within approximately 60 fence heights for the $\sigma_c = 0.44$ case. This feature, in addition to the maximum C_p at the wall/fence juncture being reduced by approximately 50%, with both effects reducing the lift force on the wall.
- The reduction in the wall pressure distribution for curved shaped fences ($\beta < 90^\circ$) in comparison to the normal fence ($\beta = 90^\circ$), though significant, does not capture the much greater reduction in the magnitude and extent of the wall pressure distribution in the viscous flow result. The simple modification to the BEM model then, of replacing the normal fence with a curved fence, does not sufficiently account for the effect of the boundary layer, although some reduction in the lift obtained does result.
- The results show that the ‘ideal’ maximum efficiency of an interceptor flow, i.e. the free-streamline flow over a wall mounted fence, is obtained at small σ_c and gives $L/D > 40$. Even with the consideration of a only ‘practical’ upstream wall length, this value is reduced to $L/D \approx 20$. The results from the example ($\sigma_c = 0.44$) analysed with CFD showed a reduction of about 50% in the C_L value, which also equates to a similar reduction in L/D , as $C_D \approx 1$ at this cavitation number. The CFD results though informative, can only be considered as preliminary at this stage. Experimental data for validation of the CFD analysis is required.
- Comparison of BEM data for the curved and flat fence geometries revealed that the cavity characteristics, e.g. length, were found to be a function of the angle of detachment of the cavity. The determining parameter was then the fence trailing edge slope with the shape of the fence upstream of the trailing edge having no effect on the resulting cavity.

These results indicate that a companion experimental study is necessary to investigate the real fluid effects, i.e. viscosity and surface tension, on foil performance. As indicated from the CFD results on the cavitating wall-mounted fence flow, the presence of the boundary layer is likely to substantially reduce the production of lift, whereas surface tension may assist in keeping the cavity detachment at the suction side trailing edge past the limit predicted by the potential flow prediction. The leading edge suction peak may also not effect

the performance as negatively as has been assumed. Only experiment will bring clarity to these issues.

6.2 Future Recommendations

- The planned companion experimental foil test program should be undertaken and the data used to compare with the BEM results of this study. The knowledge thus gained, then used to select an improved foil section profile or to further optimise the chosen profile shape.
- Quantify experimentally end effects and hence enable comparison of 2-D and 3-D hydrodynamic performance.
- Extend the experimental program to include oscillating tests to investigate unsteady flow effects on: cavity establishment and stability; hydrodynamic performance, i.e the time scales involved for circulation and therefore lift production.
- A cavitation tunnel study of the cavitating flow over a wall-mounted fence to more fully investigate the flow physics involved, and to enable validation and further development of the CFD modelling of these flows. This may include the use of PIV to investigate the flow field in front of the fence, i.e. the separation zone, and to measure the cavity detachment angle from the fence tip.
- Extend the BEM to include boundary layer calculation and viscous drag estimates.
- Refinement of the existing CFD model to further investigate the behaviour of the separation region in front of the fence, with changes in both the cavitation number and boundary layer thickness. Further development of the model to obtain convergent solutions for cavity lengths greater than 100 fence heights. This may include investigating alternative cavitation models and/or solution methods other than unsteady RANS.
- To develop a 2-D (and 3-D) viscous CFD model to simulate the intercepted foil supercavitating flow.

Appendix A

Publications Arising from the Work Undertaken in this Thesis

The following refereed conference papers have arisen out of the work conducted whilst undertaking this thesis:

- Pearce, B. W. and P. A. Brandner. (2007). Limitations on 2D supercavitating hydrofoil performance. In *Proceedings of the 16th Australasian Fluid Mechanics Conference*. Gold Coast, Queensland, Australia, pp. 1399-1404.
- Pearce, B. W., P. A. Brandner and J. R. Binns. (2010). A numerical investigation of the viscous 2-D cavitating flow over a wall-mounted fence. In *Proceedings of the 17th Australasian Fluid Mechanics Conference*. Auckland, New Zealand: Paper 305.

Appendix B

Experimental Design

B.1 Introduction

The following is a description of a future experimental program, companion to the numerical foil analysis presented in this thesis. It was planned that this program would have been included in the present study but due to unforeseen delays to the completion of a major upgrade to the AMC CRL cavitation tunnel, the experimental facility has not been available within the time to complete the present study. The upgraded AMC CRL cavitation tunnel is expected to be commissioned and in use by early to mid 2011. A description of the new facility is given by Brandner et al. (2006, 2007).

B.2 Aims

The purpose of the planned experimental program is to

- obtain force data and cavity geometry data to compare with the numerical prediction obtained with SUPCAV, particularly to assess viscous effects
- investigate the effects of viscosity and surface tension, in particular with respect to the cavity detachment from the suction side trailing edge (i.e. the conditions under which the cavity detachment moves forward onto the foil surface)
- investigate the effect that leading edge vapour cavitation has on the hydrodynamic performance
- effect of the ventilation rate into the trailing cavity
- finite span effect.

B.3 Experimental Setup

B.3.1 Foil Models

The foil profile shapes were chosen on the basis of the analysis presented in Chapter 4. A series of 5 foil profiles were selected by systematically varying both t/c and γ (with $r = r_{max}$) to cover a substantial region of the parameter space. The chosen foil shapes are shown shaded black in Figure B.1 and the main details are listed in Table B.1. A rectangular planform has been used so that a direct comparison with the numerical method can be made. In addition, 4 interceptor blades giving a range of fence heights $h/c = 1, 2, 3$ and 4% , can be attached to each of the 5 models.

| Foil | t/c % | γ ° | c mm | t mm | r mm | b mm |
|-------|------------|---------------|-----------|-----------|-----------|-----------|
| Foil1 | 20 | 3 | 140 | 28 | 1.64 | 276 |
| Foil2 | 20 | 4 | 140 | 28 | 0.66 | 276 |
| Foil3 | 25 | 4 | 140 | 35 | 2.2 | 276 |
| Foil4 | 25 | 5 | 140 | 35 | 1.03 | 276 |
| Foil5 | 30 | 5 | 140 | 42 | 2.84 | 276 |

Table B.1: Experimental foil model main details

An example of the assembled foil with interceptor, shown with an end cap attached, is given in Figure B.2b. The end cap is added to enable a 3-D test to be undertaken with the same foil model. An exploded view of the same foil arrangement is shown in Figure B.2a to enable particular features to be more apparent. The interceptor is attached to the foil base by screws as indicated and can be fixed to either the upper or lower trailing edge. There is an additional interceptor piece which is attached to the end cap in the case of the 3-D test. Ventilation air is supplied to the trailing cavity through a manifold of 6 equi-spaced passages along the centerline of the foil base. The foil is shown transparent in the figure to reveal the detail of the internal passages. The six outlets through the base are supplied from a central passage which is connected, via a flexible tube passing out through the force balance, to the external air ventilation supply system.

A tapping for measurement of the cavity pressure protrudes behind the foil at the mid-span. It transits through the ventilation air passage out through the force balance to the external pressure measurement system. The foil assembly is mounted on a force balance via the mounting flange. The disc shown in the figure is an infill disc. This is located flush with the test section side wall but not in contact with the foil model. The disc is also mounted off the non-measurement side of the balance. In this way forces acting on the disc do not need to be tared from the test data, as would be the case if the disc was

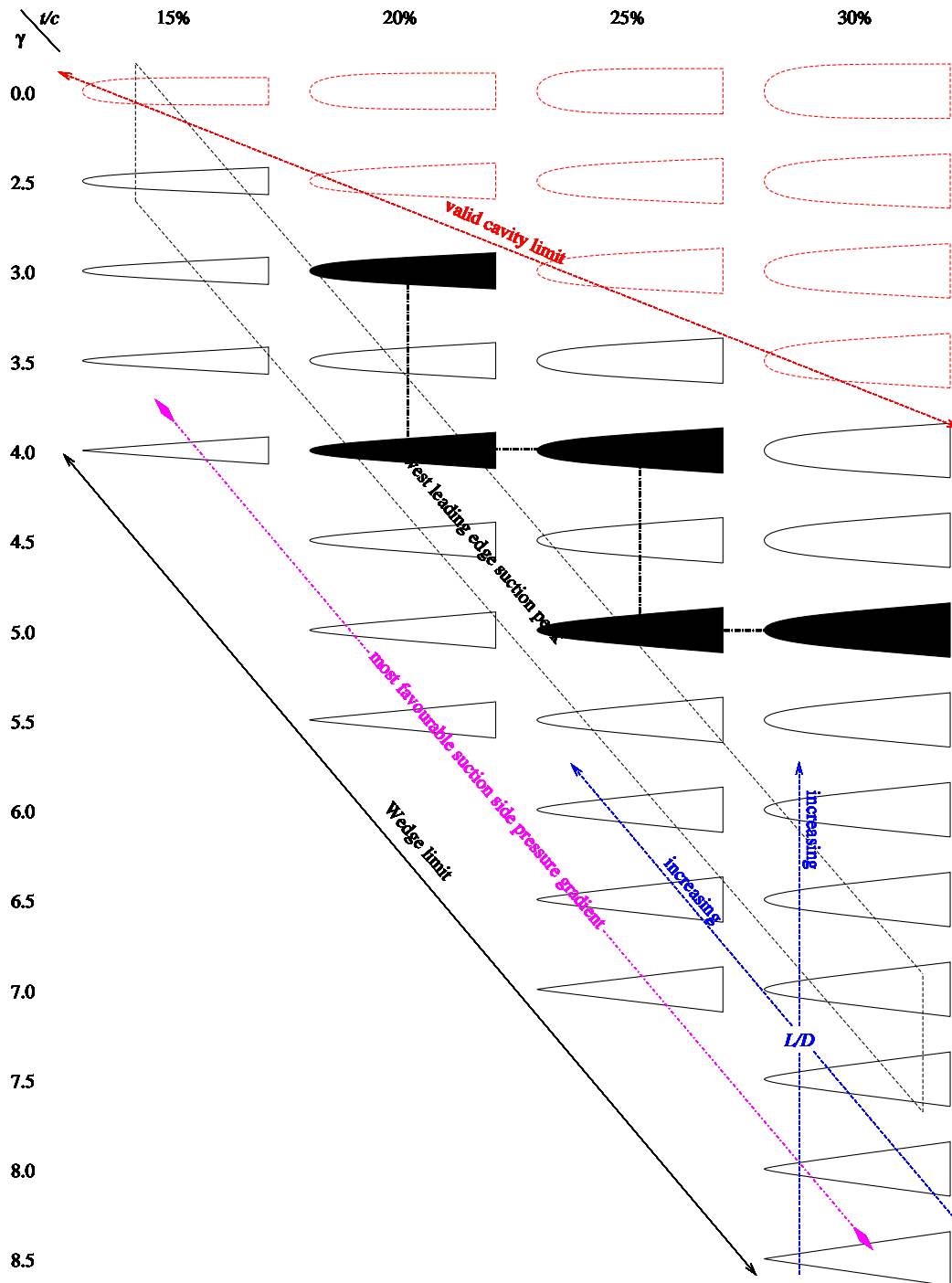


Figure B.1: Repeat of Figure 4.33 with the 5 profiles chosen for the experimental program shaded black.

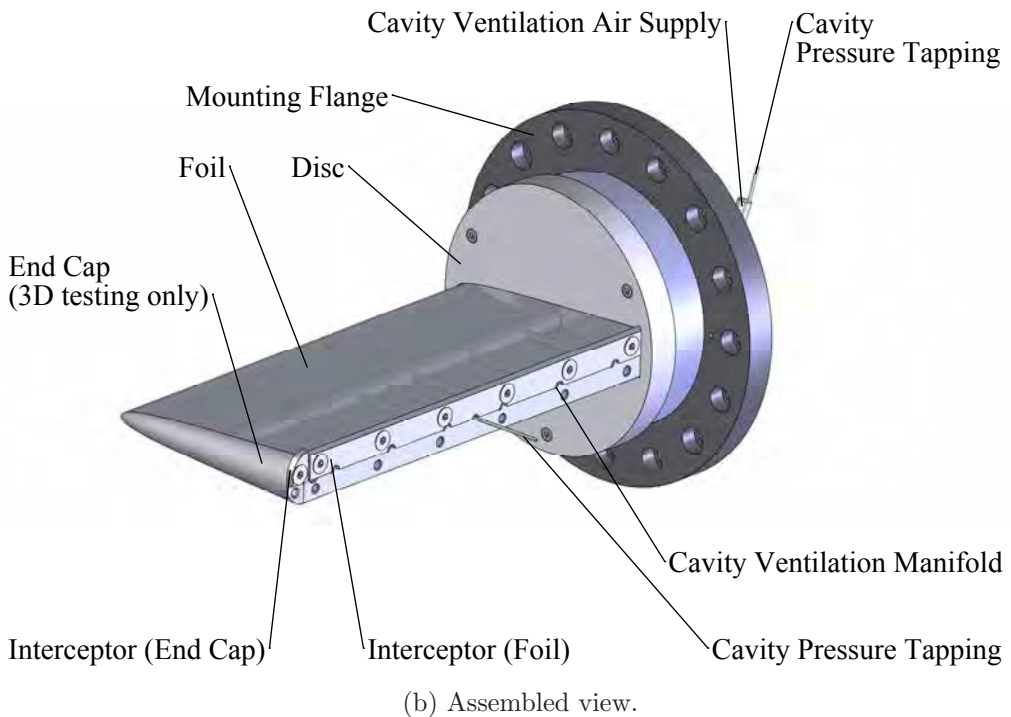
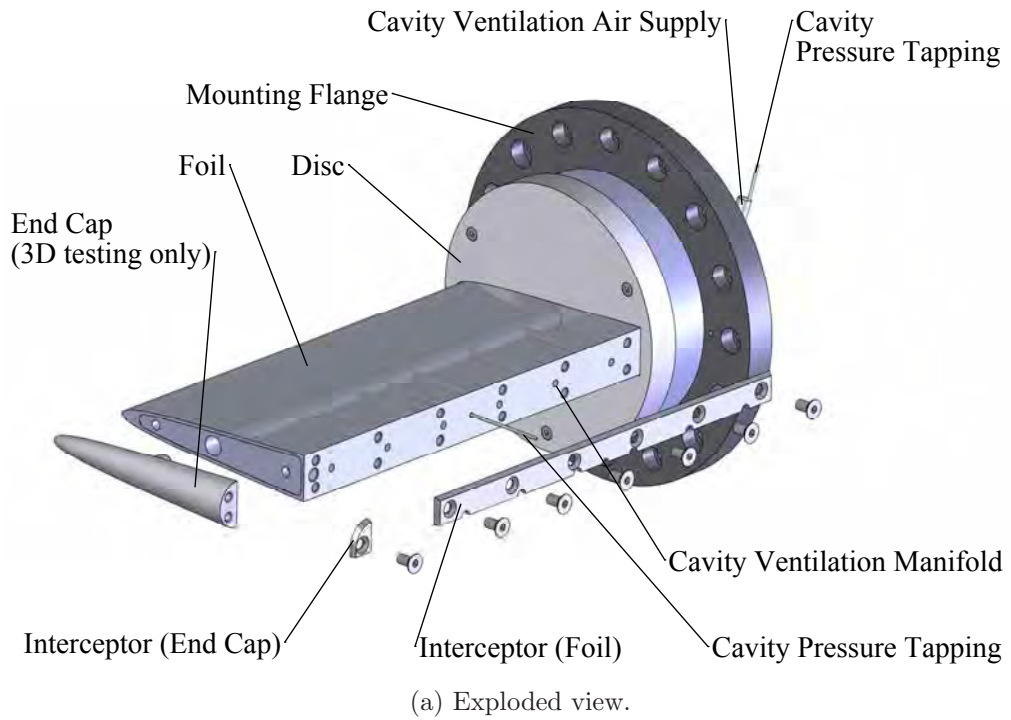


Figure B.2: CAD model of the typical foil arrangement shown with interceptor, end cap and infill disc. The ventilation manifold detail is shown via transparency of the foil. The main air passage runs through the centre of the foil with six outlet passages spaced evenly along the blunt base. The cavity pressure tapping runs down through the main air supply passage and protrudes out behind the foil through a mid-span drilling.

integral with the model.

The foils have been manufactured from aluminium to minimise the mass, in comparison with other metals suitable for the purpose, e.g. stainless steel. This is important as the models may also be used for oscillating foil tests. The foils have been black anodised to give corrosion protection and the colour is also advantageous for surface flow visualization studies and to minimise reflection in laser velocimetry measurements. A photograph of the 5 foil models, without interceptors fitted, is given in Figure B.3. The end caps are shown fitted to the foils and the infill discs are positioned in front of their respective models. The interceptors are made from 3 mm thick stainless steel flat bar with a 30° bevel along the top to provide a sharp edge for cavity detachment.



Figure B.3: Photograph of the 5 physical foil models shown bare, i.e. without interceptors but with end caps attached. The infill discs are separated from the foil and positioned in the foreground.

B.3.2 AMC CRL Cavitation Tunnel Particulars

A description of the upgraded cavitation tunnel which will be used for this experimental program is given by Brandner et al. (2006, 2007). The main specifications of the facility are:

- Test section 0.6 m square x 2.6 m long
- Max flow speed 12 m/s
- Pressure range from 4 to 400 kPa absolute
- Test section velocity uniformity at mid section 0.25%
- Test section turbulence intensity at mid section 0.3%
- Test section temporal stability of: velocity 0.01%; pressure 0.01%
- Cavitation number from 0.07 to 200
- Tunnel volume 365 m³
- Minimum bubble residence 85 s
- Main pump motor power 200 kW.

The significant ancillary systems and items of instrumentation are:

- High speed microbubble degasser 20% saturation at atmospheric pressure in 2 hours
- Waterjet propulsor test loop maximum flow 150 l/s
- Test section ceiling boundary layer control using injection/suction at maximum of 50 l/s (0 to 0.1 m total thickness)
- Continuous nuclei injection and removal 0.1 to 10/cm³ in sizes ranging from 10 to 100 μm
- 200 l/s continuous removal of non-condensable gases
- 2 Propeller dynamometers
- 4 six-component force balances
- High-speed camera, time-resolved particle imaging velocimetry (PIV), stereo PIV and shadowgraphy system
- Scanning laser vibrometer
- 3D automatic traverse and 1D/3D fast response pressure probes.

The main circuit of the CRL cavitation tunnel is shown in Figure B.4. A detailed description of the circuit and its main components is given by Brandner et al. (2006, 2007). The feature with particular application to the experimental program of interest here is the continuous removal of non-condensable gases via the large downstream tank at the discharge from the diffuser. As an external supply of air is being fed into the cavity, this needs to be removed continuously so as to not pass around the circuit and within some tens of seconds, obscuring the model from view as the fraction of free air in the form of large bubbles increases. The free stream would thus quickly become a multiphase flow and not the desired single-phase flow test condition.

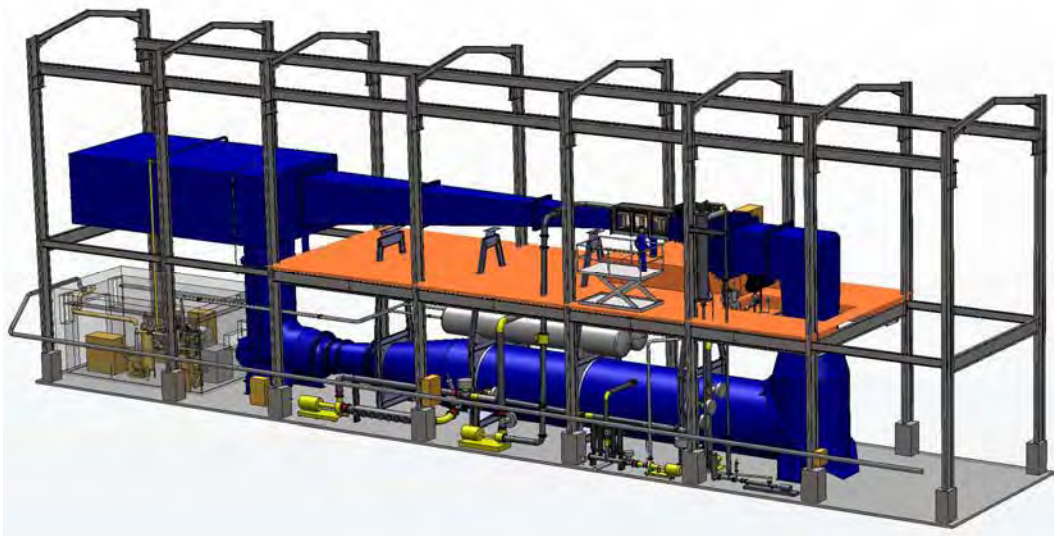
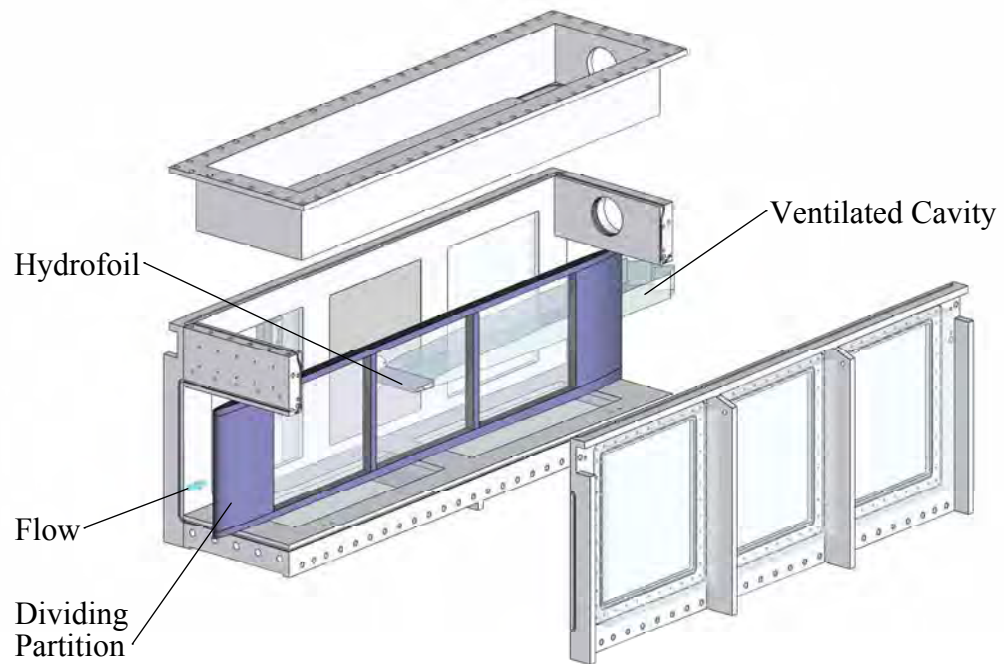


Figure B.4: AMC CRL cavitation tunnel main circuit.

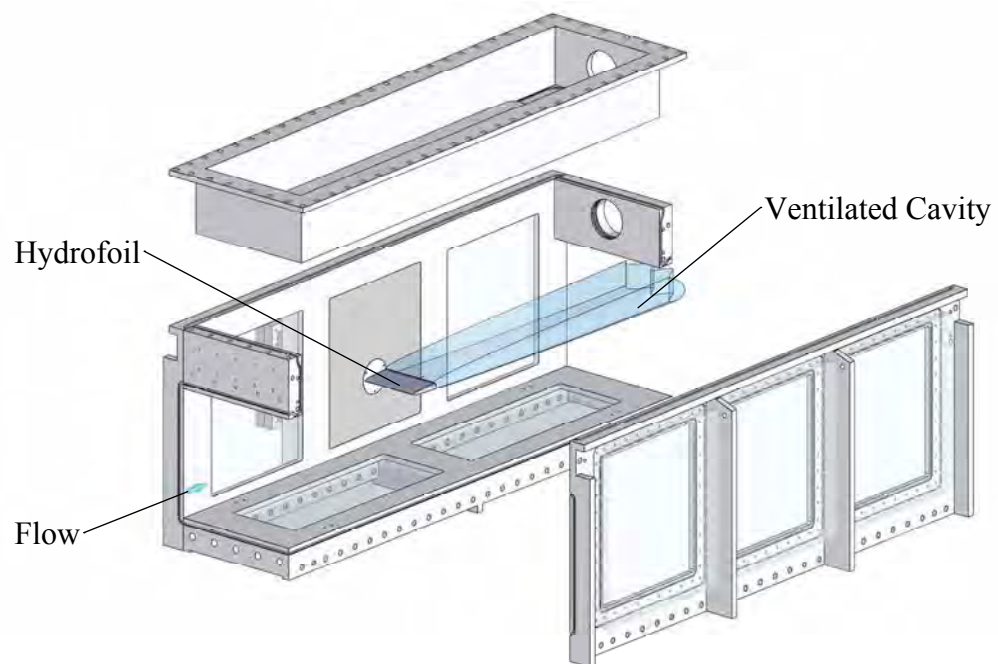
B.3.3 Model Arrangement in Test Section

A CAD representation of the arrangement of the model foil positioning in the test section is shown in Figure B.5. The upper figure shows the arrangement for a 2-D foil test where a dividing partition is installed to reduce the test section width by half. This is necessary as a foil spanning across the full width of 600 mm could have forces acting on it in excess of the safe limit for the force balance. The bending moment at the root of the foil span may also become excessive. The lower figure shows the arrangement for a 3-D foil test, using the same foil with the end cap fitted, with the dividing partition removed.

The dividing partition has been designed for this test program by the author in conjunction with the primary supervisor. It is made up from three 46 mm thick acrylic panels which are held in place by an upper and lower rail, separated by columns, and contained at the ends by leading edge and trailing edge pieces. All of these additional components have been manufactured from aluminium for ease of installation and black anodised for corrosion protection and to reduce light reflections.



(a) Test section arrangement for 2-D foil test.



(b) Test section arrangement for 3-D foil test.

Figure B.5: Views of the test section arrangement shown: (a) for 2-D testing with partition installed; (b) for 3-D testing with partition removed. A partially exploded view is shown to enable the test section internal detail to be seen. Flow direction is from left to right.

Before installation into the test section, the foil model is first connected to a six-component force balance via the mounting flange. This assembly is then mounted onto a stainless steel window, and the window/balance combination placed into one of the six side-window positions in the test section. Figure B.6 shows the force balance positioned in one of the center side window positions. The force balance to be used for the foil test program is a new instrument, designed by the author in collaboration with the primary supervisor and CRL staff. The new force balance has been designed to: more accurately measure the drag and lift force components; and has an internal mechanism for changing the model incidence whilst the tunnel is operating.

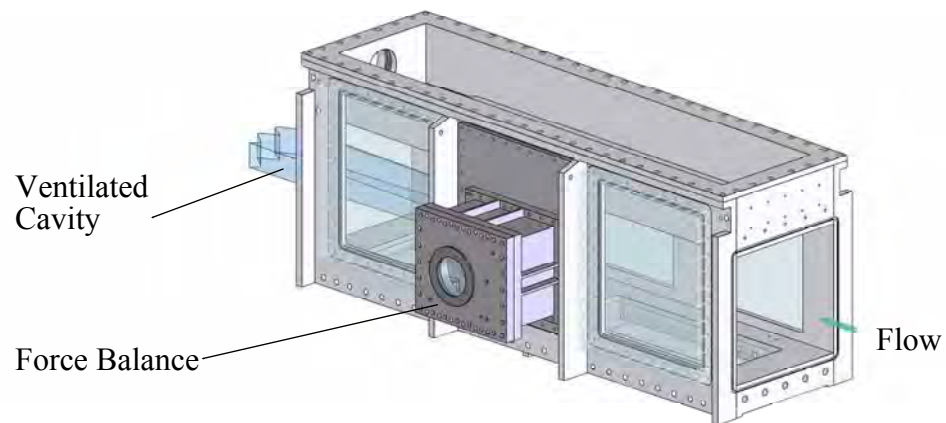


Figure B.6: View of test section from the opposite side (to that in Figure B.5 showing the mounting of the force balance in the centre side window position.

B.4 Experimental Procedure

B.4.1 Basic Test Procedure

The basic procedure, common to most experiments conducted in the cavitation tunnel, to measure foil hydrodynamic performance is to:

- Re-calibrate the force balance and connect the model to the balance measurement side mounting face
- Connect balance/model to an appropriate window and positioned in the test section
- Secure tunnel; fill with water; carry out degassing process; purge all pressure tapings of any free bubbles
- Re-calibrate pressure transducers, both those directly connected to the tunnel for control, and the transducers for model related measurements
- Run tunnel at desired Reynolds number and free stream cavitation number
- Record data at desired incidences and ventilation rates
- Repeat last two points to carry out test matrix
- Tunnel water may require re-degassing depending on time period of testing, i.e. degas over lunch break if continuing to test in the afternoon.

The test matrix will cover a range of:

- Incidence so as to establish the conditions under which the suction side cavity detachment no longer remains at the foil trailing edge
- Reynolds number to investigate the influence of viscosity (i.e. the foil surface boundary layer thickness) on cavity parameters and foil performance
- Ventilation rates to gain an understanding of the role that base ventilation plays in establishing and maintaining the cavity and the resulting foil performance.

B.4.2 Measurement of cavity pressure/cavitation number

The pressures required to determine the cavitation number are measured (using a Validyne Model DP15TL differential pressure transducer) via a multiplexing valve (Model 4817-1 Scanivalve pressure multiplexer), as shown schematically in Figure B.7. In this way the cavitation number based on cavity pressure:

$$\sigma_c = \frac{p_1 - p_c}{\frac{1}{2}\rho U_\infty^2} \quad (\text{B.1})$$

can be obtained directly by the sequential measurement of the cavity pressure and the free stream static and dynamic pressures. The latter is derived from the contraction pressure differential multiplied by the calibrated contraction constant, $K_{con}(p_2 - p_1)$. Through the use of the Scanivalve the span and zero errors can be eliminated in the measurement of the cavitation number. The zero error is eliminated or minimised by the re-zeroing of the Scanivalve each time it is returned to home, i.e. the reference pressure (p_1), after each measurement cycle. By measuring all pressures with the same transducer to derive σ_c , the span error cancels.

The cavity pressure is measured relative to the free stream static pressure p_1 via a gas/liquid interface, i.e. the numerator in Equation B.1. Likewise the dynamic pressure (denominator of Equation B.1) is measured from the contraction pressure differential and the calibrated contraction constant, $\frac{1}{2}\rho U_\infty^2 = K_{con}(p_2 - p_1)$.

Finally it is also possible to correct for small temporal changes in velocity between each sequential measurement by using the online, or continuously measured, contraction pressure differential used for tunnel closed loop control.

The cavity pressure tapping needs to be purged with air once the cavity is established to ensure the tubing contains no liquid. It also follows that the connection from the cavity to the Scanivalve needs to be made via an air/water interface, as all other connections to the multiplexer are filled with liquid. The purge valve and air/water interface device in the cavity pressure measurement line are arranged as shown in Figure B.7.

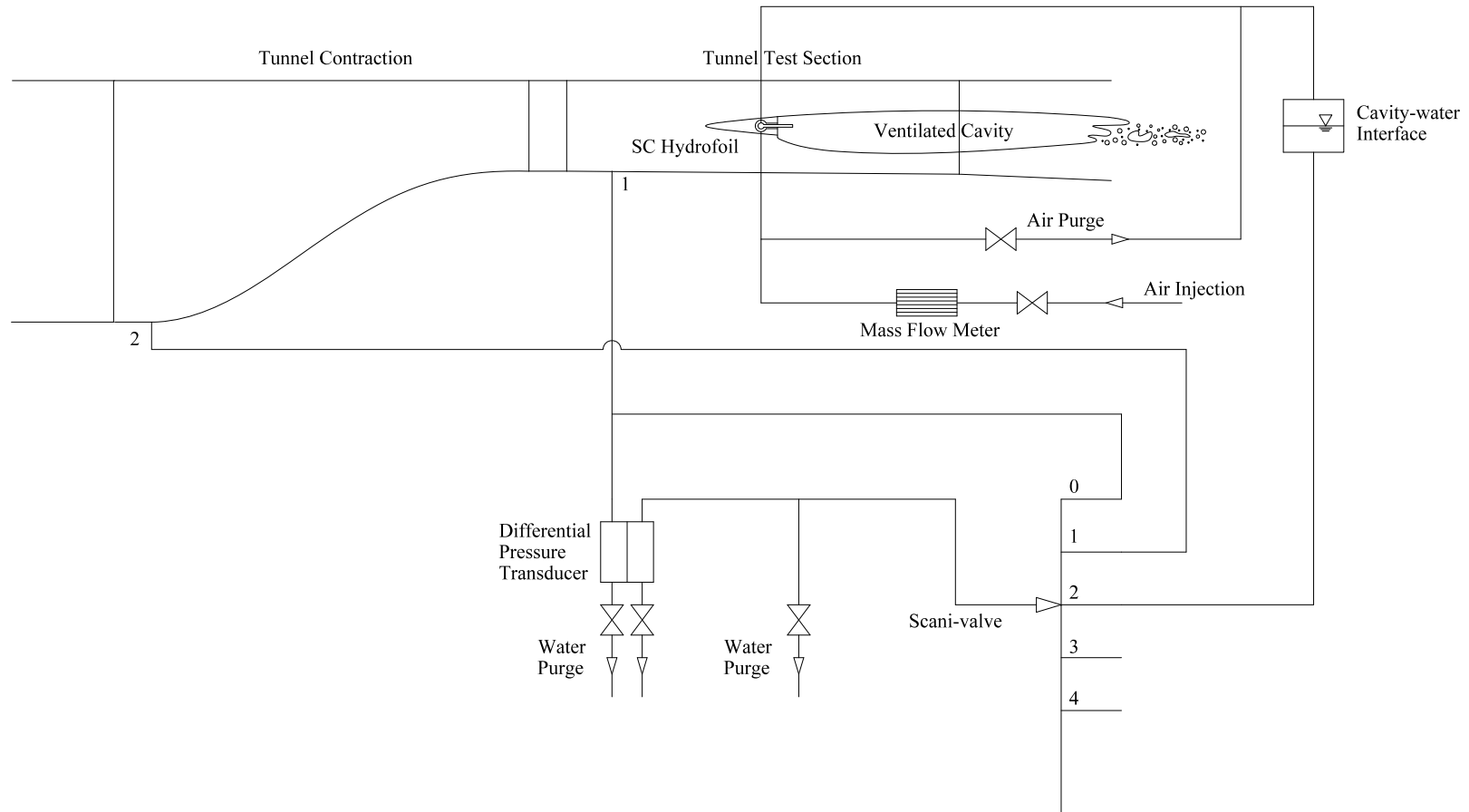


Figure B.7: Schematic diagram showing measurement of cavitation number using Scanivalve arrangement; and air injection via a mass flow meter.

B.4.3 Ventilation Air Supply and Measurement

Included in Figure B.7 is the ventilation air line which supplies air to the cavity via an Alicat Scientific MCR-500-SLPM-D mass flow meter from an external compressed air system. The output from the mass flow meter is fed directly to the data acquisition system. A photograph of the mass flow meter and associated components is given in Figure B.8.



Figure B.8: Photograph of the mass flow meter and associated items for the measurement and control of the injected air. From left to right the items are: filter/regulator; mass flow meter; pressure gauge; flow control valve; isolation valve.

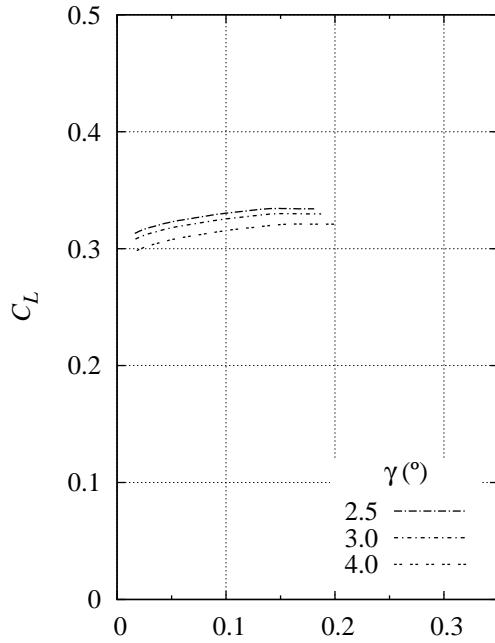
Appendix C

Additional Foil Numerical Analysis Data

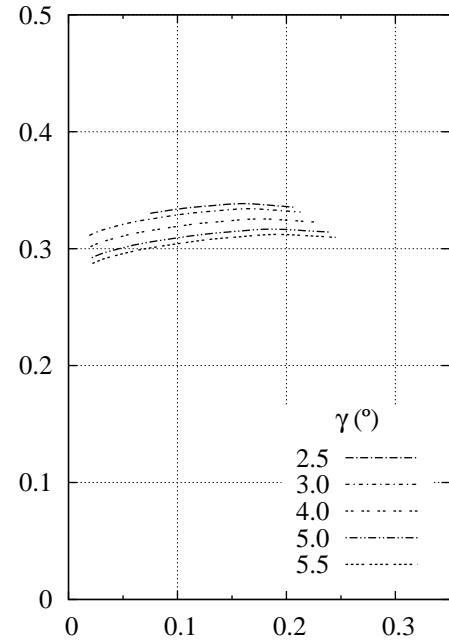
This appendix includes the complete data set of which only a portion was given in Figures 4.30 and 4.31 as typical examples.

C.1 Hydrodynamic coefficients versus σ_c with γ a parameter

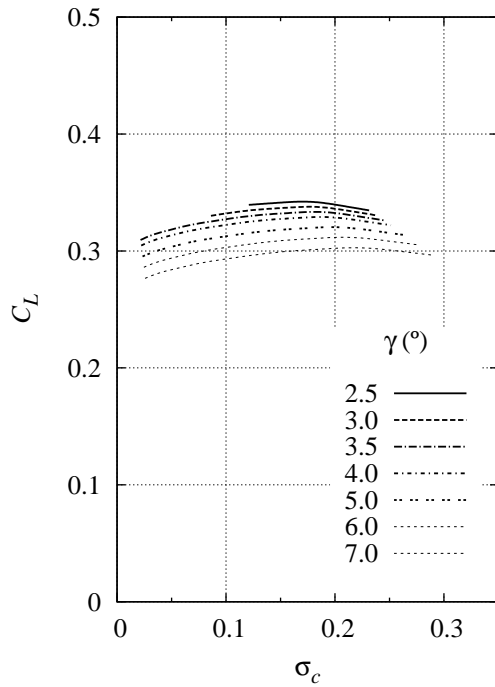
- Figure C.1: C_L versus σ_c with γ a parameter for $t/c = 15, 20, 25$ and 30% ($h/c = 1\%$, $\alpha = 0^\circ$ and r_{max})
- Figure C.2: C_D versus σ_c with γ a parameter for $t/c = 15, 20, 25$ and 30% ($h/c = 1\%$, $\alpha = 0^\circ$ and r_{max})
- Figure C.3: C_M versus σ_c with γ a parameter for $t/c = 15, 20, 25$ and 30% ($h/c = 1\%$, $\alpha = 0^\circ$ and r_{max})
- Figure C.4: L/D versus σ_c with γ a parameter for $t/c = 15, 20, 25$ and 30% ($h/c = 1\%$, $\alpha = 0^\circ$ and r_{max}).



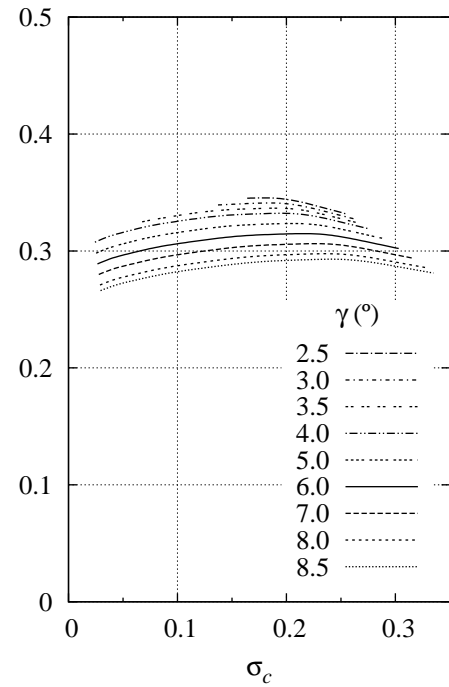
(a) $t/c = 15\%$.



(b) $t/c = 20\%$.

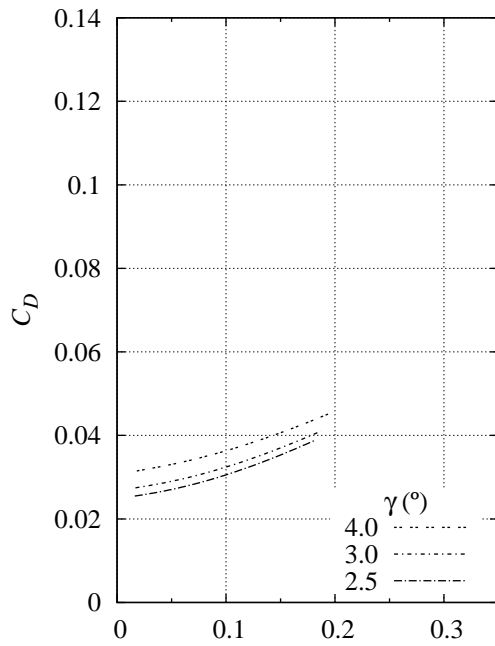


(c) $t/c = 25\%$.

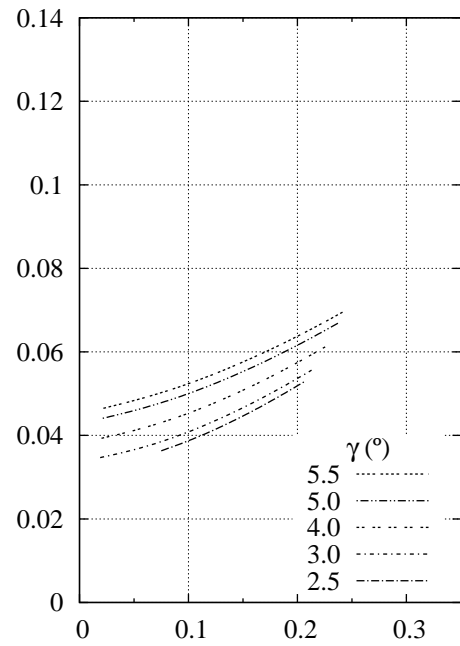


(d) $t/c = 30\%$.

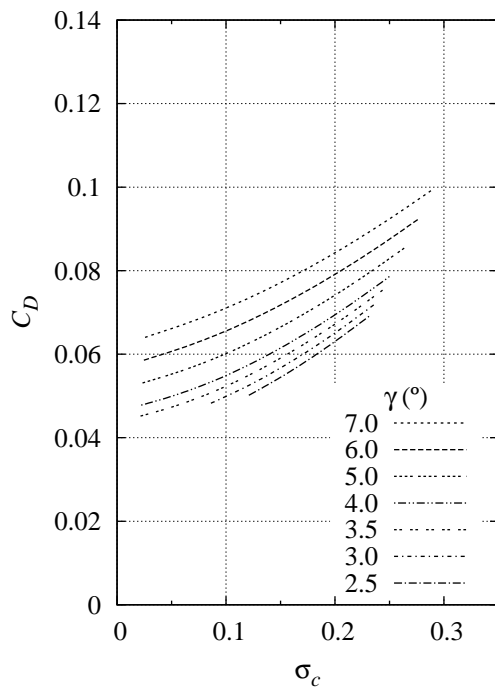
Figure C.1: C_L versus σ_c with γ a parameter for $t/c =$ (a) 0.15; (b) 0.20; (c) 0.25; (d) 0.30. ($h/c = 1\%$, $\alpha = 0^\circ$ and r_{max}).



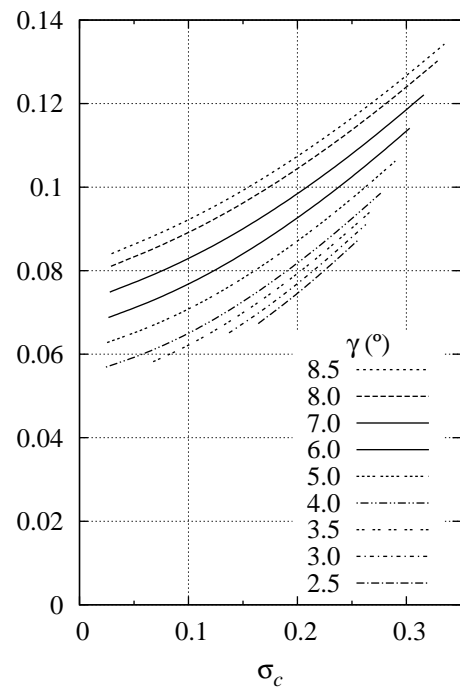
(a) $t/c = 15\%$.



(b) $t/c = 20\%$.

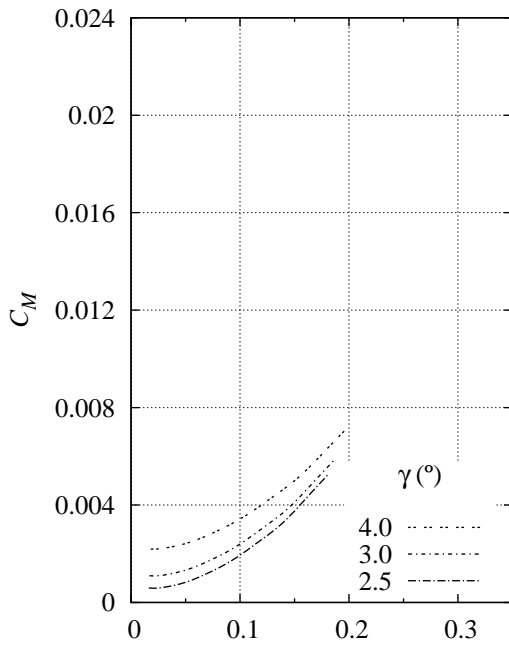


(c) $t/c = 25\%$.

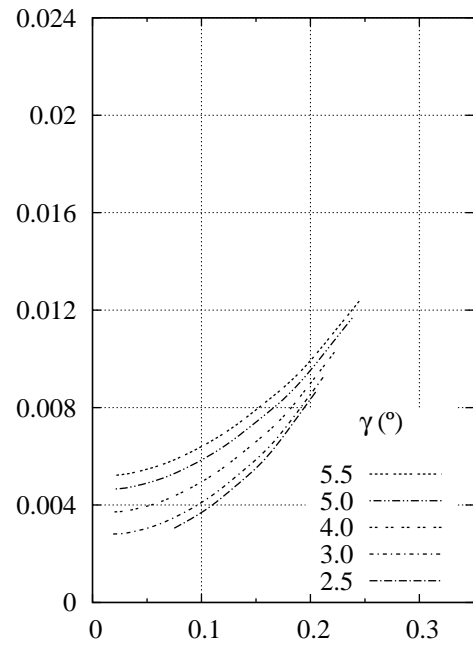


(d) $t/c = 30\%$.

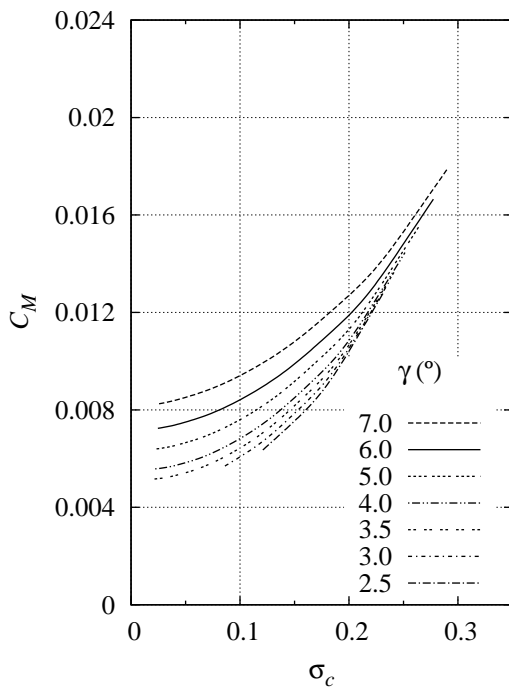
Figure C.2: C_D versus σ_c with γ a parameter for $t/c =$ (a) 0.15; (b) 0.20; (c) 0.25 and (d) 0.30. ($h/c = 1\%$, $\alpha = 0^\circ$ and r_{max}).



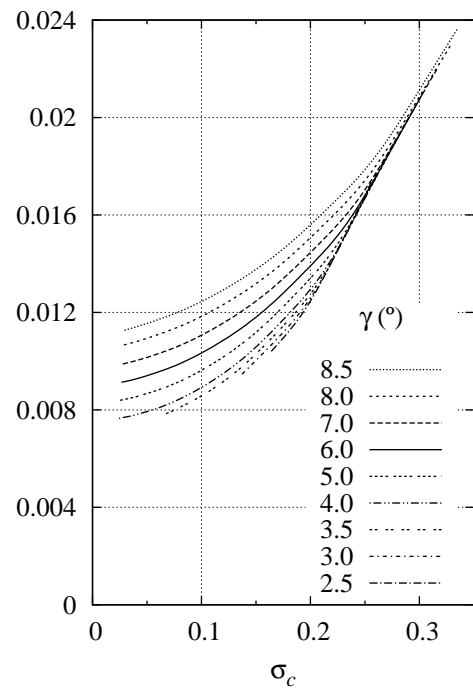
(a) $t/c = 15\%$.



(b) $t/c = 20\%$.



(c) $t/c = 25\%$.



(d) $t/c = 30\%$.

Figure C.3: C_M versus σ_c with γ a parameter for $t/c =$ (a) 0.15; (b) 0.20; (c) 0.25 and (d) 0.30. ($h/c = 1\%$, $\alpha = 0^\circ$ and r_{max}).

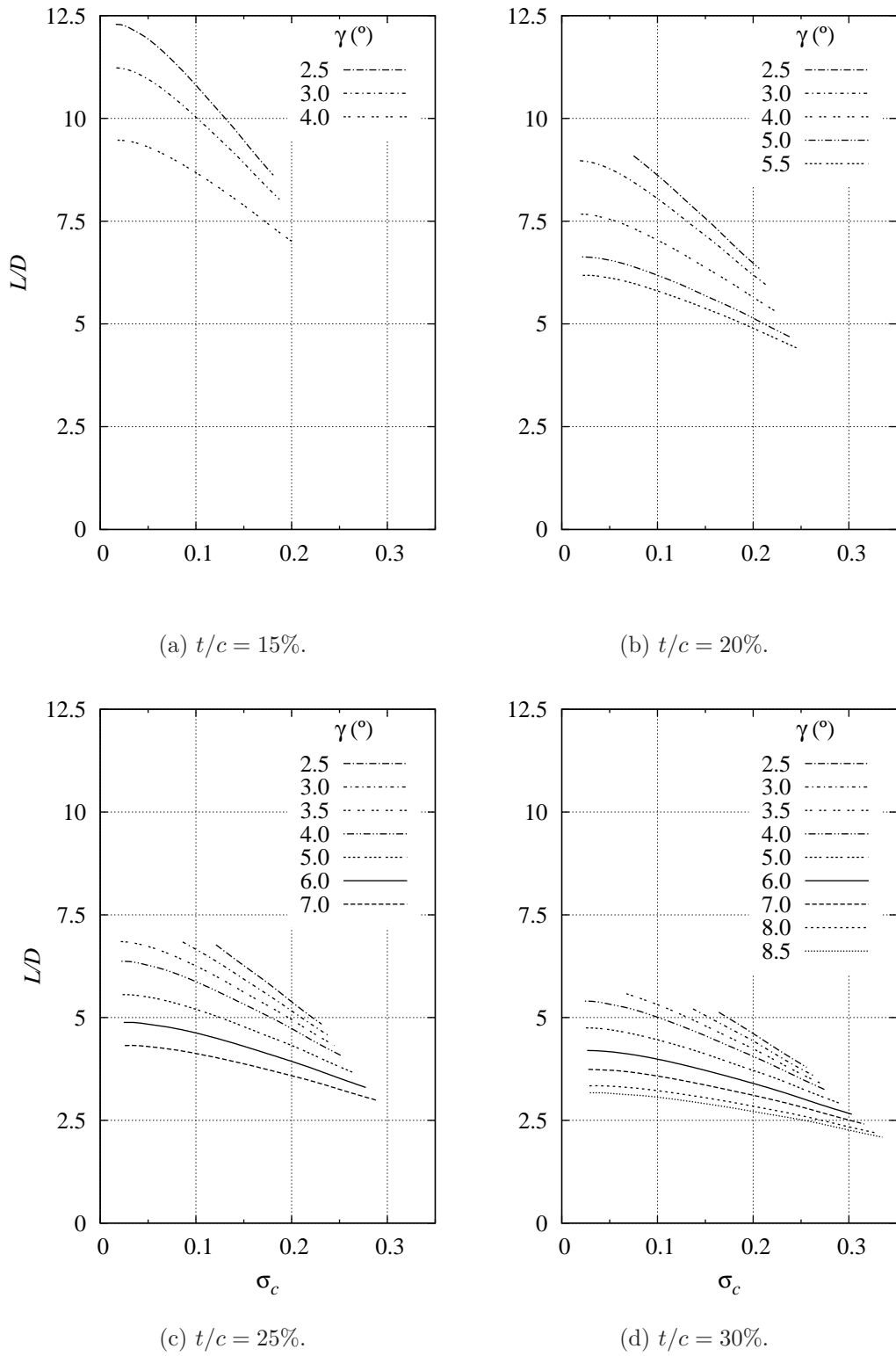
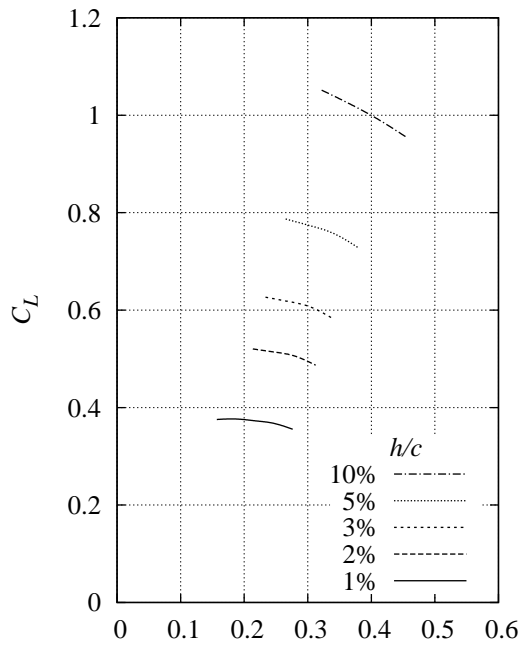


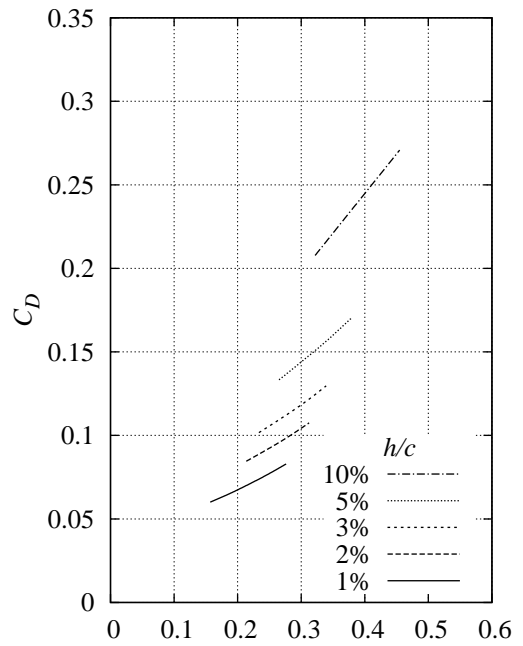
Figure C.4: Hydrodynamic efficiency versus σ_c with γ a parameter for $t/c =$ (a) 0.15; (b) 0.20; (c) 0.25 and (d) 0.30. ($h/c = 1\%$, $\alpha = 0^\circ$ and r_{max}).

C.2 Hydrodynamic coefficients versus σ_c with h/c a parameter

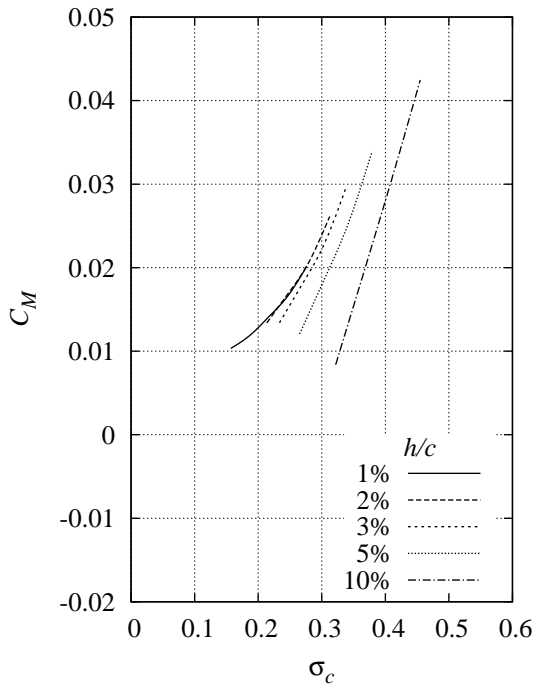
- Figure C.5: Hydrodynamic forces versus σ_c with h/c a parameter. ($\gamma = 2.5^\circ$, $t/c = 0.25$, $\alpha = 0^\circ$, r_{max})
- Figure C.6: Hydrodynamic forces versus σ_c with h/c a parameter. ($\gamma = 5^\circ$, $t/c = 0.25$, $\alpha = 0^\circ$, r_{max})
- Figure C.7: Hydrodynamic forces versus σ_c with h/c a parameter. ($\gamma = 6^\circ$, $t/c = 0.25$, $\alpha = 0^\circ$, r_{max})
- Figure C.8: Hydrodynamic forces versus σ_c with h/c a parameter. ($\gamma = 7^\circ$, $t/c = 0.25$, $\alpha = 0^\circ$, r_{max}).



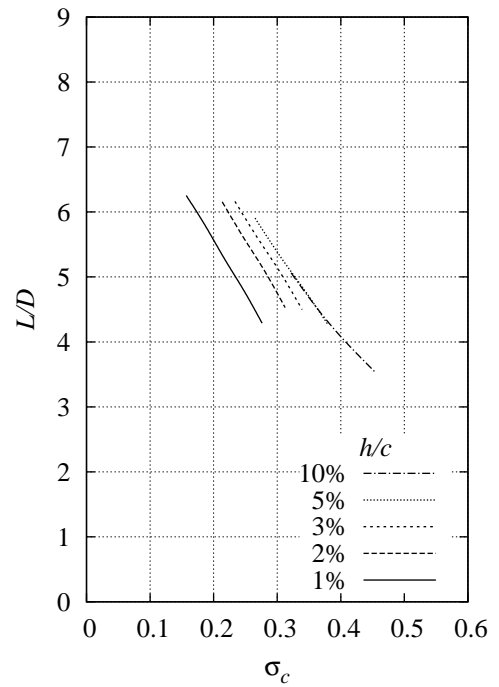
(a) Lift.



(b) Drag.

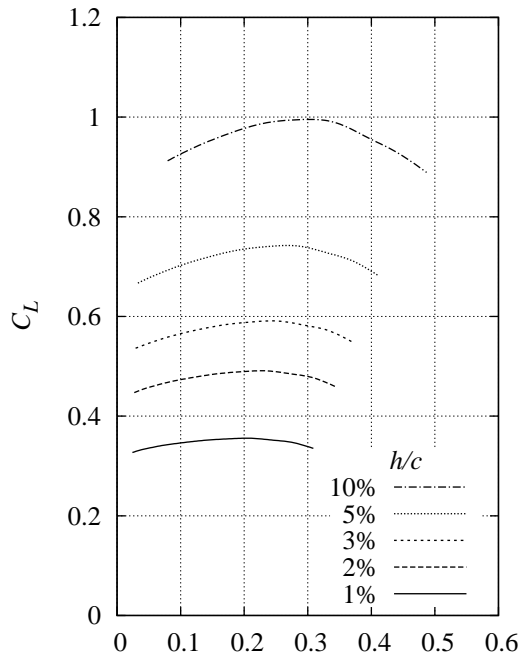


(c) Moment.

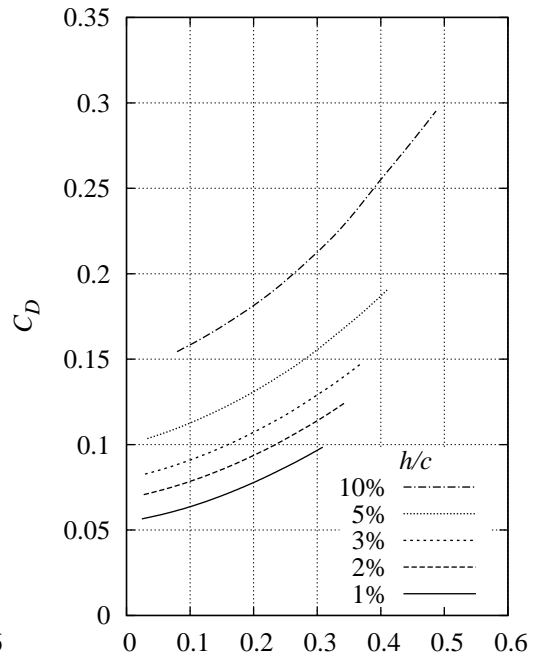


(d) Efficiency.

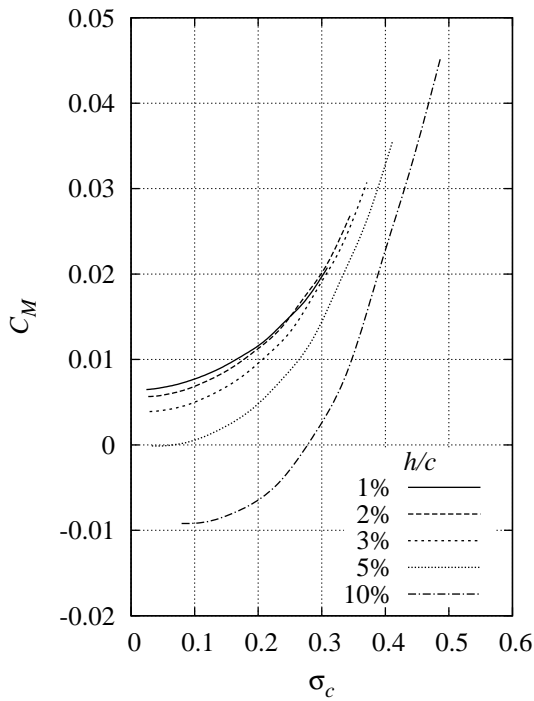
Figure C.5: Hydrodynamic forces versus σ_c with h/c a parameter. ($\gamma = 2.5^\circ$, $t/c = 0.25$, $\alpha = 0^\circ$, r_{max}): a) C_L ; b) C_D ; c) C_M ; and d) L/D .



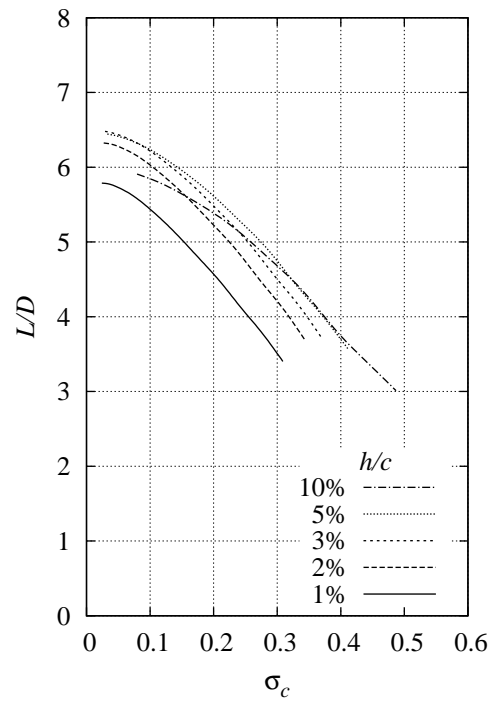
(a) Lift.



(b) Drag.

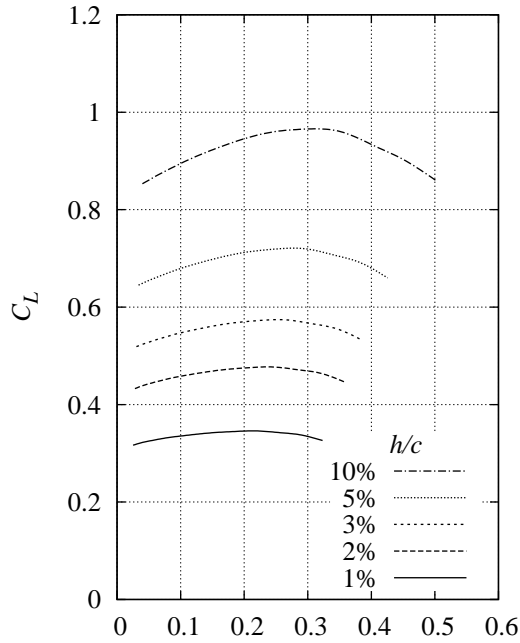


(c) Moment.

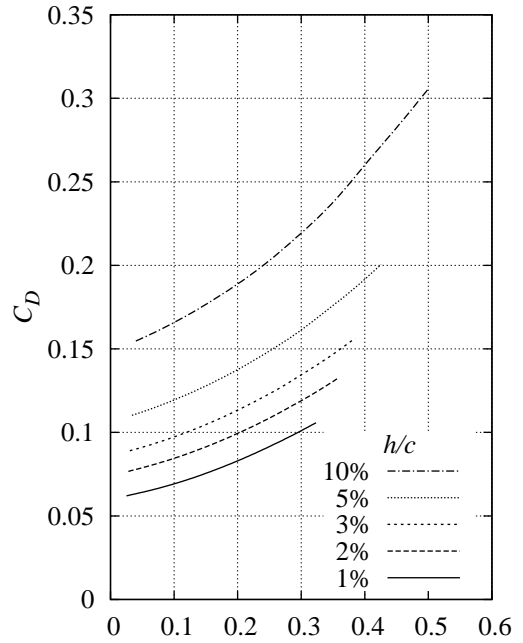


(d) Efficiency.

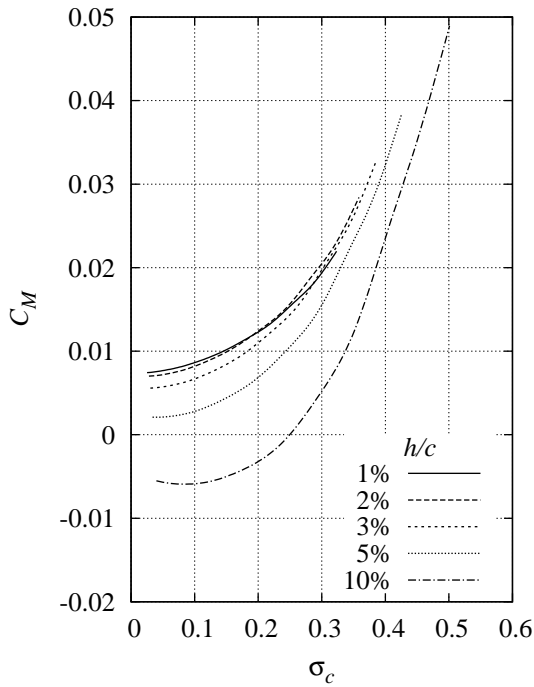
Figure C.6: Hydrodynamic forces versus σ_c with h/c a parameter. ($\gamma = 5^\circ$, $t/c = 0.25$, $\alpha = 0^\circ$, r_{max}): a) C_L ; b) C_D ; c) C_M ; and d) L/D .



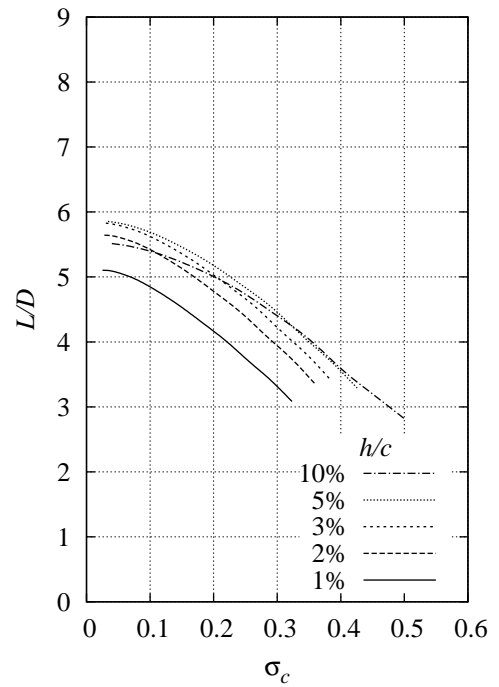
(a) Lift.



(b) Drag.

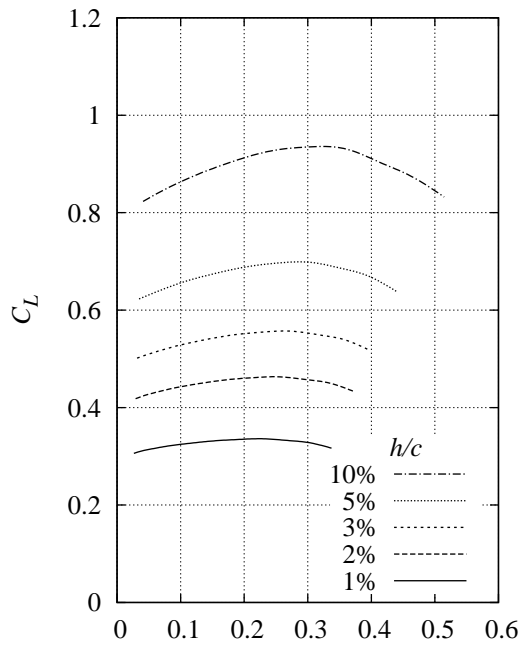


(c) Moment.

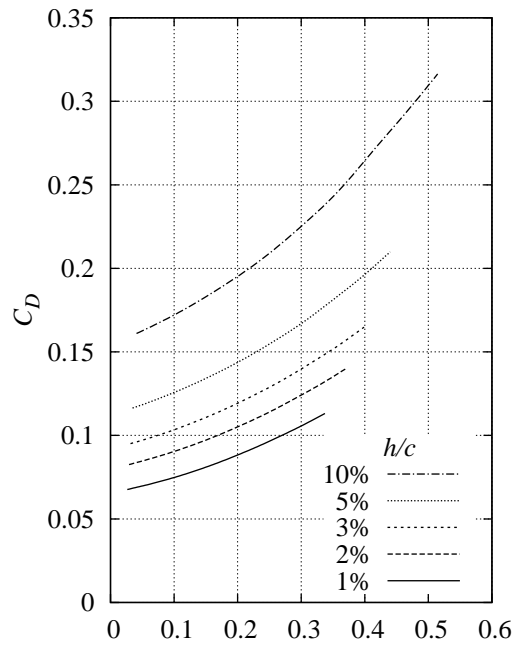


(d) Efficiency.

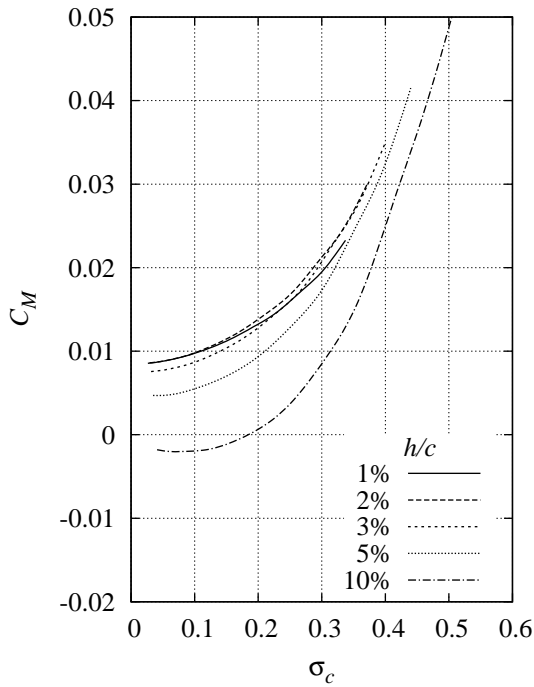
Figure C.7: Hydrodynamic forces versus σ_c with h/c a parameter. ($\gamma = 6^\circ$, $t/c = 0.25$, $\alpha = 0^\circ$, r_{max}): a) C_L ; b) C_D ; c) C_M ; and d) L/D .



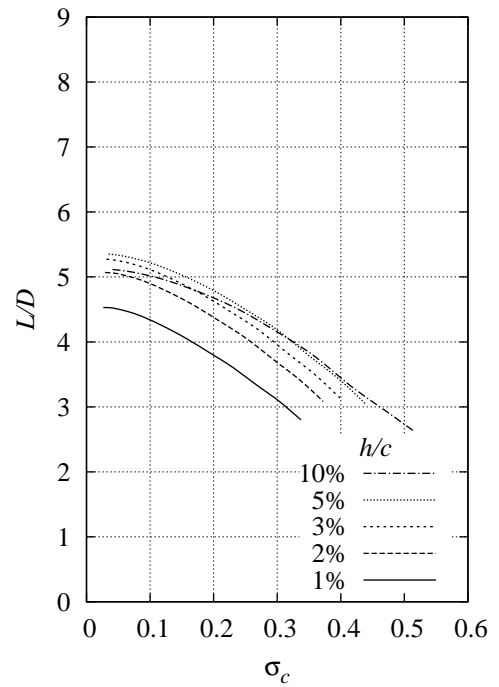
(a) Lift.



(b) Drag.



(c) Moment.



(d) Efficiency.

Figure C.8: Hydrodynamic forces versus σ_c with h/c a parameter. ($\gamma = 7^\circ$, $t/c = 0.25$, $\alpha = 0^\circ$, r_{max}): a) C_L ; b) C_D ; c) C_M ; and d) L/D .

Appendix D

Additional Foil Numerical Analysis Blockage Data

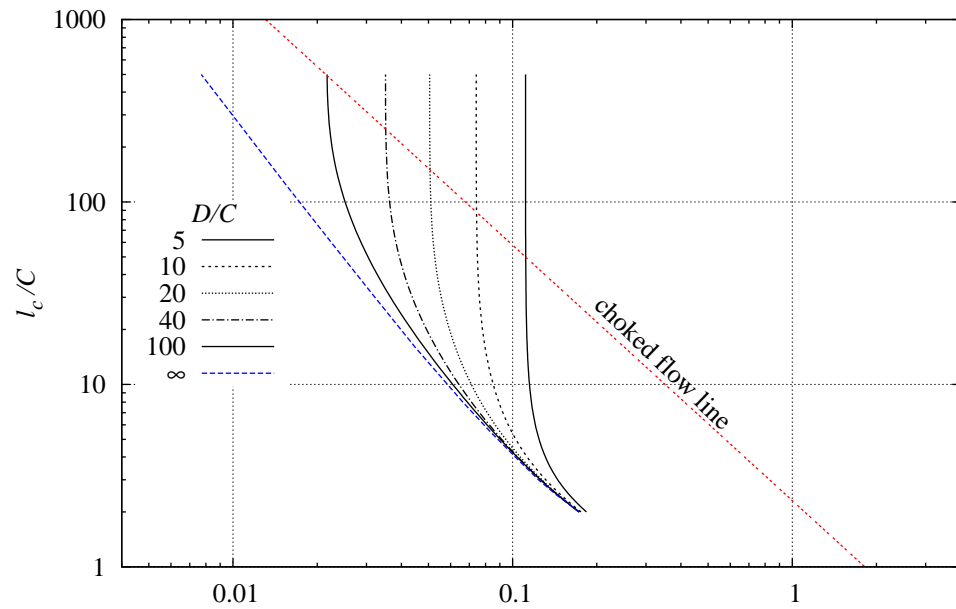
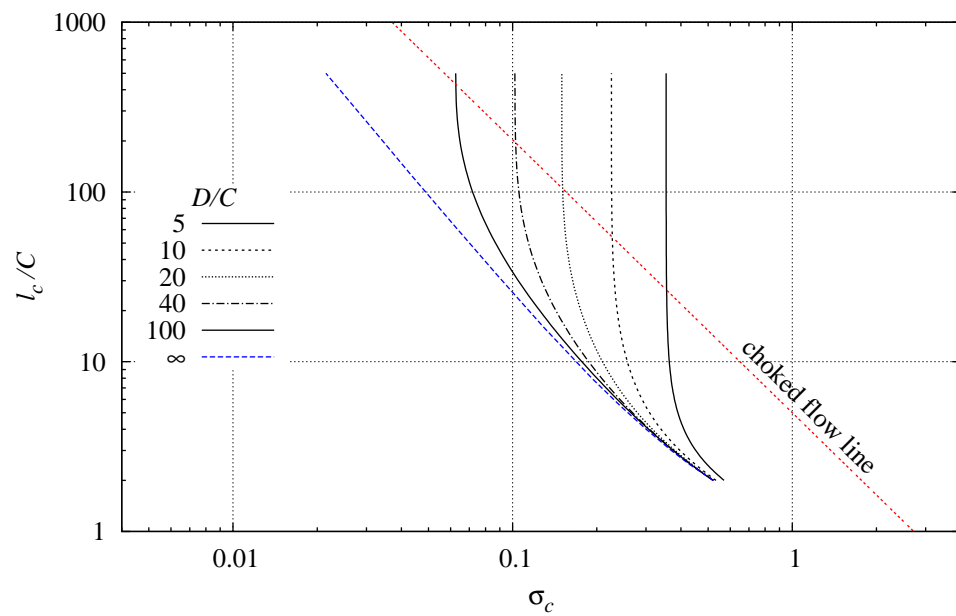
This appendix includes the complete data set of which only a portion was given in Chapter 5 as typical examples.

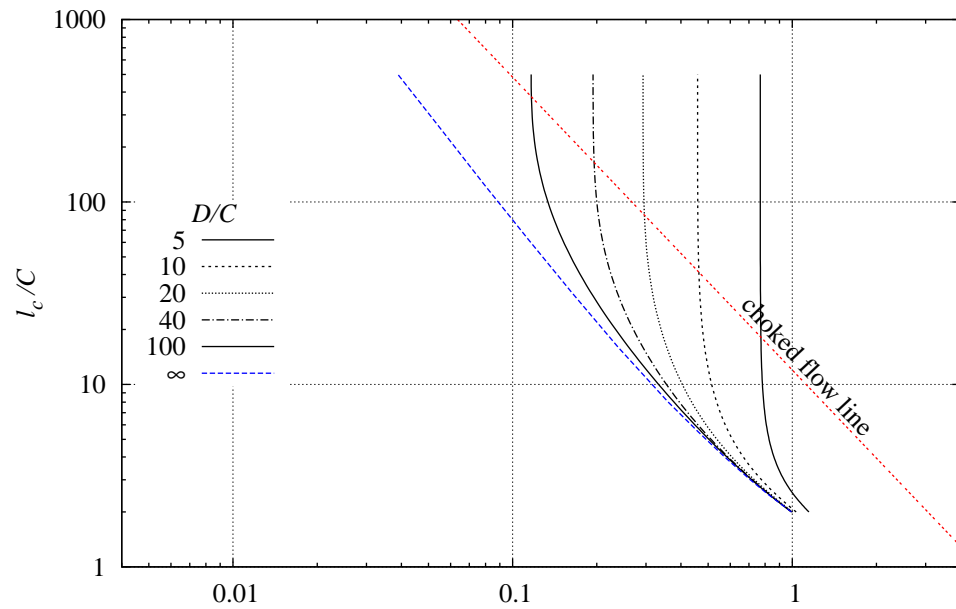
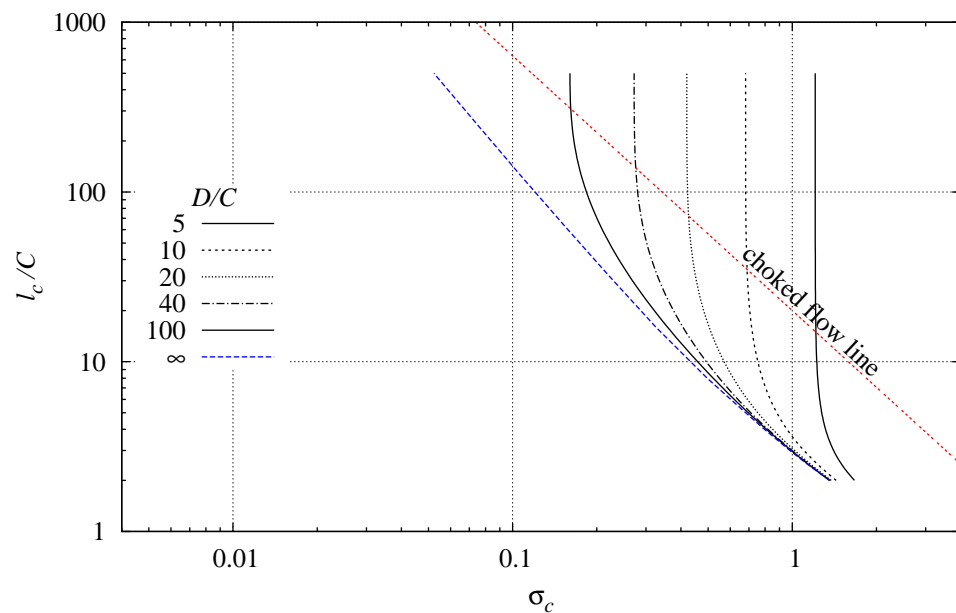
D.1 Flat-Plate Foil Data

D.1.1 Cavity Shape

Dimensionless cavity length versus σ_c with D/C a parameter for:

- Figure D.1: $\alpha = 5^\circ$ and 15°
- Figure D.2: $\alpha = 30^\circ$ and 45°
- Figure D.3: $\alpha = 60^\circ$ and 75°
- Figure D.4: $\alpha = 90^\circ$.

(a) $\alpha = 5^\circ$ (b) $\alpha = 15^\circ$ Figure D.1: Dimensionless cavity length versus σ_c for $\alpha = 5^\circ$ and 15° with D/C a parameter.

(a) $\alpha = 30^\circ$ (b) $\alpha = 45^\circ$ Figure D.2: Dimensionless cavity length versus σ_c for $\alpha = 30^\circ$ and 45° with D/C a parameter.

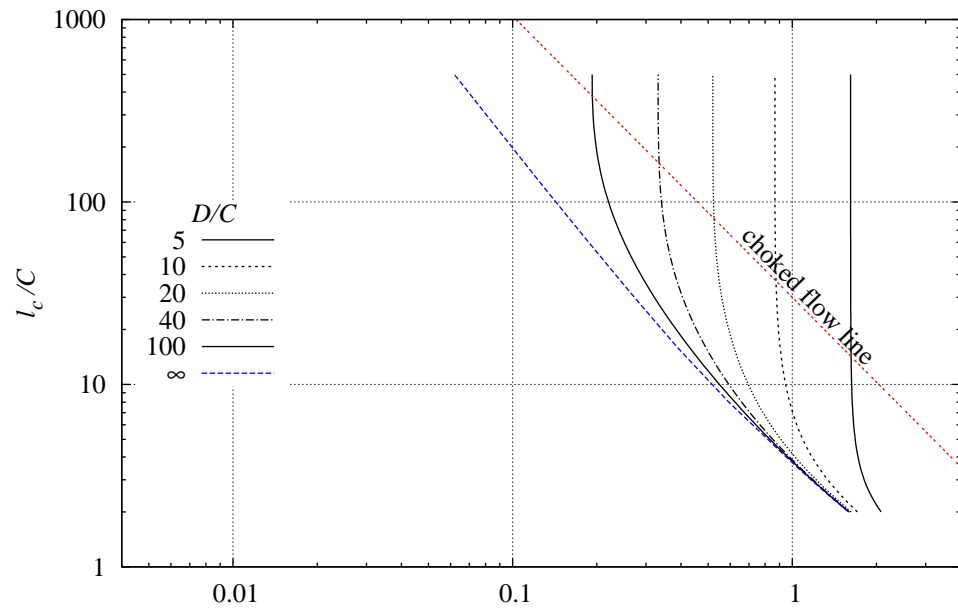
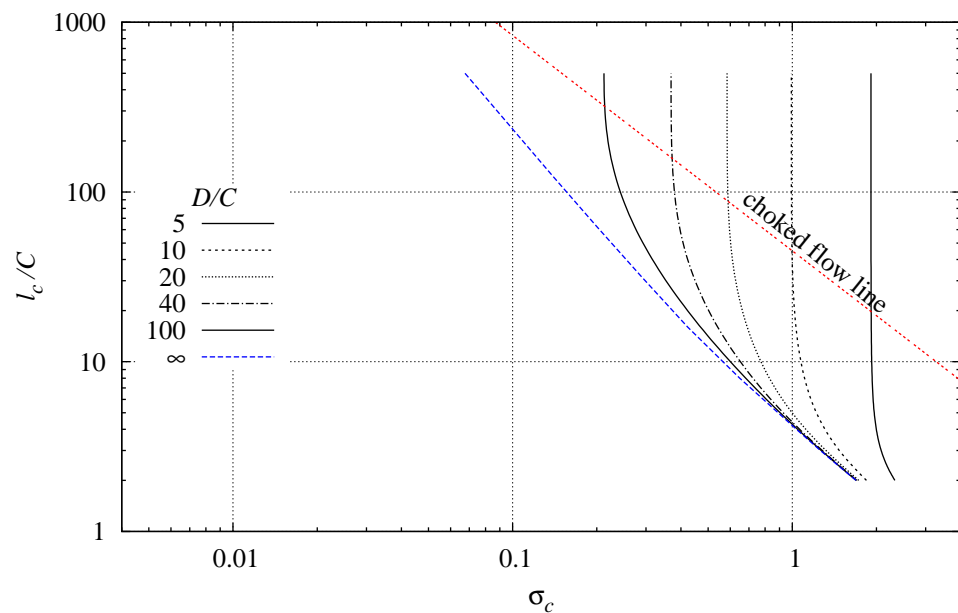
(a) $\alpha = 60^\circ$ (b) $\alpha = 75^\circ$

Figure D.3: Dimensionless cavity length versus σ_c for $\alpha = 60^\circ$ and 75° with D/C a parameter.

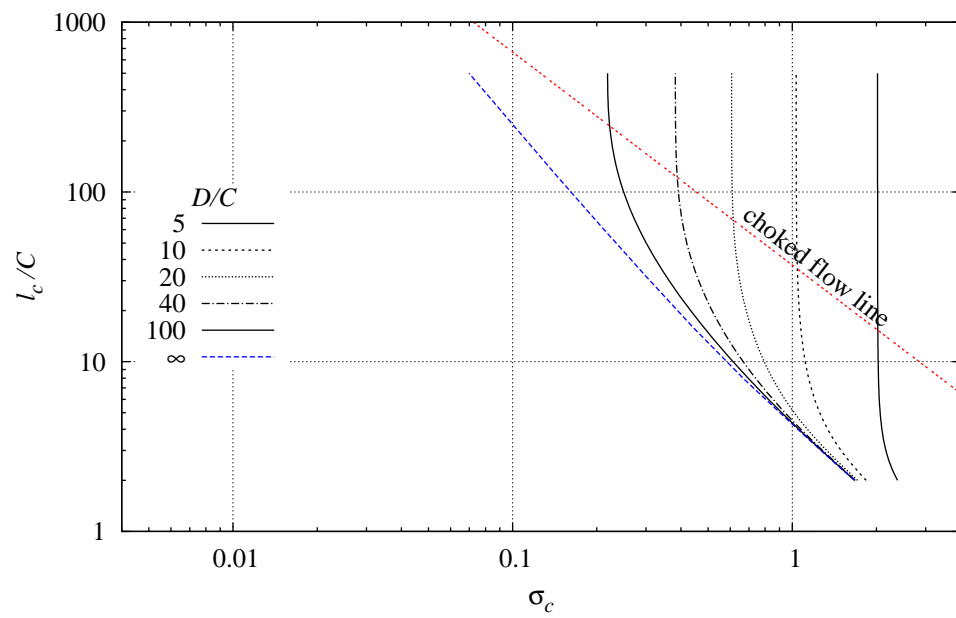


Figure D.4: Dimensionless cavity length versus σ_c for $\alpha = 90^\circ$ with D/C a parameter.

D.1.2 Hydrodynamic Forces

Blocked C_L versus σ_c with D/C a parameter for:

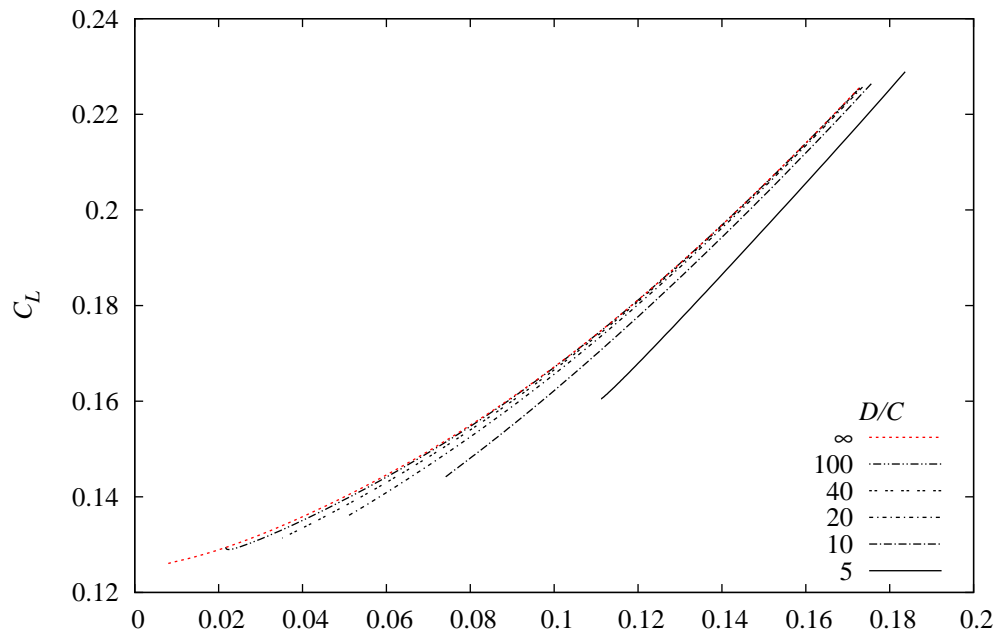
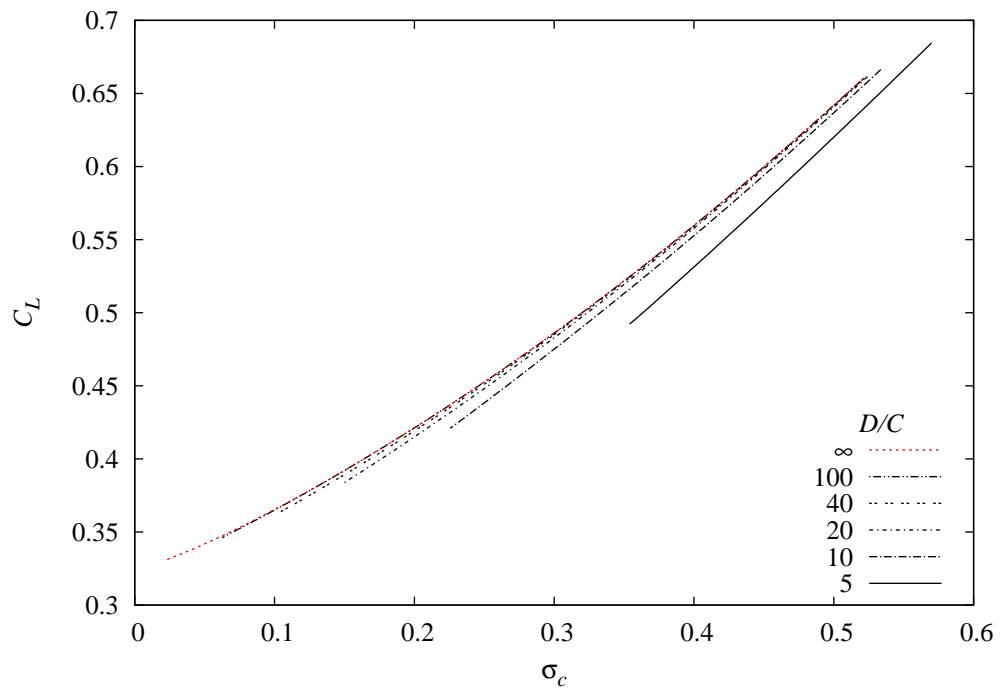
- Figure D.5: $\alpha = 5^\circ$ and 15°
- Figure D.6: $\alpha = 30^\circ$ and 45°
- Figure D.7: $\alpha = 60^\circ$ and 75° .

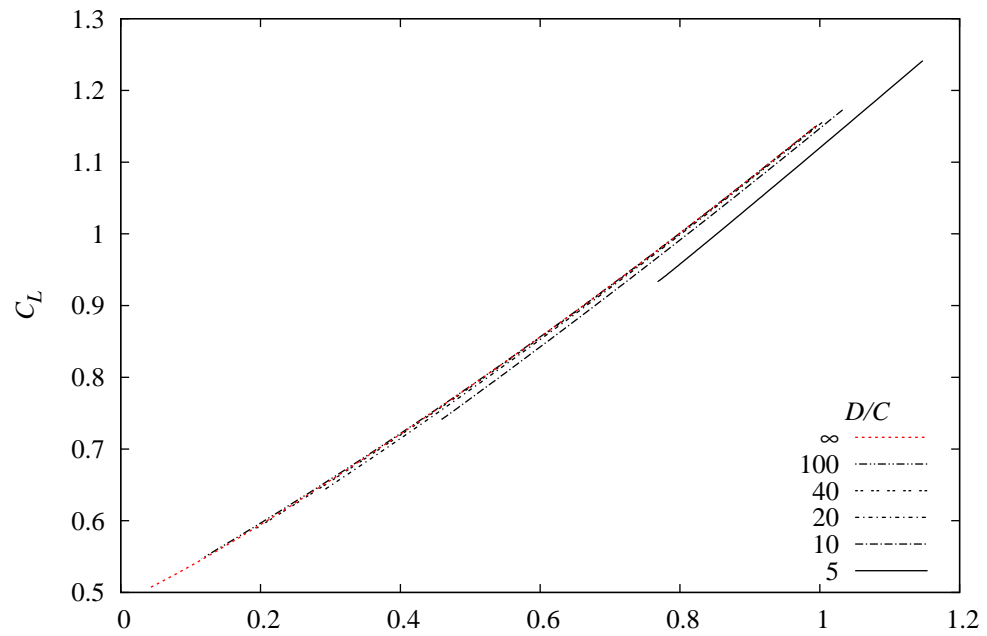
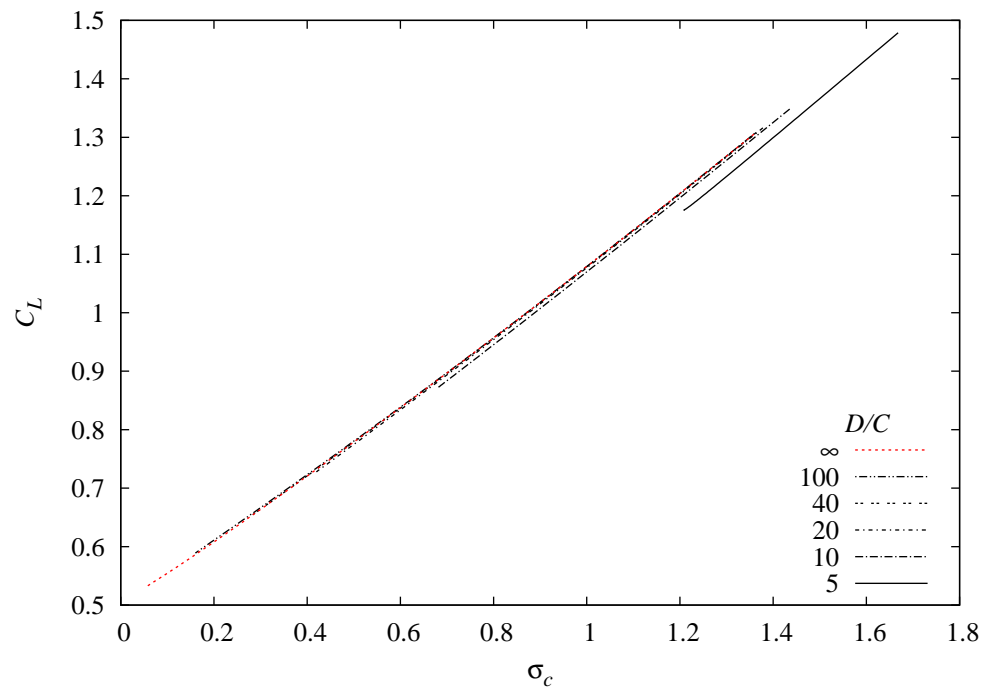
Blocked C_D versus σ_c with D/C a parameter for:

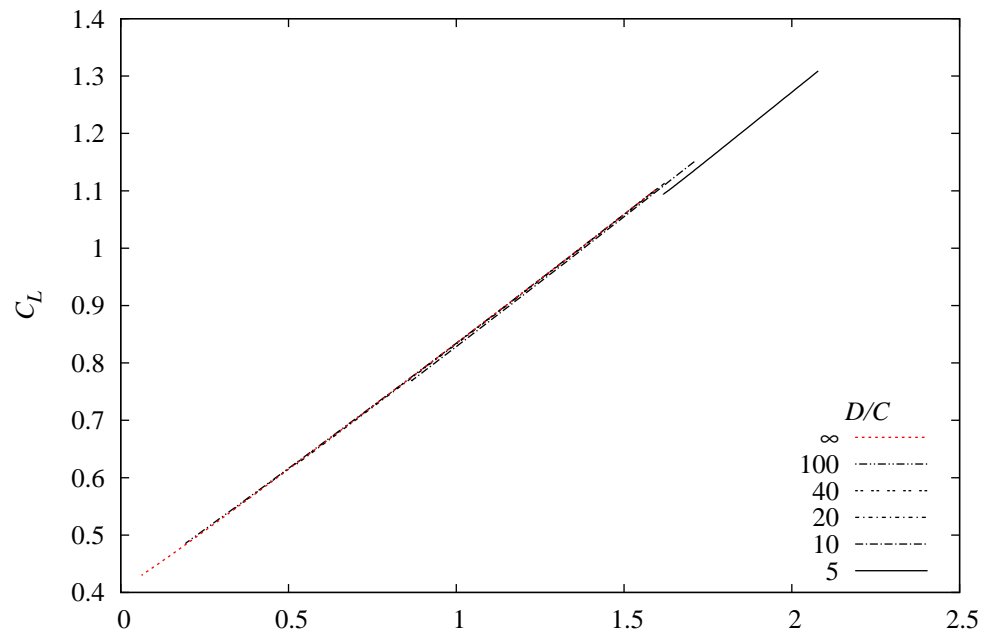
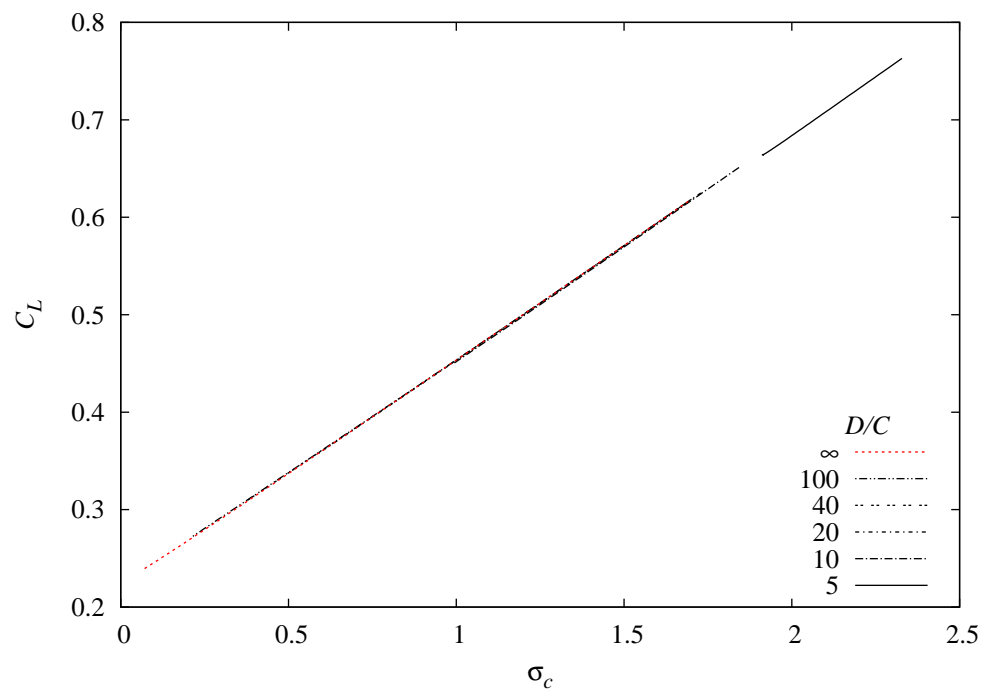
- Figure D.8: $\alpha = 5^\circ$ and 15°
- Figure D.9: σ_c for $\alpha = 30^\circ$ and 45°
- Figure D.10: $\alpha = 60^\circ$ and 75°
- Figure D.11: $\alpha = 90^\circ$.

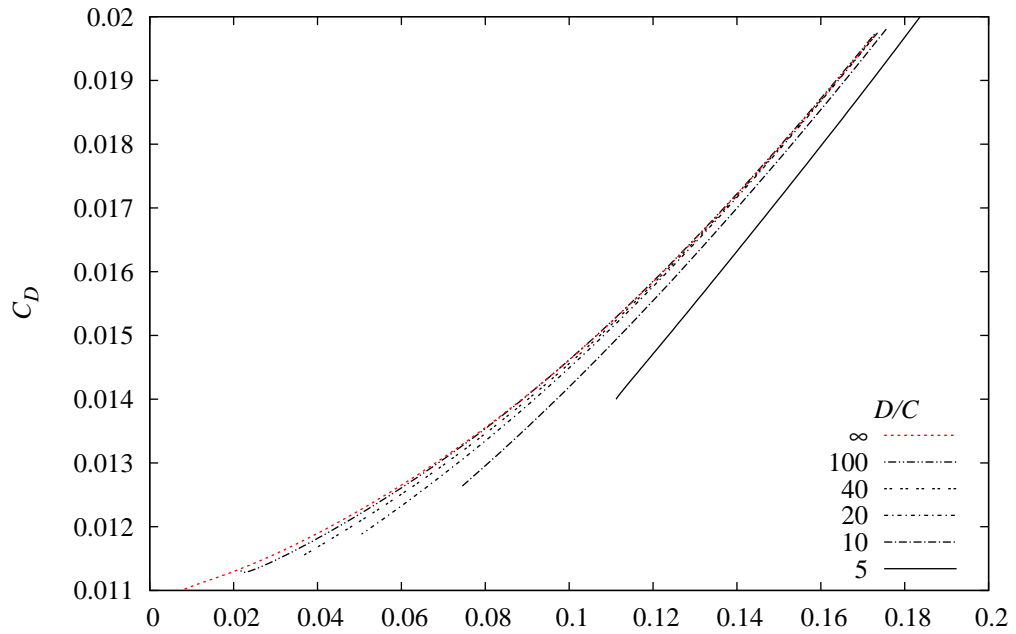
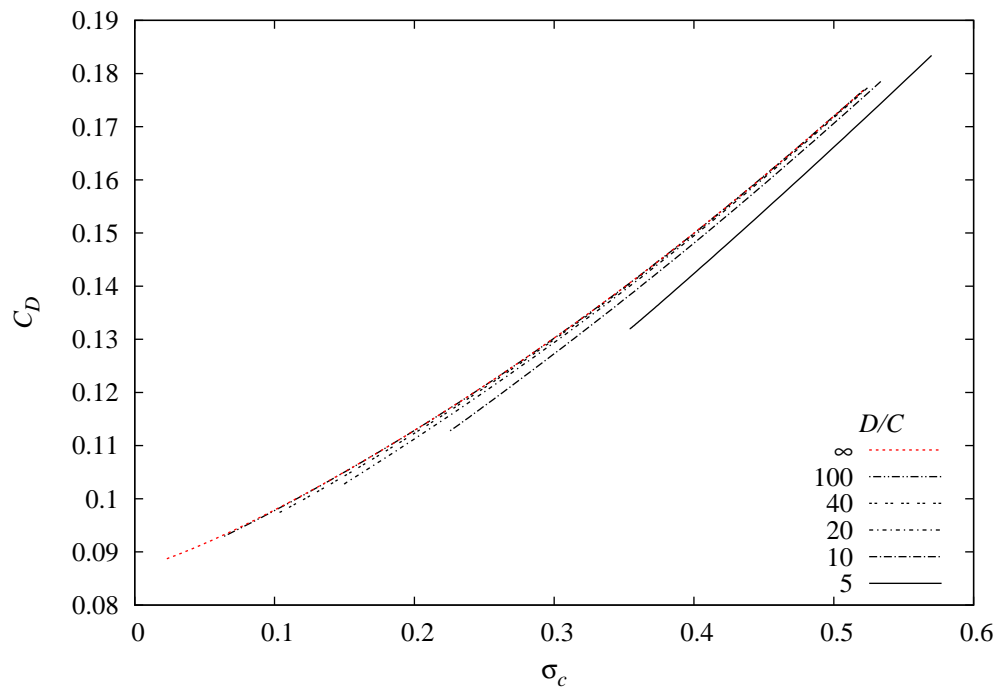
Blocked C_M versus σ_c with D/C a parameter for:

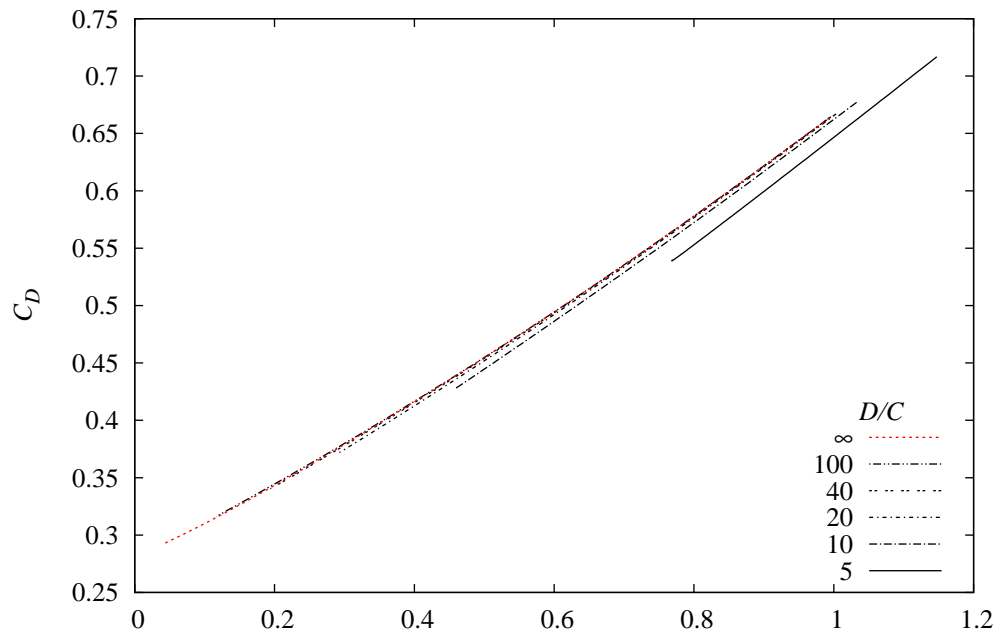
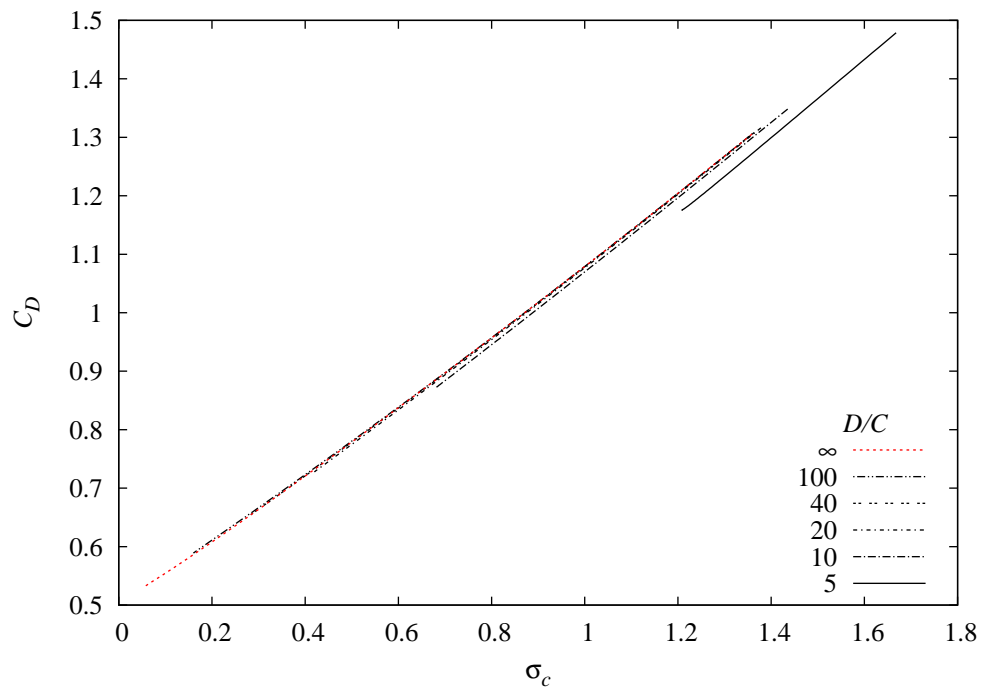
- Figure D.12: $\alpha = 5^\circ$ and 15°
- Figure D.13: $\alpha = 30^\circ$ and 45°
- Figure D.14: $\alpha = 60^\circ$ and 75° .

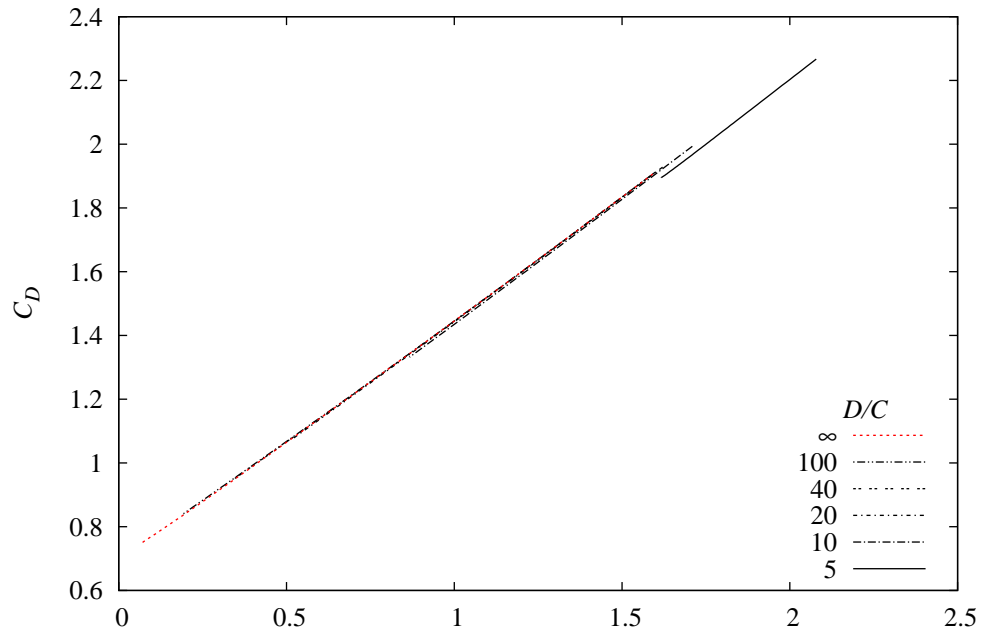
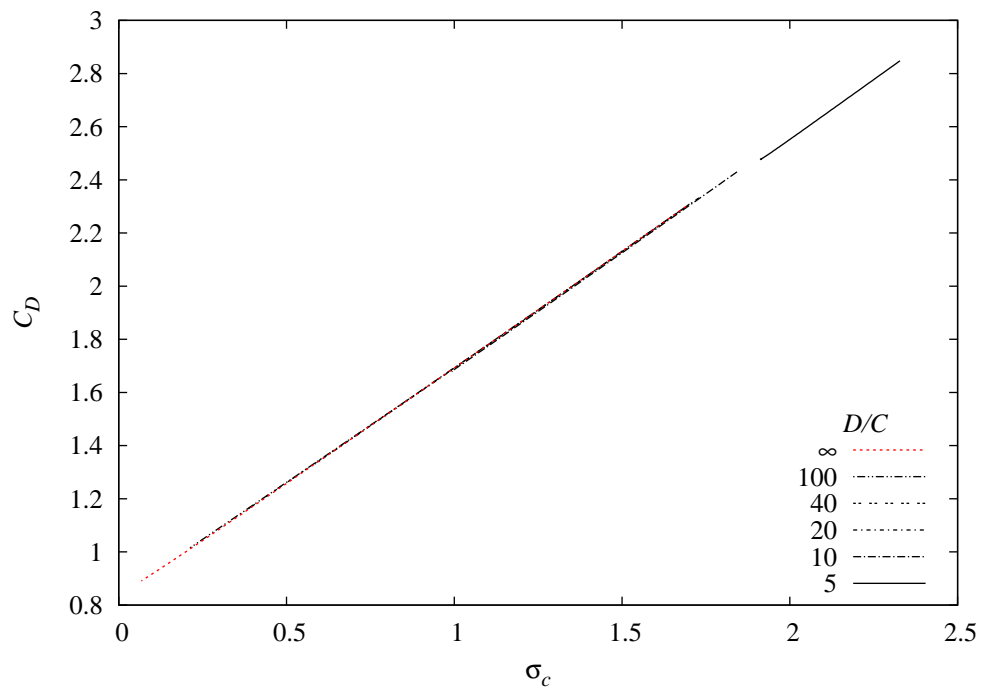
(a) $\alpha = 5^\circ$ (b) $\alpha = 15^\circ$ Figure D.5: Blocked C_L versus σ_c for $\alpha = 5^\circ$ and 10° with D/C a parameter.

(a) $\alpha = 30^\circ$ (b) $\alpha = 45^\circ$ Figure D.6: Blocked C_L versus σ_c for $\alpha = 30^\circ$ and 45° with D/C a parameter.

(a) $\alpha = 60^\circ$ (b) $\alpha = 75^\circ$ Figure D.7: Blocked C_L versus σ_c for $\alpha = 60^\circ$ and 75° with D/C a parameter.

(a) $\alpha = 5^\circ$ (b) $\alpha = 15^\circ$ Figure D.8: Blocked C_D versus σ_c for $\alpha = 5^\circ$ and 10° with D/C a parameter.

(a) $\alpha = 30^\circ$ (b) $\alpha = 45^\circ$ Figure D.9: Blocked C_D versus σ_c for $\alpha = 30^\circ$ and 45° with D/C a parameter.

(a) $\alpha = 60^\circ$ (b) $\alpha = 75^\circ$ Figure D.10: Blocked C_D versus σ_c for $\alpha = 60^\circ$ and 75° with D/C a parameter.

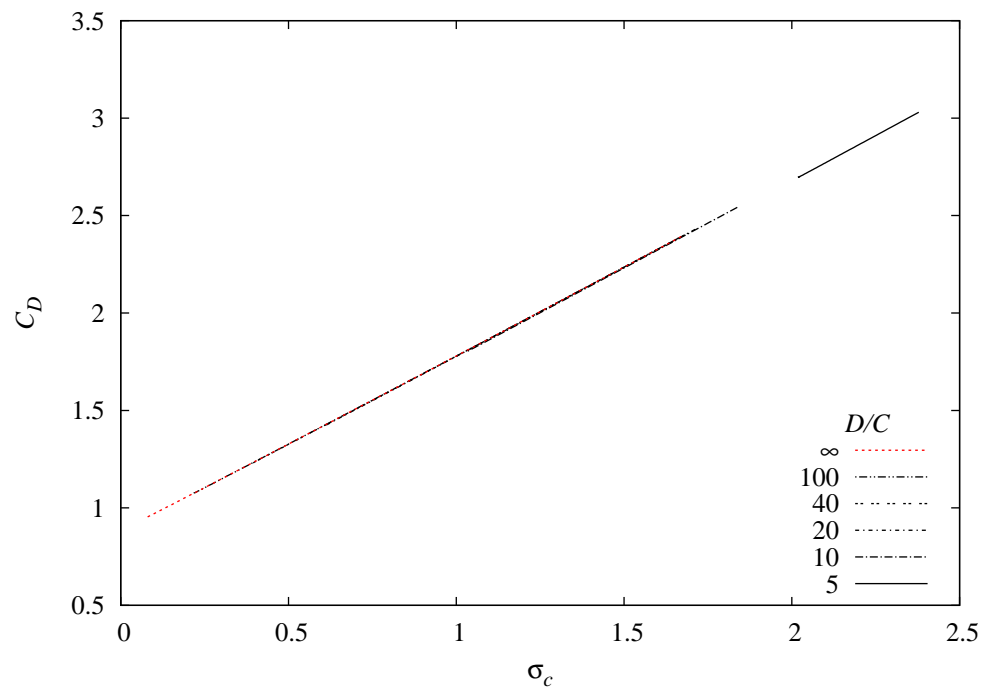
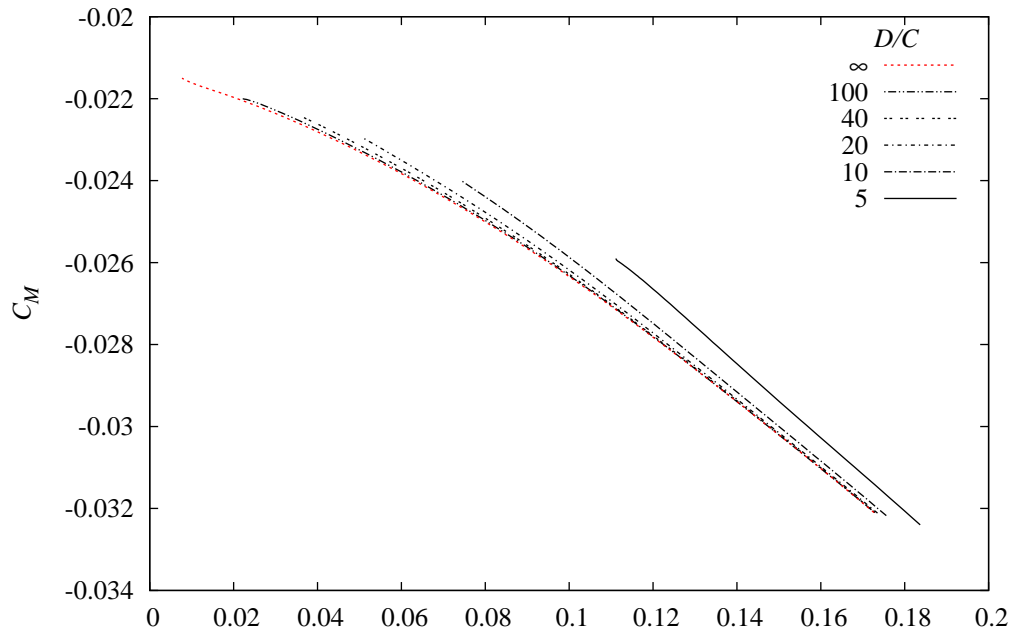
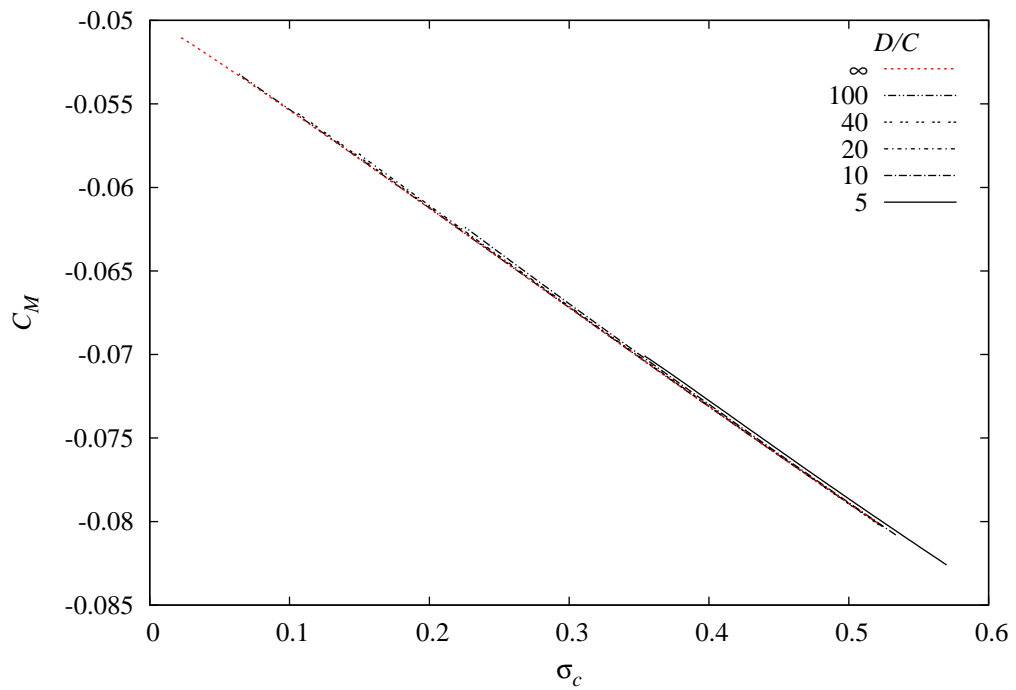
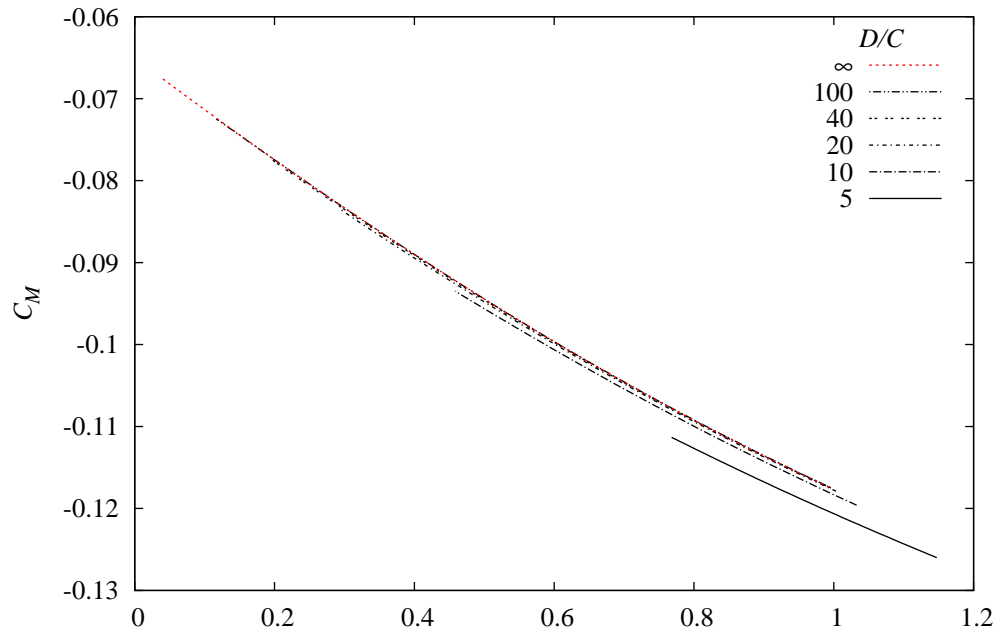
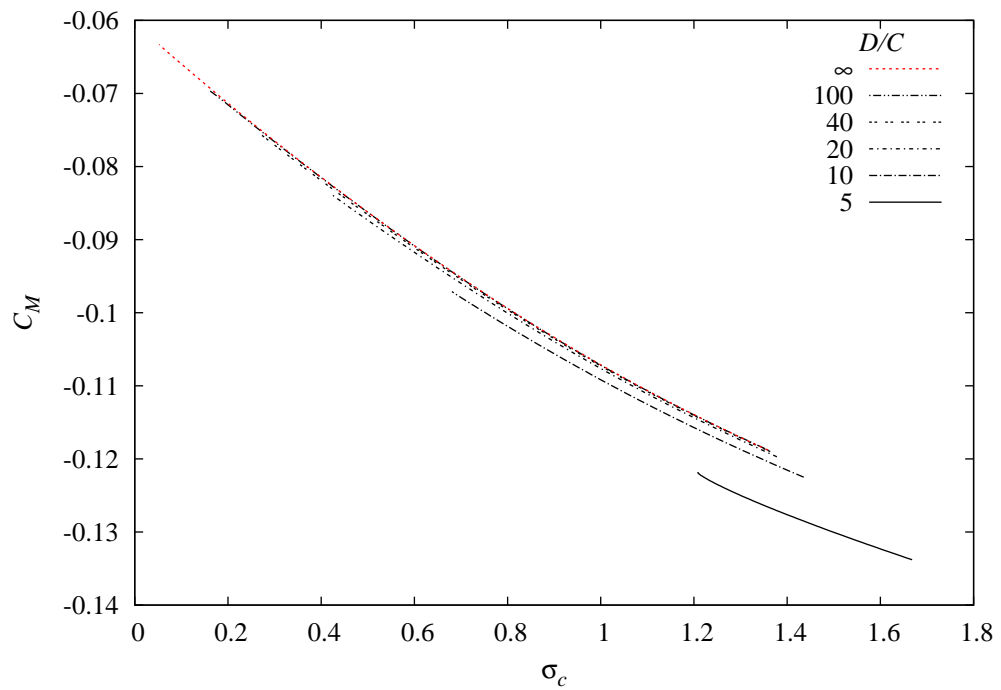
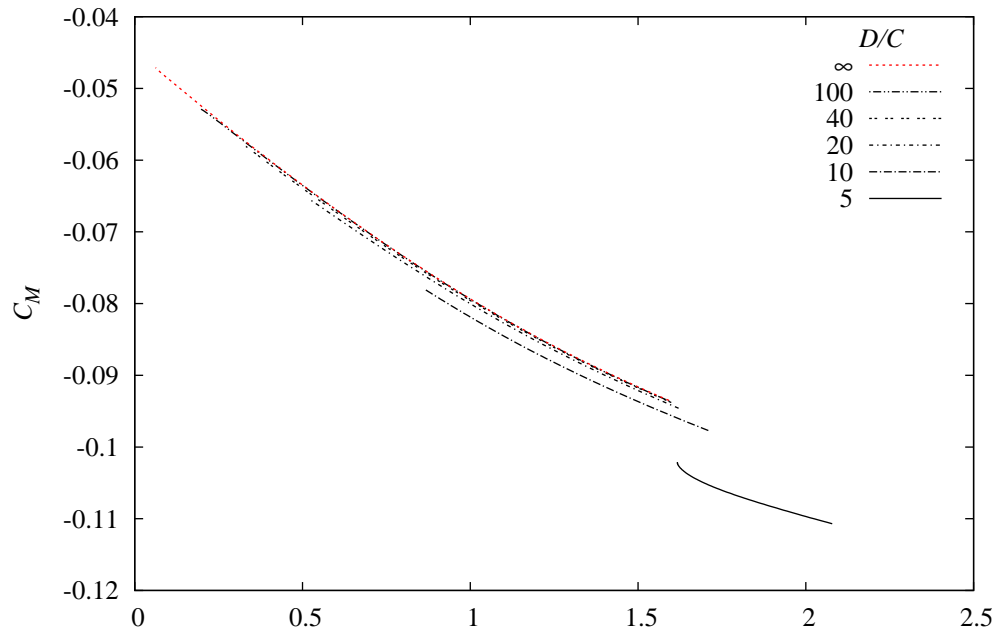
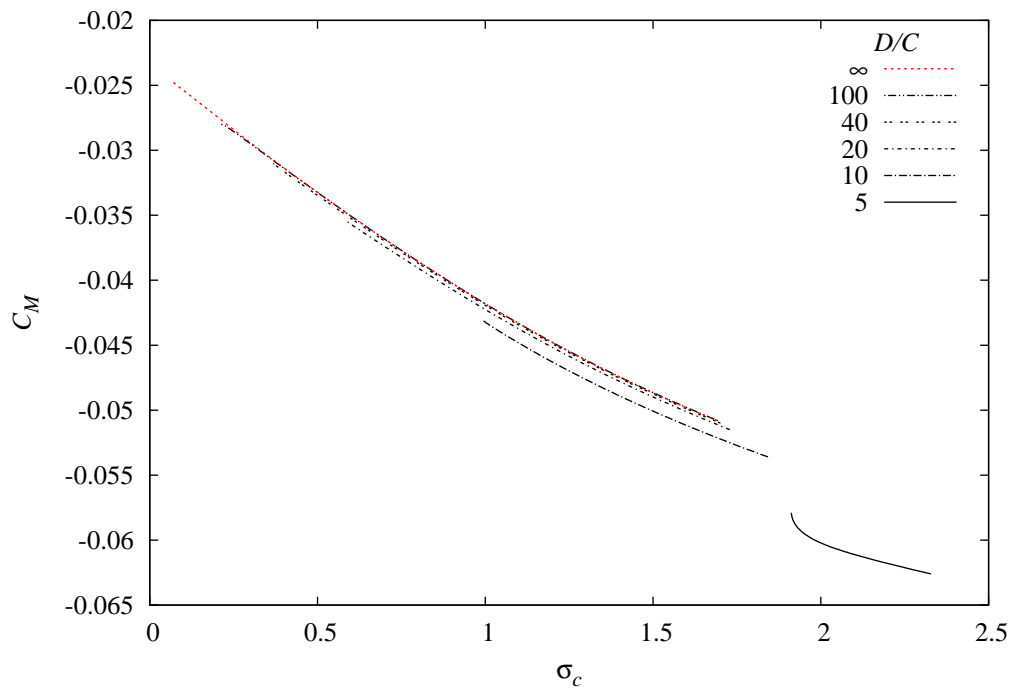


Figure D.11: Blocked C_D versus σ_c for $\alpha = 90^\circ$ with D/C a parameter.

(a) $\alpha = 5^\circ$ (b) $\alpha = 15^\circ$ Figure D.12: Blocked C_M versus σ_c for $\alpha = 5^\circ$ and 10° with D/C a parameter.

(a) $\alpha = 30^\circ$ (b) $\alpha = 45^\circ$ Figure D.13: Blocked C_M versus σ_c for $\alpha = 30^\circ$ and 45° with D/C a parameter.

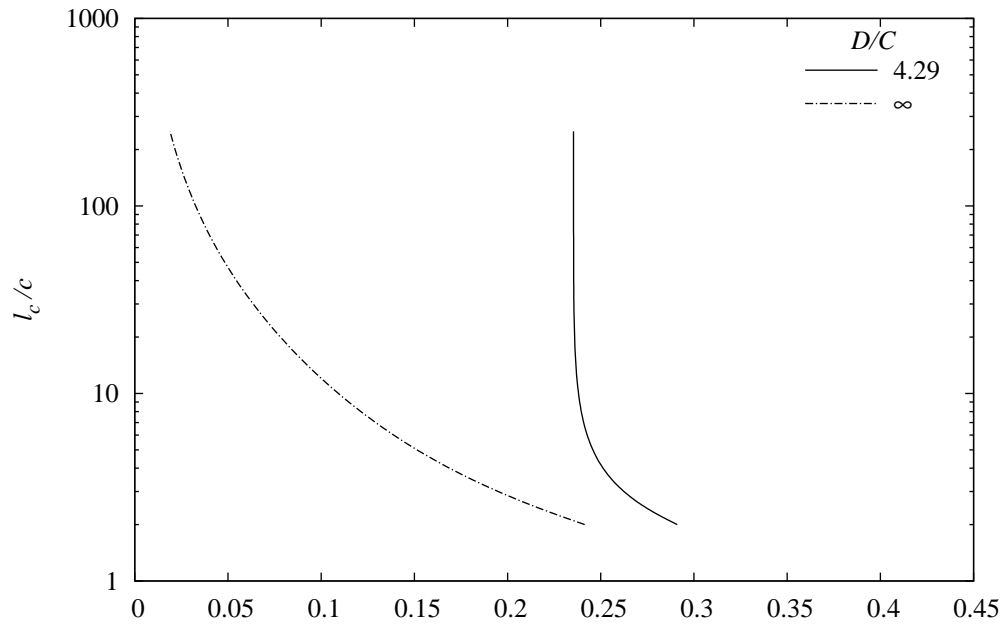
(a) $\alpha = 60^\circ$ (b) $\alpha = 75^\circ$ Figure D.14: Blocked C_M versus σ_c for $\alpha = 60^\circ$ and 75° with D/C a parameter.

D.2 Intercepted Foil Data

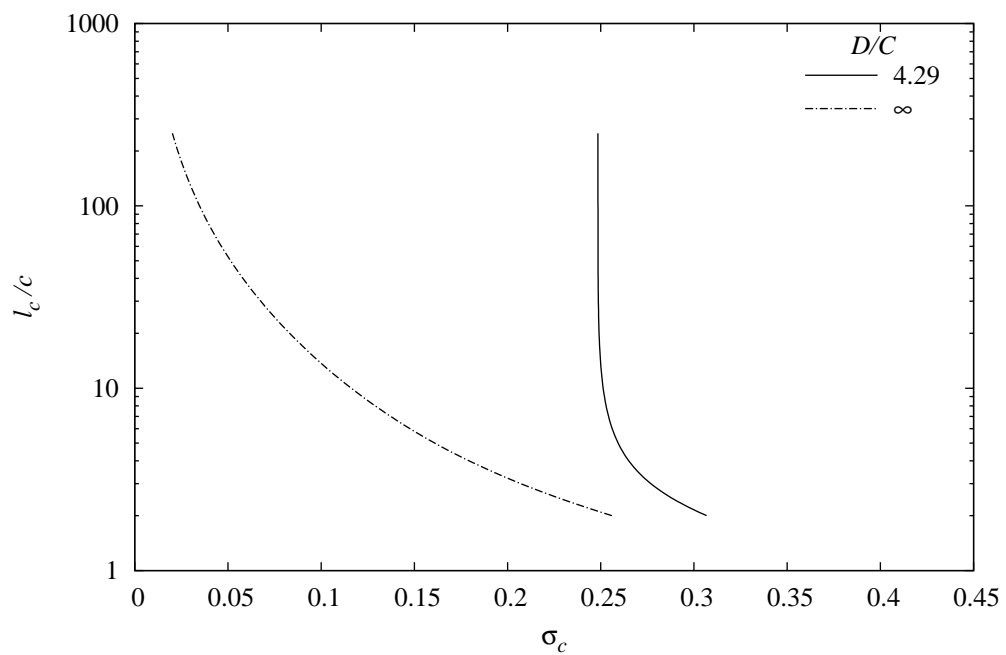
D.2.1 Cavity Shape

l_c/c versus σ_c ($\alpha = 0^\circ$) for:

- Figure D.15: Foil1 and Foil2
- Figure D.16: Foil3 and Foil4
- Figure D.17: Foil5.

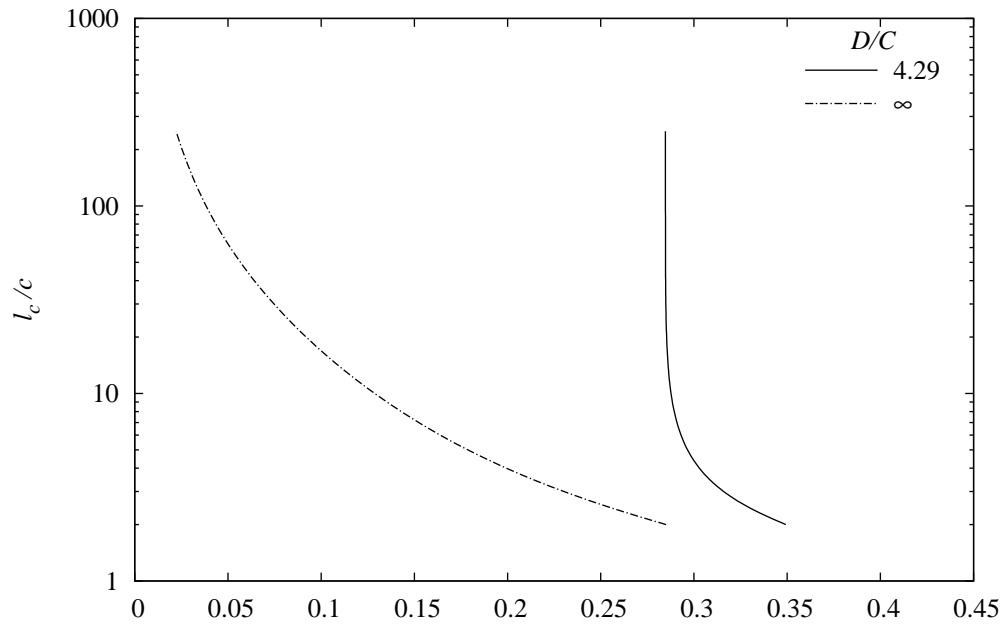


(a) Foil1.

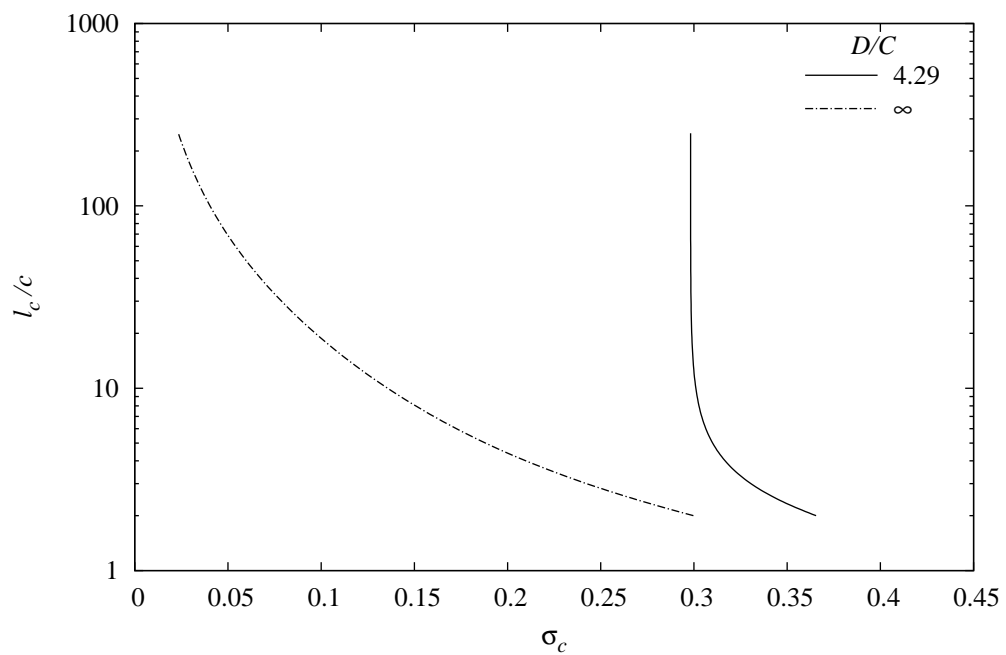


(b) Foil2.

Figure D.15: l_c/c versus σ_c for intercepted foils at zero incidence: (a) Foil1 (Geometry: $t/c = 20\%$, $\gamma = 3^\circ$ and $h/c = 1\%$); (b) Foil2 (Geometry: $t/c = 20\%$, $\gamma = 4^\circ$ and $h/c = 1\%$). Comparison of the model in CRL cavitation tunnel ($D/c = 4.29$) with the infinite flow case.



(a) Foil3.



(b) Foil4.

Figure D.16: l_c/c versus σ_c for intercepted foils at zero incidence: (a) Foil3 (Geometry: $t/c = 25\%$, $\gamma = 4^\circ$ and $h/c = 1\%$); (b) Foil4 (Geometry: $t/c = 25\%$, $\gamma = 5^\circ$ and $h/c = 1\%$). Comparison of the model in CRL cavitation tunnel ($D/c = 4.29$) with the infinite flow case.

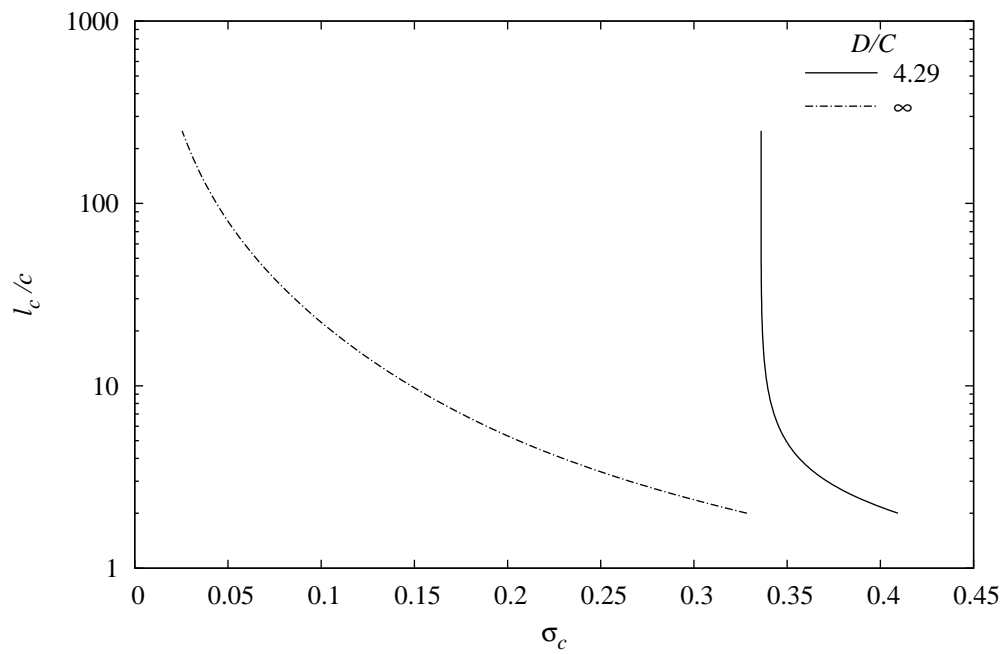


Figure D.17: l_c/c versus σ_c for model 'Foil5' at zero incidence. Comparison of the model in CRL cavitation tunnel ($D/c = 4.29$) with the infinite flow case. (Foil5 geometry: $t/c = 30\%$, $\gamma = 5^\circ$ and $h/c = 1\%$).

D.2.2 Wall Pressure Distribution

Plots of C_p distribution on the upper and lower confining walls ($D/c = 4.29$) with l_c/c a parameter for:

- Figure D.18: Foil1
- Figure D.19: Foil2
- Figure D.20: Foil3
- Figure D.21: Foil4
- Figure D.22: Foil5.

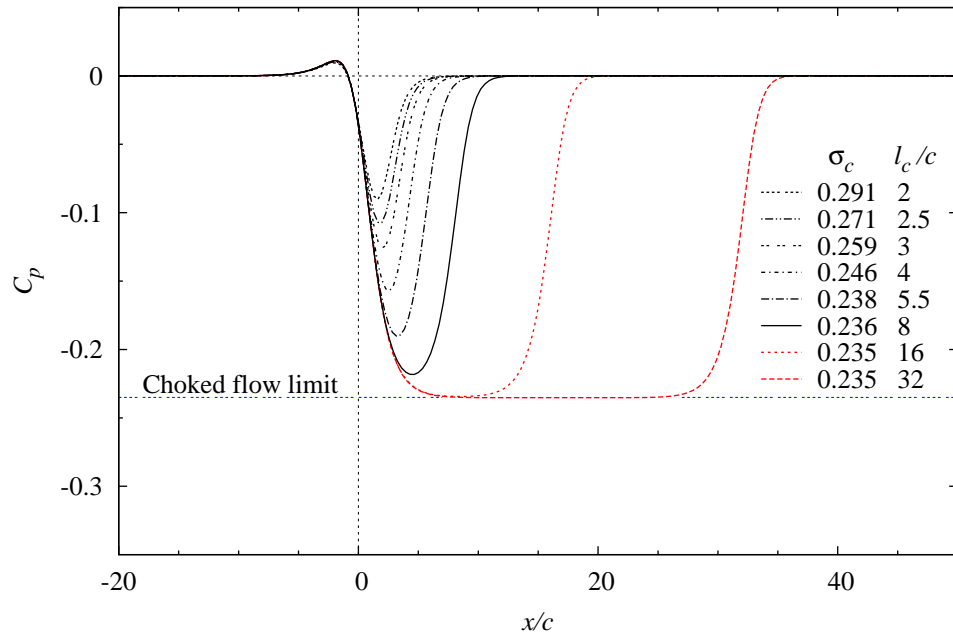
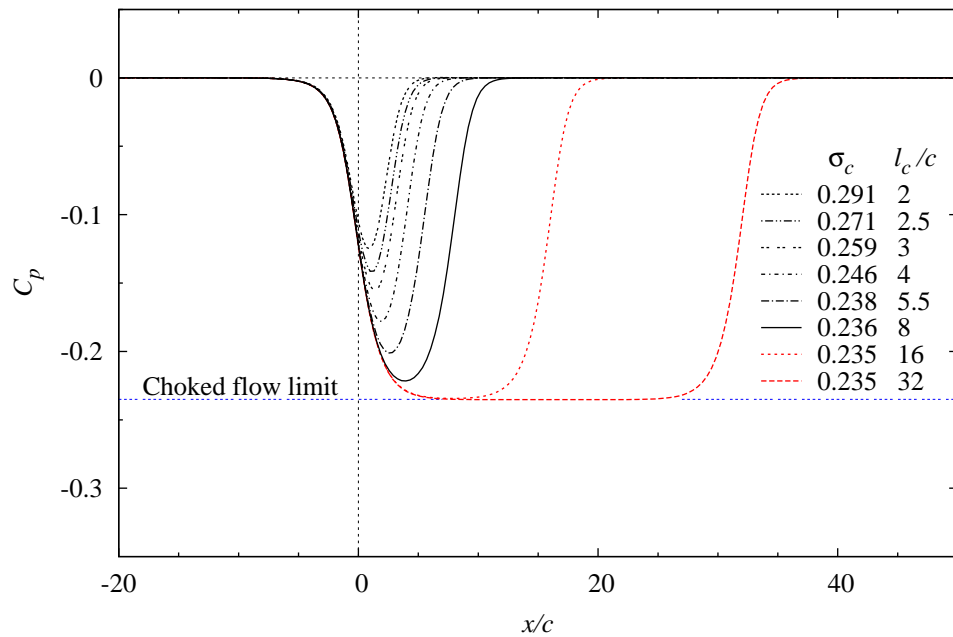
(a) C_p distribution on upper wall.(b) C_p distribution on lower wall.

Figure D.18: Plots of C_p distribution on the upper and lower confining walls for Foil1 at $D/c = 4.29$ and l_c/c a parameter. Equivalent analysis of the model foil in CRL water tunnel. (Foil1 geometry: $\alpha = 0^\circ$, $t/c = 20\%$, $h/c = 1\%$ and $\gamma = 3^\circ$). The choked flow limit is reached when $C_p = -\sigma_{ch} = -0.235$.

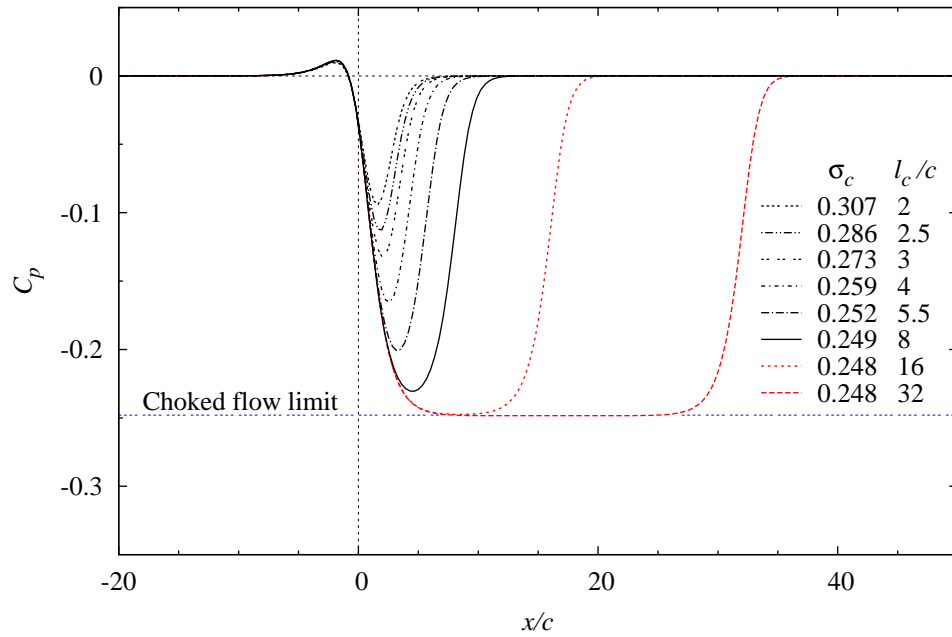
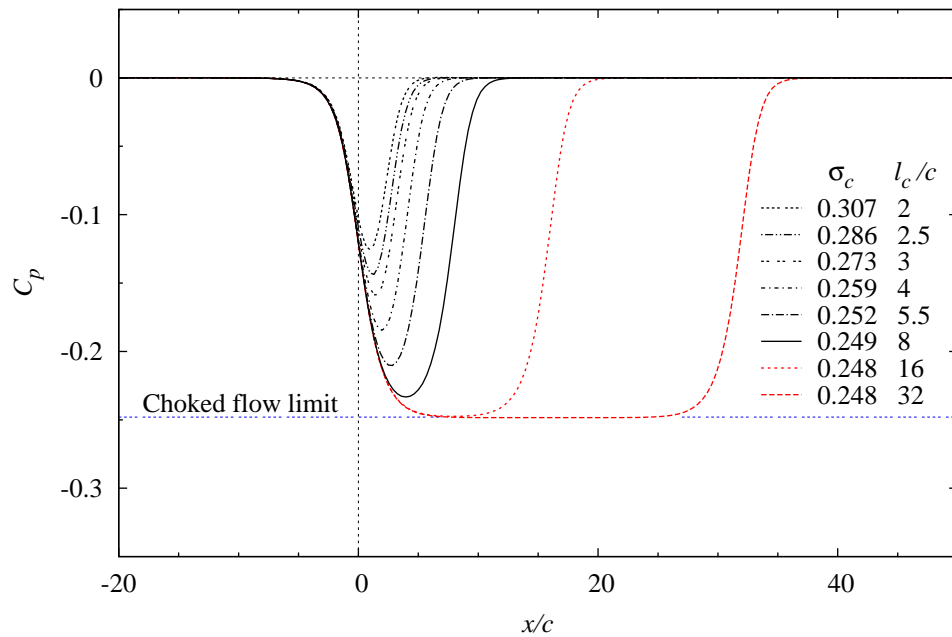
(a) C_p distribution on upper wall.(b) C_p distribution on lower wall.

Figure D.19: Plots of C_p distribution on the upper and lower confining walls for Foil2 at $D/c = 4.29$ and l_c/c a parameter. Equivalent analysis of the model foil in CRL water tunnel. (Foil2 geometry: $\alpha = 0^\circ$, $t/c = 20\%$, $h/c = 1\%$ and $\gamma = 4^\circ$). The choked flow limit is reached when $C_p = -\sigma_{ch} = -0.248$.

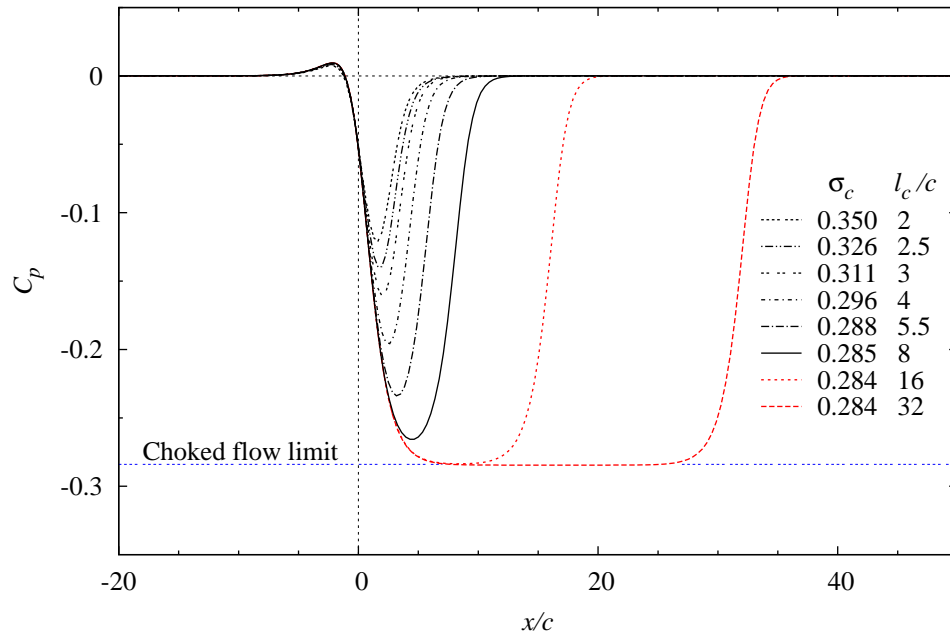
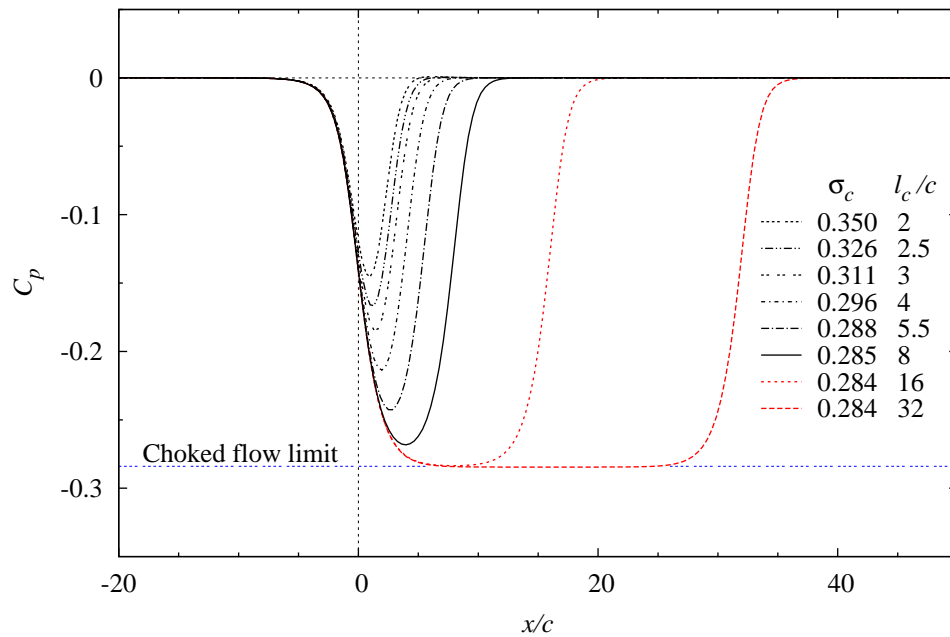
(a) C_p distribution on upper wall.(b) C_p distribution on lower wall.

Figure D.20: Plots of C_p distribution on the upper and lower confining walls for Foil3 at $D/c = 4.29$ and l_c/c a parameter. Equivalent analysis of the model foil in CRL water tunnel. (Foil3 geometry: $\alpha = 0^\circ$, $t/c = 25\%$, $h/c = 1\%$ and $\gamma = 4^\circ$). The choked flow limit is reached when $C_p = -\sigma_{ch} = -0.284$.

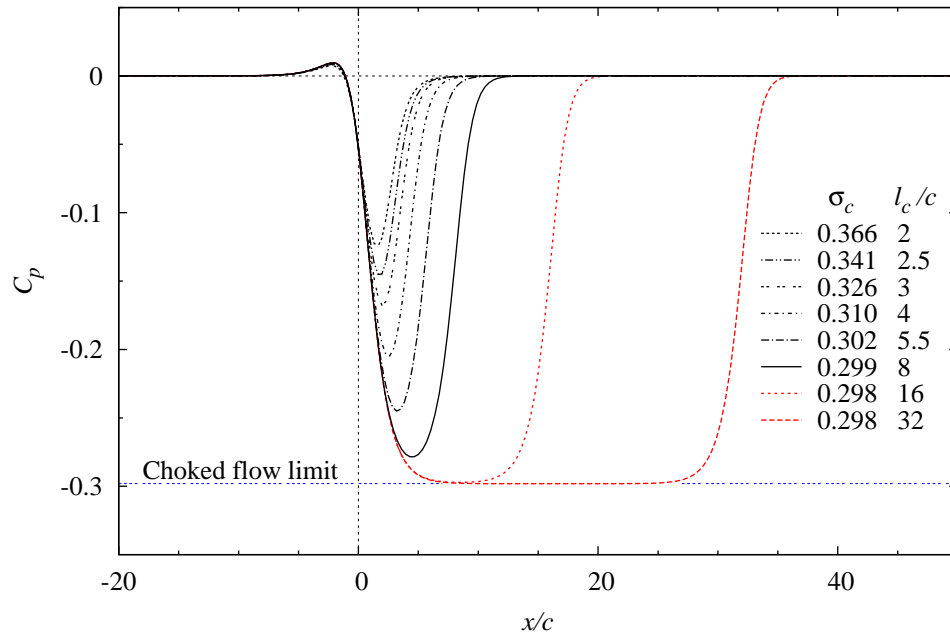
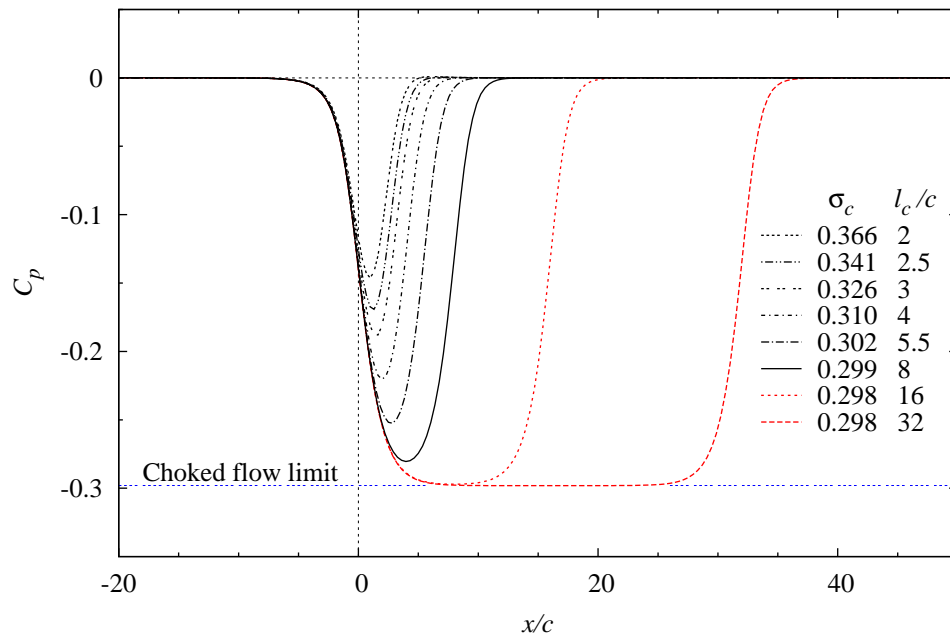
(a) C_p distribution on upper wall.(b) C_p distribution on lower wall.

Figure D.21: Plots of C_p distribution on the upper and lower confining walls for Foil4 at $D/c = 4.29$ and l_c/c a parameter. Equivalent analysis of the model foil in CRL water tunnel. (Foil4 geometry: $\alpha = 0^\circ$, $t/c = 25\%$, $h/c = 1\%$ and $\gamma = 5^\circ$). The choked flow limit is reached when $C_p = -\sigma_{ch} = -0.298$.

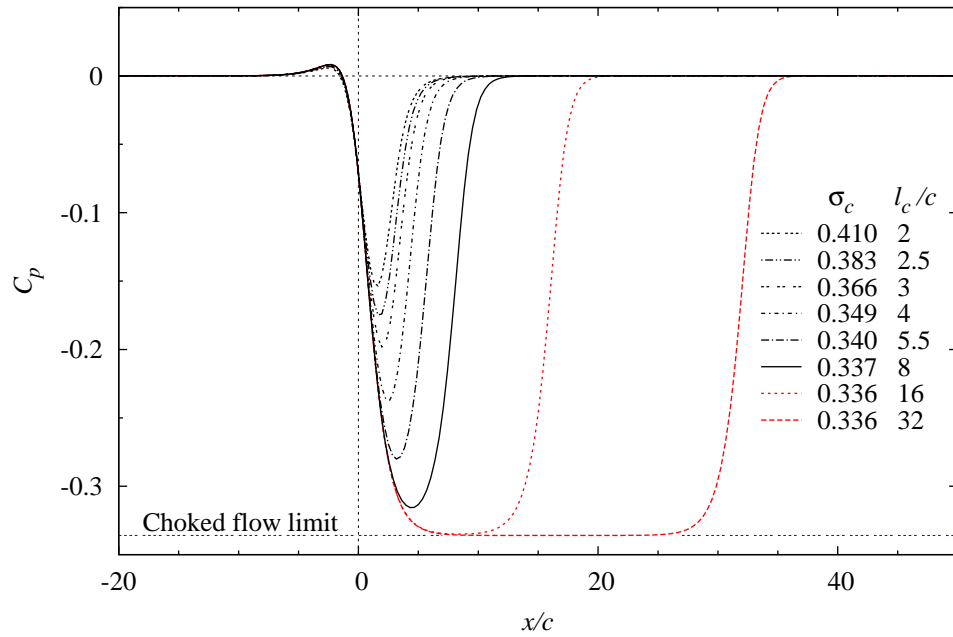
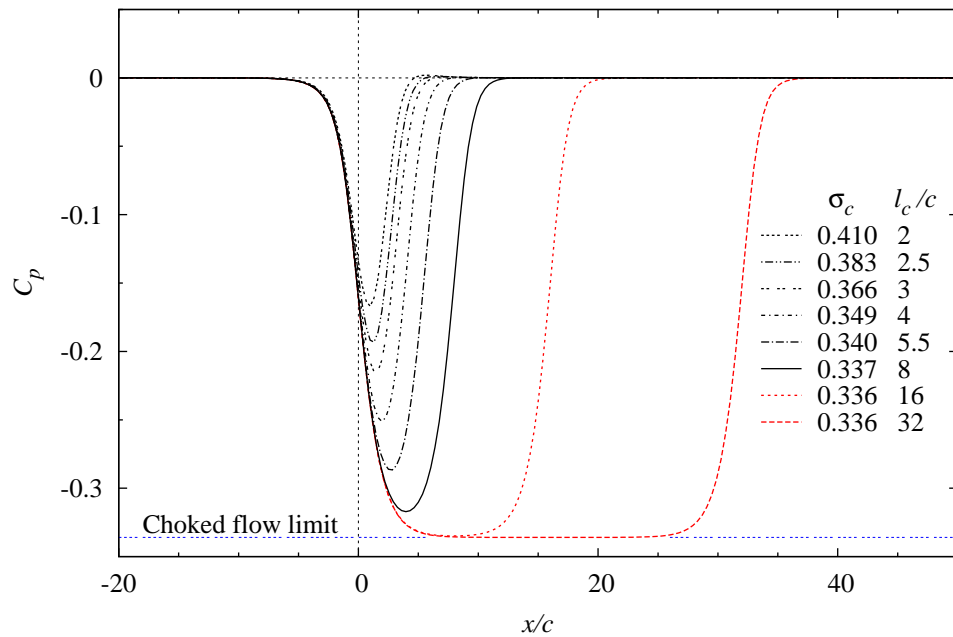
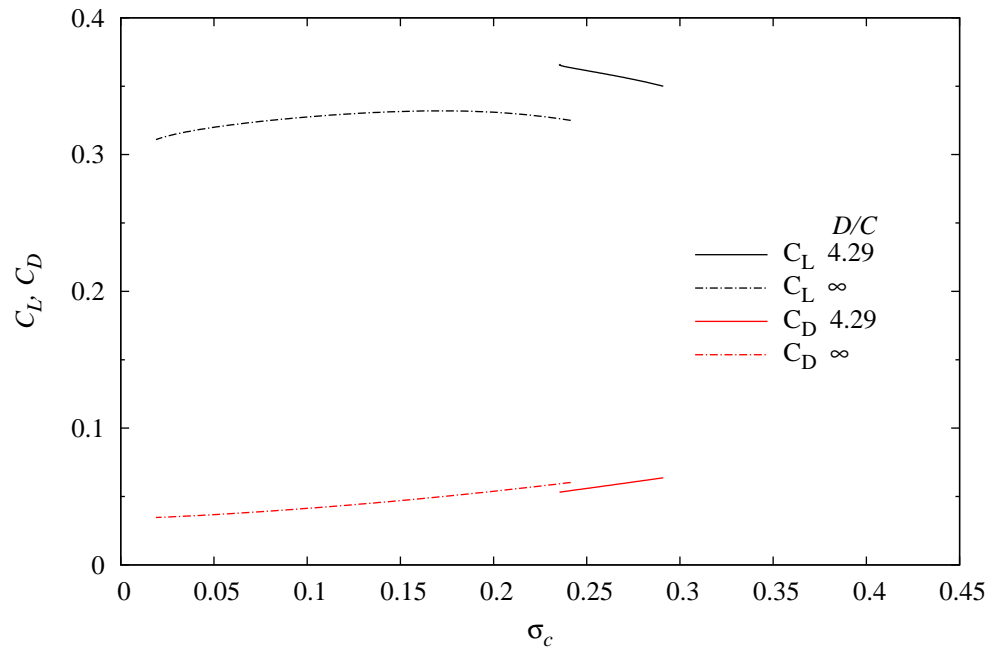
(a) C_p distribution on upper wall.(b) C_p distribution on lower wall.

Figure D.22: Plots of C_p distribution on the upper and lower confining walls for Foil5 at $D/c = 4.29$ and l_c/c a parameter. Equivalent analysis of the model foil in CRL water tunnel. (Foil5 geometry: $\alpha = 0^\circ$, $t/c = 30\%$, $h/c = 1\%$ and $\gamma = 5^\circ$). The choked flow limit is reached when $C_p = -\sigma_{ch} = -0.336$.

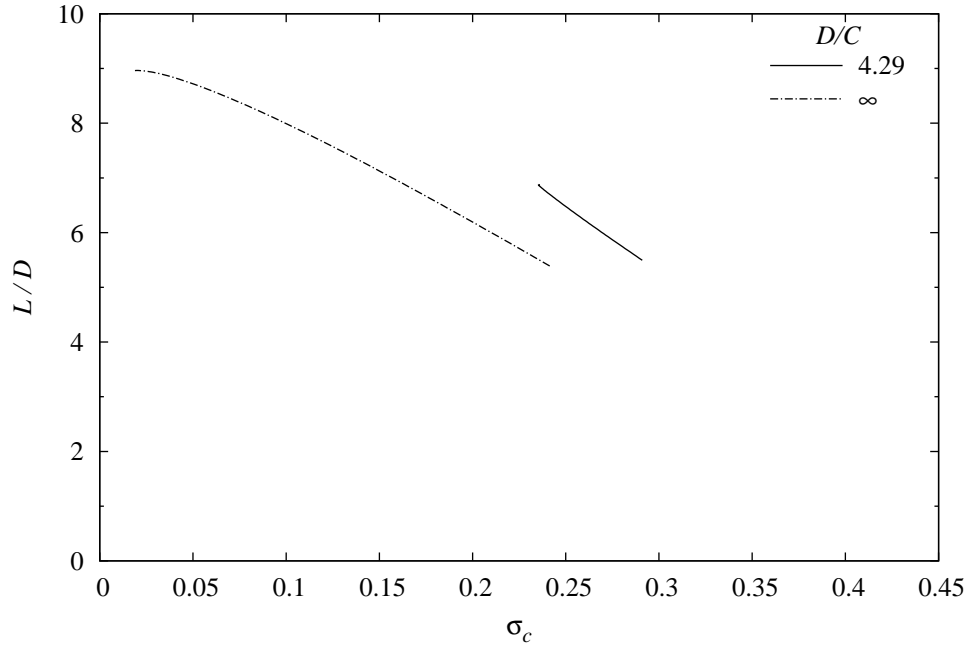
D.2.3 Hydrodynamic Data

C_L , C_D and L/D versus σ_c ($\alpha = 0^\circ$) for:

- Figure D.23: Foil1
- Figure D.24: Foil2
- Figure D.25: Foil3
- Figure D.26: Foil4
- Figure D.27: Foil5.

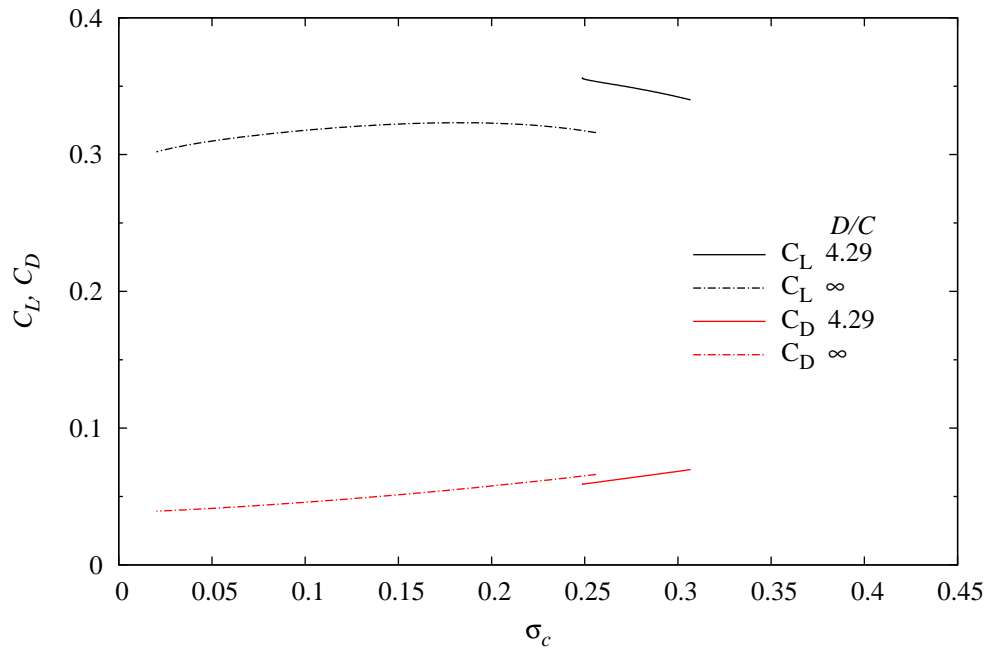


(a) C_L and C_D versus σ_c .

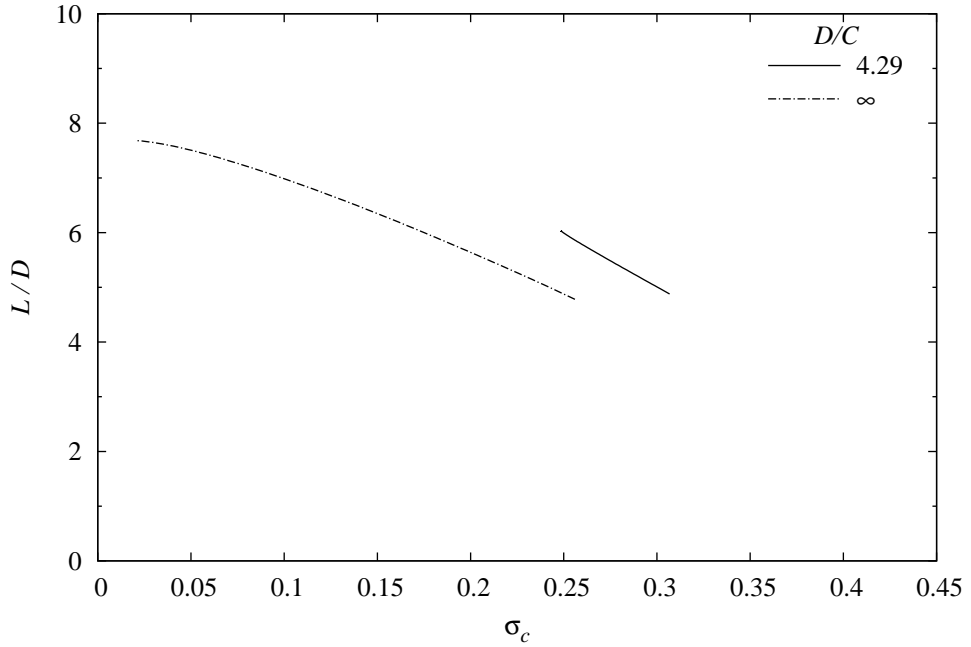


(b) L/D versus σ_c .

Figure D.23: C_L , C_D and L/D versus σ_c for model 'Foil1' at zero incidence. Comparison of the model in CRL water tunnel ($D/c = 4.29$) with the infinite flow case. (Foil1 geometry: $t/c = 20\%$, $\gamma = 3^\circ$ and $h/c = 1\%$).



(a) C_L and C_D versus σ_c .



(b) L/D versus σ_c .

Figure D.24: C_L , C_D and L/D versus σ_c for model ‘Foil2’ at zero incidence. Comparison of the model in CRL water tunnel ($D/c = 4.29$) with the infinite flow case. (Foil2 geometry: $t/c = 20\%$, $\gamma = 4^\circ$ and $h/c = 1\%$).

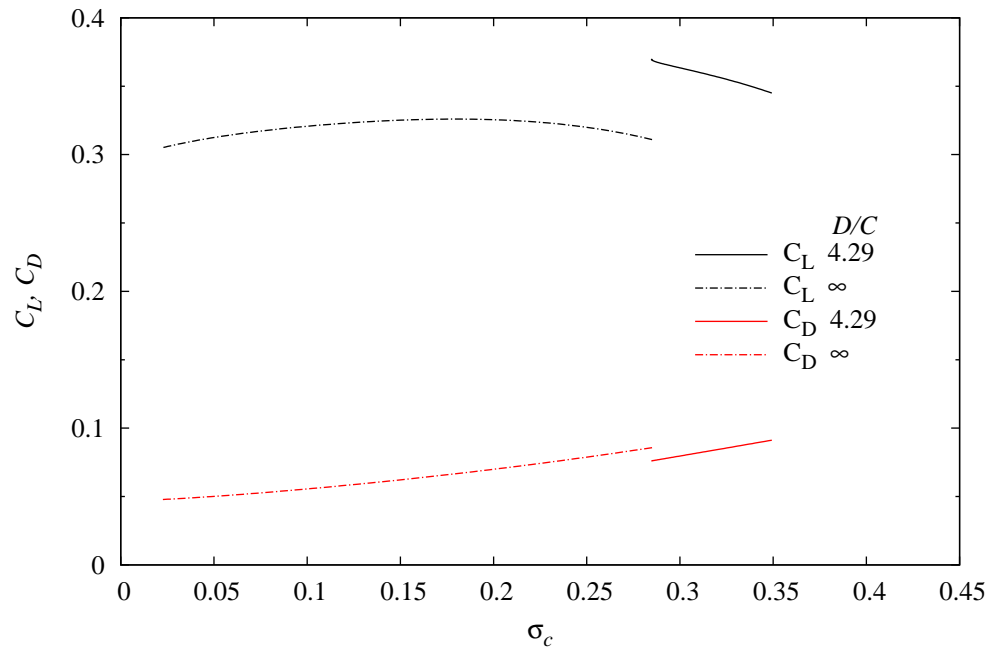
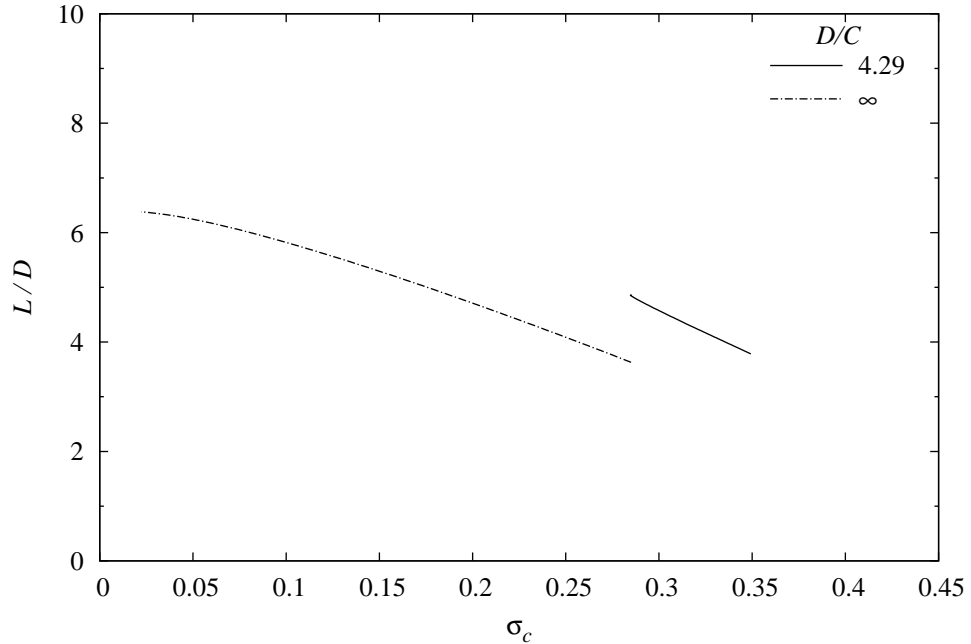
(a) C_L and C_D versus σ_c .(b) L/D versus σ_c .

Figure D.25: C_L , C_D and L/D versus σ_c for model 'Foil3' at zero incidence. Comparison of the model in CRL water tunnel ($D/c = 4.29$) with the infinite flow case. (Foil3 geometry: $t/c = 25\%$, $\gamma = 4^\circ$ and $h/c = 1\%$).

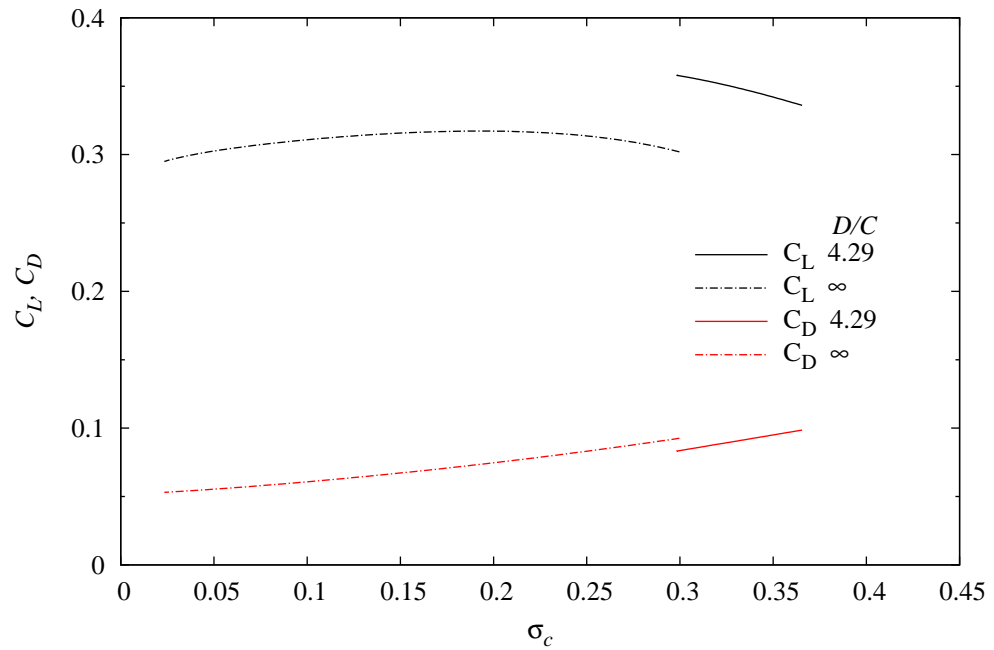
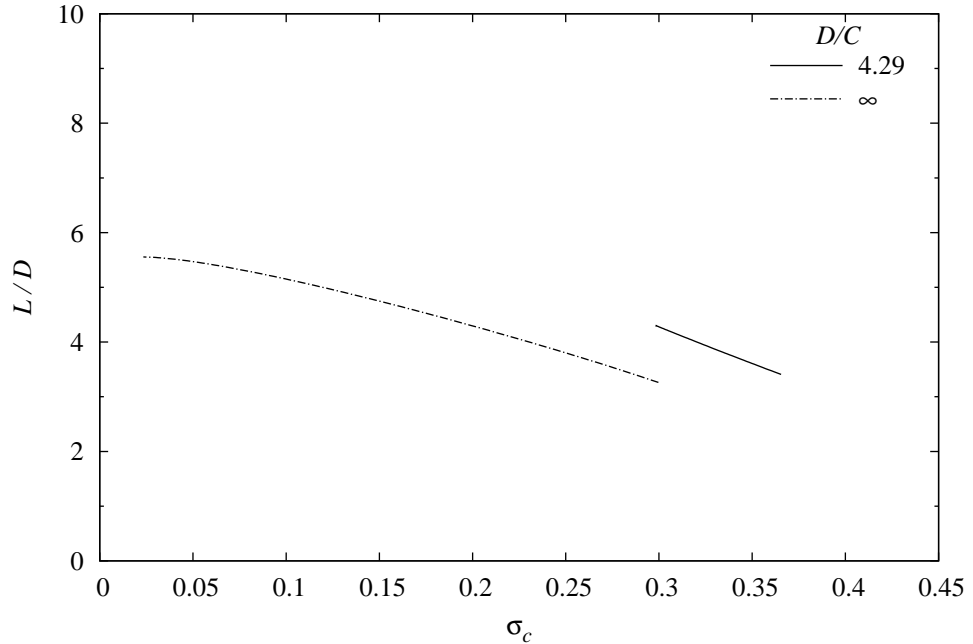
(a) C_L and C_D versus σ_c .(b) L/D versus σ_c .

Figure D.26: C_L , C_D and L/D versus σ_c for model 'Foil4' at zero incidence. Comparison of the model in CRL water tunnel ($D/c = 4.29$) with the infinite flow case. (Foil4 geometry: $t/c = 25\%$, $\gamma = 5^\circ$ and $h/c = 1\%$).

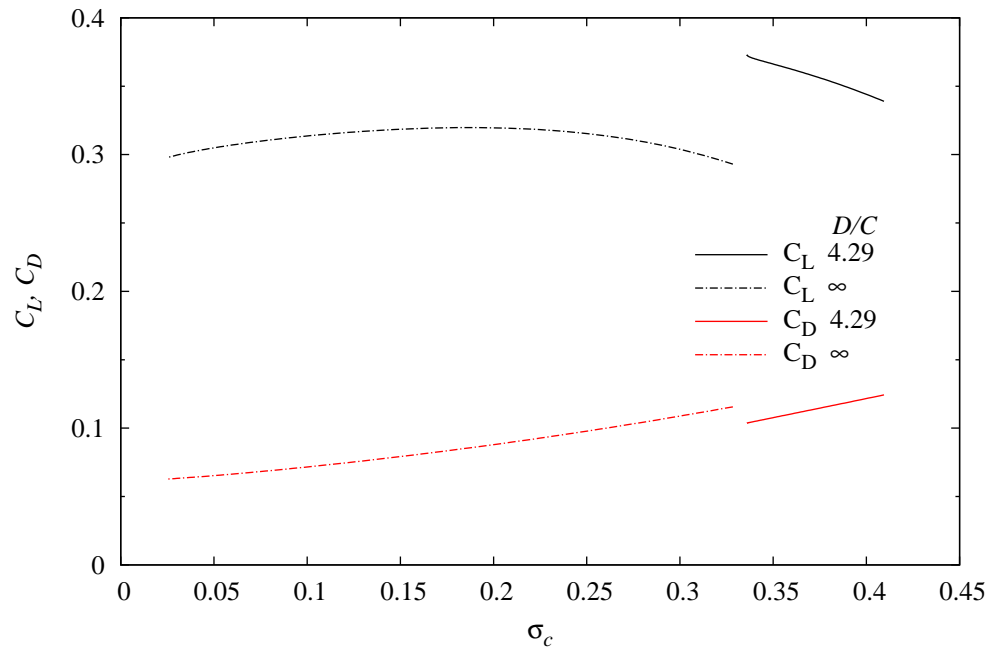
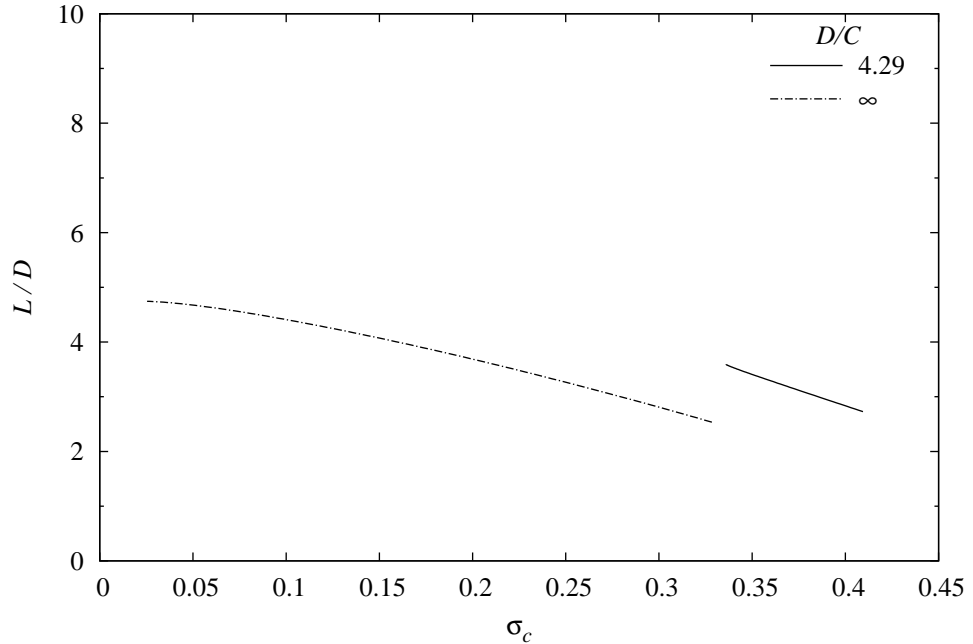
(a) C_L and C_D versus σ_c .(b) L/D versus σ_c .

Figure D.27: C_L , C_D and L/D versus σ_c for model 'Foil5' at zero incidence. Comparison of the model in CRL water tunnel ($D/c = 4.29$) with the infinite flow case. (Foil5 geometry: $t/c = 30\%$, $\gamma = 5^\circ$ and $h/c = 1\%$).

Appendix E

Numerical analysis of basic base-ventilated supercavitating foil sections

E.1 Introduction

A preliminary two-dimensional analysis was performed to assess the effect of various geometric parameters on the hydrodynamic performance of an intercepted supercavitating foil. The selection of the foil cross-section was determined by consideration of the following aspects.

- Section symmetry
- Positive derivative at trailing edge (to ensure a favourable pressure gradient along the foil surface to maintain flow attachment up to the cavity separation points)
- Effect of thickness to chord ratio
- Effect of leading edge radius.

E.2 Foil Geometry

To assess the effect of these geometric parameters two basic mathematically defined foil profiles were selected for analysis. Both of these functions enabled the first derivative at the trailing edge, z'_{te} , as well as the trailing edge thickness for the half-foil, t^* , to be prescribed. For the same z'_{te} and t^* the functions used gave foil shapes with differing leading edge radii, i.e. one sharper than the other. To obtain the complete symmetrical foil profile the resulting curves were mirrored about the horizontal axis.

One foil definition curve used was that defined by a single term n^{th} order polynomial as defined by equation E.1 and shown in Figure E.1.

$$z = ax^{1/n} \quad (\text{E.1})$$

where $a = t^*$ and $n = t^*/z'_{te}$

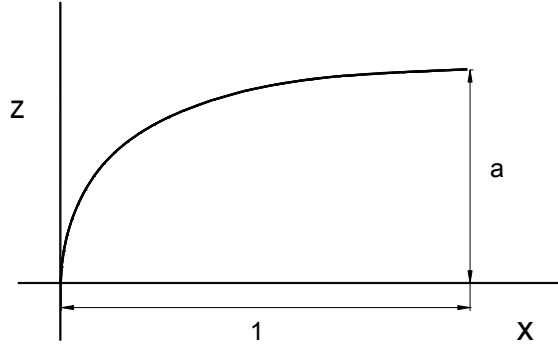


Figure E.1: Foil curve 1 - Single term n^{th} order polynomial.

The second foil shape was defined by taking a portion of an ellipse as defined by equation E.2 and is shown in Figure E.2.

$$z = b\sqrt{1-x^2} \quad (\text{E.2})$$

With a major axis of length $a = 1$ then the portion of the ellipse to give the required foil shape is obtained with

$$t^*/c = z/(1-x) \quad \text{giving} \quad b = \sqrt{t^*/c^2 - 2t^*/cz'_{te}}$$

To each base foil section curve a ramp was added at the trailing edge of one surface to represent the influence of the presence of the interceptor on the flow field. This ramp curve was defined as a single term n^{th} -order polynomial as follows

$$z = ax^n \quad (\text{E.3})$$

with $a = h/l_r$ and $n = z'_{rte}/h/l_r$

An example of the foil shapes produced by this procedure is given in Figure E.3. Both of these foils have the same t/c and γ and the ramp added to the lower surface. The foil derived from the ellipse is the sharper of the two, i.e. the foil with the smaller leading edge radius.

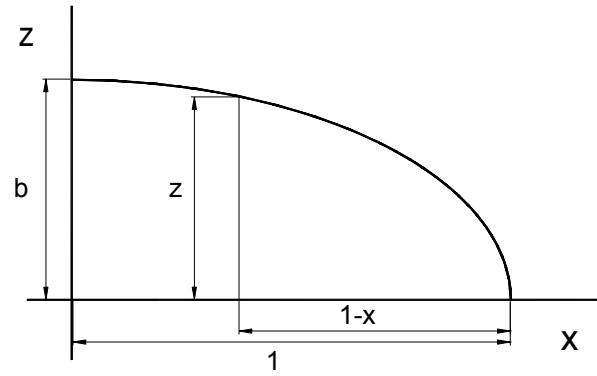


Figure E.2: Foil curve 2 - Ellipse portion.

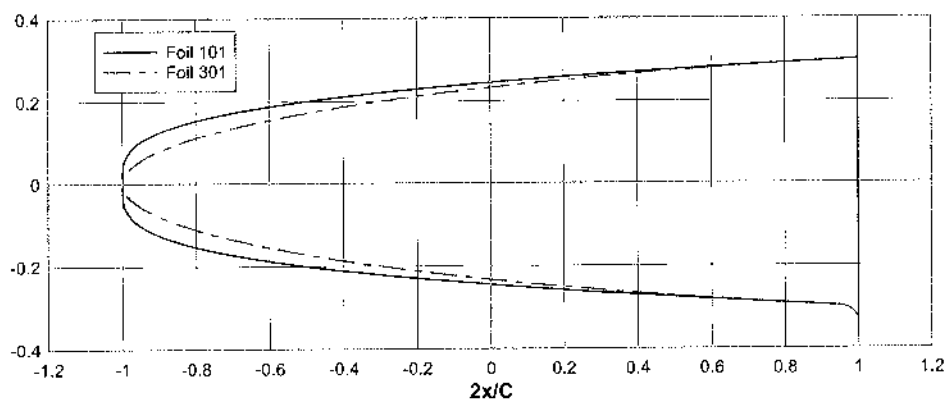


Figure E.3: Foil profile geometry for preliminary analysis.

E.3 Numerical Analysis

The analysis was performed using the boundary element code SUPCAVF. A description of SUPCAVF is given in Chapter 2. For a description of the surface discretization used and the convergence behaviour of the numerical solution refer to Section 4.5 where the main analysis is reported.

E.4 Parameter Space

The values of the geometric parameters determining the foil shapes that were analysed are listed in Table E.1. The ramp was set at a $h/c1.5$ and $h/l_r = 25\%$ for all cases. As shown in the first column the polynomial derived foils were designated the 1-series and the ellipse derived foils the 3-series. Foils 101 & 301 had identical values of all the geometric parameters whilst foil 102 varied only in the value of t/c and foil 311 varied only in the value of the ramp trailing edge angle, β . The range of foil incidence covered was $-2.5^\circ \leq \alpha \leq 2.5^\circ$ in increments of 0.5° .

| Foil | Form | t/c | γ | β |
|------|------------|-------|-------------|------------|
| 101 | Polynomial | 30% | 2.5° | 60° |
| 102 | Polynomial | 15% | 2.5° | 60° |
| 301 | Ellipse | 30% | 2.5° | 60° |
| 311 | Ellipse | 30% | 2.5° | 76° |

Table E.1: Foil section shape parameters.

E.5 Results

E.5.1 Cavity Shape

Figure E.4 shows a family of foil and cavity surface plots for Foil 301 at $\alpha = [^\circ 0]$ showing the effect of σ_c on cavity shape. An increase in cavity length, and to a lesser extent cavity thickness, results as σ_c is decreased. The general shape of the cavity surface is convex when viewed from the liquid. This is a necessary condition for a cavity shape to be valid as the pressure in the cavity is assumed to be the minimum in potential flow theory (Brennen, 1995; Milne-Thomson, 1968).

As the foil incidence is increased there is a point, α_{crit} , beyond which the cavity surface shape changes to be initially concave upon detachment from the foil trailing edge without fence. It then returns to the valid convex shape within approximately one chord length. An example of this inflection along the cavity surface is shown in Figure E.5. Within SUPCAVF the cavity surface detachment points are set at the foil trailing edges. In the cases where $\alpha > \alpha_{crit}$ the detachment point would move forward of the trailing edge along the foil

surface. This is an undesirable condition resulting in possibly sudden changes in the magnitude of hydrodynamic forces and moments occurring as has been found in experimental investigations on uncambered blunt-based foils (Johnson and Rasnick, 1959; Brentjes, 1962). To a lesser extent the same effect has also been observed on a cambered blunt-based foil (Lang and Daybell, 1961). From Figure E.5 the effect of the slope of the ramp trailing edge, β , can be seen. For the same value of σ_c the steeper ramp trailing edge produces a longer and slightly thicker cavity shape.

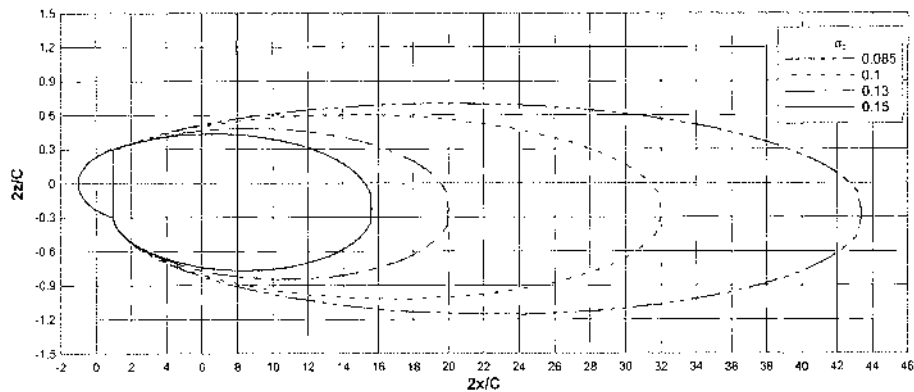


Figure E.4: Effect of σ_c on cavity shape - Foil 301, $\alpha = 0^\circ$.

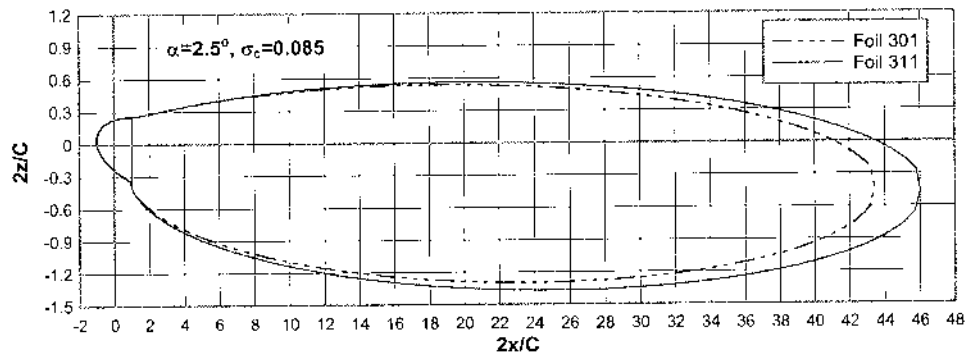


Figure E.5: Effect of δ_{te} on cavity shape - Foils 301 & 311, $\alpha = 2.5^\circ$, $\sigma_c = 0.085$.

E.5.2 Pressure Coefficients

Figure E.6 shows a family of pressure coefficient plots for Foil 301 at $\sigma_c = 0.1$. The adverse pressure gradients as seen on the foil low-pressure side are also indicative of possible cavity detachment forward of the trailing edge. If this does

occur then from the detachment point onwards, C_P would be equal to σ_c . This issue could only be investigated further numerically with the present method involving excessive assumptions and will be addressed in a future companion experimental program. Another issue with regards the C_P distributions obtained is the magnitude of the leading edge suction peaks at the higher angles of incidence. Vapour cavities may be formed at these positions if $-C_P \geq \sigma_c$. For a ride control foil with a 1m chord, operating at a water depth of 2m and speed of 40 knots, gives $\sigma_v = 0.6$. Foil 301 then would be likely to develop leading edge cavitation at angles of incidence above 1.5° . Both of these effects would serve to limit the development of lift by reducing or limiting the negative pressure acting on the suction side of the foil. Figure E.7 shows that for both foil shapes $C_{P_{min}}$ is significantly affected by incidence over the range of σ_c analysed. This results in a limit to the amount positive incidence due to leading edge cavitation occurrence. The elliptical shape (Foil 301) shows the better performance between the two profiles in this regard.

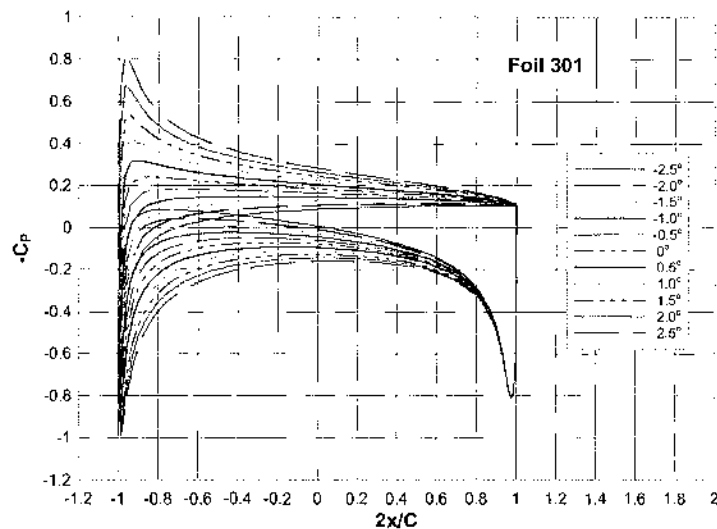


Figure E.6: C_P distribution over Foil 301, $-2.5^\circ < \alpha < 2.5^\circ$, $\sigma_c = 0.1$.

E.5.3 Hydrodynamic Forces

Plots of C_L , C_D & L/D versus α for Foils 101 and 301 are shown in Figures E.8 and E.9. From these results it is observed, as expected, that C_L & L/D are significantly affected by incidence. The effect of σ_c is only slight however showing an increase in L/D and decrease in both C_L & C_D as σ_c is reduced. The L/D shows an upward trend due to the relatively larger reduction in C_D compared with C_L . While the L/D for the polynomial foil (Foil 101) is better, this foil is likely to suffer from leading edge cavitation for all positive angles of incidence.

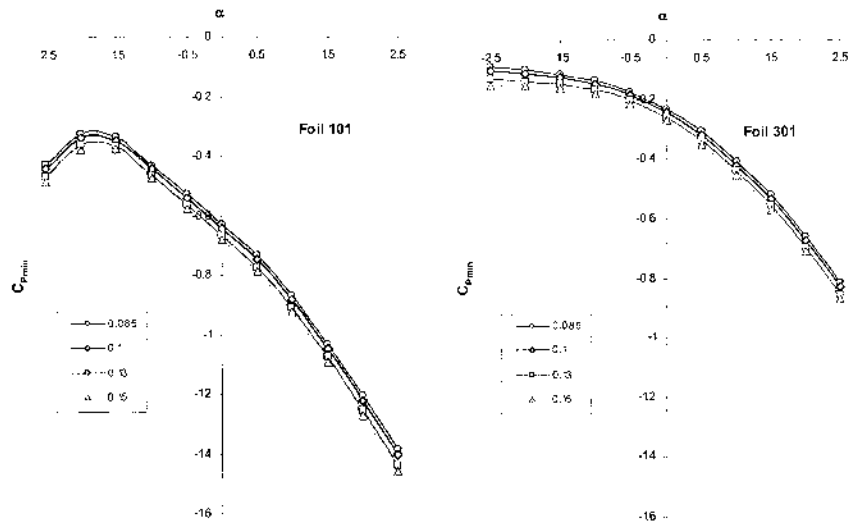


Figure E.7: $C_{p_{min}}$ versus α .

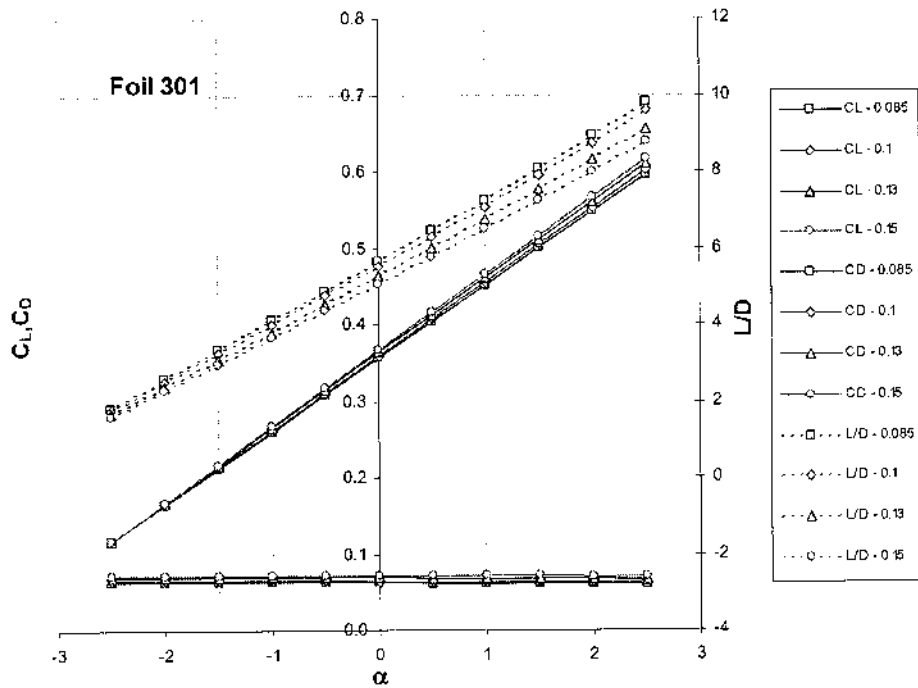


Figure E.8: Hydrodynamic force coefficients and efficiency as a function of α for Foil 301.

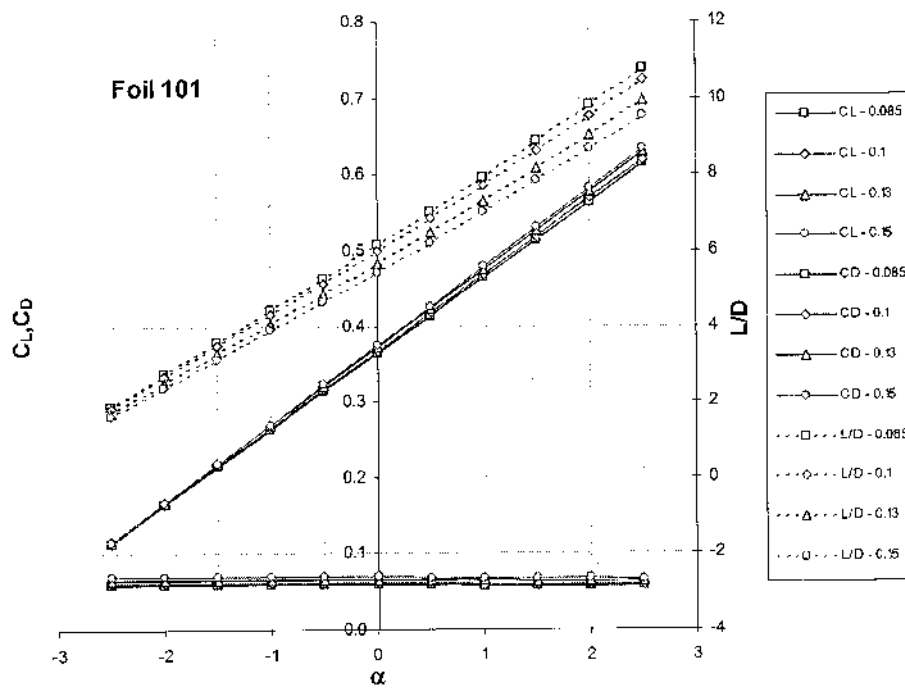


Figure E.9: Hydrodynamic force coefficients and efficiency as a function of α for Foil 101.

The effect of t/c on L/D is shown in Figure E.10 with Foil 102 having a thickness half that of Foil 101. Reducing the foil thickness improves the L/D but has an adverse effect on the likelihood of leading edge cavitation occurring as shown in Figure E.11. This demonstrates the trade off between efficiency and serviceability (L/D & C_{pmin}) between the two profiles examined.

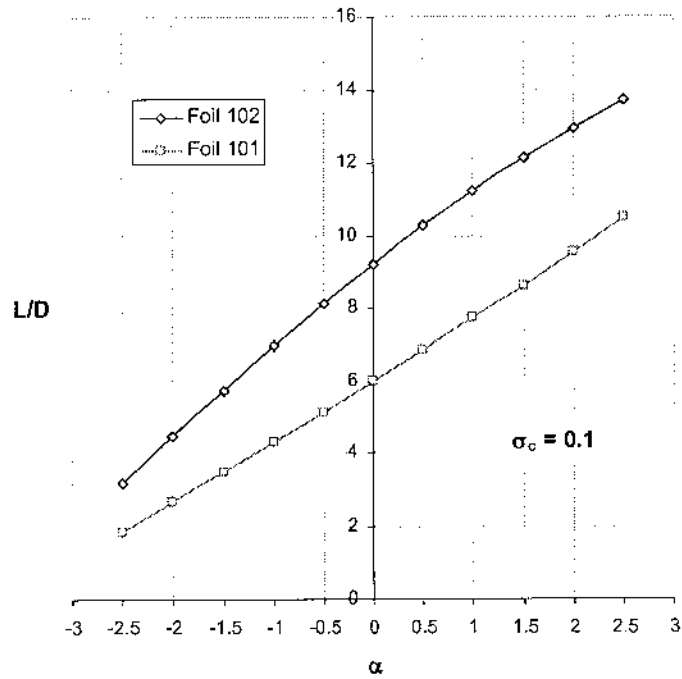


Figure E.10: L/D versus α for Foils 101 & 102 at $\sigma_c = 0.1$.

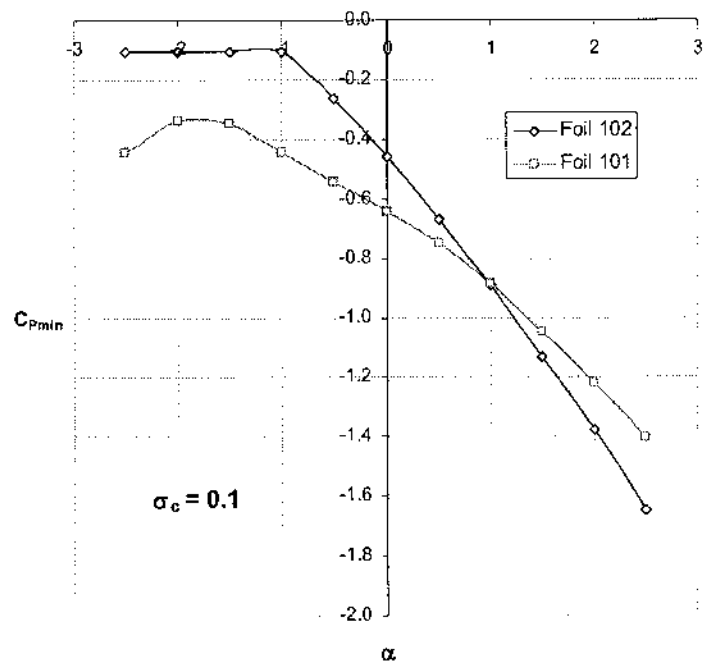


Figure E.11: C_{pmin} versus α for Foils 101 & 102 at $\sigma_c = 0.1$.

Bibliography

- Abbott, I. H. and A. E. von Doenhoff (1959). *Theory of Wing Sections (Including a summary of airfoil data)*. New York: Dover Publications, Inc.
- Acosta, A. J. (1973). Hydrofoils and hydrofoil craft. *Annual Review of Fluid Mechanics* 5, 161–184.
- Acosta, A. J. and O. Furuya (1975). A note on three-dimensional supercavitating hydrofoils. *Journal of Ship Research* 19(3), 164–165.
- Ai, D. K. (1966). The wall effect in cavity flows. *Journal of Basic Engineering* 88, 132–138.
- Ai, D. K. and Z. L. Harrison (1965). The wall effect in cavity flow. Report 111.3, Hydrodynamics Laboratory, California Institute of Technology.
- ANSYS (2009). *ANSYS CFX-Solver Theory Guide, Release 12.1*. Canonsburg, USA: ANSYS Inc.
- Arie, M. and H. Rouse (1956). Experiments on two-dimensional flow over a normal wall. *Journal of Fluid Mechanics* 1, 129–141.
- Athavale, M. M., H. Y. Li, Y. Jiang, and A. K. Singhal (2002). Application of the full cavitation model to pumps and inducers. *International Journal of Rotating Machinery* 8(1), 45–56.
- Auslaender, J. (1962). Low drag supercavitating hydrofoil sections. Technical Report 001-7, Hydronautics Inc.
- Baker, E. S. (1977). Review of wall effects on fully developed cavity flows. In B. Johnson and B. Nehrling (Eds.), *18th American Towing Tank Conference*, Volume 2, Annapolis, Maryland, pp. 309–348.
- Bakir, F., R. Rey, A. G. Gerber, T. Belamri, and B. Hutchinson (2004). Numerical and experimental investigations of the cavitating behavior of an inducer. *International Journal of Rotating Machinery* 10(1), 15–25.
- Barlow, J. B., J. Rae, W. H., and A. Pope (1999). *Low-speed Wind Tunnel Testing* (Third ed.). New York: John Wiley & Sons, Inc.

- Batchelor, G. K. (1967). *An Introduction to Fluid Dynamics*. Cambridge: Cambridge University Press.
- Birkhoff, G. (1950). *Hydrodynamics - A Study in Logic, Fact and Similitude*. New York: Dover Publications.
- Birkhoff, G., M. Plesset, and N. Simmon (1950). Wall effects in cavity flow – i. *Quarterly of Applied Mathematics* 8, 151–168.
- Birkhoff, G., M. Plesset, and N. Simmon (1952). Wall effects in cavity flow – ii. *Quarterly of Applied Mathematics* 9, 413–421.
- Birkhoff, G. and E. H. Zarantonello (1957). *Jets, Wakes, and Cavities*, Volume 2. New York: Academic Press Inc.
- Bradshaw, P. and F. Y. F. Wong (1972). The reattachment and relaxation of a turbulent shear layer. *Journal of Fluid Mechanics* 52(1), 113–135.
- Brandner, P. A., Y. Lecoffre, and G. J. Walker (2006). Development of an Australian National Facility for cavitation research. In *Sixth International Symposium on Cavitation - CAV2006*, MARIN, Wageningen, The Netherlands.
- Brandner, P. A., Y. Lecoffre, and G. J. Walker (2007). Design considerations in the development of a modern cavitation tunnel. In *16th Australasian Fluid Mechanics Conference*, Crown Plaza, Gold Coast, Australia, pp. 630–637.
- Brandner, P. A., G. Wright, B. Pearce, L. Goldsworthy, and G. J. Walker (2010). An experimental investigation of microbubble generation in a confined turbulent jet. In *17th Australasian Fluid Mechanics Conference*, Auckland, New Zealand. Paper No. 292.
- Brebbia, C. A. (1984). *The Boundary Element Method for Engineers* (2nd ed.). London: Pentech Press.
- Breivik, K. B. (2005). *Dynamic response of interceptors*. Msc thesis, Norwegian University of Science and Technology.
- Brennen, C. (1969). The dynamic balances of dissolved air and heat in natural cavity flows. *Journal of Fluid Mechanics* 37(1), 115–127.
- Brennen, C. E. (1995). *Cavitation and Bubble Dynamics*. Oxford University Press.
- Brentjes, J. (1962, June). Free-surface water tunnel studies of a family of base-ventilated hydrofoils. Internal Memorandum E-108.12, Hydrodynamics Laboratory, Karman Laboratory of Fluid Mechanics and Jet Propulsion, California Institute of Technology.

- Breslin, J. P. and P. Andersen (1994). *Hydrodynamics of Ship Propellers*. Cambridge Ocean Technology Series. Cambridge: Cambridge University Press.
- Brice, R. (2006). *Ventilated super-cavitating flow past a backward facing step*. Undergraduate thesis, Australian Maritime College.
- Brizzolara, S. (2003). Hydrodynamic analysis of interceptors with CFD methods. In *Seventh International Conference on Fast Sea Transportation - FAST 2003*, Naples, Italy, pp. 49–56.
- Castro, I. P. and J. E. Fackrell (1978). A note on two-dimensional fence flows, with emphasis on wall constraint. *Journal of Wind Engineering and Industrial Aerodynamics* 3(1), 1–20.
- Choi, J. K. and S. A. Kinnas (1998). Numerical water tunnel in two and three dimensions. *Journal of Ship Research* 42(2), 86–98.
- Christopher, K. W. (1961). Experimental investigation of a high-speed hydrofoil with parabolic thickness distribution and an aspect ratio of 3. Technical Note D-728, NASA.
- Conolly, A. C. (1975). Prospects for very-high-speed hydrofoils. *Marine Technology* 12(4), 367–377.
- Davis, M. R. (1980). Design of flat plate leading edges to avoid flow separation. *AIAA Journal* 18(5), 598–600.
- Dawson, T. E. and J. Bate, E. R. (1962). An experimental investigation of a fully cavitating two-dimensional flat plate hydrofoil near a free surface. Technical Report E-118.12, California Institute of Technology.
- Dengel, P., H. H. Fernholz, and J.-D. Vagt (1982). Turbulent and mean flow measurements in an incompressible axisymmetric boundary layer with incipient separation. In L. Bradbury, F. Durst, B. Launder, F. Schmidt, and J. Whitelaw (Eds.), *Turbulent Shear Flows* 3, pp. 225–236. Berlin: Springer-Verlag.
- Durst, F. and A. K. Rastogi (1980). Turbulent flow over two-dimensional fences. In L. Bradbury, F. Durst, B. Launder, F. Schmidt, and J. Whitelaw (Eds.), *Turbulent Shear Flows* 2, pp. 218–232. Berlin: Springer-Verlag.
- Elms, A. R. (1999). Improved hydrofoil device. *International Patent Number* WO 99/57007, World Intellectual Property Organisation.
- Elms, A. R. (2003). Personal communication.
- Fabula, A. G. (1961, March). Linearized theory of vented hydrofoils. NAVWEPS Report 7637, U.S. Naval Ordnance Test Station.

- Fage, A. and F. C. Johansen (1927). On the flow of air behind an inclined flat plate of infinite span. *Proceedings of the Royal Society. Series A* 116(773), 170–197.
- Faltinsen, O. M. (2005). *Hydrodynamics of high-speed marine vehicles*. Cambridge, Eng.: Cambridge University Press.
- Franc, J.-P. (2001). Partial cavity instabilities and re-entrant jet. In C. E. Brennen, R. Arndt, and S. Ceccio (Eds.), *Fourth International Symposium on Cavitation*, California Institute of Technology.
- Franc, J.-P. and J.-M. Michel (2004). *Fundamentals of Cavitation*. Fluid Mechanics and Its Applications. Dordrecht: Kluwer Academic Publishers.
- Fridman, G., K. Rozhdestvensky, and A. Shlyakhtenko (2007). Theory and practice of application of the interceptors on high-speed ships. In W. Cui, S. Dong, B. Kang, and M. Zhang (Eds.), *Ninth International Conference on Fast Sea Transportation - FAST2007*, Shanghai, China.
- Fridman, G. M. (1998). Matched asymptotics for two-dimensional planing hydrofoils with spoilers. *Journal of Fluid Mechanics* 358, 259–281.
- Gadd, G. E. and S. Grant (1965). Some experiments on cavities behind disks. *Journal of Fluid Mechanics* 23(4), 645–656.
- Gasser, D., H. Thomann, and P. Dengel (1993). Comparison of four methods to measure wall shear stress in a turbulent boundary layer with separation. *Experiments in Fluids* 15(1), 27–32.
- Gerontakos, P. and T. Lee (2008). Particle image velocimetry investigation of flow over unsteady airfoil with trailing-edge strip. *Experiments in Fluids* 44(4), 539–556.
- Glauert, H. (1947). *The elements of aerofoil and airscrew theory* (2nd ed.). Cambridge University Press.
- Good, M. C. and P. N. Joubert (1968). The form drag of two-dimensional bluff-plates immersed in turbulent boundary layers. *Journal of Fluid Mechanics* 31(3), 547–582.
- Hall, W. S. (1994). *The boundary element method*. Kluwer Academic Publisher.
- Hansvik, T. and S. Steen (2006). Use of interceptors and stepped hull to improve performance of high-speed planing catamarans. In *International Conference on High speed craft ACVs, WIGs and Hydrofoils*, London, UK, pp. 67–73. Royal Institution of Naval Architects.
- Helmholtz, H. (1868). On discontinuous movements of fluids. *Philosophical Magazine* 36, 337–346.

- Hess, J. L. (1990). Panel methods in computational fluid dynamics. *Annual Review of Fluid Mechanics* 22, 255–274.
- Hess, J. L. and A. M. O. Smith (1966). Calculation of potential flow about arbitrary bodies. *Progress in Aeronautical Sciences* 8, 1–138.
- Hsu, C. C. (1984). On wall effects in cavity flows. *Journal of Ship Research* 28(1), 70–75.
- Huang, T. T. (1965, December). Investigation of base vented hydrofoils. Technical Report 465-1, Hydronautics, Inc.
- Jacobs, A. F. G. (1985). The normal-force coefficient of a thin closed fence. *Boundary-Layer Meteorology* 32(4), 329–335.
- Johnson, V. E., J. (1957). Theoretical determination of low-drag supercavitating hydrofoils and their two-dimensional characteristics at zero cavitation number. Technical Memorandum RM-L57G11a, NACA.
- Johnson, V. E., J. (1958). The influence of depth of submersion, aspect ratio, and thickness on supercavitating hydrofoils operating at zero cavitation number. In *2nd Symposium on Naval Hydrodynamics*, Washington, U.S.A., pp. 317–366.
- Johnson, V. E., J. and T. Hsieh (1966). The influence of the trajectories of gas nuclei on cavitation inception. In R. D. Cooper and S. W. Doroff (Eds.), *Sixth Symposium on Naval Hydrodynamics*, pp. 163–182.
- Johnson, V. E., J. and S. E. Starley (1962). The design of base vented struts for high speed hydrofoil systems. In *Symposium on Air Cushion Vehicles and Hydrofoils*, Washington, D.C., pp. 35–57. Inst. of Aeronautical Sciences.
- Johnson, V. E. and T. A. Rasnick (1959). Investigation of a high-speed hydrofoil with parabolic thickness distribution. Technical Note D-119, NASA.
- Katz, J. and A. Plotkin (2001). *Low-Speed Aerodynamics* (2nd ed.), Volume 13 of *Cambridge Aerospace Series*. Cambridge, UK: Cambridge University Press.
- Kermeen, R. W. (1961). Experimental investigations of three-dimensional effects on cavitating hydrofoils. *Journal of Ship Research* 5(2), 22–43.
- Kim, H.-B. and S.-J. Lee (2001a). Hole diameter effect on flow characteristics of wake behind porous fences having the same porosity. *Fluid Dynamics Research* 28(6), 449–464.
- Kim, H. B. and S. J. Lee (2001b). Time-resolved velocity field measurements of separated flow in front of a vertical fence. *Experiments in Fluids* 31(3), 249–257.

- Kimura, K., T. Kawamura, A. Fujii, T. Taketani, and Z. Huang (2009). Study on unsteady cavitating flow simulation around marine propeller using a RANS CFD code. In *Seventh International Symposium on Cavitation - Cav2009*, University of Michigan, Ann Arbor, USA. Paper No. 68.
- Kinnas, S. A. (1998). The prediction of unsteady sheet cavitation. In J. Michel and H. Kato (Eds.), *Third International Symposium on Cavitation*, Volume 1, Grenoble, France, pp. 19–36.
- Kinnas, S. A. and N. E. Fine (1991). Non-linear analysis of the flow around partially or super-cavitating hydrofoils by a potential based panel method. In *Boundary Integral Methods – Theory and Applications (Symposium papers)*, pp. 289–300. Springer-Verlag.
- Kinnas, S. A. and N. E. Fine (1993). A numerical nonlinear analysis of the flow around two- and three-dimensional partially cavitating hydrofoils. *Journal of Fluid Mechanics* 254, 151–181.
- Kinnas, S. A. and C. H. Mazel (1993). Numerical versus experimental cavitation tunnel (A supercavitating hydrofoil experiment). *Journal of Fluids Engineering* 115(4), 760–765.
- Kirchhoff, G. (1869). Zur theorie freier flüssigkeitsstrahlen. *Journal für die reine und angewandte Mathematik* 70, 289–298.
- Kunz, R. F., D. A. Boger, T. S. Chyczewski, D. R. Stinebring, H. J. Gibeling, and T. R. Govindan (1999). Multi-phase CFD analysis of natural and ventilated cavitation about submerged bodies. In *3rd ASME/JSME Joint Fluids Engineering Conference*, San Francisco, California.
- Laali, A. R. and J. M. Michel (1984). Air entrainment in ventilated cavities: case of the fully developed “half-cavity”. *Journal of Fluids Engineering* 106, 327–335.
- Laberteaux, K. R. and S. L. Ceccio (2001). Partial cavity flows. Part 1. Cavities forming on models without spanwise variation. *Journal of Fluid Mechanics* 431, 1–41.
- Ladson, C. L., C. W. Brooks, A. S. Hill, and D. W. Sproles (1996). Computer program to obtain ordinates for NACA airfoils. Technical Memorandum 4741, NASA.
- Lamb, H. (1932). *Hydrodynamics* (sixth ed.). Cambridge: Cambridge University Press.
- Lang, T. G. (1959). Base-vented hydrofoils. Report NAVORD 6606, US Naval Ordnance Test Station.

- Lang, T. G. and D. A. Daybell (1961). Water tunnel tests of three vented hydrofoils in two-dimensional flow. *Journal of Ship Research* 5(3), 1–15.
- Largeau, J. F. and V. Moriniere (2007). Wall pressure fluctuations and topology in separated flows over a forward-facing step. *Experiments in Fluids* 42(1), 21–40.
- Lecoffre, Y. (1999). *Cavitation – Bubble Trackers*. Rotterdam/Brookfield: A.A. Balkema.
- Lee, C.-S., Y.-G. Kim, and J.-T. Lee (1992). A potential-based method for the analysis of a two-dimensional super- or partially-cavitating hydrofoil. *Journal of Ship Research* 36(2), 168–181.
- Lee, S.-J. and H.-B. Kim (1999). Laboratory measurements of velocity and turbulence field behind porous fences. *Journal of Wind Engineering and Industrial Aerodynamics* 80(3), 311–326.
- Lee, S.-J. and H.-C. Lim (2001). A numerical study on flow around a triangular prism located behind a porous fence. *Fluid Dynamics Research* 28(3), 209–221.
- Lee, S.-J., K.-C. Park, and C.-W. Park (2002). Wind tunnel observations about the shelter effect of porous fences on the sand particle movements. *Atmospheric Environment* 36(9), 1453–1463.
- Leehey, P. and T. S. Stellingner (1975). Force and moment measurements of supercavitating hydrofoils of finite span with comparison to theory. *Journal of Fluids Engineering* 97(4), 453–464.
- Li, Y., J. Wang, and P. Zhang (2003). Influences of mounting angles and locations on the effects of gurney flaps. *Journal of Aircraft* 40(3), 494–498.
- Lysdahl, L. A. (2005). *Interceptor characteristics with focus on lift and drag*. Project report, Norwegian University of Science and Technology.
- Maitre, T. and C. Pellone (2001). Numerical modelling of unsteady partial cavities behind a backward facing step. In C. E. Brennen, R. Arndt, and S. Ceccio (Eds.), *Fourth International Symposium on Cavitation*, California Institute of Technology.
- Miau, J. J. and M. N. Chen (1991). Flow structures behind a vertically oscillating fence immersed in a flat-plate turbulent boundary layer. *Experiments in Fluids* 11(2-3), 118–124.
- Miau, J. J., K. C. Lee, C. N. Chen, and J. H. Chou (1991). Control of separated flow by a two-dimensional oscillating flat plate. *AIAA Journal* 29(7), 1140–1149.

- Milne-Thomson, L. M. (1968). *Theoretical Hydrodynamics* (Fifth ed.). New York: Dover Publications, Inc.
- Moran, J. (1984). *An introduction to theoretical and computational aerodynamics*. New York: Wiley.
- Morgan, W. B. (1966). The testing of hydrofoils and propellers for fully-cavitating or ventilated operation. In *Eleventh International Towing Tank Conference*, Tokyo, Japan, pp. 202–218.
- Morino, L. and C.-C. Kuo (1974). Subsonic potential aerodynamics for complex configurations: A general theory. *AIAA Journal* 12(2), 191–197.
- Neuhart, D. H. and J. Pendergraft, O. C. (1988). A water tunnel study of gurney flaps. Technical Memorandum 4071, NASA.
- Nohmi, M., A. Goto, Y. Iga, and T. Ikohagi (2003). Cavitation CFD in a centrifugal pump. In *Fifth International Symposium on Cavitation - Cav2003*, Osaka, Japan, pp. OS-4–010.
- Ojha, S. K. and G. R. Shevare (1985). Exact solution for wind tunnel interference using the panel method. *Computers & Fluids* 13(1), 1–14.
- Økland, K. (2004). *Interceptors on planing and semi-planing craft*. Msc thesis, Norwegian University of Science and Technology.
- Pankhurst, R. C. and D. W. Holder (1952). *Wind Tunnel Technique: an account of experimental methods in low and high-speed wind tunnels*. London: Pitman and Sons.
- Park, C. W. and S. J. Lee (2001). The effects of a bottom gap and non-uniform porosity in a wind fence on the surface pressure of a triangular prism located behind the fence. *Journal of Wind Engineering and Industrial Aerodynamics* 89(13), 1137–1154.
- Park, C.-W. and S.-J. Lee (2002). Verification of the shelter effect of a wind-break on coal piles in the POSCO open storage yards at the Kwang-Yang works. *Atmospheric Environment* 36(13), 2171–2185.
- Parkin, B. R. (1956). Experiments on circular-arc and flat plate hydrofoils in noncavitating and full-cavity flows. Report 47-6, Hydrodynamics Laboratory, California Institute of Technology.
- Pearce, B. W. and P. A. Brandner (2007). Limitations on 2D super-cavitating hydrofoil performance. In *16th Australasian Fluid Mechanics Conference*, Crown Plaza, Gold Coast, Australia, pp. 1399–1404.

- Pearce, B. W., P. A. Brandner, and J. R. Binns (2010). A numerical investigation of the viscous 2-D cavitating flow over a wall-mounted fence. In *17th Australasian Fluid Mechanics Conference*, Auckland, New Zealand. Paper No. 305.
- Ramamurthy, A. S., R. Balachandar, and H. S. G. Ram (1991). Some characteristics of flow past backward facing steps including cavitation effects. *Journal of Fluids Engineering* 113(2), 278–284.
- Ranga Raju, K. G., J. Loeser, and E. J. Plate (1976). Velocity profiles and fence drag for a turbulent boundary layer along smooth and rough flat plates. *Journal of Fluid Mechanics* 76(2), 383–399.
- Reboud, J.-L., B. Stutz, and O. Coutier (1998). Two-phase flow structure of cavitation: Experiment and modelling of unsteady effects. In J. Michel and H. Kato (Eds.), *Third International Symposium on Cavitation*, Volume 1, Grenoble, France, pp. 203–208.
- Robertson, J. M. (1965). *Hydrodynamics in Theory and Application*. Prentice-Hall International Series in Theoretical and Applied Mechanics – Fluid Mechanics Series. N.J.: Prentice-Hall Inc.
- Roshko, A. (1954). A new hodograph for free-streamline theory. Technical Note 3168, NACA.
- Rowe, A. (1979). Evaluation study of a three-speed hydrofoil with wetted upper side. *Journal of Ship Research* 23(1), 55–65.
- Rowe, A. and J.-L. Kueny (1980). Supercavitating hydrofoils with wetted upper sides. *Journal de Mécanique* 19(2), 249–294.
- Rowe, A. and J. M. Michel (1975). Two-dimensional base-vented hydrofoils near a free surface: Influence of the ventilation number. *Journal of Fluids Engineering* 97(4), 465–474.
- Rozhdestvensky, K. V. and G. M. Fridman (1991). Matched asymptotics for free surface lifting flows with spoilers. In T. Miloh (Ed.), *Mathematical approaches in hydrodynamics*, pp. 499–517. Philadelphia: SIAM - Society for Industrial and Applied Mathematics.
- Schiebe, F. R. and J. M. Wetzel (1961, December). Ventilated cavities on submerged three-dimensional hydrofoils. Technical Paper, Series B, no. 36, St. Anthony Falls Hydraulic Laboratory, University of Minnesota.
- Schlichting, H. and K. Gersten (2000). *Boundary-Layer Theory* (8th ed.). Berlin: Springer.
- Sims-Williams, D. B., A. J. White, and R. G. Dominy (1999). Gurney flap aerodynamic unsteadiness. *Sports Engineering* 2(4), 221–233.

- Singhal, A. K., M. M. Athavale, H. Li, and Y. Jiang (2002). Mathematical basis and validation of the full cavitation model. *Journal of Fluids Engineering* 124(3), 617–624.
- Sonnenberger, R. (2002). Simultaneous PIV- and pressure measurements upstream and downstream of a fence. In *11th International Symposium on Applications of Laser Techniques to Fluid Mechanics*, Lisbon, Portugal.
- Stack, J. and A. E. Von Doenhoff (1934). Tests of 16 related airfoils at high speeds. Report 492, NACA.
- Steen, S. (2007). Experimental investigation of interceptor performance. In W. Cui, S. Dong, B. Kang, and M. Zhang (Eds.), *Ninth International Conference on Fast Sea Transportation - FAST2007*, Shanghai, China, pp. 237–244.
- Storms, B. L. and C. S. Jang (1994). Lift enhancement of an airfoil using a gurney flap and vortex generators. *Journal of Aircraft* 31(3), 542–547.
- Swales, P. D., B. N. Cole, and G. L. Smith (1971). Some aspects of the ventilation of surface piercing rods and struts. *RINA Transactions* 113, 365–374.
- Swales, P. D., A. J. Wright, R. C. McGregor, and R. Rothblum (1974). The mechanism of ventilation inception on surface piercing foils. *Journal of Mechanical Engineering Science* 16(1), 18–24.
- Troolin, D. R., E. K. Longmire, and W. T. Lai (2006). Time resolved piv analysis of flow over a NACA 0015 airfoil with gurney flap. *Experiments in Fluids* 41(2), 241–254.
- Tryggvason, G., M. Sussman, and M. Y. Hussaini (2007). Immersed boundary methods for fluid interfaces. In A. Prosperetti and G. Tryggvason (Eds.), *Computational Methods for Multiphase Flow*, pp. 37–77. Cambridge University Press.
- Tsai, J.-F., J.-L. Hwang, S.-W. Chau, and S.-K. Chou (2001). Study of hydrofoil assistance for catamaran with stern flap and interceptor. In *Sixth International Conference on Fast Sea Transportation - FAST 2001*, Volume 3, Southampton, UK, pp. 69–78. RINA.
- Tsen, L. F. and M. Guilbaud (1974). A theoretical and experimental study on the planform of superventilated wings. *Journal of Ship Research* 18(3), 169–184.
- Tulin, M. P. (1953). Steady two-dimensional cavity flows about slender bodies. Report 834, DTMB.

- Tulin, M. P. (1955). Supercavitating flow past foils and struts. In *Symposium on Cavitation in Hydrodynamics*, Teddington, England. Paper No.16.
- Tulin, M. P. (1961). Supercavitating flows. In V. L. Streeter (Ed.), *Handbook of Fluid Dynamics* (First ed.), pp. 12.24–12.46. New York: McGraw-Hill Book company, Inc.
- Tulin, M. P. (1964). Supercavitating flows – small perturbation theory. *Journal of Ship Research* 7(3), 16–37.
- Uhlman, J. S., J. (1987). The surface singularity method applied to partially cavitating hydrofoils. *Journal of Ship Research* 31(2), 107–124.
- Uhlman, J. S., J. (1989). The surface singularity or boundary integral method applied to supercavitating hydrofoils. *Journal of Ship Research* 33(1), 16–20.
- Vallentine, H. R. (1969). *Applied Hydrodynamics* (Second ed.). London: Butterworths.
- van Dam, C. P. and D. T. Yen (1999). Gurney flap experiments on airfoils and wings. *Journal of Aircraft* 36(2), 484–486.
- Verron, J. and J.-M. Michel (1984). Base-vented hydrofoils of finite span under a free surface: an experimental investigation. *Journal of Ship Research* 28(2), 90–106.
- Wadlin, K. L. (1958). Mechanics of ventilation inception. In *2nd Symposium on Naval Hydrodynamics*, Washington, U.S.A., pp. 425–446.
- Watanabe, S., Y. Tsujimoto, and A. Furukawa (2001). Theoretical analysis of transitional and partial cavity instabilities. *Journal of Fluids Engineering* 123(3), 692–697.
- White, F. M. (2010). *Fluid Mechanics* (Seventh ed.). McGraw-Hill Series in Mechanical Engineering. New York: McGraw-Hill.
- Widmark, C. (2001). Interceptor steering - an efficient means of providing directional control of waterjet propelled craft. In *Waterjet Propulsion III, International Conference*, Gothenburg, Sweden, pp. 1–9. RINA.
- Woods, L. C. (1953a). Theory of aerofoil spoilers. Technical Report 2969, A.R.C.
- Woods, L. C. (1953b). Theory of aerofoils on which occur bubbles of stationary air. Technical Report 3049, A.R.C.
- Wu, T. Y.-T. (1956). A free streamline theory for two-dimensional fully cavitating hydrofoils. *Journal of Mathematics and Physics* 35, 236–265.

- Wu, T. Y.-T. (1962). A wake model for free streamline flow theory. Part 1: Fully and partially developed wake flows and cavity flows past an oblique flat plate. *Journal of Fluid Mechanics* 13(2), 161–181.
- Wu, T. Y.-T. (1968). Inviscid cavity and wake flows. In M. Holt (Ed.), *Basic Developments in Fluid Dynamics*, Volume 2, pp. 1–116. New York: Academic Press.
- Wu, T. Y.-T., A. K. Whitney, and C. Brennen (1971). Cavity-flow wall effects and correction rules. *Journal of Fluid Mechanics* 49(2), 223–256.
- Yaragal, S. C., H. S. G. Ram, and K. K. Murthy (1997). An experimental investigation of flow fields downstream of solid and porous fences. *Journal of Wind Engineering and Industrial Aerodynamics* 66(2), 127–140.
- Young, A. C. H. and C. C. S. Song (1975). Gravity and free surface effects on a fully cavitating flow. *Journal of Fluids Engineering* 97(4), 492–500.
- Zaninovic, A. (1997). Interceptor and its influence on the propulsion of a high speed boat. In *Fourth International Symposium on High Speed Marine Vehicles - HSMV*, Volume 2, Sorrento, Italy, pp. 5.3–5.12.